1-10-2013 12:00 AM

A Study of Gamma Radiation Induced Carbon Steel Corrosion

Kevin Daub
The University of Western Ontario

Supervisor
Dr. J.C. Wren
The University of Western Ontario

Graduate Program in Chemistry
A thesis submitted in partial fulfillment of the requirements for the degree in Doctor of Philosophy

A STUDY OF GAMMA RADIATION INDUCED CARBON STEEL CORROSION

(Spine title: A Study of Gamma Radiation Induced Carbon Steel Corrosion)

(Thesis format: Integrated-Article)

by

Kevin J. Daub

Graduate Program in Chemistry

A thesis submitted in partial fulfillment
of the requirements for the degree of
Doctor of Philosophy

The School of Graduate and Postdoctoral Studies
The University of Western Ontario
London, Ontario, Canada

THE UNIVERSITY OF WESTERN ONTARIO
School of Graduate and Postdoctoral Studies

CERTIFICATE OF EXAMINATION

Supervisor	Examiners
Dr. Clara Wren	Dr. François Lagugné-Labarthet
Supervisory Committee	Dr. Oleg Semenikhin
Dr. Brian Pagenkopf	Dr. Andy (Xueliang) Sun
	Dr. John Scully

The thesis by

Kevin James Daub

entitled:

A STUDY OF GAMMA RADIATION INDUCED CARBON STEEL CORROSION

is accepted in partial fulfillment of the
requirements for the degree of
Doctor of Philosophy

Date_____ _____
Chair of the Thesis Examination Board

Abstract

This thesis presents work on the development of a mechanistic understanding of the effect of ionizing radiation on the aqueous corrosion kinetics of carbon steel. Exposed to ionizing radiation, water decomposes into a range of oxidizing (O_2, •OH, HO_2•, H_2O_2) to reducing (•e_{aq}^-, •O_2^-, •H) species. The production of the redox active species by radiolysis can have a significant effect on the corrosion behaviour of a metal. Of particular interest is the effect of radiolysis on corrosion when the solution environment, such as temperature, pH, and concentrations of chemical additives, changes over time. Since these solution parameters also affect the radiolysis behaviour, it was important to develop a clear understanding of separate effects of these parameters.

To achieve a better understanding, a number of electrochemical and surface analytical techniques were employed. The combination of electrochemical and surface analyses provided a picture of oxidation that largely resulted in the formation of a magnetite oxide layer, but the further oxidation, dissolution, and reactivity of the oxide was sensitive to all parameters studied. The production of water radiolysis products via gamma irradiation was seen to have a net oxidizing effect on the growing oxide film, increasing the oxide film resistance. At all temperatures studied, irradiation did not result in significant oxide structural changes or oxide film breakdown events.

Keywords:

carbon steel, iron oxides, film conversion, oxide dissolution, interfacial reactions, electrochemical reactions, water radiolysis

Co-Authorship Statement

This thesis includes published data (Chapters 3, 4, and 7) and manuscripts in preparation (Chapters 5, 6, and 8). For the published and prepared results I was the lead experimental investigator and writer. The research presented in Chapter 7 includes co-authored work. A fellow group member (Lei Wang) performed principal experimentation, with my assistance, while I performed a significant portion of data analysis and writing.

Acknowledgements

Firstly, I would like to thank my supervisor, Dr. Clara Wren, for offering her input, direction, and interpretation of my project throughout my years of study. I have learned countless things both personally and professionally working under her guidance. Clara always worked tirelessly to create a fulfilling graduate student experience. I have traveled to international conferences in North America and was given the opportunity to spend a term in South Korea. The opportunity to perform unique research and to travel across South Korea is an experience I will not forget.

Over my time as a graduate student I have had tremendous assistance from a number of people. Dr. Jeiwon Yeon from the Korean Atomic Energy Research Institute guided me through my time in Korea and was always there for support both in and out of the lab. Dr. David Shoesmith taught me an unbelievable amount through numerous undergraduate and graduate courses and helped guide me into the direction of corrosion research. Dr. Jamie Noël taught invaluable assets and skills, all the while maintaining a great sense of humor. Dr. Zack Qin helped guide many meetings on impedance when my understanding of results hit a wall. Finally, Dr. Xueyuan (John) Zhang provided great mentorship through all experimental studies during my graduate research.

I would also like to thank all the students, past and present, in the Wren lab. I am truly grateful to have worked with such a diverse group of fun people who were always there for support.

Table of Contents

Certificate of Examination ii

Abstract iii

Co-Authorship Statement iv

Acknowledgements v

Table of Contents vi

List of Symbols, Acronyms, and Iron Oxides xv

List of Tables xvii

List of Figures xvii

Chapter 1: Introduction 1

1.1 Thesis Objectives and Methods 1

1.2 Materials Background 3

1.2.1 Carbon Steel 3

1.2.2 Carbon Steel Corrosion 5

1.2.2.1 Iron Oxides 9

1.2.2.1.1 Magnetite (Fe_3O_4) 10

1.2.2.1.2 Maghemite (γ-Fe_2O_3) 11

1.2.2.1.3 Hematite (α-Fe_2O_3) 11

1.2.2.1.4 Goethite (α-FeOOH) 12

1.2.2.1.5 Lepidocrocite (γ-FeOOH) 13

1.2.2.1.6 Feroxyhyte (δ-FeOOH) 14

1.2.2.1.7 Green Rusts 14
1.2.2.2 Review of Iron Oxide Formation 15
1.3 Radiation and Water Radiolysis 19
1.3.1 Radiation Chemistry 19
1.3.2 Application of Research to the Nuclear Power Industry 24
1.3.2.1 Heat Transport System 24
1.3.2.2 Waste Disposal 27
1.3.3 Corrosion Studies of Steel in Radiation Environments 29
1.3.3.1 Low LET Exposure 29
1.3.3.1.1 Electrochemical Studies 29
1.3.3.1.2 Waste Disposal Corrosion Studies 34
1.3.3.2 High LET Exposure 36
1.4 References 38

Chapter 2: Experimental Principles and Details 44
2.1 Electrochemical Principles of Aqueous Corrosion 44
2.2 Electrochemical Techniques 53
2.2.1 Electrochemical Cell Setup 53
2.2.2 Corrosion Potential 54
2.2.3 Cyclic Voltammetry 55
2.2.4 Potentiostatic Polarization 56
2.2.5 Linear Polarization Measurements 56

2.2.6 Electrochemical Impedance Spectroscopy.....57
2.3 Surface Analysis.....62
2.3.1 Scanning Electron Microscopy.....62
2.3.2 Transmission Electron Microscopy.....63
2.3.3 X-ray Photoelectron Spectroscopy.....64
2.3.4 Raman Spectroscopy.....65
2.4 Experimental Procedures.....66
2.4.1 Electrochemical Cell.....66
2.4.2 Surface Analytical Instrumentation.....68
2.4.3 Solution Analysis.....68
2.5 References.....69

Chapter 3: Oxide Growth and Conversion on Carbon Steel as a Function of Temperature Over 25 and 80 °C under Ambient Pressure.....70

3.1 Introduction.....70
3.2 Experimental.....71
3.2.1 Solutions.....71
3.2.2 Procedure.....72
3.3 Results and Discussion.....72
3.3.1 Cyclic Voltammetry.....72
3.3.1.1 Anodic Peak A1.....77
3.3.1.2 Anodic Peak A2/Cathodic Peak C3.....81
3.3.1.3 Anodic Peak A3' and A3/Cathodic Peaks C1 and C2.....82

3.3.1.4 Anodic Peak A4 85

3.3.1.5 Potential Regions of Film Growth and Conversion 85

3.3.2 Current Behaviour During Potentiostatic Growth and EIS Analysis....86

3.3.2.1 Current Behaviour at –0.7 V_{SCE} in Ox I....88

3.3.2.2 Current Behaviour at –0.2 V_{SCE} in Ox II....89

3.3.2.3 Current Behaviour at 0.2 V_{SCE} in Ox III 91

3.3.3 Oxide Film Characterization by EIS 91

3.3.3.1 Film Growth at –0.7 V_{SCE} in Ox I....91

3.3.3.2 Film Growth at –0.2 V_{SCE} in Ox II....97

3.3.3.3 Film Growth at 0.2 V_{SCE} in Ox III 99

3.3.4 Surface Analysis....102

3.4 Conclusions....104

3.5 References....105

Chapter 4: Effects of γ-Radiation Versus H_2O_2 on Carbon Steel Corrosion 107

4.1 Introduction....107

4.2 Experimental....108

4.2.1 Solutions....108

4.2.2 Irradiation Source....108

4.2.3 Procedure....108

4.3 Results and Discussion 109

4.3.1 Electrochemical Growth and Conversion of Oxide on Carbon Steel 109

4.3.2 Corrosion Potential of Carbon Steel in a γ-Irradiation Field 110

4.3.3 Water Radiolysis in a γ-Irradiation Field 113

4.3.4 Corrosion Potential of Carbon Steel in H_2O_2 Solution 115

4.3.5 Comparison of E_{CORR} During Exposure to γ-Radiation and to H_2O_2 119

4.3.6 Oxide Film Growth and Conversion in H_2O_2Solutions 122

4.3.6.1 EIS and XPS Analyses 122

4.3.6.2 Linear Polarization and EIS 132

4.3.7 Comparison of the Influence of Exposure to Gamma Irradiation and to H_2O_2 on R_P 133

4.4 Conclusions 135

4.5 References 136

Chapter 5: Deconvoluting the Effects of pH, Temperature and Electrolyte Concentration on Carbon Steel Corrosion 138

5.1 Introduction 138

5.2 Experimental 139

5.2.1 Experimental Setup 139

5.2.2 Surface Analysis 142

5.3 Results 144

5.3.1 Corrosion at 80 °C 144

5.3.1.1 Effect of Electrolyte Concentration at pH 10.6 144

5.3.1.2 Effect of pH in 10 mM Borate Solutions 148

5.3.2 Corrosion at 150 °C 149

5.3.2.1 Varying Electrolyte Concentration at pH 10.6 149

5.3.2.2 Effect of pH.....155
5.4 Discussion.....157
5.4.1 Corrosion Potential and the Oxide Chemical Phase and Composition.....157
5.4.2 Competing Kinetics and Oxide Formation.....160
5.4.2.1 Effects of Temperature and pH on Metal Solubility.....160
5.4.2.2 Effect of pH on Oxide Growth.....162
5.4.2.3 Effect of Temperature on Oxide Growth.....164
5.4.2.4 Effect of Electrolyte Concentration on Oxide Growth.....165
5.5 Conclusions.....167
5.6 References.....168

Chapter 6: Varying Effect of γ-Irradiation on Carbon Steel Corrosion Depending on Solution pH, Temperature and Electrolyte Corrosion.....170

6.1 Introduction.....170
6.2 Experimental.....170
5.2.1 Cover Gas.....171
6.2.1.1 Argon Cover Gas.....171
6.2.1.2 Oxygen.....171
6.2.2 Gamma Radiation Source.....172
6.3 Results.....172
6.3.1 Corrosion at 80 °C.....172
6.3.1.1 Effect of Radiation and Electrolyte Concentration at pH 10.6.....172
6.3.1.2 Effect of Radiation at pH 8.4.....176

6.3.2 Corrosion at 150 °C....177
6.3.2.1 Effect of Radiation and Electrolyte Concentration at pH 10.6 177
6.3.2.2 Effect of Radiation with Varying pH....182
6.3.3 Corrosion at 150 °C in Aerated Conditions....183
6.4 Discussion....185
6.4.1 Initial Oxidation Process on a Bare Metal Surface....186
6.4.2 Prolonged Growth of an Oxide Film....187
6.4.2.1 Effect of pH with Irradiation....187
6.4.2.2 Effect of Temperature with Irradiation....190
6.4.3 Effect of the Oxidant....195
6.5 Conclusions....197
6.6 References....198

Chapter 7: Effect of Dissolved Ferrous Iron on Oxide Film Formation....200
7.1 Introduction....200
7.2 Experimental....201
7.2.1 Solutions....201
7.2.2 Procedure....201
7.3 Results and Discussion....202
7.3.1 Cyclic Voltammetry....202
7.3.2 Potentiostatic Film Growth....208
7.3.2.1 Experimental Results....208
7.3.2.2 Oxide Formation at –0.7 V_{SCE}....217

7.3.2.3 Oxide Formation at –0.5 V_{SCE} 225

7.3.2.4 Oxide Formation at 0.3 V_{SCE} 227

7.4 Conclusions 229

7.5 References 230

Chapter 8: Oxide Growth and Conversion on Carbon Steel as a Function of Temperature Between 100 and 280 °C 232

8.1 Introduction 232

8.2 Experimental 232

8.2.1 Pressure Vessel (Static Cell) 232

8.2.2 Solutions 234

8.2.3 Procedure 234

8.2.4 Korean Atomic Energy Research Institute (KAERI) Flow Cell 235

8.3 Results and Discussion 237

8.3.1 Cyclic Voltammetry 237

8.3.1.1 Anodic Peak A1 243

8.3.1.2 Anodic Peak A3’ and A3/Cathodic Peaks C1 and C2 245

8.3.1.4 Anodic Peak A4 247

8.3.2 Current Behaviour During Potentiostatic Growth and EIS Analysis 247

8.3.2.1 Current Behaviour in Ox I 250

8.3.2.2 Current Behaviour in Ox II 251

8.3.2.3 Current Behaviour in Ox III 252

8.3.2.4 Temperature Dependence of Steady-State Current 254

8.3.3 Oxide Film Characterization by EIS and Surface Analysis 255
8.3.3.1 Film Growth in Ox I.....256
8.3.3.2 Film Growth in Ox II 260
8.3.3.3 Film Growth in Ox III 262
8.4 Conclusions.....264
8.5 References.....265

Chapter 9: Summary and Future Work.....267
9.1 Summary.....267
9.2 Future Work.....270

Symbols, Acronyms, and Iron Oxides

Symbols

a_x	Activity of species x
a_A	Anodic transfer coefficient
a_C	Cathodic transfer coefficient
atm	Atmosphere pressure
$\overleftrightarrow{a}$	Transfer coefficient
$\overleftarrow{a}$	Transfer coefficient in reverse (anodic) direction
$\vec{a}$	Transfer coefficient in forward (cathodic) direction
C	Capacitance
°C	Degrees Celsius
E	Electrochemical potential
E_{amp}	Amplitude of EIS sinusoidal potential
E_{eq}	Equilibrium potential
E^o	Standard potential
E_{APP}	Applied potential
E_{CORR}	Corrosion potential
ΔE_{Ox}	Oxide potential drop
$\Delta E_{vibration}$	Vibrational energy gap
$E_{initial}$	Initial potential
E_{final}	Final potential
F	Faraday constant
Gy	Gray
$\Delta_r G$	Free energy change of a reaction
$\Delta_r G^o$	Standard free energy of a reaction
h	Plank constant
i	Current (density)
i_o	Exchange current
i_a	Anodic current
i_{amp}	EIS current amplitude
i_c	Cathodic current
i_{CORR}	Corrosion current
k	Rate constant
k_0	Pre-exponential factor
K_{eq}	Equilibrium constant
n	Number of electrons
Q	Charge

R	Universal gas constant
R_x	General resistance
R_P	Solution resistance
R_s	Solution resistance
R_{film}	Film resistance
t	Time
T	Absolute temperature (K)
V_{SCE}	Potential vs. SCE
Y_0	CPE parameter
Z	Impedance
Z’	Real impedance
Z’’	Imaginary impedance
Z_{CPE}	Impedance from CPE
α	CPE exponent
η	Overpotential
θ	Phase shift
λ	Debye length
ν	Light frequency
Φ	Work function
ω	Angular frequency

Acronyms

BE	Binding Energy
CANDU	CANada Deuterium Uranium
CPE	Constant Phase Element
CV	Cyclic Voltammetry/Voltammogram
EIS	Electrochemical Impedance Spectroscopy
HTS	Heat Transport System
IASCC	Irradiation-Assisted Stress Corrosion Cracking
KAERI	Korean Atomic Energy Research Insitute
KE	Kinetic Energy
LET	Linear Energy Transfer
LP	Linear Polarization
PTFE	Polytetrafluoroethylene
RID	Radiation Induced Depletion
RIS	Radiation Induced Segregation
SCC	Stress Corrosion Cracking

SCE	Saturated Calomel Electrode
SEM	Scanning Electron Microscopy
SHE	Standard Hydrogen Electrode
TEM	Transmission Electron Microscopy
XPS	X-Ray Photoelectron Spectroscopy

Iron Oxides

Fe_3O_4	Magnetite
α-Fe_2O_3	Hematite
γ-Fe_2O_3	Maghemite
α-FeOOH	Goethite
γ-FeOOH	Lepidocrocite
δ-FeOOH	Feroxyhyte

List of Tables

Table 5.1 Changes in pH for all solutions studied 142

Table 5.2 Iron Concentration in solution after 170 h 148

Table 5.3 Oxide thickness for samples corroded at 150 °C 154

Table 6.1 Changes in pH for all solutions studied 171

Table 6.2 Iron Concentration in solution after 170 h 176

Table 6.3 Oxide thickness for samples corroded at 150 °C 181

Table 6.4 Ratio of the Raman intensities at 540 cm^{-1} and 670 cm^{-1} 192

Table 7.1 Raman peaks (in wavenumbers) for iron oxides and hydroxides not studied as standards 215

List of Figures

Figure 1.1 The iron-iron carbide phase diagram 4

Figure 1.2 Solubility of hydrolyzed Fe^{II} and Fe^{III} as a function of pH at 25 °C 7

Figure 1.3 Pourbaix diagram of the Fe-H_2O system at 25 °C with all ions at an activity of 10^{-6} M. The area between the dashed lines is the region of water stability. Below the bottom dashed line water will be reduced to hydrogen and above the top dashed line water will be oxidized to oxygen. The potential scale is the standard hydrogen electrode (SHE) scale (see Chapter 2). This Pourbaix diagram assumes certain solid species to be present and much more complex diagrams can be generated with additional species.....8

Figure 1.4 Structure of magnetite: (a) Polyhedral model with alternating octahedral and tetrahedra-octahedra layers, (b) ball and stick model with the unit cell outlined, and (c) ball and stick model of the octahedra and tetrahedra arrangement 11

Figure 1.5 Structure of hematite: (a) hexagonal close packing of oxygen with cations in the octahedral interstices, (b) ball and stick model with the unit cell outlined, and (c) ball and stick model of the O_3-Fe-O_3-Fe-O_3 triplets 12

Figure 1.6 Structure of goethite: (a) Hexagonal close packed anion arrangement, (b) ball and stick model with the unit cell outlined, and (c) projection of the atomic structure on a single plane 13

Figure 1.7 Structure of lepidocrocite: (a) Arrangement of octahedral double chains in corrugated layers, with H-bonds between the layers, (b) ball and stick model with the unit cell outlined, and (c) projection of the atomic structure on a single plane 14

Figure 1.8 Structure of feroxyhyte: (a) Arrangement of octahedral layers and (b) projection of the atomic structure on a single plane 14

Figure 1.9 System of corroding iron in irradiated water 26

Figure 2.1 Current-potential relationship for a redox active species 48

Figure 2.2 Schematic of a three-electrode cell setup. 54

Figure 2.3 The potential-time profile applied in a cyclic voltammetry experiment 55

Figure 2.4 Relationship between the input sinusoidal voltage across (a) a resistor and (b) a capacitor and the current output 59

Figure 2.5 Relationship of real and imaginary components of impedance in a series one-RC circuit.....60

Figure 2.6 A (a) Nyquist plot and (b) Bode plot of a (c) one-time constant electrical equivalent circuit occurs 61

Figure 3.1 (a) Third and (b) first cycles of cyclic voltammograms recorded on carbon steel in Ar-sparged 0.01 M borate solution at pH 10.6. Cycles were recorded from –1.1 V_{SCE} to 0.4 V_{SCE} to –1.1 V_{SCE} at a scan rate of 5 $mV \cdot s^{-1}$. The arrow represents the direction of change when temperature increased from 25 °C to 50, 70, and 80 °C. See the text for the description of the labeled anodic and cathodic peaks.....74

Figure 3.2 Cyclic voltammograms recorded on carbon steel in Ar-sparged 0.01 M borate solution at pH 10.6 at (a) 25 °C, (b) 50 °C, (c) 70 °C, and (d) 80 °C. Shown are the scans as a function of five consecutive cycles (–1.1 V_{SCE} to 0.4 V_{SCE} to –1.1 V_{SCE}) recorded at a scan rate of 0.17 $mV \cdot s^{-1}$. The arrows show the direction of change as the number of cycles increased from 2 to 3, 4, and 5 75

Figure 3.3 Calculated equilibrium potentials for various iron redox reactions on the electrochemical potential scale; where the equilibrium potentials are indicated by vertical lines and the potential values are those at pH 10.6 and 25 ºC. The three oxidation potential regions are also indicated 77

Figure 3.4 Simplified schematic of the oxide/solution interface and electron hopping between Fe^{II} and Fe^{III} sites in the spinel structure. For simplification, O^{2-} is not shown in the schematics of the oxide.....79

Figure 3.5 Log current vs. log time during potentiostatic film growth at (a) –0.7 V_{SCE}, (b) –0.2 V_{SCE}, and (c) 0.2 V_{SCE}.....87

Figure 3.6 Electrochemical impedance spectra for the films grown at (a) –0.7 V_{SCE}, (b) –0.2 V_{SCE}, and (c) 0.2 V_{SCE} as a function of temperature after 35 h of film growth.....93

Figure 3.7 Equivalent circuit fitting results for the resistance and capacitance for potentiostatic film growth at -0.7_{SCE} V and 25 °C as a function of time. Inset is a single time-constant equivalent circuit fit to all EIS experimental data.....94

Figure 3.8 Equivalent circuit fitting results of (a) constant phase element CPE1 and (b) capacitance of films grown at –0.7 V_{SCE}, for all temperatures studied, as a function of time 95

Figure 3.9 Equivalent circuit fitting results for the resistance and capacitance of films grown at –0.2 V_{SCE}, for all temperatures, studied as a function of time.....98

Figure 3.10 Two equivalent circuits tested to fit to all EIS experimental data for the films grown at 0.2 V_{SCE}: (a) Circuit 2a and (b) Circuit 2b 100

Figure 3.11 Constant phase element CPE 2 equivalent circuit fitting results using Circuit 2b for films grown at 0.2 V_{SCE}, for all temperatures studied, as a function of time 101

Figure 3.12 SEM images of carbon steel surfaces following 7-d potentiostatic film growth at (a) –0.7 V_{SCE} (surface morphology), (b) –0.7 V_{SCE} (cross section), (c) –0.2 V_{SCE} (morphology) and (d) 0.2 V_{SCE} (morphology). The potentiostatic experiments were performed at 80 °C, pH 10.6 in Ar-sparged 0.01 M borate solutions 103

Figure 4.1 Corrosion potential as a function of time during and post 6 h irradiation and without irradiation. Prior to the E_{CORR} measurement, oxide films were grown potentiostatically at 0.2 V_{SCE}, –0.2 V_{SCE}, or –0.7 V_{SCE} 112

Figure 4.2 Concentration of water radiolysis products during and post 6 h irradiation. The lines indicate the calculated concentrations and the symbols represent the measured concentrations of H_2O_2. 113

Figure 4.3 E_{CORR} as a function of time following exposure to various concentrations of H_2O_2 for the films pre-grown potentiostatically at (a) –0.7 V_{SCE}, (b) –0.2 V_{SCE}, and (c) 0.2 V_{SCE}. [H_2O_2] ranged from 10^{-6} to 10^{-2} M. The concentrations added were, 10^{-6}, 10^{-5}, 10^{-4}, 10^{-3}, and 10^{-2} M. 116

Figure 4.4 Steady-state E_{CORR} as a function of [H_2O_2] for the films pre-grown potentiostatically for 2.5 h at –0.7 V_{SCE}, –0.2 V_{SCE}, and 0.2 V_{SCE} for 2.5 h 117

Figure 4.5 E_{CORR} observed (a) during and after exposure to 6 h γ-irradiation; and (b) during exposure to H_2O_2 for the films pre-grown at 0.2 V_{SCE}, –0.2 V_{SCE}, and –0.7 V_{SCE}. Two sets of data obtained in 10^{-4} M H_2O_2 and 10^{-6} M H_2O_2 are shown in (b) 119

Figure 4.6 Electrochemical impedance spectra for the film pre-grown at –0.7 V_{SCE} during exposure to [H_2O_2] of; (a) 1×10^{-6} M, (b) 1×10^{-4} M, and (c) 1×10^{-2} M. The EIS were taken at 0, 1, 8, 24, and 37 h after the addition of H_2O_2. The arrows show the progression of EIS spectra as a function of time. The initial experiment on each plot represents EIS run at the film growth potential (–0.7 V_{SCE}), before the addition of H_2O_2. The experimental data was fit with an equivalent circuit (inset) as described in the text. 123

Figure 4.7 Polarization resistance and capacitance determined from the equivalent circuit (Figure 8a inset) for films pre-grown at (a) –0.7 V_{SCE}, (b) –0.2 V_{SCE}, (c) 0.2 V_{SCE} after the addition of H_2O_2. [H_2O_2] = 1×10^{-6} M (×), 1×10^{-5} M (□), 1×10^{-4} M (◆), 1×10^{-3} M (△), and 1×10^{-2} M (★).....125

Figure 4.8 Steady-state a) polarization resistance and b) capacitance as a function of added H_2O_2 for the films pre-grown at (□) 0.2 V_{SCE}, (O) –0.2 V_{SCE}, and (Δ) –0.7 V_{SCE}. 127

Figure 4.9 High resolution XPS spectra for the Fe–2p region. The Fe–2p band around 710 eV from iron oxides/hydroxides was deconvoluted using reference XPS spectra. The inset figure represents the multiple-peak per oxide approach before their combination for our experimental analysis 129

Figure 4.10 Fitting analysis of high-resolution Fe-2p XPS spectra. The individual peak area contributions of γ-Fe_2O_3, γ-FeOOH, and Fe_3O_4 are summed and presented as a ratio 130

Figure 4.11 Comparison of R_P calculated from a) EIS and b) LP fitting after the addition of H_2O_2 to films pre-grown at –0.7 V_{SCE}. $[H_2O_2] = 1 \times 10^{-6}$ M (×), 1×10^{-5} M (□), 1×10^{-4} M (◆), 1×10^{-3} M (△), and 1×10^{-2} M (★) 133

Figure 4.12 Comparison of R_P values calculated from LP fitting a) during and after γ-irradiation and b) after the addition of H_2O_2 to pre-grown films 134

Figure 5.1 Schematic diagram of the experimental set-up, showing the test vial arrangement in the pressure vessel 140

Figure 5.2 Sample spectra for the Fe–2p region and deconvoluted contributions of Fe oxide and Fe^0 143

Figure 5.3 SEM micrographs of the carbon steel coupon surfaces after 66 and 170 h at 80 °C 145

Figure 5.4 Oxide thickness as a function of corrosion time and borate concentration determined by XPS analysis 146

Figure 5.5 **(**a) Sample Raman spectra of carbon steel coupon surfaces after exposure at 80 °C (concentrations of borate are labelled) and (b) Raman spectra of reference iron oxide minerals 147

Figure 5.6 High magnification SEM micrographs of steel coupon surfaces after 66 and 170 h corrosion at 150 °C 150

Figure 5.7 Low magnification SEM micrographs of steel coupon surfaces after 66 and 170 h corrosion at 150 °C 151

Figure 5.8 Raman spectra of carbon steel coupon surfaces after exposure for 170 h at 150 °C. Labelled are the pH and borate concentrations 152

Figure 5.9 SEM images of the cross section of the carbon steel coupons subject to 66 h corrosion at 150 °C for (a) pH 10.6, 10 mM borate, (b) pH 10.6, 0 mM borate, and (c) pH 8.4, 10 mM borate. Arrows indicate the oxide film 153

Figure 5.10 TEM images of the cross section of carbon steel coupons subject to 170 h corrosion at 150 °C for (a) pH 10.6 and 0 mM borate and (c) pH 6.0 and 0 mM borate. Also shown is (b) the interfacial region for pH 10.6 and 0 mM borate that was labelled in a red box in (a) and (d) the interfacial region for pH 6.0 and 0 mM borate that was labelled in a red box in (c) 154

Figure 5.11 SEM images of the cross section of the carbon steel coupons subject to 170 h corrosion at 150 °C for (a) pH 10.6, 0 mM borate and (b) pH 6.0, 0 mM borate. Arrows indicate the oxide film 157

Figure 5.12 Calculated equilibrium potentials for various iron redox reactions (at pH 10.6 and 25ºC) are indicated by vertical lines and oxidation potential regions are indicated at the bottom of the figure 158

Figure 5.13 Corrosion potential as a function of time for carbon steel in $pH_{25°C}$ 10.6 and 8.4 borate solutions at 25 °C and 80 °C.....159

Figure 5.14 (a) Schematic of oxide film growth involving the injection of Fe^{n+} at the metal/oxide interface and O^{2-} at the oxide/aqueous interface and (b) potential drop, ΔE_{ox}, across the oxide and overpotentials, η, at both interfaces.....160

Figure 5.15 Solubility of hydrolyzed Fe^{II} and Fe^{III} as a function of pH at 25 °C 161

Figure 6.1 SEM micrographs of the carbon steel coupon surfaces after 66 h in all solutions at 80 °C for irradiated and unirradiated experiments 173

Figure 6.2 Fitting analysis of high-resolution Fe-2p XPS spectra to determine the thickness of a Fe_3O_4 oxide layer 80 °C for (a) irradiated and (b) unirradiated experiments.....174

Figure 6.3 Sample Raman spectra of carbon steel coupon surfaces after exposure to all solutions at 80 °C for 170 h for (a) irradiated and (b) unirradiated experiments. The bracketed numbers are the magnification of the Raman intensity signal.....175

Figure 6.4 Low magnification SEM micrographs of the steel coupon surfaces after 66 h at 150 °C for irradiated and unirradiated experiments 178

Figure 6.5 High magnification SEM micrographs of the steel coupon surfaces in pH 10.6 10 mM borate at 150 °C for irradiated and unirradiated experiments178

Figure 6.6 SEM images of the cross section of the carbon steel coupons subject to 170 h heating at 150 °C for pH 10.6 0 mM borate and pH 10.6 10 mM borate for irradiated and unirradiated experiments 179

Figure 6.7 HRTEM images of the cross section of the carbon steel coupons subject to 170 h heating at 150 °C for pH 6.0 0 mM borate and pH 10.6 0 mM borate for irradiated and unirradiated experiments.....180

Figure 6.8 Raman spectra of carbon steel coupon surfaces after exposure for 66 h at 150 °C for (a) irradiated and (b) unirradiated experiments. Labelled are concentrations of borate and increase in magnification of intensity is indicated in brackets 181

Figure 6.9 SEM images of the cross section of the carbon steel coupons subject to 170 h heating at 150 °C for pH 6.0 0 mM borate and pH 8.4 10 mM borate for irradiated and unirradiated experiments 182

Figure 6.10 SEM micrographs of the steel coupon surfaces after 20 h at 150 °C in solutions of (a) pH 6.0 and (b) pH 7.0.....183

Figure 6.11 SEM micrographs of the carbon steel coupon surfaces in aerated systems subject to 66 h heating at 150 °C for pH 10.6 0 mM borate and pH 6.0 0 mM borate for irradiated and unirradiated experiments.....184

Figure 6.12 Raman spectra of the carbon steel coupon surfaces in aerated system after 66 h at 150 °C for irradiated and unirradiated experiments 184

Figure 6.13 Photographs of the carbon steel coupon surfaces in aerated system after 66 h at 150 °C under radiation conditions.....185

Figure 6.14 Corrosion potential as a function of time for carbon steel in $pH_{25°C}$ 10.6 borate solutions at 25 °C in deaerated solutions, aerated solutions, and under gamma irradiation.....191

Figure 6.15 Raman spectra of carbon steel coupon surfaces after room temperature radiation, followed by radiation exposure and heating at 150 °C for 170 h194

Figure 6.16 SEM micrographs of the carbon steel coupon surface and cross section after room temperature radiation, followed by radiation exposure and heating at 150 °C for 170 h. Shown are the (a) surface from pH 10.6 10 mM borate and (b) cross section from pH 10.6 0 mM borate.....195

Figure 7.1 CVs recorded on carbon steel in pH 8.4 borate solutions with (a) no initial $Fe^{2+}_{(aq)}$ or (b) 0.1 mM $Fe^{2+}_{(aq)}$. The CV scan rate was 5 $mV \cdot s^{-1}$ and the electrode was rotated at 200 rpm 203

Figure 7.2 CVs recorded on carbon steel in pH 8.4 borate solutions containing 0.1 mM $Fe^{2+}_{(aq)}$ with different sweep vertices of 0.4 V_{SCE}, 0.2 V_{SCE}, 0 V_{SCE}, and –0.2 V_{SCE}. The CV scan rate was 5 $mV \cdot s^{-1}$ and the electrode was rotated at 200 rpm 205

Figure 7.3 The (a,c) first and (b,d) fifth cycles for CVs recorded on carbon steel in pH 8.4 borate with (a,b) no initial $Fe^{2+}_{(aq)}$ or (c,d) 0.1 mM $Fe^{2+}_{(aq)}$. The CV scan rate was 5 $mV \cdot s^{-1}$ and a range of electrode rotation rates were employed 206

Figure 7.4 Calculated equilibrium potentials (vertical lines) for various iron redox reactions at pH 8.4 and 25°C 207

Figure 7.5 Log current vs. log time for films grown at: (a) –0.7 V_{SCE}, (b) –0.5 V_{SCE}, and (c) 0.3 V_{SCE} in pH 8.4 borate solutions with no initial $Fe^{2+}_{(aq)}$ or 0.1 mM $Fe^{2+}_{(aq)}$ 209

Figure 7.6 Bode and Nyquist plots obtained from EIS analysis for films grown at various potentials in pH 8.4 borate solutions with no initial $Fe^{2+}_{(aq)}$. The labels 1, 2, 3 correspond to 4, 8, and 14 h of immersion time respectively. Arrows for the Nyquist plots and impedance modulus in the Bode plots show the progression with time 211

Figure 7.7 Bode and Nyquist plots obtained from EIS analysis for films grown at various potentials in pH 8.4 borate solutions with 0.1 mM $Fe^{2+}_{(aq)}$. The labels 1, 2, 3 correspond to 4, 8, and 14 h of immersion time respectively. Arrows for the Nyquist plots and impedance modulus in the Bode plots show the progression with time 211

Figure 7.8 SEM micrographs of films grown for 22 h at various potentials in pH 8.4 borate solutions with 0 or 0.1 mM $Fe^{2+}_{(aq)}$ 213

Figure 7.9 Raman spectra of carbon steel films grown for 22 h at various potentials in pH 8.4 borate solutions with (a) no initial $Fe^{2+}_{(aq)}$ or (b) 0.1 mM $Fe^{2+}_{(aq)}$. These spectra are compared to the spectra of reference iron-oxide minerals at 25°C, (c). All spectra are shifted in magnitude to prevent overlap 214

Figure 7.10 High-resolution XPS spectra of Fe-2p containing experimental data, composite of Fe^{0}, $Fe^{II/III}$, and Fe^{III} fits, and weighted composite of all fitted peaks. Inset is the deconvoluted XPS spectra with fitting for individual iron oxides and hydroxides used to obtain the composition of oxidation states 216

Figure 7.11 XPS analysis results: (a,b) Fe^{0}, $Fe^{II/III}$, and Fe^{III} components of the Fe 2p band, (c) Fe^{0}/Fe ratio in the Fe 2p band, and (d) area ratio of $OH^{-}/(OH^{-}+O^{2-})$ in the O 1s band.....217

Figure 7.12 Schematic of proposed oxidation mechanism at (a) –0.7 V_{SCE}, (b) –0.5 V_{SCE}, and (c) 0.3 V_{SCE} and solutions (i) with pre dissolved $Fe^{2+}_{(aq)}$ and (ii) without pre dissolved $Fe^{2+}_{(aq)}$. Oxidation and reduction processes are labelled as solid red arrows and transport processes are labelled as dashed black arrows. For figures (b) and (c), some transport processes have been removed for figure clarity 221

Figure 8.1 Photograph labeling some key components of the high-temperature flow system developed at KAERI.....236

Figure 8.2 First (gray line) and third (black line) cycles of CVs at (a) 25 °C, (b) 80 °C, (c) 150 °C, and (d) 220 °C. All CVs were performed immediately after the system reached the desired temperature and were performed at a scan rate of 5 $mV \cdot s^{-1}$ 238

Figure 8.3 Calculated equilibrium potentials for various iron redox reactions on the electrochemical potential scale; where the equilibrium potentials are indicated by vertical lines and the potential values are those at pH 10.6 and 25 ºC. The three oxidation potential regions are also indicated 240

Figure 8.4 (a) First and (b) third cycles of CVs recorded at 220 °C at a scan rate of 5 $mV \cdot s^{-1}$. Compared are CVs recorded immediately after the system reached 220 °C (Before) and CVs recorded after a 7 d potentiostatic film growth of E_{APP} = –0.2 V_{SCE} (After).....242

Figure 8.5 CV recorded at 220 °C at a scan rate of 5 $mV \cdot s^{-1}$. The CV was recorded immediately after the system reached 220 °C 244

Figure 8.6 (a) First and (b) third cycles of CVs recorded at a scan rate of 5 $mV \cdot s^{-1}$ in the flow system. The CVs at both temperatures were recorded after a 6 h potentiostatic film growth of E_{APP} = –0.2 V_{SCE} 246

Figure 8.6 Log current vs. log time during potentiostatic film growth in the (a-c) autoclave system and (d-f) flow system. Film growth was recorded at (a,d) –0.7 V_{SCE}, (b,e) –0.2 V_{SCE}, and (c,f) 0.2 V_{SCE} 249

Figure 8.7 Arrhenius plot of measured steady state currents for 0.2 V_{SCE} and –0.2 V_{SCE} 255

Figure 8.8 Electrochemical impedance spectra for the films grown at (a) –0.7 V_{SCE}, (b) –0.2 V_{SCE}, and (c) 0.2 V_{SCE} as a function of temperature after 70 h of film growth. The equivalent circuit (d) that was fit to all data is shown.....256

Figure 8.9 Equivalent circuit fitting results for the resistance and capacitance for potentiostatic film growth at –0.7 V_{SCE} 257

Figure 8.10 Raman spectra of reference iron oxide minerals 258

Figure 8.11 Raman spectra and SEM micrographs of samples removed after film growth at 220 °C and potentials of (a) –0.7 V_{SCE}, (b) –0.2 V_{SCE}, and (c) 0.2 V_{SCE} 259

Figure 8.12 Equivalent circuit fitting results for the resistance and capacitance for potentiostatic film growth at –0.2 V_{SCE} 261

Figure 8.13 Equivalent circuit fitting results for the resistance and capacitance for potentiostatic film growth at 0.2 V_{SCE} 264

Chapter 1

Introduction

1.1 THESIS OBJECTIVES AND METHODS

The main goal of this thesis research was to develop a mechanistic understanding of the effect of ionizing radiation on the aqueous corrosion kinetics of carbon steel. Exposed to ionizing radiation, water decomposes into a range of oxidizing (O_2, •OH, HO_2•, H_2O_2) to reducing (•e_{aq}^-, •O_2^-, •H) species. The aqueous corrosion of a metal or alloy involves metal oxidation coupled with the reduction of aqueous species, including water. Thus, corrosion kinetics depend on the aqueous redox environment as well as metallurgical properties of carbon steel. The production of the redox active species by radiolysis can have a significant effect on the corrosion behaviour of a metal. While a range of individual studies have been performed on the effects of radiation on steel corrosion (reviewed in this chapter), they often lack a complete understanding of changing oxide film properties with the changing solution environment. Of particular interest is the effect of radiolysis on corrosion when the solution environment, such as temperature, pH, and concentrations of chemical additives, changes. Since these solution parameters also affect the radiolysis behaviour, it is important to develop a clear understanding of the separate effects of these parameters.

To achieve the objectives, a number of electrochemical and surface analytical techniques were employed, which are further described in Chapter 2. The experimental parameters studied, which are separated into individual chapters include:

- The effect of temperature on the oxide growth on carbon steel was examined. Studies were limited to ambient pressure and temperatures ≤ 80 °C. Both electrochemical and surface analyses were performed.
- The change in the corrosion potential of carbon steel when subjected to gamma irradiation at room temperature was examined. The oxides that formed were studied both electrochemically and using surface analysis. Further experiments on the role of the aqueous environment were performed with the use of chemical additives to simulate the effects of gamma irradiation.
- The effect of changing solution parameters on the corrosion of carbon steel at 80 °C and 150 °C was examined. Analysis focused on the effect of pH on iron dissolution, and on the effect of electrolyte concentration. A range of surface analytical techniques were employed to characterize the oxide films.
- The effects of gamma irradiation on the mechanism of carbon steel corrosion at 80 °C and 150 °C were studied. A range of surface analytical techniques were employed to characterize the oxide films.
- The effects of dissolved ferrous ions on the mechanism of carbon steel corrosion at room temperature using electrochemical techniques were studied. A range of surface analytical techniques were employed to characterize the oxide films.
- The effect of temperature on the oxide growth on carbon steel at temperatures ≥ 100 °C was examined. Electrochemical analysis was performed in pressurized environments. Additional analysis was performed with the use of a high-temperature pressurized flow system.

1.2 MATERIALS BACKGROUND

1.2.1 Carbon Steel

Carbon steel, also known as plain steel or mild steel, is an iron-based alloy containing small amounts of impurities such as Si, Mn, P and S [1]. As suggested in the name, carbon is the important secondary component of this alloy. Carbon molecules fit into interstitial sites within the body-centered cubic structure of crystalline iron [2]. This makes the material harder and inhibits dislocation movement, thereby increasing the strength of the alloy. Depending on its carbon content, steel is classified into three major categories: low-carbon steel (> 0.25 wt.% C), medium-carbon steel (between 0.25 and 0.6 wt.% C), and high-carbon steel (between 0.6 and 1.4 wt.% C) [1]. Low-carbon steels are produced in the greatest quantities and are commonly used for pipes, tubing, and casings [2]. Low-carbon steels are comparatively soft and weak, but they possess high ductility and toughness. Also, they are readily machinable and weldable, and the least expensive carbon steel to produce, since purity is a less rigorous requirement than it is for other carbon steels [1]. Medium-carbon steels are stronger than the low-carbon steels, but their ductility is lower [1]. High-carbon steels are the hardest, strongest, and least ductile of the carbon steels [1]. They are usually used in a hardened and tempered condition, are wear resistant, and can hold a sharp cutting edge [2]. The carbon steel used in this study, A516 Gr70, is a low-carbon steel with a carbon content of 0.23 %. Figure 1.1 shows the composition of carbon up to 6.70 wt% C, which corresponds to the formation of iron carbide, or cementite (Fe_3C). When slowly cooled, the microstructure of iron-carbon alloys consists of two phases: α iron and Fe_3C, where α iron is the body-centered cubic structure of iron, also called ferrite. The two phases form simultaneously

during the transformation and are referred to as pearlite. Mechanically, pearlite has properties intermediate between the soft, ductile ferrite and hard, brittle cementite because carbon atoms diffuse away from the 0.02 wt% ferrite regions and to the 6.7 wt% cementite layers, as the pearlite extends [3].

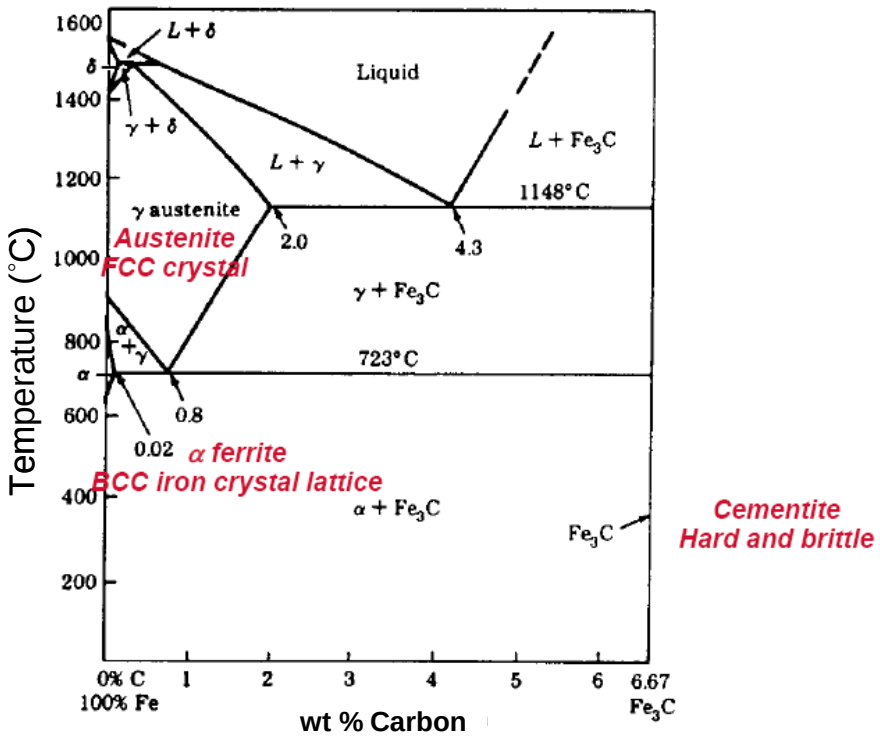

Figure 1.1: The iron-iron carbide phase diagram [3].

While having advantageous material properties, carbon steel does have limited corrosion resistance. In instances where higher corrosion resistance is required, chromium is added as an alloying element The resulting steel is referred to as stainless steel if the chromium content is above 11% [2]. Some of the literature reviewed in this

Chapter covers stainless steel. When the single term “steel” is used in the thesis it is in reference to both carbon steels and stainless steels.

1.2.2 Carbon Steel Corrosion

Corrosion is an important mechanism for carbon steel degradation and it frequently limits the possible applications and the useful lifetimes of carbon steel components. The mechanism of corrosion can vary greatly, but in general terms involves the oxidation of the metal [4]. Since carbon steel is largely composed of iron, corrosion is associated with the oxidation of that iron. The driving force for corrosion is the difference in the electrochemical potentials of the two reacting phases. When a bulk metal comes in contact with water having a different chemical potential than the metal phase, the two phases change their chemical states to reduce the inequality in electrochemical potential to reach equilibrium. This can be accomplished typically by the oxidation of the metal and reduction of aqueous species. The metal oxidation can be envisioned as,

$$M \rightarrow M^{n+} + ne^{-} \tag{1.1}$$

where M represents the solid metal, M^{n+} represents the oxidized metal species, and n is the number of electrons transferred. The reduction, involving an aqueous species such as water or dissolved oxygen, is illustrated by the reaction:

$$Ox + ne^{-} \rightarrow Red \tag{1.2}$$

where Ox represents the soluble oxidant and Red the reduced form of the oxidant.

The rate of the oxidation (anodic) reaction and the reduction (cathodic) reaction must be equal in terms of the number of electrons in order to satisfy the Law of

Conservation of Charge [5]. Since charge can move, typically electrons in the metal phase and ions in the water phase, the metal oxidation and the aqueous reduction do not necessarily have to occur at the same atomic sites. The result is a current flow. The potential difference developed at the reacting atomic sites are:

$$\Delta\phi_a = \phi_{M,a} - \phi_{S,a} \tag{1.3a}$$

$$\Delta\phi_c = \phi_{M,c} - \phi_{S,c} \tag{1.3b}$$

where $\Delta\phi_a$ and $\Delta\phi_c$ are the electrical potential differences between the metal and solution at the anodic and cathodic sites respectively and the subscripts a and c represent the anodic and cathodic sites and M and S represent the metal and solution phases [6]. The driving potential for the current in solution, $\Delta\phi_S$, (or in general, rate of corrosion), is:

$$\Delta\phi_S = \Delta\phi_c - \Delta\phi_a \tag{1.4}$$

In practice, the differences in potential at interfaces, $\Delta\phi$, are given values relative to a standard reference and the potentials are designated by E [6]. Further development of the fundamental equations and experimental techniques are discussed in Chapter 2.

Once formed, the oxidized metal, M^{n+}, can dissolve into the aqueous phase or combine with an oxygen or hydroxide ion to form an oxide/hydroxide layer. The extent of dissolution is highly dependent on the environment. For example, the hydrolyzed ferrous and ferric species are in an acid-base equilibrium and their relative solubility is highly pH dependent [7], Figure 1.2.

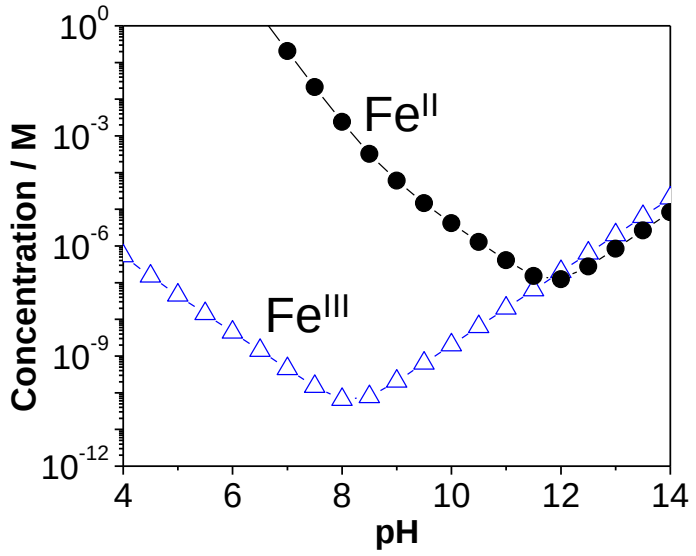

Figure 1.2: Solubility of hydrolyzed Fe^{II} and Fe^{III} as a function of pH at 25 °C.

If the solubility is not sufficiently high, an insoluble product (an oxide film) may be produced, slowing down the corrosion process and protecting, or passivating, the underlying metal. A metal is described as being passivated if it possesses a protective film that resists corrosion despite being in an environment where there is thermodynamic tendency to react [8]. The reason an oxide film can make a metal passive is because it slows the movement of cations from the base metal, through the oxide film, to the oxide/solution interface. This makes the loss of metal slow, or even negligible. To maintain the passivity, the oxide film itself must have low solubility. An extreme example of the benefits of passivation is the iron pillar of Delhi. It is composed of 98 % iron, yet it has withstood corrosion for 1600 years due to the formation of a passive oxide layer [9].

Thermodynamically, under most conditions, the most stable iron species in an iron and water system are iron oxides and oxyhydroxides. One of the most common ways to represent the thermodynamic stabilities of the different possible species is through a Pourbaix diagram. A Pourbaix diagram is a potential-pH diagram that shows the regions of potential and pH within which a particular species is the most thermodynamically stable. The diagram can be generated from the Nernst equations of the metal oxides [10]. The Nernst equation is derived in Chapter 2. A Pourbaix diagram for the Fe-H_2O system at 25 °C is presented in Figure 1.3 [10, 11].

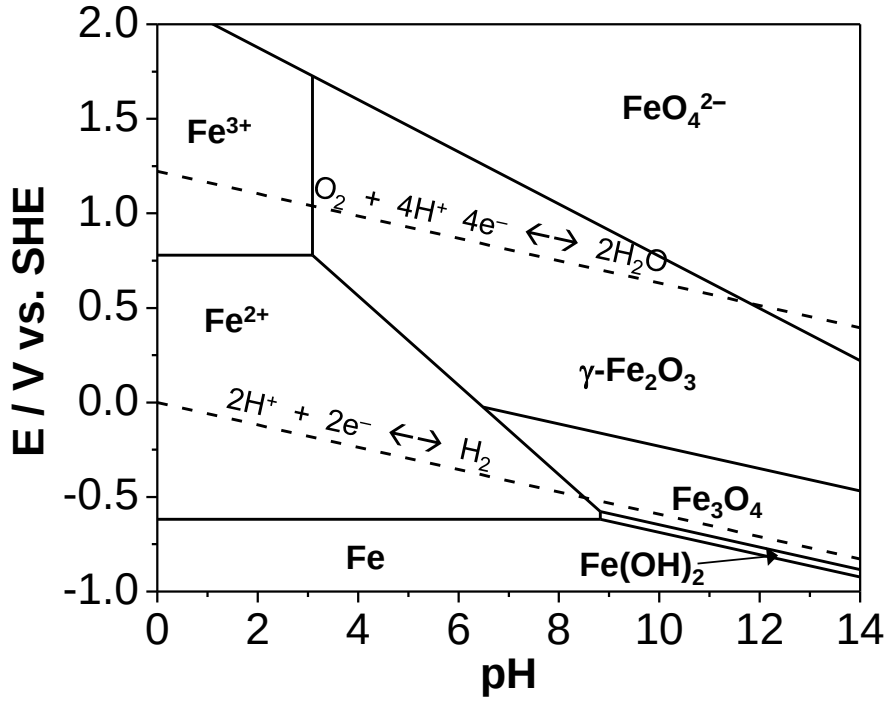

Figure 1.3: Pourbaix diagram of the Fe-H_2O system at 25 °C with all ions at an activity of 10^{-6} M. The area between the dashed lines is the region of water stability. Below the bottom dashed line water will be reduced to hydrogen and above the top dashed line water will be oxidized to oxygen. The potential scale is the standard hydrogen electrode (SHE) scale (see Chapter 2). This Pourbaix diagram assumes certain solid species to be present and much more complex diagrams can be generated with additional species [11].

It can be seen from Figure 1.3 that if the system started at pH 10 and a potential of –1.0 V_{SHE} and the potential was increased, iron that was initially present would could be oxidized in the order $Fe \rightarrow Fe(OH)_2 \rightarrow Fe_3O_4 \rightarrow Fe_2O_3$. At a lower pH, for example pH 6, the oxidation can follow $Fe \rightarrow Fe^{2+} \rightarrow Fe_2O_3$. Since the diagrams do not include any kinetic information, equilibrium is assumed to be instantaneously achieved at all times. The oxide thermodynamics and stoichiometries in the Pourbaix diagram are based on bulk oxides as well. Any deviations in thermodynamic properties associated with extremely thin (nanometer thick) oxides are not considered [12]. Because Pourbaix diagrams do not include kinetic information, they only provide an indication of the driving direction for a system. Iron (or carbon steel) placed in an environment represented by any point in the potential-pH diagram will have a tendency to form the dominant oxide indicated, but a metastable oxide, or complex layered structure may actually be present due to restrictions on electrochemical reaction rates. It is an understanding of the metastable oxide structures and those restrictions that is an objective of this thesis. Although there is a general understanding that the passivity of carbon steel is associated with the formation of protective oxide layers, there is still not comprehensive understanding of the nature, composition, structure, and formation mechanism of many passive films.

1.2.2.1 Iron Oxides

A brief overview of some of the properties of oxides and oxyhydroxides is provided below. The oxides and oxyhydroxides reviewed are those that are most

commonly formed on carbon steel and these are the species that are observed in the experiments detailed in later chapters.

1.2.2.1.1 Magnetite (Fe_3O_4)

Magnetite is a black oxide that has an inverse spinel structure. The entire spinel unit cell can be thought of as cubic close-packed array of oxygen ions with cations in the octahedral and tetrahedral interstices, Figure 1.4 [13]. The unit cell contains 32 O^{2-} anions, providing 16 octahedral sites and 8 tetrahedral sites for Fe cations. The tetrahedral sites are located at the corners, face centres, and quadrant centres in one-half of the quadrants. The octahedral sites are located in the other half of the quadrants, immediately above or below the oxide anions. For a general spinel structure ($B_2^{III}A^{II}O_4$), B^{III} occupy octahedral sites and A^{II} occupy tetrahedral sites. In an inverse spinel, such as magnetite, both A^{II} and ½ of the B^{III} occupy octahedral sites and ½ of the B^{III} occupy tetrahedral sites. In magnetite, the 8 tetrahedral sites and 8 of the octahedral sites are occupied by Fe^{III} ions, while the remaining 8 octahedral sites are occupied by Fe^{II} ions resulting a formula $Fe_8^{II}Fe_{16}^{III}O_{32}$ or Fe_3O_4 [14]. Magnetite has a band gap of 0.1 eV and is electronically conductive [13].

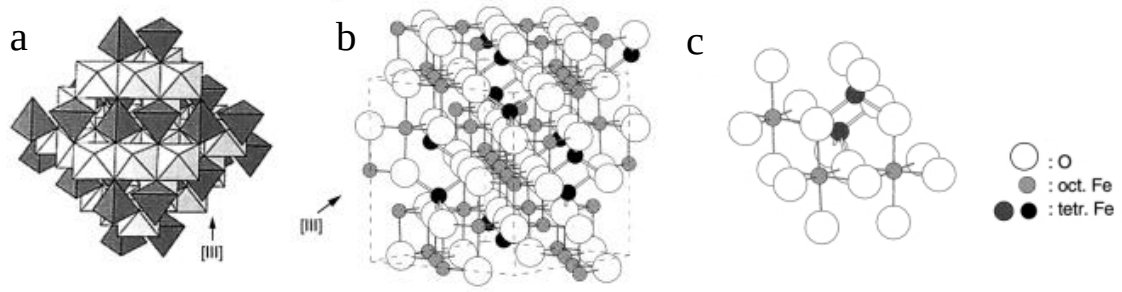

Figure 1.4: Structure of magnetite: (a) Polyhedral model with alternating octahedral and tetrahedra-octahedra layers, (b) ball and stick model with the unit cell outlined, and (c) ball and stick model of the octahedra and tetrahedra arrangement.

1.2.2.1.2 Maghemite (γ-Fe_2O_3)

Maghemite is another inverse spinel and it has the same structure as magnetite [13]. Maghemite consists of 8 tetrahedral cation sites that are fully occupied and 16 octahedral cation sites that are only fractionally occupied with, on average, 13.33 Fe^{III} per unit cell. The total formula for one unit cell is $(Fe_8^{III})_{tetra}(Fe_{40/3}^{III}V_{M\ 8/3})_{oct}O_{32}$ where V_M represents a vacancy, hence giving an overall stoichiometry of Fe_2O_3. Maghemite can be considered as an Fe^{II} deficient magnetite, or magnetite can be considered as maghemite doped with Fe^{II} [15]. As a result, the conversion between magnetite and maghemite can be very facile. Maghemite has a band gap of 2.03 eV [13].

1.2.2.1.3 Hematite (α-Fe_2O_3)

Hematite is a red oxide that has a corundum crystal structure [13]. Hematite consists of hexagonal close-packed arrays of stacked oxygen ions, with two thirds of the octahedral sites filled with Fe^{III} cations. There are some structural similarities between certain planes in the hematite structure and the structures of other iron oxides.

Specifically, structural similarities between the (001) plane of hematite and the (111) plane of magnetite allow for preferred nucleation and growth of magnetite on the (001) plane of hematite. However, due to a differing crystal structure, the conversion between magnetite and hematite may not be as facile as the conversion between magnetite and maghemite. Hematite has a band gap of 2.2 eV [13].

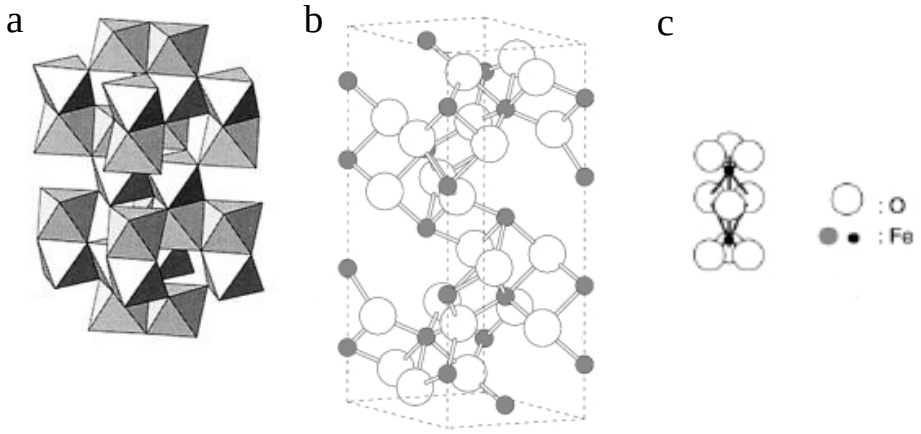

Figure 1.5: Structure of hematite: (a) hexagonal close packing of oxygen with cations in the octahedral interstices, (b) ball and stick model with the unit cell outlined, and (c) ball and stick model of the O_3-Fe-O_3-Fe-O_3 triplets.

1.2.2.1.4 Goethite (α-FeOOH)

Goethite is an oxyhydroxide with an orthorhombic unit cell [13]. All ferric ion oxyhydroxides can be regarded as FeO(OH), but they have different structures and are given different Greek prefixes. The structure of Goethite consists of a hexagonal close-packed array of anions (O^{2-}/OH^-), with Fe^{III} ions occupying half of the octahedral interstitial sites. Each Fe^{III} is surrounded by three O^{2-} and three OH^- to give an $FeO_3(OH)_3$ octahedron. The chains of octahedrons are further supported by hydrogen

bonds joining across the empty cation sites in the structure. Goethite has a band gap of 2.10 eV [13].

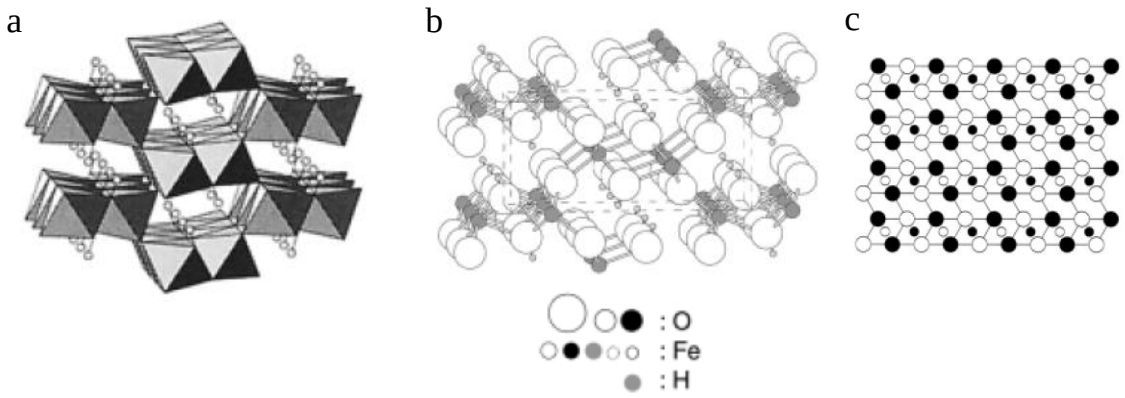

Figure 1.6: Structure of goethite: (a) Hexagonal close packed anion arrangement, (b) ball and stick model with the unit cell outlined, and (c) projection of the atomic structure on a single plane.

1.2.2.1.5 Lepidocrocite (γ-FeOOH)

γ-FeOOH is an oxyhydroxide with an orthorhombic unit cell [16]. There are 8 oxide anions in 8 octahedral sites in each unit cell which consists cubic close-packed anions (O^{2-}/OH^{-}) stacked with Fe^{III} ions occupying the octahedral interstices, i.e., 4 of the 8 octahedral sites are occupied by Fe^{III} cations. The cations form an octahedral arrangement in corrugated layers. The layers are held together by hydrogen bonding via hydroxide sites. Lepidocrocite has a band gap of 2.06 eV [13].

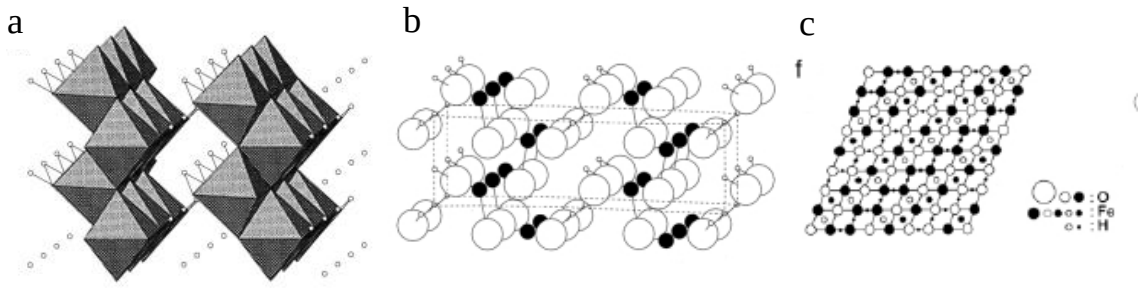

Figure 1.7: Structure of lepidocrocite: (a) Arrangement of octahedral double chains in corrugated layers, with H-bonds between the layers, (b) ball and stick model with the unit cell outlined, and (c) projection of the atomic structure on a single plane.

1.2.2.1.6 Feroxyhyte (δ-FeOOH)

δ-FeOOH is an oxyhydroxide with an array of anions (O^{2-}/OH^{-}) in a hexagonal close packed array and Fe^{III} ions distributed over half of the octahedral sites. The structure is composed of sheets of edge sharing octahedral. Feroxyhyte has a band gap of 1.94 eV [13].

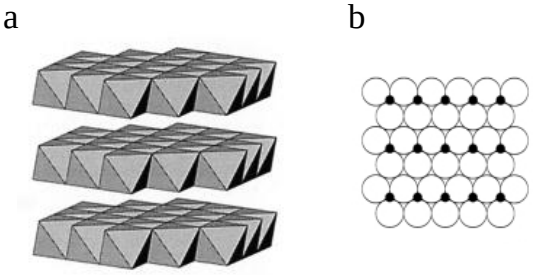

Figure 1.8: Structure of feroxyhyte: (a) Arrangement of octahedral layers and (b) projection of the atomic structure on a single plane.

1.2.2.1.6 Green Rusts

Green rusts are bluish-green Fe^{II}-Fe^{III} hydroxy compounds that can be formed under anoxic conditions in soil and during the corrosion of steel. Their structures are composed of sheets of hexagonally close-packed $Fe^{II}(OH)_6$ octahedra in which some of

the Fe^{II} are replaced by Fe^{III}, giving Fe^{II}/Fe^{III} ratios ranging between 0.8 and 3.6 [13]. The substituted Fe^{III} creates a positive layer of charge, which is balanced by anions located between the sheets of octahedra. Depending on the soil or corrosion environment, the substituted anions may include Cl^-, CO_3^{2-}, NO_3^-, or SO_4^{2-}. If none of those anions are present, the substituted anion may simply be OH^-, giving compositions between $Fe_2^{II}Fe^{III}(OH)_7$ and $Fe^{II}Fe_2^{III}(OH)_8$ [13]. This has been observed to form on magnetite surfaces [17].

1.2.2.2 Review of Iron Oxide Formation

The corrosion of iron alloys, or more generally, iron, has been studied for centuries, with famous scientists of the 19th century, including Faraday and Schöenbein, conducting early studies on the electrochemical properties and passivity of iron [18, 19]. With the advancement of both in-situ and ex-situ surface analysis techniques, the oxidation of iron in water has been studied extensively [14, 15, 17, 20-77] and, therefore, only a brief summary is possible here. Research has been performed at both acidic conditions (< pH 2) [20-25, 76] and high basicity (> pH 12) [20, 23, 26-31, 77], but most extensive research has been performed at a mildly basic pH of 8.4 [14, 17, 22, 23, 28, 29, 32-75].

One of the earliest studies of the structure of the oxide film forming on iron was conducted by Nagayama and Cohen in 1962 [32]. Through transmission electron microscopy analysis they were able to determine that the film that formed on iron in a borate buffer solution at pH 8.4 was a dual layer, with an inner magnetite layer and an outer maghemite layer [32]. A similar dual layer structure was found by Ord and DeSmet

in 1966 through the use of ellipsometry [33]. More recently, opinion has moved away from the existence of a dual layer and most research has suggested that the oxide can be treated as a single homogenous mixture [14]. A series of electrochemical studies have characterized the passive layer as a depleted or enriched oxide structure. This can be envisioned as either magnetite depleted in Fe^{II} or maghemite enriched in Fe^{II} [15, 39, 40]. Using electrochemical analysis and in-situ X-ray absorption, Oblonsky et al. characterized the oxide film as a single layer, mixed spinel with an Fe^{II}/Fe^{III} ratio that decreases as the potential increases [47]. In other words, as the potential increases the oxide goes from being more "magnetite-like" to being more "maghemite-like". Additional X-ray absorption studies by Long et al. have characterized the oxide layer as an unidentifiable phase that does not correspond to any particular iron oxide and which resides between a magnetite and maghemite structure [69, 70]. In 2000, Davenport et al. completed a thorough review of the results of their own research and that of others. They concluded that the oxide film growing on iron was a unique phase in between magnetite and maghemite [14].

While the dual layer model of magnetite and maghemite in the corrosion film has been largely dispelled, a layered oxide can still be seen in corrosion films. This consists of an inner layer of a mixed spinel (as described above) and the outer of a mixed ferric oxide and hydroxide that is more "maghemite-like" [56]. Whether the second component of the oxide film is seen or not highly depends on how the oxide film is grown. If the film is grown at a constant potential (a constant oxidizing condition), a single homogenous film is seen. If the film is grown while the potential is changing, a multi-layered and multi-component film is seen [56]. Under these conditions, using in-situ

vibrational spectra analysis, Gui and Devine characterized the layers as an inner spinel and an outer layer with characteristics similar to green rust and containing a mixed valence oxide/hydroxide [50]. For these types of films, it has been shown that hydroxyl anions are only incorporated into the outer layer and not incorporated into the inner spinel layer [42].

Some of the variations in the experimental results may be due to discrepancies that may have arisen from in-situ versus ex-situ film analysis. There are conflicting reports on whether ex-situ, dried passive iron films do [36] or do not [44] undergo structural changes. As well, distinguishing between different spinel phases with many characterization techniques is still difficult. For example, magnetite, maghemite, or a mixed homogenous phase of both species, all have similar spinel oxygen packing. Raman spectroscopy is commonly used to identify the oxides that are present and a number of the active Raman vibrational modes of spinel oxides involve only oxygen ions. The structural similarities make the use of those Raman modes inconclusive in distinguishing between the oxides that may be present [17].

When conditions are moved away from pH 8.4 buffered solutions, more oxides are seen in the thin films. Generally, however, the oxide remains largely composed of a magnetite-like spinel phase over a wide range of pHs and elevated temperatures. Hugot-Le Goff et al. performed electrochemical analysis and Raman spectroscopy of films grown in solutions of both 1 M H_2SO_4 [76] and 1 M NaOH [77]. They found that the oxide remained largely composed of magnetite in both cases. However, in films grown in acidic solutions, some conversion of magnetite to hematite was seen, and in basic solutions, the formation of iron hydroxides and oxyhydroxides on the outer film

layer was seen [76, 77]. As well, after prolonged periods of oxidation at high potentials in NaOH, maghemite began to form [77]. It was unclear as to whether the maghemite was arising from a conversion of the base magnetite layer to a more maghemite-like layer or whether the oxyhydroxides were undergoing a dehydration and structural change to form maghemite [77]. The formation of oxyhydroxide layers at high basicity (> pH 12) has commonly been observed [27, 30]. It has been shown that the conversion of magnetite to iron oxyhydroxide phases increases as pH increases [30] and that the intermediate phase may be a type of green rust [27].

Hematite is most commonly observed in corrosion films formed at elevated temperatures, especially in the presence of dissolved oxygen [31, 73-75]. The amount of magnetite that is oxidized to hematite is highly sensitive to the concentration of oxygen in the water and heating time, with the oxidation rate increasing with increasing oxygen concentration [75]. Due to the large difference in crystal structure between the two oxides, layering is clearly observed with an inner magnetite layer and an outer hematite layer [75]. Studying stainless steel alloys with a Cr content between 5 and 13 % at 288 °C, Kumai and Devine found the oxide formed in deaerated water to be composed of a uniform and passive magnetite-like inner layer and a non-uniform deposited magnetite outer layer [74]. As oxygen was introduced into the system, the outer layer changed to be composed of hematite [74].

There are still conflicts regarding the exact composition and phase structure of passive films on iron. Beyond the uncertainties in the nature of the layered or mixed structure that forms between Fe_3O_4 and Fe_2O_3 phases, the occurrence of other oxides and oxyhydroxides varies greatly. In general, the nature and phase structure of oxide films on

iron, or more specifically, carbon steel, strongly depends on factors such as the electrode potential, pH, and temperature.

1.3 RADIATION AND WATER RADIOLYSIS

1.3.1 Radiation Chemistry

Many fission products and neutron activation products, which can be generated in environments such as nuclear reactors, are radioactive. A radioactive nuclide decays to a stable nuclide by emitting a charged particle, α- or β-particle. An alpha particle is a high energy (or fast) helium nucleus, ${}^{4}_{2}He^{2+}$, and a beta particle is a fast electron [78]. The particle emission is accompanied by the emission of electromagnetic radiation, X-ray or γ-ray. The energy of the particle or photon from the decay of a radionuclide is typically in the range of 10 keV to 10 MeV [78]. The alpha particles emitted from a radionuclide have a discrete energy that is characteristic of the radionuclide. For example, the α-particles from the decay of polonium-210 all have an energy of 5.304 MeV, whereas the α-particles from the decay of radon-222 all have an energy of 5.49 MeV [78]. The energy of a β-particle also depends on the decay of a particular radioactive isotope. However, instead of having a discrete energy, the energy of β-particles range from near zero up to a maximum energy, which is characteristic of the radionuclide. For example the β-particles from the decay of cobalt-60 have an energy from zero to 0.314 MeV. The characteristic energy of the electromagnetic radiation emitted from a radionuclide is also discrete but can have more than one value. The β-decay of cobalt-60, for example, emits γ-rays of 1.332 or1.173 MeV [78]. On the electromagnetic spectrum, light with a wavelength shorter than 30 Å, corresponding to energy greater than ~ 40 keV, is referred

to as γ-rays whereas X-rays cover the range of wavelengths between ultra-violet light (3000 Å) and γ-rays and energies between 0.4 keV and 40 keV.

The high-energy charged particles and electromagnetic radiation are often referred to as ionizing radiation due to their ability to ionize molecules and atoms. When passing through a medium, ionizing radiation continually transfers its energy to the interacting medium through a series of small energy transfer steps. The energy transfer interactions involve collision of the radiation particle with the electrons in the matter and, therefore, the initial energy transfer from ionizing radiation depends on the density of electrons in the matter. Since electron density is nearly proportional to the mass of an atom (except H), the energy transfer per unit mass is nearly the same for all types of matter. Therefore, in dilute aqueous solutions the radiation energy is transferred almost entirely to water, with very small probabilities of directly interacting with solute molecules. For this reason, a chemical process induced by ionizing radiation, such as radiolysis, is often referred to as a solvent-oriented process, compared to the selective solute-oriented process induced by low energy radiation such as photolysis, where photons can match the excitation energies of solute molecules [79]. The extent of chemistry induced by ionizing radiation depends on the energy absorbed by the medium. The absorbed energy from ionizing radiation (or dose) is often expressed in units of Gray (Gy), where 1 Gy = 1 $J \cdot kg^{-1}$. The rate of radiation energy absorption by the interacting medium depends on the intensity of the radiation source and the rate of the energy transfer in the medium.

In determining the chemical effects of ionizing radiation on a medium it is the energy transfer rate per volume and not per mass since the rate of a chemical reaction

depends on concentration. For this reason the linear energy transfer (LET) rate is the more useful parameter. The LET rate depends on the type of radiation and the interacting medium. For a given medium, it is higher for α-particles (due to their large size and charge), then β-particles, and lowest for γ-photons [78]. The different LET rates result in different penetration depths, 20 – 25 μm for α-particles, to 0.5 – 1.0 cm for β-particles, to tens of cm for ½ reduction of γ-ray intensity in water at room temperature. For α-radiation, the energy is deposited in a small volume very near the radiation source. Therefore, in systems shielded from the radiation source by any significant amount of material (such as water) β- or γ-radiation is of more importance.

The initial interaction between ionizing radiation and a water molecule is ionization or excitation of the water molecule, creating an ion pair ($H_2O\bullet^+$ and e^-_{hot}) or an excited species (H_2O^*) along the radiation track. The e^-_{hot} represents an energetic electron which may have sufficient energy to produce a second ion pair ($H_2O\bullet^+$ and e^-) and an excited species. Any secondary ionization it produces will be situated close to the original ionization, giving a small cluster of 2-3 ionized and excited species near the place of the collision. The cluster of 2-3 ion pairs and excited species is referred to as "spur". Radiation of different types and energy will lose energy in matter at different rates. Consequently, it will form tracks that may be densely or sparsely populated with the active species. The differences observed in the chemical effect of different radiations, i.e., differences in the quantities and proportions of the chemical products, stems from the different density of active species in the particle tracks [79].

The ion-pair formation stage is followed by various inter- and intramolecular energy transfer processes including energy relaxation to vibrational and rotational

motions, dissociation, ion-molecule reaction and geminate recombination. These processes occur in spurs or solvent cages, while the size of the spurs is expanding. The spurs overlap and the distribution of the radiolysis products along the ionizing radiation track become uniform and homogeneous. The time to reach this homogeneous out-of-spur distribution stage is 10^{-7} s in water at room temperature [79]. This time scale is very short compared to the time scale for bulk aqueous chemical reactions or solid/water interfacial reactions. Thus, for the bulk phase chemical reaction kinetics that follow, the products and their concentrations at the homogeneous distribution stage can be considered as the reactants and their starting concentrations. Hence, the radiolysis products formed at this stage are often referred to as the primary radiolysis products although they are not the first species formed upon irradiation.

The initial homogeneous yields are referred to as primary yields and their production is expressed using G-values. A G-value is the number of ions, radicals or molecular species produced per 100 eV of absorbed energy, or $\mu mol \cdot J^{-1}$ in SI units. For a given medium, the G-values are a function of the LET rate of the ionizing radiation. For example, the primary yields from γ-radiolysis versus α-radiolysis of liquid water at 25 °C are [78]:

for γ-radiolysis:

$$H_2O\ (-0.43) \rightarrow \bullet OH(0.28),\ \bullet e_{aq}^{-}(0.28),\ H\bullet(0.062),\ H_2(0.047),\ H_2O_2(0.073),\ H^{+}(0.28) \quad (1.5)$$

for α-radiolysis:

$$H_2O\ (-0.27) \rightarrow \bullet OH(0.021),\ \bullet e_{aq}^{-}(0.021),\ H\bullet(0.010),\ H_2(0.12),\ H_2O_2(0.12),\ H^{+}(0.021),\ HO_2\bullet\ (0.0040) \quad (1.6)$$

where the numbers in brackets are the G values in units of $\mu mol \cdot J^{-1}$.

The primary yields are also a strong function of solvent properties such as dielectric constant. For example, the primary yields from γ-radiolysis of water at 25 °C are different for gas and liquid states. For γ-radiolysis in the gas state they are:

$$H_2O\ (-0.85) \rightarrow \bullet OH(0.85),\ \bullet e^-(0.31),\ H\bullet(0.75),\ H_2(0.052),$$
$$H_2O_2(0.0),\ H_2O\bullet^+\ (0.31) \qquad (1.7)$$

As described above, the primary radiolysis products are not actually the first species formed upon the absorption of radiation energy, but rather the first set of chemical species that will undergo bulk phase chemistry. These species are chemically reactive and will continually react with one another in the bulk aqueous phase or, if present, with solute species.

When exposed to a continuous source of radiation, the primary radiolysis products are continuously formed while they are undergoing aqueous phase reactions [80, 81]. For example,

$$\bullet e_{aq}^- + H^+ \rightarrow \bullet H \qquad (1.8a)$$

$$\bullet e_{aq}^- + O_2 \rightarrow \bullet O_2^- \qquad (1.8b)$$

$$\bullet OH + H_2 \rightarrow \bullet H + H_2O \qquad (1.8c)$$

$$\bullet OH + \bullet O_2^- \rightarrow O_2 + OH^- \qquad (1.8d)$$

Since most of these reactions are fast, the concentrations of radiolytic decomposition products in an irradiated aqueous system reach steady state relatively quickly on a time scale of seconds [79-81]. Solid/liquid interfacial reactions, such as corrosion, occur in a much longer time scale (hours and days). Thus, the rates of the interfacial reactions are affected by the steady-state concentrations and not by the concentrations reached in a

short time scale. The concentrations of the chemically reactive species will remain at steady-state concentrations as long as the irradiation remains constant.

The radiolysis products range from highly oxidizing (e.g., •OH, H_2O_2) to highly reducing ($\bullet e_{aq}^-$, $\bullet O_2^-$) and hence will participate in many surface redox reactions (e.g., corrosion). Their concentrations at steady state are a function of absorption dose rate ($Gy \cdot s^{-1}$) since the dose rate with the G-values determines the primary radiolysis production rate. However, chemical additives, pH, and temperature affect the rates of bulk aqueous phase reactions and hence will strongly influence the steady-state concentrations of the radiolysis products [79-82]. On the other hand, these factors have negligible influences on the primary radiolysis yields.

1.3.2 Application of Research to the Nuclear Power Industry

Carbon steels have a wide array of industrial applications from the oil and gas industry to the maritime industry [2, 83]. Carbon steel is also a material of choice for the Canadian nuclear industry and this application is of particular relevance to the work of this thesis, since there are many instances in the nuclear industry where carbon steel is used in an aqueous environment which includes exposure to ionizing radiation. As well, the corrosion of carbon steel materials, and particularly coolant circuit piping, is a serious concern for the safe and effective operation of a nuclear power plant.

1.3.2.1 Heat Transport System

A key component of the CANDU® (CANada Deuterium Uranium) nuclear reactor is the heat transport system (HTS), or reactor cooling system. This system

circulates the coolant (D_2O) that carries the heat released from fission of UO_2 fuel in the reactor core to steam generators. The nuclear fission in the core heats the circulating water from 250 °C at the reactor inlet to 300 °C at the reactor outlet [84]. The HTS of a CANDU reactor includes a horizontal array of zirconium alloy pressure tubes in the reactor core that are connected to individual carbon steel feeder pipes outside the core.

Corrosion of pipes used in the HTS is an important issue for obvious reasons related to material replacement costs, reactor performance/downtime, and the lifetime of the reactor. Establishing the corrosion kinetics under reactor coolant conditions is important for optimal coolant chemistry control and monitoring of piping status (e.g., rate of possible wall thinning due to corrosion). Reactor coolant systems operate with very carefully controlled chemistry (low impurity levels, tight pH limits and tight dissolved oxygen limits) to ensure low, predictable rates of corrosion. The chemistry control parameters are largely established on the basis of corrosion studies performed where no ionizing radiation was present. However, the high radiation field in the reactor core will cause water radiolysis and the radiolysis products can migrate to other parts of the coolant system where, even at low concentrations, they can control the water redox conditions and influence corrosion.

The transition metals have several stable oxidation states (like Fe^{2+}/Fe^{3+}) and redox active species can react with dissolved metal ions to change their oxidation state. This means that the presence of dissolved metal ions will interfere with the steady-state balance between water radiolysis products [85, 86]. A representation of the system for corroding iron in water is represented in Figure 1.9.

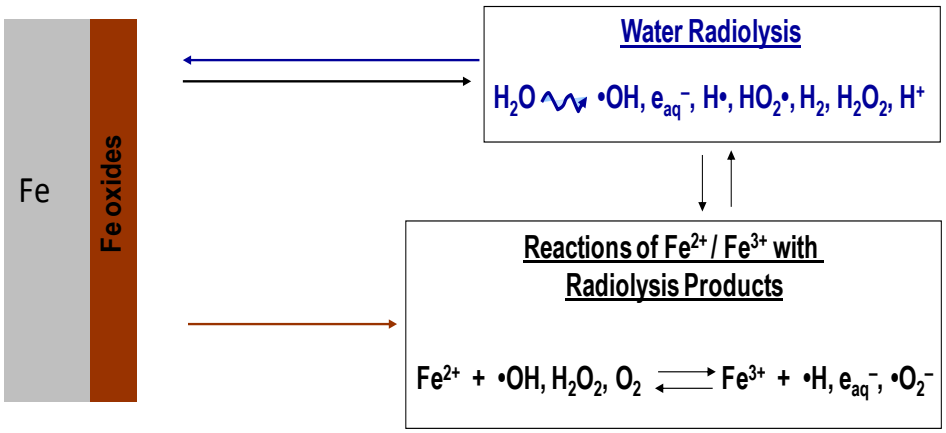

Figure 1.9: System of corroding iron in irradiated water.

In a nuclear reactor, dissolved metal ions can migrate through the coolant system. They will tend to condense (or precipitate as particles) at locations where their solubilities are lowest (normally low temperature regions). Deposition of insulating metal oxides on the interior walls of the small diameter tubing used in steam generators can reduce the heat transfer efficiency of the tubing. Alternatively, corrosion products that enter the reactor core may deposit there and absorb neutrons to become radioactive. For example, ^{59}Co can absorb a neutron and become hazardous, gamma emitting ^{60}Co [78]. If the neutron activation products are transported and precipitate on piping outside the core, the radioactivity level in the reactor containment building will rise and these activated corrosion products become a safety issue for reactor maintenance during reactor shutdown.

To limit the rate of oxidation, CANDU reactors, and other reactor designs, maintain a reducing environment in the coolant by adding H_2 to the coolant water [87-89]. Although the use of hydrogen water chemistry does create a more reducing environment, it does not eliminate the creation of oxidizing species in locations where

water radiolysis is occurring. Even with well controlled hydrogen water chemistry, controlling or limiting the concentration of oxidizing species does not necessarily prevent corrosion. A highly reducing environment may limit the formation of a passive oxide film on a metal surface and, in turn, this may make the material more susceptible to corrosion during upset conditions (such as air ingress during reactor shutdown for maintenance). Insufficient amounts of hydrogen may make the system "too oxidizing" and materials can become susceptible to either bulk corrosion, or for more corrosion resistant materials like stainless steel, stress corrosion cracking. Beyond the addition of hydrogen, the CANDU coolant chemistry conditions are also controlled at a pH selected to minimize the corrosion of carbon steel pipes with the addition of LiOD. The target is to maintain a $pH_{25°C}$ near 10.2-10.8 [31, 90].

Most studies performed under the thesis research are carried out at $pH_{25°C}$ 10.6, near the HTS pH range. Also, the reason for this choice of pH for the studies is that this pH is sufficiently away from the pKa of H_2O_2 (11.75) and from the pKa of $\bullet e_{aq}^-$ (9.7). At pHs above the pKa of H_2O_2 its anion (HO_2^-) having a different redox property is prevalent. At pH 9 - 10 around the pKa of $\bullet e_{aq}^-$ the steady-state concentrations of radiolysis products are a highly sensitive function of pH [80].

1.3.2.2 Waste Disposal

In addition to corrosion of metal piping in nuclear reactors, corrosion of metals used in other applications where ionizing radiation is present is of concern. One such application is the storage and disposal of radioactive waste and particular high level (highly radioactive) waste such as used nuclear fuel [91-109]. Countries using nuclear

power have independently researched options for used nuclear fuel disposal including fuel reprocessing and deep geological fuel storage [93, 104, 106, 107]. In most proposed plans for geological storage, carbon steel is a candidate material for the packaging of spent nuclear fuel. The chemical environments for proposed spent fuel storage are different from those of a nuclear power plant coolant system, with lower temperatures and pressures, the presence of groundwater cations and anions, and neutral to basic pH. Although systems vary, all models assume the system should reach a state of anaerobic corrosion over a period of time that may take a few decades to hundreds of years. Spent nuclear fuel will generate heat during storage and this will create elevated temperatures which could range from 50 °C to 150 °C initially [99]. Eventually the container will cool to the ambient geological storage temperature (nominally assumed to be ~ 30 °C) after thousands of years [99].

As in the case of the heat transport system, the corrosion process will be determined by the nature of oxide films present and their interaction with water radiolysis products. Due to the varying environmental conditions, a single corrosion rate for carbon steel as a waste disposal material cannot be obtained. However, the complex range of environments makes fundamental understanding of the mechanisms of oxide formation and interfacial reactions even more important in predicting corrosion for fuel disposal containers.

1.3.3 Corrosion Studies of Steel in Radiation Environments

1.3.3.1 Low LET Exposure

1.3.3.1.1 Electrochemical Studies

Electrochemical studies of the corrosion of carbon steel with radiation present date back to as early as 1958 [110]. While the research does date back many decades, the number of studies are limited and understanding of the oxidative and reductive behaviour of steel under irradiation remains somewhat unclear [110-127]. The number of electrochemical studies under reactor conditions are very few and often provide poor results and little usable kinetic data [122]. The majority of electrochemical studies have focused on various stainless steel alloys and research has shown irradiation to both decrease [97, 98, 110, 118, 123] and increase [112, 120, 126, 127] the measured corrosion potential on an alloy. The corrosion potential is the potential that a corroding metal in an aqueous solution at equilibrium will establish. It is the potential at which the rates of oxidation and reduction reactions are equal, and is further explained in Chapter 2. When the potential is seen to decrease under gamma irradiation, the behaviour is often attributed to the electrode acting as a hydrogen indicator electrode; the measured potential is simply that of the oxidation of H_2 produced due to water radiolysis. The behaviour of a metal as a hydrogen indicator electrode under irradiation is confirmed when stainless steel is replaced with the more noble metal, platinum. Platinum is very responsive to H_2 and can act as a catalyst for H_2 oxidation. When a platinum electrode is placed under irradiation, the potential on it drops immediately and, when irradiation is stopped, the potential slowly increases as H_2 is no longer produced and any remaining H_2 diffuses away from the electrode [120]. It has also been suggested that the potential drop

of stainless steel under irradiation could partially be caused by a reaction of the alloy with one of the reducing water radiolysis products, specifically superoxide ($\bullet O_2^-$) [97].

In studies where the potential on steel was seen to increase under gamma irradiation, the increase is attributed to the reaction of the steel with an oxidizing water radiolysis product. The oxidizing species may be H_2O_2 [113-115, 120], O_2 [112, 127], or •OH [117, 120]. Unlike the studies where a reduction in potential was observed, when the stainless steel potential increased under irradiation, chemical changes in the steel surface occurred. When stainless steel electrodes were removed from the radiation environment, the potential on them decreased only slightly and did not return to the lower pre-irradiated potential. This suggests that changes in the oxide structure on the stainless steel surface had occurred [114, 120]. When H_2O_2 is used as a solution additive to simulate the effect of gamma irradiation of water, similar changes are seen in the measured potential [114]. It has also been shown that in studies where the oxidation associated with water radiolysis is simulated using H_2O_2, there are correlations between the relative passivity of an oxide and hydrogen peroxide concentrations [114, 115]. Through the potential regions of passivation, the potential is proportional to the concentration of peroxide [113]. At the highest peroxide concentrations, the peroxide may decompose on the electrode surface without significant potential changes [113, 114] or it may increase the potential into a transpassive region where film breakdown occurs due to defects in the oxide [115].

In determining which water radiolysis product is acting as the key oxidant, the structure of the oxide film formed on steel can be used as an indicator. For example, an analysis of iron deposit products suspended in solution found that when O_2 was the key

oxidizing species the main oxidation product was magnetite, while when H_2O_2 was the key oxidizing species the main oxidation product was maghemite [128]. Also, the oxide on stainless steel has been shown to be thicker with H_2O_2 exposure compared to O_2 exposure and the oxide thickness decreases with increasing [H_2O_2], but increases with increasing [O_2]. This behaviour has been attributed to the relative effects on both dissolution and oxide growth rate that the different oxidizing species have on stainless steel [116].

In addition to an incomplete understanding of how the corrosion potential will change with irradiation, there are also conflicting reports as to whether irradiation increases or decreases the susceptibility of stainless steel to pitting corrosion. Localized corrosion events, which include pitting, involve corrosive attack on localized sites on a surface, while the rest of the surface corrodes at a lower rate, leading to high localized currents (high corrosion rates). Glass et al. showed that the pitting susceptibility (defined as the difference between the corrosion potential and pitting potential) of Type-316L stainless steel increased under gamma irradiation [120]. However, the difference between the corrosion potential and the pitting potential only decreased minimally with irradiation (the difference was still approximately 0.2 V) and, therefore, irradiation would not cause spontaneous pitting. Pitting potential is a potential in a given environment above which localized corrosive pits form on the metal surface [129]. Lillard et al. found that proton irradiation of stainless steel foil caused an increase in both the corrosion potential and pitting potential. The net result was an overall decrease in the likelihood of pitting for irradiated versus unirradiated stainless steel [126].

Another area of interest related to the steel corrosion process and water radiolysis is the formation of concentration cells. A concentration cell contains two separate areas of metal that are in electrical contact, but in different redox environments. Concentration cells can be separated by up to 100 m in underground pipelines due to oxygen concentration gradients [130]. Fujita et al. [131] performed an experiment in which 4 iron samples were analyzed. Two samples were irradiated; one of the irradiated samples was electrically isolated and the second sample was electronically connected to a third unirradiated sample. A fourth unirradiated sample was electronically isolated. Experiments were performed in pressure vessels at 250 °C with pure water. The irradiation was provided by a ^{60}Co gamma source with a dose rate of 0.48 kGy·h^{-1}. Magnetite was found on all samples. The irradiated samples were both seen to have a similar corrosion rate. The unirradiated, electronically connected sample had lower corrosion rates than the isolated unirradiated sample. The observations were attributed to the existence of a concentration cell in which reducing species produced by water radiolysis caused a cathodic reaction with the sample under irradiation and the electronic contact caused the unirradiated sample to be anodically polarized, producing a passive oxide. Detailed thermodynamic calculations related to the redox properties of various water radiolysis products, with particular emphasis on the solvated electron, have shown that in some nuclear reactor systems significant concentration cells can form [132]. It has been shown that in some cases the strong reducing power of the solvated electron, whose concentration depends highly on factors such as solution chemistry and dose rate, can cause the materials inside the reactor core to behave as a giant cathode (site of reduction). Since the piping of the coolant system outside of the core is in electrical contact, there is

the possibility for the out of core components to be anodically polarized to potentials beyond any level that could be due to the oxidizing effects of any water radiolysis products (such as H_2O_2) that could be present. It was predicted that the in-core and out-of-core components could have potential differences of 0.4 V to 0.1 V, depending on reactor design [132].

Beyond effects on the solution, absorption of ionizing radiation energy by semiconducting oxides can induce photoelectric effects in the oxides leading to the creation of electron/hole pairs. If a pair was to separate and the components migrate to either interface, a number of possible reactions could occur. The migration of the separated pair would depend on the band bending of the valence and conduction bands of the semiconducting oxide at the oxide/metal or oxide/solution interface [133]. If the electron moved to the oxide/metal interface and the hole moved to the oxide/solution interface, the hole could cause dissolution to occur. If the opposite occurred and the electron moved to the oxide/solution interface, the electron would accelerate the cathodic (reduction) reaction, which could then accelerate a coupled oxidation reaction [133]. It is expected that photo-induced corrosion is a relatively inefficient process for carbon steel for two reasons. Firstly, for most cases of interest, the oxide film is composed of magnetite. As noted above, magnetite is a near conductive oxide, so that it cannot support the formation of separated ion pairs readily. Secondly, for low LET radiation like gamma radiation, a thin oxide film can absorb very little energy and direct photo-induced events will be few. For stainless steel, with even thinner oxides than carbon steel, the relative energy transfer to the film by gamma radiation would be even less.

However, the layering of various semiconductor oxides on stainless steel [134] may enhance photo-induced corrosion in stainless steel over carbon steel.

1.3.3.1.2 Waste Disposal Corrosion Studies

One of the most thorough studies on the effects of irradiation on carbon steel corrosion as it relates to nuclear waste disposal was performed by Marsh et al. [91]. They measured carbon steel corrosion under granitic water conditions at pH 9.4, for 5000 h, temperatures up to 90 °C, and with gamma radiation present [91]. They determined that the gamma radiation increased the corrosion rate, with the rate increasing with increasing radiation dose rate. The increase in corrosion rate was observed only during an initial, short period of time, after which the corrosion rate decreased to a steady-state level near that observed with no radiation present. The authors did observe some localized corrosion of some samples under irradiated and noted that this could have affected some of the corrosion rate determinations. More recent studies by others have also found irradiation to increase the corrosion rate of carbon steel [92, 94, 95, 101]. These studies have been performed in under both acidic [92] and basic [101] conditions. A commonality in all studies is the possible occurrence of localized corrosion. Under acidic conditions, the presence of gamma radiation had no observable impact on the corrosion of various steels for low dose rates (1, 10 and 100 $Gy \cdot h^{-1}$). However, at higher dose rates (1000 $Gy \cdot h^{-1}$) the corrosion rate increased [92]. At 1000 $Gy \cdot h^{-1}$ significant pitting and crevice corrosion occurred and no passive film formed on the steel surface. Reda et al. [94] studied Type 1018 carbon steel corrosion in a saturated brine solution (NaCl and $MgCl_2$) exposed to high-level gamma irradiation and found an increase in the rate of

corrosion. The type of corrosion with radiation present was stress corrosion cracking and only uniform corrosion was observed under no radiation. Smart et al. [101] studied carbon steel corrosion in high salinity solutions at mildly basic pHs of 8.8 and 10.4 and found that the corrosion rate of a carbon steel wire exposed to a dose of 300 $Gy \cdot h^{-1}$ was higher than the corrosion rate with no radiation present. Their test solutions were described as a dark and milky sludge after prolonged tests, indicating that aggressive corrosion occurred, most likely forming magnetite. In their experiments, nitrogen was used as a cover gas and the authors did note that dissolved nitrogen may have been converted by radiolysis reactions into nitric acid [101]. The production of nitric acid in nitrogen saturated water exposed to irradiation is a well known process [135]. In other tests it was found that the use of helium as a cover gas led to reduced rates of corrosion, presumably due to the absence of nitric acid production [100]. The pH of the test solutions did decrease by 1 to 2 pH units with a nitrogen cover gas present, however, it was unclear what fraction of the pH change was due to the formation of nitric acid and what fraction arose from the hydrolysis of ferrous ions in solution [100].

In some cases, radiation has been shown to lower the corrosion rates of various steels [92, 96]. Ahn et al. [96] studied the corrosion of several steel alloys which differed in their carbon content (0.07 to 0.25 %) in high concentration solutions at pH 10.3, with temperatures between 80 °C and 150 °C, and a gamma radiation dose rate of 10 $kGy \cdot h^{-1}$. They found, for tests lasting two months, the corrosion rates of irradiated samples were 2 to 5 times lower than those of unirradiated samples. For 4 month-long tests the corrosion rates of both irradiated and unirradiated samples were similar.

For all reported work, the main oxide formed was found to be magnetite [91, 93, 98, 100, 101]. In some of the tests with irradiation, further oxidation of magnetite occurred. The result was the formation of layered oxides including minor amounts of Fe_2O_3 [93] and oxyhydroxides, such as γ-FeOOH [93, 100].

1.3.3.2 High LET Exposure

While high LET radiation sources were not used for the work of this thesis, extensive research has been performed on the effects of high LET radiation on steel corrosion, and therefore, a very brief review of studies on this phenomena is provided. Due to the very limited penetration depth of high LET radiation, studies have focused on materials in contact with radiation sources, such as fuel cladding [136].

A great concern for material integrity is the possible occurrence of localized corrosion events. Localized corrosion may occur through many mechanisms, but the one that has undergone the most research as it relates to radiation-induced corrosion is irradiation-assisted stress corrosion cracking (IASCC) [136-148]. Stress-corrosion cracking (SCC) is the growth of cracks due to the simultaneous occurrence of both a stress in a material and reactive environment [149]. Although the exact mechanism for stress corrosion cracking may not be clear, it often occurs along grain boundaries in the microstructures of materials and there is evidence that dealloying dominates the SCC mechanism [149]. Dealloying occurs when one component from an alloy is removed, either by dissolution into the solution or migration within the microstructure [2]. While SCC can occur on carbon steel, it is more common in higher alloy steels, and therefore, it is of much more studied for various stainless steels than carbon steels. The interest in

IASCC is high because it is a known problem in nuclear power plants [150]. In addition, new advanced nuclear reactor designs aim to increase the temperature of the water coolant (up to supercritical levels) and this will put reactor materials under conditions where the risk of IASCC is increased [136, 137, 145].

In considering IASCC, the direct effect on material properties of heavy particle radiation (alpha particles, neutrons) needs to be considered. The high energy particles can alter the microstructure or a metal by processes that include radiation induced segregation (RIS), radiation induced depletion (RID), and the formation or movement of dislocations. Radiation induced segregation involves the redistribution of alloying elements in steel and either their enrichment or depletion in grains or grain boundaries. It is similar to the effects of thermal segregation, however concentration changes can be orders of magnitudes larger in RIS [143]. Radiation induced segregation is a strong function of irradiation temperature, dose rate, and total absorbed dose [136]. In general, it has been shown for stainless steel that as RIS increases, Fe and Cr depletion at the grain boundaries occurs, while Ni in the boundaries is enriched [137, 143, 146, 147]. While the segregation, or depletion of major alloying elements is known to occur, attempts to isolate the effects of RIS from other radiation-induced processes have shown that RIS alone cannot cause IASCC[146]. It has also been shown that minor alloying elements, such as C, Si, or P also undergo RIS [137, 143, 146, 147]. Although more difficult to detect, results suggest that the segregation of minor alloying elements do not alone cause IASCC. Recent advancements in analytical techniques such as atom-probe tomography, neutron scattering, and electron microscopy are allowing for enhanced analysis of the movement of all alloying elements, however the exact effect of segregation of each

element remains unresolved [139]. More recently, research has focused on the formation and movement of dislocations formed due to radiation, although seen to be a factor in IASCC, it alone is not a cause of IASCC [145].

Since SCC results from both a material stress and a corrosive aqueous environment, attempts have been made to isolate the effects of water radiolysis products on the corrosion mechanism. Such studies of IASCC on various stainless steels have been performed [86], but the presence of water radiolysis products and a shift in the corrosion potential has not been shown to be sufficient to cause IASCC. Water radiolysis may play a significant role in IASCC, but does not act alone.

1.4 REFERENCES

[1] W.D. Callister Jr., D.G. Rethwisch, Types and Applications of Materials in Fundamentals of Materials Science and Engineering: An Integrated Approach, John Wiley & Sons, Hoboken, NJ, (2008) pp. 516-567.

[2] R. Heidersbach, Metallurgy and Corrosion Control in Oil and Gas Production, John Wiley & Sons, Hoboken, NJ, (2011).

[3] W.D. Callister Jr., Materials Science and Engineering and Introduction, 6th Ed., John Wiley and Sons, New York, NY, (2003).

[4] D. Landolt, Introduction to Surface Reactions: Electrochemical Basis of Corrosion in Corrosion Mechanism in Theory and Practice, P. Marcus, J. Oudar (Eds.), Marcel Dekker, New York, NY, (1995) pp. 1-18.

[5] D.W. Shoesmith, Kinetics of Aqueous Corrosion in ASM Handbook on Corrosion, ASM Internationals, Materials Park, OH, (2003) pp. 42-51.

[6] E.E. Stansbury, R.A. Buchanan, Fundamentals of Electrochemical Corrosion, ASM Internationals, Materials Park, OH, (2000).

[7] C.F. Baes Jr., R.E. Mesmer, The Hydrolysis of Cations, Krieger Publishing Co., Florida, USA, (1986).

[8] H.H. Uhlig, Passivity of Metals in Corrosion Monograph Series, R.P. Frankenthal, J. Kruger (Eds.), The Electrochemical Society, Princeton, NJ, (1978) pp. 1-28.

[9] R. Balasubramaniam, Corros. Sci., 42 (2000) 2103-2129.

[10] D.C. Silverman, Corros., 38 (1982) 541-549.

[11] T. Misawa, Corros. Sci., 13 (1973) 659-676.

[12] B. Macdougall, M.J. Graham, Growth and Stability of Passive Films in Corrosion Mechanisms in Theory and Practice, P. Marcus, J. Oudar (Eds.), Marcel Dekker, New York, NY, (1995) pp. 143-173.

[13] R.M. Cornell, U. Schwertmann, The Iron Oxides: Structures, Properties, Reactions, Occurrences and Uses, 2nd Ed., Weinheim, New York, NY, (2003).
[14] A.J. Davenport, L.J. Oblonsky, M.P. Ryan, M.F. Toney, J. Electrochem. Soc., 147 (2000) 2162-2173.
[15] P. Schmuki, M. Buchler, S. Virtanen, H. Bohni, R. Muller, L.J. Gauckler, J. Electrochem. Soc., 142 (1995) 3336-3342.
[16] R.W.G. Wyckoff, Crystal Structures, 2nd Ed., Interscience Publishers, New York, NY, (1963).
[17] S.P. Harrington, F. Wang, T.M. Devine, Electrochim. Acta, 55 (2010) 4092-4102.
[18] M. Faraday, Philos. Mag., 9 (1836) 57-65.
[19] C.T. Schönbein, Philos. Mag., 9 (1836) 53-57.
[20] C.L. Foley, J. Kruger, C.J. Bechtoldt, J. Electrochem. Soc., 114 (1967) 994-1001.
[21] N. Sato, K. Kudo, T. Noda, Electrochim. Acta, 16 (1971) 1909-1921.
[22] J.A. Bardwell, B. Macdougall, M.J. Graham, J. Electrochem. Soc., 1988 (1988) 413-418.
[23] P. Schmuki, S. Virtanen, A.J. Davenport, C.M. Vitust, J. Electrochem. Soc., 143 (1996) 574-582.
[24] B.G. Ateya, F.M.A. Kharafi, R.M. Abdalla, Mater. Chem. Phys., 78 (2002) 534-541.
[25] G.L. Song, C.N. Cao, S.H. Chen, Corros. Sci., 47 (2005) 323-339.
[26] D. Geana, A.A. Elmiligy, W.J. Lorenz, J. Appl. Electrochem., 4 (1974) 337-345.
[27] A.A. Olowe, Y. Marie, P. Refait, J.M.R. Génin, Hyperfine Interact., 93 (1994) 1783-1788.
[28] P.A. Castro, E.R. Vago, E.J. Calvo, J. Chem. Soc., Faraday Trans., 92 (1996) 3371-3379.
[29] M. Buchler, P. Schmuki, H. Bohni, J. Electrochem. Soc., 144 (1997) 2307-2312.
[30] Y.T. He, S.J. Traina, Clay Miner., 42 (2007) 13-19.
[31] K.-S. Jung, L.d. Pierrefeu, Corros. Sci., 52 (2010) 817-825.
[32] M. Nagayama, M. Cohen, J. Electrochem. Soc., 109 (1962) 781-790.
[33] J.L. Ord, D.J. DeSmet, J. Electrochem. Soc., 113 (1966) 1258-1262.
[34] U. Stimming, J.W. Schultze, Ber. Bunsenges. Phys. Chem., 80 (1976) 1297-1302.
[35] R.S. Schrebler Guzman, J.R. Vilche, A.J. Arvia, Electrochim. Acta, 24 (1979) 395-403.
[36] W.E. O'Grady, J. Electrochem. Soc., 127 (1980) 555-563.
[37] S.C. Tjong, E. Yeager, J. Electrochem. Soc., 128 (1981) 2251-2254.
[38] K. Kuroda, B.D. Cahan, G. Nazri, E. Yeager, T.E. Mitchell, J. Electrochem. Soc., 129 (1982) 2163-2169.
[39] B.D. Cahan, C.-T. Chen, J. Electrochem. Soc., 129 (1982) 474-480.
[40] C.-T. Chen, B.D. Cahan, J. Electrochem. Soc., 129 (1982) 17-26.
[41] N. Ramasubramanian, N. Preocanin, R.D. Davidson, J. Electrochem. Soc., 132 (1985) 793-798.
[42] D.F. Mitchell, M.J. Graham, J. Electrochem. Soc., 133 (1986) 936-938.
[43] M.E. Brett, K.M. Parkin, M.J. Graham, J. Electrochem. Soc., 133 (1986) 2031-2035.
[44] J. Eldridge, R.W. Hoffman, J. Electrochem. Soc., 136 (1989) 955-961.

[45] M.P. Ryan, R.C. Newman, G.E. Thompson, J. Electrochem. Soc., 142 (1995) L177-L179.
[46] L.J. Oblonsky, T.M. Devine, Corros. Sci., 37 (1995) 17-41.
[47] L.J. Oblonsky, A.J. Davenport, M.P. Ryan, H.S. Isaacs, R.C. Newman, J. Electrochem. Soc., 144 (1997) 2398-2404.
[48] L.J. Oblonsky, S. Virtanen, V. Schroeder, T.M. Devine, J. Electrochem. Soc., 144 (1997) 1604-1609.
[49] J. Gui, T.M. Devine, J. Electrochem. Soc., 138 (1991) 1376-1384.
[50] J. Gui, T.M. Devine, Corros. Sci., 138 (1991) 1105-1124.
[51] J. Gui, T.M. Devine, Corros. Sci., 37 (1995) 1177-1189.
[52] M. Toney, A. Davenport, L.J. Oblonsky, M.P. Ryan, C. Vitus, Phys. Rev. Lett., 79 (1997) 4282-4285.
[53] M. Buchler, P. Schmuki, H. Bohni, J. Electrochem. Soc., 145 (1998) 609-614.
[54] A.J. Davenport, J.A. Bardwell, C.M. Vitus, J. Electrochem. Soc., 142 (1995) 721-724.
[55] A.J. Davenport, M. Sansone, J. Electrochem. Soc., 142 (1995) 725-730.
[56] V. Schroeder, T.M. Devine, J. Electrochem. Soc., 146 (1999) 4061-4070.
[57] S.J. Ahn, H.S. Kwon, Electrochim. Acta, 49 (2004) 3347-3353.
[58] S.J. Ahn, H.S. Kwon, J. Electroanal. Chem., 579 (2005) 311-319.
[59] W.S. Li, S.Q. Cai, J.L. Luo, J. Electrochem. Soc., 151 (2004) B220-B226.
[60] I.V. Sieber, H. Hildebrand, S. Virtanen, P. Schmuki, Corros. Sci., 48 (2006) 3472-3488.
[61] I. Diez-Pérez, F. Sanz, P. Gorostiza, Curr. Opin. Solid State Mater. Sci., 10 (2006) 144-152.
[62] I. Diez-Pérez, F. Sanz, P. Gorostiza, Electrochem. Commun., 8 (2006) 1595-1602.
[63] B. Beverskog, M. Bojinov, A. Englund, P. Kinnunen, T. Laitinen, K. Mäkelä, T. Saario, P. Sirkiä, Corros. Sci., 44 (2002) 1901-1921.
[64] B. Beverskog, M. Bojinov, P. Kinnunen, T. Laitinen, K. Mäkelä, T. Saario, Corros. Sci., 44 (2002) 1923-1940.
[65] J. Flis, I. Flis-Kabulska, T. Zakroczymski, Electrochim. Acta, 54 (2009) 1810-1819.
[66] T. Yamamoto, K. Fushimi, S. Miura, H. Konno, J. Electrochem. Soc., 157 (2010) C231-C237.
[67] D.B. Gibbs, M. Cohen, J. Electrochem. Soc., 119 (1972) 416-419.
[68] Y.F. Cheng, J.L. Luo, Electrochim. Acta, 44 (1999) 2947-2957.
[69] G.G. Long, J. Kruger, D.R. Black, M. Kuriyama, J. Electrochem. Soc., 130 (1983) 240-242.
[70] G.G. Long, J. Kruger, D.R. Black, M. Kuriyama, J. Electroanal. Chem., 150 (1983) 603-610.
[71] E.M.A. Martini, I.L. Muller, Corros. Sci., 42 (2000) 443-454.
[72] A.U. Gehring, H. Fischer, M. Louvel, K. Kunze, P.G. Weidler, Geophys. J. Int., 179 (2009) 1361-1371.
[73] B. Pujilaksono, T. Jonsson, M. Halvarsson, J.-E. Svensson, L.-G. Johansson, Corros. Sci., 52 (2010) 1560-1569.
[74] C.S. Kumai, T.M. Devine, Corros., 61 (2005) 201-218.

[75] J. Wielant, V. Goossens, R. Hausbrand, H. Terryn, Electrochim. Acta, 52 (2007) 7617-7625.
[76] A. Hugot-Le Goff, C. Pallotta, J. Electrochem. Soc., 132 (1985) 2805-2806.
[77] A. Hugot-Le Goff, J. Flis, N. Boucherit, S. Joiret, J. Wilinski, J. Electrochem. Soc., 137 (1990) 2684-2690.
[78] J.W.T. Spinks, R.J. Woods, An Introduction to Radiation Chemistry, John Wiley & Sons, New York, NY, (1990).
[79] J.C. Wren, Steady-State Radiolysis: Effects of Dissolved Additives in Nuclear Energy and the Environment, ACS Symposium Series, (2010) pp. 271-295.
[80] J.M. Joseph, B.S. Choi, P. Yakabuskie, J.C. Wren, Radiat. Phys. Chem., 77 (2008) 1009-1020.
[81] P. Yakabuskie, J.M. Joseph, J.C. Wren, Radiat. Phys. Chem., 79 (2010) 777-785.
[82] P. Yakabuskie, J.M. Joseph, C.R. Stuart, J.C. Wren, J. Phys. Chem. A, 115 (2011) 4270-4278.
[83] S.W. Dean, G.H. Delgadillo, J.B. Bushman, Marine Corrosion in Tropical Environments, American Society for Testing and Materials, West Conshohocken, PA, (2000).
[84] A.A. Harms, Thermal-Hydraulic Analysis in An Introduction to the CANDU Nuclear Energy Conversion System, McMaster University, (1975) pp. 85-96.
[85] C.C. Lin, Y.J. Kim, L.W. Niedrach, K.S. Ramp, Corros., 8 (1996) 618-625.
[86] K. Ishigure, T. Nukii, S. Ono, J. Nucl. Mater., 15 (2006) 56-65.
[87] P. Fejes, in proceedings of Countermeasures for BWR Pipe Cracking, Electric Power Res. Inst., Palo Alto, CA, (1980), pp. 79-174.
[88] R.L. Cowan, M.E. Indig, J.N. Kass, R.J. Law, L.L. Sundberg, in proceedings of International Conference on Water Chemistry of Nuclear Reactor Systems, Water Chemistry 4, Br. Nucl. Energy Soc., Bournemouth, (1986), pp. 29-36.
[89] H. Takiguchi, M. Sekiguchi, A. Abe, K. Akamine, M. Sakai, Y. Wada, S. Uchida, J. Nucl. Sci. Technol., 36 (1999) 179-188.
[90] J.P. Slade, T.S. Gendron, in proceedings of Proceedings of the 12th International Conference on Environmental Degradation of Materials in Nuclear Power System – Water Reactors, The Minerals, Metals and Materials Society Warrendale, PA, (2005), pp. 773-782.
[91] G.P. Marsh, K.J. Taylor, Corros. Sci., 28 (1988) 289-320.
[92] E. Smailos, W. Schwarzkopf, R. Koster, B. Fiehn, G. Halm, Kernforschungszentrum Karlsruhe Report, KFK-4723, (1990).
[93] N.R. Smart, Corros., 65 (2009) 195-212.
[94] R.J. Reda, S.L. Akers, J.L. Kelly, Trans. Amer. Nucl. Soc., 53 (1986) 224-225.
[95] J.L. Nelson, R.E. Westerman, F.S. Gerber, in proceedings of Scientific Basis For Nuclear Waste Management VII, Materials Research Society, Boston, MA, (1984), pp. 121-128.
[96] T.M. Ahn, P. Soo, Waste Manage., 15 (1995) 471-476.
[97] P. Bouniol, A. Aspart, Cem. Concr. Res., 28 (1998) 1669-1681.
[98] R.J. Winsley, N.R. Smart, A.P. Rance, P.A.H. Fennell, B. Reddy, B. Kursten, Corros. Eng., Sci. Technol., 46 (2011) 111-116.
[99] F. King, Nuclear Waste Management Organization Report, NWMO TR-2007-01, (2007).

[100] V. Cuba, R. Silber, V. Múčka, M. Pospíšil, S. Neufuss, J. Bárta, A. Vokál, Radiat. Phys. Chem., 80 (2011) 440-445.
[101] N.R. Smart, A.P. Rance, L.O. Werme, J. Nucl. Mater., 379 (2008) 97-104.
[102] D.W. Shoesmith, F. King, Atomic Energy of Canada Report, AECL 11999, (1999).
[103] R.E. Westerman, J.L. Nelson, W.L. Kuhn, S.G. Basham, D.A. Moak, S.G. Pitman, Pacific Northwest Laboratories Report, PNL-SA-11713, (1983).
[104] R.E. Westerman, J.H. Haberman, S.G. Pitman, B.A. Pulsipher, L.A. Sigalla, Pacific Northwest Laboratory Report, PNL-5426, (1986).
[105] E. Smailos, W. Schwarzkopf, R. Koster, B. Fiehn, G. Halm, Commission of the European Communities Report, EUR-13672-EN, (1991).
[106] B. Kursten, F. Druyts, D.D. Macdonald, N.R. Smart, R. Gens, L. Wang, E. Weetjens, J. Govaerts, Corros. Eng., Sci. Technol., 46 (2011) 91-97.
[107] F. King, C. Padovani, Corros. Eng. Sci. Technol., 46 (2011) 82-90.
[108] E. Smailos, Corros., 56 (2000) 1071-1074.
[109] E. Onumonu, N.P.C. Stevens, in proceedings of Scientific Basis For Nuclear Waste Management XXXI, Materials Research Society, Sheffield, UK, (2008), pp. 313-322.
[110] W.E. Clark, J. Electrochem. Soc., 105 (1958) 483-485.
[111] X. Gao, X. Wu, Z. Zhang, H. Guan, E.-h. Han, J. Supercrit. Fluids, 42 (2007) 157-163.
[112] R.H. Lamoreaux, D. Cubicciotti, J. Electrochem. Soc., 140 (1993) 2197-2205.
[113] S. Sunder, N.H. Miller, D.W. Shoesmith, Corros. Sci., 46 (2004) 1095-1111.
[114] T.H. Song, I.S. Kim, S.K. Rho, J. Korean Nuclear Society, 27 (1995) 453-462.
[115] G. Bellanger, J. Mater. Sci., 30 (1995) 1259-1265.
[116] T. Miyazawa, T. Terachi, S. Uchida, T. Satoh, T. Tsukada, Y. Satoh, J. Nucl. Sci. Technol., 43 (2006) 884-895.
[117] E. Leoni, C. Corbel, V. Cobut, D. Simon, D. Féron, M. Roy, O. Raquet, Electrochim. Acta, 53 (2007) 495-510.
[118] N. Fujita, C. Matsuura, K. Saigo, Radiat. Phys. Chem., 50 (1997) 457-463.
[119] S. Delaunay, C. Mansour, E.-M. Pavageau, G. Cote, G. Lefèvre, M. Fédoroff, Corrosion, 67 (2011) 015003-015001-015003-015010.
[120] S. Glass, G.E. Overturf, R.A. Van Konynenburg, R.D. McCright, Corros. Sci., 26 (1986) 577-590.
[121] T. Yamamoto, S. Tsukui, S. Okamoto, T. Nagai, M. Takeuchi, S. Takeda, Y. Tanaka, J. Nucl. Mater., 228 (1996) 162-167.
[122] R.W. Bosch, M. Vankeerberghen, Electrochim. Acta, 52 (2007) 7538-7544.
[123] N. Fujita, C. Matsuura, K. Saigo, Radiat. Phys. Chem., 49 (1997) 357-362.
[124] R.S. Lillard, D.L. Pile, D.P. Butt, J. Nucl. Mater., 278 (2000) 277-289.
[125] M. Urquidi-Macdonald, J. Pitt, D.D. Macdonald, J. Nucl. Mater., 362 (2007) 1-13.
[126] R.S. Lillard, G. Vasquez, J. Electrochem. Soc., 155 (2008) C162-C168.
[127] A.N. Scott, W.R. Mawhinney, Corros., 65 (2009) 49-60.
[128] M.A. Nejad, M. Jonsson, J. Nucl. Mater., 334 (2004) 28-34.
[129] B. Baroux, Further Insights on the Pitting Corrosion of Stainless Steels in Corrosion Mechanisms in Theory and Practice, P. Marcus, J. Oudar (Eds.), Marcel Dekker, New York, NY, (1995) pp. 265-309.

[130] R. Pope, Corros., 12 (1956) 31-32.
[131] N. Fujita, C. Matsuura, K. Saigo, Radiat. Phys. Chem., 58 (2000) 139-147.
[132] G. Saji, Nucl. Eng. Des., 240 (2010) 1340-1354.
[133] T.D. Burleigh, C. Ruhe, J. Forsyth, Corros., 59 (2003) 774-779.
[134] P. Schmuki, J. Solid State Electrochem., 6 (2002) 145-164.
[135] H. Karasawa, E. Ibe, S. Uchida, Y. Etoh, T. Yasuda, Int. J. Radiat. Appl. Instrum. Part C, 37 (1991) 193-197.
[136] G.S. Was, P.L. Andresen, Corros., 63 (2007) 19-45.
[137] E.A. Marquis, R. Hu, T. Rousseau, J. Nucl. Mater., 413 (2011) 1-4.
[138] K. Ishigure, T. Nukii, S. Ono, Journal of Nuclear Materials, 350 (2006) 56-65.
[139] E.A. Marquis, J.M. Hyde, D.W. Saxey, S. Lozano-Perez, V. de Castro, D. Hudson, C.A. Williams, S. Humphry-Baker, G.D.W. Smith, Mater. Today, 12 (2009) 30-37.
[140] I.M. Neklyudov, V.N. Voyevodin, Russ. Phys. J., 51 (2008) 400-413.
[141] G.R. Odette, M.J. Alinger, B.D. Wirth, Ann. Rev. Mater. Res., 38 (2008) 471-503.
[142] S. Teysseyre, Z. Jiao, E. West, G.S. Was, J. Nucl. Mater., 371 (2007) 107-117.
[143] G.S. Was, S.M. Bruemmer, J. Nucl. Mater., 216 (1994) 326-347.
[144] T. Tsukada, S. Jitsukawa, K. Shiba, Y. Sato, I. Shibahara, H. Nakajima, J. Nucl. Mater., 207 (1993) 159-168.
[145] Z. Jiao, G.S. Was, J. Nucl. Mater., 408 (2011) 246-256.
[146] J.T. Busby, G.S. Was, E.A. Kenik, J. Nucl. Mater., 302 (2002) 20-40.
[147] R.G. Faulkner, J. Nucl. Mater., 15 (1997) 269-275.
[148] G.S. Was, Y. Ashida, P.L. Andresen, Corros. Rev., 29 (2011) 7-49.
[149] R.C. Newman, Stress-Corrosion Cracking Mechanisms in Corrosion Mechanisms in Theory and Practice, P. Marcus, J. Oudar (Eds.), Marcel Dekker, New York, NY, (1995) pp. 311-372.
[150] F.P. Ford, P.L. Andresen, Corrosion in Nuclear Systems: Environmentally Assisted Cracking in Light Water Reactors in Corrosion Mechanisms in Theory and Practice, P. Marcus, J. Oudar (Eds.), Marcel Dekker, New York, NY, (1995) pp. 501-546.

Chapter 2

Experimental Principles and Details

2.1 ELECTROCHEMICAL PRINCIPLES OF AQUEOUS CORROSION

As discussed in Chapter 1, corrosion is an electrochemical process that involves a series of oxidation and reduction reactions and occurs at the interface between the material of interest (for this thesis carbon steel) and its environment. The two redox reactions can be expressed as:

$$M \rightarrow M^{n+} + ne^{-} \tag{2.1}$$

where M represents the solid metal, M^{n+} represents the oxidized metal species, and n is the number of electrons transferred and

$$Ox + ne^{-} \rightarrow Red \tag{2.2}$$

where Ox represents the soluble oxidant and Red the reduced form of the oxidant [1].

Since the above reactions involve both chemical reactions and the movement of charged species (electrons or ions), the free energy change for an electrochemical reaction is potential dependent [2, 3],

$$\Delta_r G = -nF\Delta E \tag{2.3}$$

where $\Delta_r G$ is the free energy of the reaction, F is the Faraday constant (96 485 $C \cdot mol^{-1}$), and ΔE is the reversible potential difference of the reaction [2].

The Van't Hoff Isotherm gives the dependence of the free energy of the reaction on the concentrations of species involved and the temperature [2],

$$\Delta_r G = \Delta_r G^0 + RT\ln K_{eq} \tag{2.4}$$

where $\Delta_r G^0$ is the standard free energy of the reaction, R is the Universal Gas Constant (8.314 $J \cdot K^{-1} \cdot mol^{-1}$), T is the absolute temperature (in Kelvin), and K_{eq} is the equilibrium constant for the reaction. Similar to equation (2.3), the standard free energy of the reaction relates to the standard potential of the reaction. The standard potential, E^0, is the equilibrium potential for the half-reaction under standard conditions, where $\Delta_r G^0 = -nFE^0$ [4]. Since potential is always a relative value, an appropriate reference point is required. For a reference, the Standard Hydrogen Electrode (SHE) is chosen.

$$2H^+ + 2e^- \leftrightarrows H_2 \tag{2.5}$$

Equation (2.5) represents the reaction taking place on the SHE (Pt at 25 °C in solution with $a_{H+} = 1$ and $P_{H2} = 1$ atm). This half-reaction has been chosen as the zero or reference point for the potential scale ($E_{SHE} = 0$). The thermodynamics of any half-reaction can then be described in terms of a potential difference from $E_{SHE} = 0$. The thermodynamics of any overall redox reaction can, in turn, be evaluated from the difference between the potentials (vs. SHE) determined for each half-reaction involved.

Substitution of equation (2.3) into (2.4) allows for the conversion of the Van't Hoff Isotherm into the electrochemical equivalent, known as the Nernst equation,

$$E_{eq} = E^0 - \frac{RT}{nF} \ln K_{eq} \tag{2.6}$$

where E_{eq} is the equilibrium potential for the half-reaction (vs. SHE). The equilibrium potential of a half reaction, for example the generalized reaction in equation (2.2), can be calculated with proper substitution into the Nernst equation.

$$E_{eq} = E^0 - \left(\frac{RT}{nF}\right) \ln \left(\frac{[Red]}{[Ox]}\right) \tag{2.7}$$

Note that the proper form of the equilibrium constant using activities has been simplified to include concentrations. Also note that the convention for a redox reaction expressed in the Nernst equation in the above form is in the form of a reduction reaction [2, 3]. The Nernst equation can be used to determine the equilibrium potential under a variety of experimental conditions, such as variation in the concentration of redox species. The difference between the equilibrium potentials of the two half-reactions can then be obtained at each condition. It is this difference in the equilibrium potential that acts as the driving force and promotes the corrosion of the metal.

The overall corrosion reaction can be represented as the sum of the two electrochemical half-reactions:

$$M + Ox \rightarrow M^{n+} + Red \tag{2.8}$$

Therefore, corrosion involves the coupling of two electrochemical reactions at the surface of the metal. The potential of a corroding metal is that at which the rates of the anodic and cathodic reactions are equal for a given set of conditions, and this potential is referred to as the corrosion potential, E_{CORR}. The anodic current represents the rate of liberation of electrons from the metal (M) and the cathodic current represents the rate of consumption of electrons by the aqueous species (Ox). Therefore, since the anodic current equals the cathodic current, the rate of liberation of corrosion products (M^{n+}) is proportional to the rate of consumption of aqueous oxidants (Ox) at the corrosion potential. Since the corrosion current is a measure of the corrosion rate, it is a kinetic variable of interest in the study of corrosive processes.

The corrosion current is the absolute value of the anodic current or the cathodic current at the corrosion potential illustrated by the equation,

$$i_{CORR} = \sum i_a = |\sum i_c| \text{ at } E_{CORR} \quad (2.9)$$

where i_{CORR} is the corrosion current, i_a is the anodic current, and i_c is the cathodic current. However, the electrons are maintained within a short-circuited reaction, and so the externally measured current is zero,

$$i_{net} = \sum i_a + \sum i_c = 0 \text{ at } E_{CORR} \quad (2.10)$$

where i_{net} is the externally measured current of the system [1]. Although the corrosion current cannot be measured directly, the corrosion potential can be measured directly, and through applications related to the Butler-Volmer equation (derived below) the corrosion current can be obtained [2, 5-7]. Also note that with the use of 'i' all currents are representative of a current density (ie. units of $A \cdot cm^{-2}$) in this chapter and the following experimental chapters.

The forward rate of one of the half reactions, for example (2.2), is proportional to the activity of the reacting species (a_{Ox}),

$$\text{Rate} = k a_{Ox} \quad (2.11)$$

where k is a rate constant. In electrochemical reactions, the rate is expressed in terms of a current,

$$i = -nFk a_{Ox} \quad (2.12)$$

Analogous to the temperature dependence of rate constants, as described by the Arrhenius equation, the rate constants of electrochemical reactions are similarly dependent on potential,

$$k = k_0 \exp\left(-\frac{\overrightarrow{a} n F \eta}{RT}\right) \quad (2.13)$$

where k_0 is the pre-exponential factor, $\overrightarrow{a}$ is the transfer coefficient (describing the symmetry of the activation barrier to the forward and reverse reactions), and η is the

overpotential. The overpotential of an electrochemical reaction is the difference between the potential and the reaction's equilibrium potential.

$$\eta = E - E_{eq} \tag{2.14}$$

The above description occurs analogously for the reverse reaction, and summing the forward and reverse kinetic relationships provides the net current.

$$i = i_0 \left[\exp\left(\frac{\overleftarrow{a} n F \eta}{RT} \right) - \exp\left(-\frac{\vec{a} n F \eta}{RT} \right) \right] \tag{2.15}$$

where $\overleftarrow{a}$ and $\vec{a}$ are the transfer coefficients for the half-reactions proceeding in the reverse (anodic) and forward (cathodic) directions, respectively ($\overleftarrow{a} + \vec{a} = 1$), and i_0 is the exchange current. The exchange current is the current at zero overpotential. Equation (2.15) is the Butler-Volmer equation and it describes the measured current as a function of applied overpotential for a given half-reaction and is shown graphically in Figure 2.1 [8].

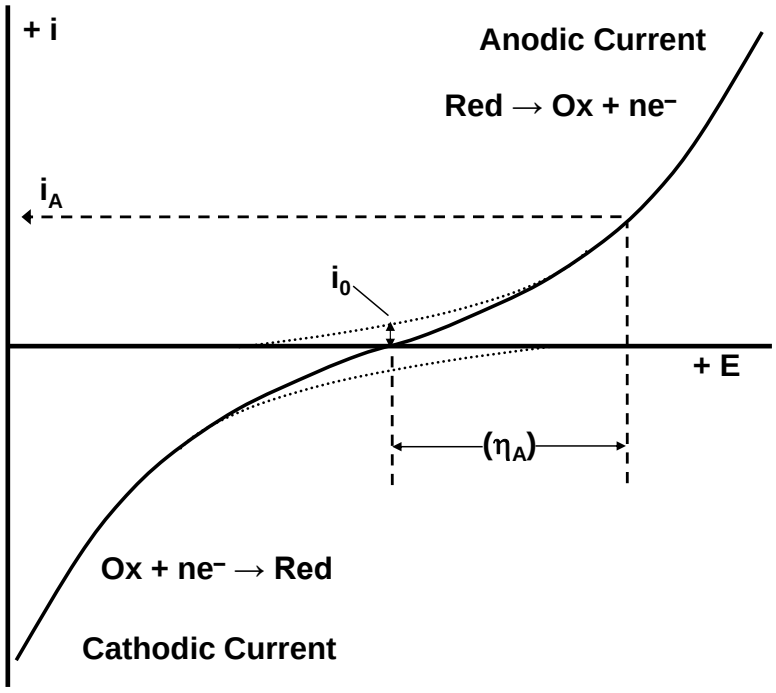

Figure 2.1: Current-potential relationship for a redox active species.

For the Butler-Volmer equation, at large positive overpotentials, the second exponential term becomes negligible in magnitude and the equation is dominated by the oxidation process, as described by the first (anodic) exponential term. Inversely, at large negative overpotentials, the first exponential term becomes negligible in magnitude and the equation is dominated by the reduction process, as described by the second (cathodic) exponential term.

For the case of a corrosion reaction (2.8), two half reactions are coupled and are reacting at the combined corrosion potential. Each half-reaction will have its own independent Butler-Volmer relationship. The net observable current-potential relationship is then obtained by the sum of the two Butler-Volmer equations. The summed Butler-Volmer equations of two half reactions of a corrosion process is called the Wagner-Traud equation [9-11].

$$i = i_{CORR}\left[\exp\left(\frac{a_A nF}{RT}(E–E_{CORR})\right) – \exp\left(–\frac{a_c nF}{RT}(E–E_{CORR})\right)\right] \qquad (2.16)$$

where a_A is the anodic transfer coefficient and a_C is the cathodic transfer coefficient.

In the Wagner-Traud equation, one half of the Butler-Volmer equation of each half reaction is negligible, resulting in an equation composed of the anodic exponential term of the oxidation reaction and the cathodic exponential term of the reduction reaction. For the Wagner-Traud equation, the transfer coefficients are similar to those in the Butler-Volmer equation, though in this case they correspond to the activation barriers for the two different half-reactions. i_{CORR}, as described above, is the corrosion current, and is the short-circuited current occurring when the system is not polarized away from the corrosion potential. $E–E_{CORR}$ represents the degree of polarization (overpotential) away from the corrosion potential.

The above description is for a theoretical kinetically controlled system; however, the rate of an electrochemical reaction may be further limited. The rate of an electrochemical reaction may be limited by the finite rate at which a reacting species diffuses to the electrode surface. The resulting exchange current is proportional to the concentration of the reacting species at the electrode/solution interface.

$$i_0 = -\eta F D_x \frac{c_x(\infty) - c_x(0)}{\delta} \tag{2.17}$$

where D_x is the diffusion coefficient of the reacting species x, $c_x(\infty)$ is the concentration of species x in the bulk solution, $c_x(0)$ is the concentration of species x at the electrode surface, and δ is the diffusion layer thickness. There may also be effects on the current from migration (the movement of ions under an electric field due to coulombic forces) or convection (the depletion or addition of reacting species to an electrode surface, often resulting from processes such as electrode rotation).

Additionally, an oxide may form and impede the rates of reactions. As discussed in Chapter 1, the corrosion of a metal is often accompanied by the formation of a surface oxide. The overpotential for the metal oxidation at the metal/oxide interface, or that for the reduction of aqueous species at the oxide/aqueous interface, will be further affected by the potential gradient across the oxide layer, ΔE_{Ox}. The potential gradient results from an oxide film resistance, R_{film}, and the current resulting from the electrochemical reaction, as shown by Ohm's Law.

$$\Delta E_{Ox} = iR_{film} \tag{2.18}$$

Since R_{film} is proportional to oxide thickness, as the oxide layer grows ΔE_{Ox} increases leading to a decrease in the overpotential. This will slow down the electrochemical half reactions at the interfaces and consequently slow the oxide

production rate. The overpotentials at the interfaces cannot be directly measured, however, E_{CORR} can be measured, and is related to overpotentials by,

$$E_{CORR} = E^{eq}_{Red/Ox} - \eta_{Red/Ox} \quad (2.19)$$

As the oxide layer grows, the oxide production rate by the electrochemical reaction,

$$2\ M(s) + n\ H_2O(l) \leftrightarrows 2\ MO_{n/2}(s) + n\ H_2(g) \quad (2.20)$$

will decrease until it eventually equals the rate of oxide dissolution,

$$2\ MO_{n/2}(s) + n\ H^+(aq) \leftrightarrows 2\ M^{n+}(aq) + n\ OH^-(aq) \quad (2.21)$$

At this point the oxide layer reaches a steady state and the corrosion rate will be dictated by the rate of oxide dissolution. The more insulating the oxide layer, the faster this approach to steady state will occur.

Furthermore, a resistance may be present in the solution between the metal electrode and the reference electrode. Akin to equation (2.18), a potential drop will occur. For electrochemical studies, a potential drop within the solution would affect the potential measure of interest between the electrode being studied and the reference electrode. As shown in equation (2.18), a small resistance would result in a small potential drop. This is obtained by using electrolytes of sufficient concentrations to lower the solution resistance to give a negligible potential drop.

Beyond potential distributions within the system, capacitance contributions may arise due to charge redistribution at interfaces. At the metal (or oxide)/solution interface, the charge redistribution results in the formation of a double-layer capacitance. At the interface, a potential difference, or overpotential, is present between a metal (or oxide) and the bulk solution (equation 2.19). An abrupt change in potential at the interface

would require a substantial redistribution of charge. The distribution of charge results from electrons in the metal (or oxide) and ionic species in solution, that may accumulate at the interface. To maintain electrical neutrality, a diffuse region of charge within the solution near the interface may be present. Various models have been developed to characterize the double-layer capacitance and a simplified description of one model is provided. At the interface, two planes, called the inner Helmholtz plane and the outer Helmholtz plane are established. The inner Helmholtz plane is associated with ions that are specifically absorbed onto the surface. The outer Helmholtz plane is the plane of closest approach for solvated ions. The inner and outer Helmholtz plane represents one half of the double-layer capacitance. The second half is the diffuse region of charge near the electrode surface. The diffuse region has a Debye length λ_D,

$$\lambda_D = \sqrt{\frac{\varepsilon\varepsilon_0 RT}{F^2 \sum_x z_x^2 c_x(\infty)}} \tag{2.22}$$

where ε is the dielectric constant, ε_0 is the permittivity of vacuum, and z is the charge number of ionic species x. The resulting double layer capacitance, C_{dl}, is dependent on the distribution of charge, dQ, and the potential difference at the interface, dE.

$$C_{dl} = \frac{dQ}{dE} \tag{2.23}$$

Additionally, a capacitance can be associated with the oxide film or deposit on the metal surface. The film capacitance, C_{film}, is,

$$C_{film} = \frac{\varepsilon_f \varepsilon_0}{\delta_f} \tag{2.24}$$

where ε_f is the dielectric constant of the oxide film material, and δ_f is the thickness of the oxide film.

As can be seen, the corrosion mechanism and resulting current-potential relationship is dependent on a number of factors, including charge transfer kinetics, diffusion, the formation of oxides, and interfacial chemistry. Through the experimental isolation of individual variables a more thorough understanding of the corrosion system can be obtained.

2.2 ELECTROCHEMICAL TECHNIQUES

2.2.1 Electrochemical Cell Setup

For all studies, a three-electrode electrochemical cell was employed. Along with the electrochemical cell, a potentiostat is used to both control and measure the potential and current. In the electrochemical cell the current of the reaction under investigation passes between the working electrode (the electrode of interest, or in the case of this thesis, carbon steel) and the counter electrode. The counter electrode should have high activity, negligible by-product production and a larger surface area compared to the working electrode. For these reasons platinum mesh is a common choice for the counter electrode and was used in this thesis. The third electrode is the reference electrode, which is a stable electrode of known potential, against which the potential of the working electrode can be controlled or measured. In the potentiostat, the working electrode and reference electrode are connected through a circuit with a high impedance voltmeter that ensures negligible current flows through the external measurement circuit between the working electrode and reference electrode, which ensures a limited iR (voltage) drop [12]. Therefore, the potential of the reference electrode remains constant.

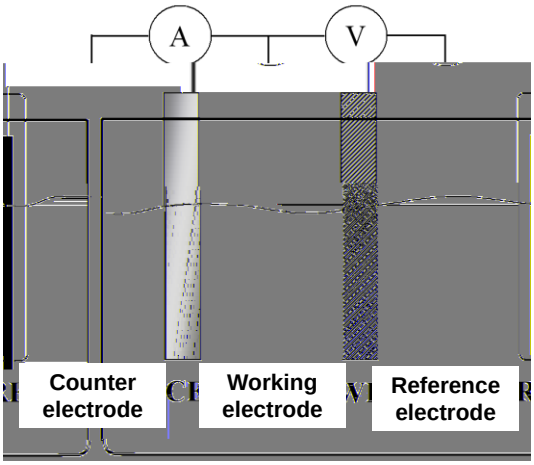

Figure 2.2: Schematic of a three-electrode cell setup.

2.2.2 Corrosion Potential

As stated in section 2.1, the corrosion potential, E_{CORR}, is the potential that is established on a corroding metal surface when there is no external current or potential applied to the system. The rates of the coupled anodic and cathodic reactions depend on factors, including: the presence or absence of an oxide film, the electronic properties of the oxide film, thickness of the oxide film, pH, temperature, and the presence of potentially oxidizing or reducing species in the aqueous phase [13]. E_{CORR} can be measured by measuring the potential between the working electrode and reference electrode.

Since E_{CORR} is typically a complicated function of not only the equilibrium potentials of the coupled redox pairs, but also the electrode surface, topography, the concentration of the redox couples, and the individual reaction rates, the prediction of E_{CORR} from known thermodynamic and kinetic parameters is often not possible.

2.2.3 Cyclic Voltammetry

Cyclic voltammetry (CV) is used to study various anodic and cathodic processes that occur at an electrode surface as a function of an applied potential. For a CV, the current density is monitored while the working electrode potential is scanned linearly from an initial potential to a final vertex potential, Figure 2.3. The scan direction is then reversed and scanned back to the initial potential and this cycle can be repeated any number of times. The initial and final vertex potentials are chosen as potentials within the water stability region (above the potential of water reduction and below the potential of water oxidation). The measured current density during the scan cycles is a measure of the net rate of charge transfer occurring on the working electrode, i.e. it may be a combination of a reductive and oxidative current.

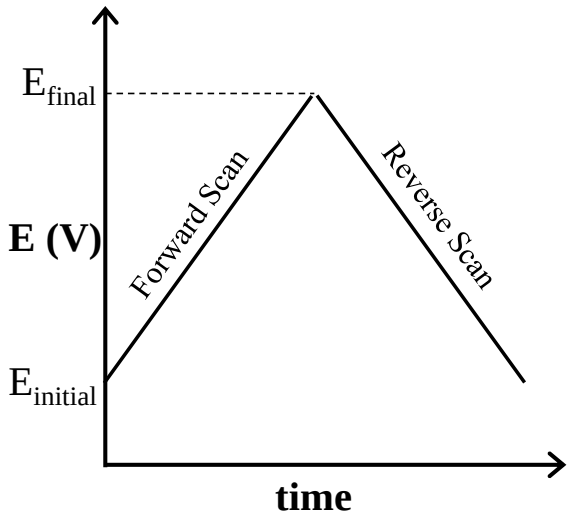

Figure 2.3: The potential-time profile applied in a cyclic voltammetry experiment.

The measured current is recorded as a function of potential and can often provide information about the sequence of electrochemical oxidation and reduction reactions occurring on the working electrode. The current response may depend on the potential scan rate, and changes to the scan rate may provide information on the relative

contribution to the current of varying reactions [13]. Also, changes to the final vertex potential can provide information on the coupling of oxidation and reduction processes.

2.2.4 Potentiostatic Polarization

In a potentiostatic polarization experiment a constant external potential, E_{APP}, is applied to the working electrode, with respect to the reference electrode, and is held for a certain length of time while the resulting current is measured. The value of the applied potential with respect to E_{CORR} will determine the direction of electron flow, thereby allowing either the anodic or cathodic reaction to be studied at the working electrode. During anodic polarization the time-dependent behavior of the observed current can often provide insight into processes such as the oxide film growth mechanism. Under potentiostatic polarization, the measured current will have a unique value if the coupled redox half reactions remain the same due to the face that i and E_{APP} are related via the Butler-Volmer equation. The change in current with time also provides insight in the changes occurring on the working electrode surface as the system approaches steady state.

2.2.5 Linear Polarization Measurements

Linear polarization (LP) measurements involve scanning the potential linearly about either E_{CORR} or E_{APP}, while measuring the current. The potential limits are kept to a minimal value, typically less than 30 mV, in order to remain within an approximately linear region of the Butler-Volmer equation (around i_0 in Figure 2.1, or i_{CORR} of the Wagner-Traud equation). Also, the small potential range minimizes perturbation of the

system away from E_{CORR} (i.e., the natural corroding system) or from the desired applied potential. Several useful parameters can be calculated from LP measurements depending on the electrode kinetics. One parameter, the polarization resistance, can be useful in interpreting passivity of a resistive film, or the relative rates of electron transfer processes on an active film.

2.2.6 Electrochemical Impedance Spectroscopy

As discussed in section 2.1, a number of resistive, capacitive, and diffusion effects may be present in an electrochemical process. One way to characterize these elements is through electrochemical impedance spectroscopy (EIS) [13, 14]. Electrochemical impedance spectroscopy is a commonly used method to determine properties of an oxide film, including resistive, capacitive, inductive, and diffusive components, and rates of charge transfer at the various interfaces [14]. The following is a simplified description of a coupled resistor and capacitor, and further discussion of elements, such as diffusive components, are addressed with experimental results in the appropriate chapters.

Generally, the system is broken down into any number of resistors and capacitors that may be electrically in series or in parallel. A resistor is an element that limits current flow and is proportional to resistivity (inversely to conductivity) and length, and inversely proportional to area. For electrochemical purposes, a resistive behaviour is often related to the resistance of an oxide film, or a charge transfer process at an interface. The measured current passing through a resistor, with a resistance R_x, can be calculated from Ohm's Law.

$$i=\frac{\Delta E}{R_x} \tag{2.25}$$

As described with the double-layer in section 2.1, a capacitance can be envisioned as the change in a charge per change in potential,

$$C=\frac{dQ}{dE} \tag{2.26}$$

and because the charge is the integration of the current over a unit time, the measured current for a capacitor is,

$$i=C\frac{dE}{dt} \tag{2.27}$$

As shown in equations (2.25) and (2.27), current-potential relationships are dependent on resistive and capacitive elements of the electrochemical system. Electrochemical impedance spectroscopy involves the input of a varied frequency potential, and the measure of a frequency dependent current. The input potential for EIS is a small sinusoidal potential (typically 10 mV amplitude) about E_{APP} or E_{CORR}.

$$E= E_{amp}\sin(\omega t) +E_{APP}(\text{or } E_{CORR}) \tag{2.28}$$

where ω is the angular frequency and E_{amp} is the maximum amplitude of the sinusoidal potential. As in linear polarization, a small perturbation is applied so that a narrow linear tangent of potential is measured of the larger scale exponential current-potential relationship, Figure 2.1. The sinusoidal potential ranges over several orders of magnitude of frequencies (f) (typically 10^4 Hz to 10^{-2} Hz), where $\omega = 2\pi f$. The applied sinusoidal potential gives a sinusoidal current response, Figure 2.4,

$$i = i_{amp}\sin(\omega t + \theta) \tag{2.29}$$

where i_{amp} is the current amplitude and θ is the phase shift. The impedance, $Z(\omega)$, of the system is determined as function of the frequency of the sinusoidal potential input and measured sinusoidal current.

$$Z(\omega t) = \frac{E_{amp}\sin(\omega t)}{i_{amp}\sin(\omega t + \theta)} \tag{2.30}$$

For the impedance relationship, if the current is in-phase with the potential ($\theta = 0°$), then the electrochemical response is purely resistive. If the current is out of phase ($\theta = -90°$), then the electrochemical response is purely capacitive, since for a capacitor the measured current is,

$$i = C\frac{dE}{dt} = \frac{d}{dt}\left(C \cdot E_{amp}(\omega t)\right) = C \cdot E_{amp}\frac{d\sin(\omega t)}{dt} \tag{2.31}$$

$$= C \cdot E_{amp}\omega\cos(\omega t) = i_{amp} \cdot \sin(\omega t - \frac{\pi}{2})$$

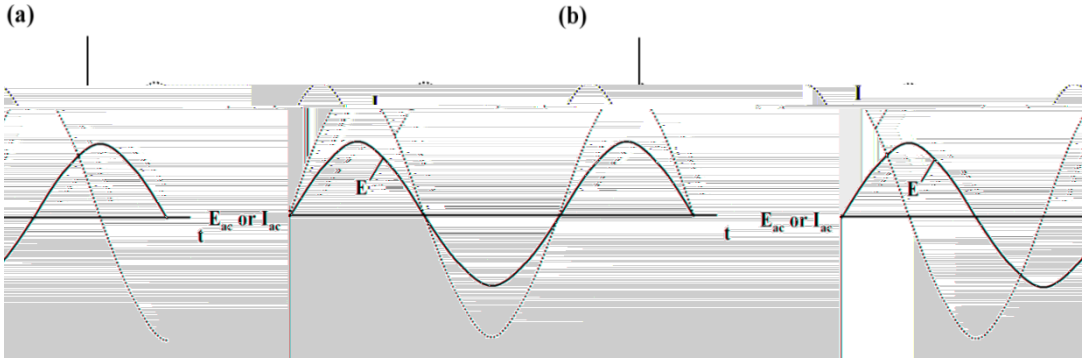

Figure 2.4: Relationship between the input sinusoidal voltage across (a) a resistor and (b) a capacitor and the current output.

Due to the phase shift, the impedance is expressed as a complex function of real, $Z'(\omega)$, and imaginary, $Z''(\omega)$, components.

$$Z(\omega t) = \frac{E_{amp}\sin(\omega t)}{i_{amp}\sin(\omega t + \theta)} = Z'(\omega t) - jZ''(\omega t) \text{ where } j^2 = -1 \tag{2.32}$$

where the resistance, R_x, contributes to the real component of the impedance and the capacitance, C, contributes to the imaginary component of the impedance.

$$Z'(\omega) = R_x \text{ and } Z''(\omega) = \frac{1}{\omega C} \tag{2.33}$$

The absolute value of impedance, $|Z(\omega)|$, is given by,

$$|Z(\omega)|^2=Z(\omega)\cdot Z(\omega)^*=Z'(\omega)^2+Z''(\omega)^2=\frac{R_x^2+\omega^2C^2}{\omega^2R_x^2C^2} \tag{2.34}$$

and the phase angle is given by,

$$\theta=\arctan\frac{Z''(\omega)}{Z'(\omega)}=\frac{1}{\omega R_xC} \tag{2.35}$$

The relation of phase angle,$|Z(\omega)|$, R_x, and C in the complex plane is shown in Figure 2.5.

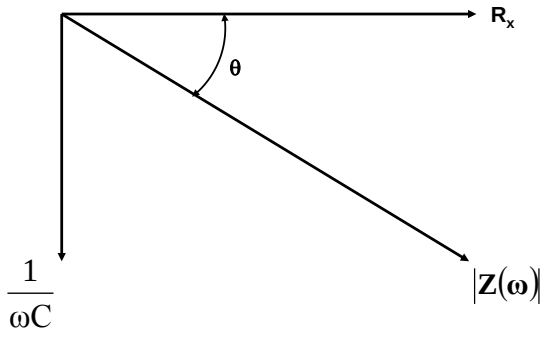

Figure 2.5: Relationship of real and imaginary components of impedance in a series one-RC circuit.

The impedance spectra are usually graphed in terms of a Nyquist plot or a Bode plot, Figure 2.6. For a Nyquist plot, the real impedance component is plotted against the imaginary component and is often extrapolated to a semicircle. For a Bode plot, which is composed of two graphs, the absolute impedance and phase angle are plotted as a function of frequency.

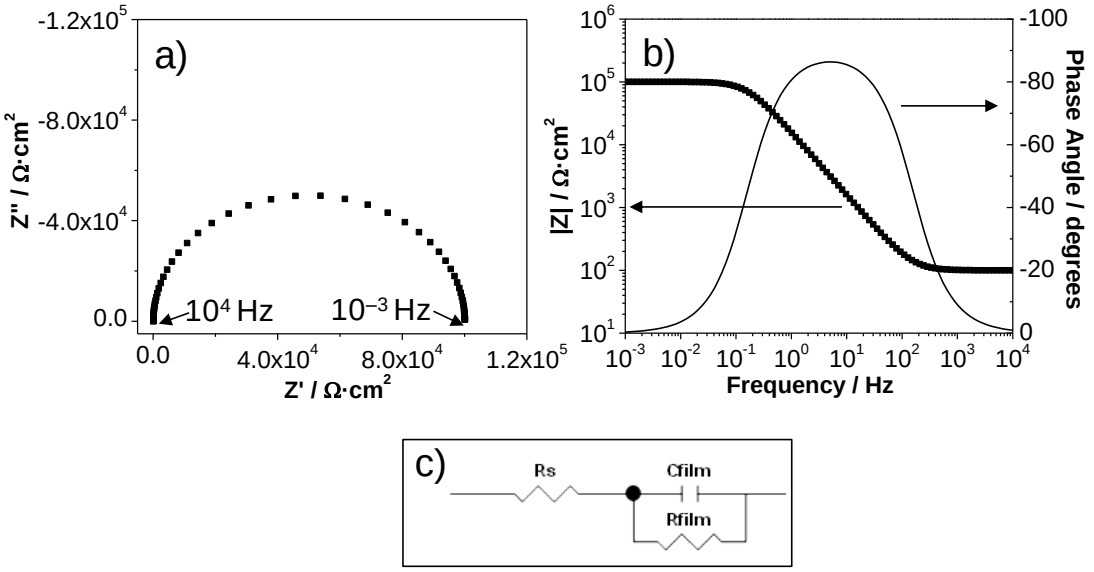

Figure 2.6: A (a) Nyquist plot and (b) Bode plot of a (c) one-time constant electrical equivalent circuit.

The Nyquist and Bode plots can be used to provide information on how the system is behaving. For example, for the circuit shown in Figure 2.6c, at very high frequencies there is no time for the charge to build up a capacitance, so the impedance is purely resistive, and specifically, the solution resistance, R_s, can be determined. At very low frequencies the capacitive charge has time to build up and dissipate, resulting in impedance that is due to the total resistance of the system, i.e. $R_s + R_{film}$ for the circuit in Figure 2.6c. In between the low and high frequencies both resistive and capacitive components contribute to the impedance. When there is more than one resistor-capacitor (RC) component in the circuit, the resistance and capacitance of individual components can be extracted from the impedance measurements as a function of ω.

Quantitatively, an equivalent circuit model, which consists of a series of RC components, can be fit to the Nyquist and Bode plots. Once an appropriate, and generally

simplest, model is determined, the individual elements of the circuit can be determined. The individual elements can provide information on oxide film resistance and capacitance, or charge transfer resistance and double-layer capacitance, which can be used to further calculate parameters such as oxide film thickness and electron transfer rates.

2.3 SURFACE ANALYSIS

2.3.1 Scanning Electron Microscopy

Scanning electron microscopy (SEM) is primarily used to investigate surface topography. A high resolution electron beam is directed onto the sample surface and the scattered electrons are detected. Samples are in a vacuum chamber in order to give both incident and resulting electrons free passage from the source to the sample and the sample to the detector. The incident electrons typically have an energy ranging from a few hundred eV to 40 keV. They are focused by one or two condenser lenses into a beam with a very fine focal spot, sized 0.4 to 5 nm. The beam passes through pairs of scanning coils or pairs of deflector plates which deflect the beam either horizontally or vertically so that a raster scan can be used to image a rectangular area of the sample [15].

When a sample surface is subjected to a focused beam of electrons, various processes can occur. Incident electrons can interact with the atoms on or very near, the surface of the sample and eject secondary electrons. These are lower in energy than the incident beam and only arise from the top few nanometers of the sample surface. Secondary electrons are used to study the sample topography. Due to varying distances from the detector, secondary electrons from areas of higher points on the sample surface

are more likely to be detected than electrons from lower points. The varying levels of detection results in a brightness contrast in the image that gives the micrograph depth perspective.

2.3.2 Transmission Electron Microscopy

Transmission electron microscopy (TEM) is used to study the microstructure and crystal structure of samples [16]. The TEM operates under the same principles as a light microscope, but uses electrons instead of light, and therefore, samples must be thin enough to transmit electrons (typically 20-200 nm). As in SEM, the samples must be under vacuum. A TEM is composed of an electron source, producing a standard energy of 100 keV, two condenser lenses to focus and adjust magnification, and magnetic coils to align the electron beams. Akin to a light microscope, in which the resolution is limited by the wavelength of the light, TEM resolution is limited by the wavelength (de Broglie wavelength) of the electron. The standard electron energy of 100 keV electrons corresponds to a wavelength of 37 pm, which is roughly 50 times smaller than neighbor separations in crystals [16].

A series of imaging methods are possible with TEM, with the most common mode being bright field imaging. In this mode, the brightness of the image is determined by the level of interaction (diffraction) of incident electrons with the sample. Thicker areas will appear dark and areas with no sample presence allow for the electron beam path to pass through creating a bright image.

2.3.3 X-Ray Photoelectron Spectroscopy

X-ray photoelectron spectroscopy (XPS) is a quantitative spectroscopic technique that can measure the elemental composition, empirical formula, chemical state, and electronic state of the elements that exist within a material. Spectra are obtained by irradiating a material with X-rays and measuring the kinetic energy (KE) and number of electrons that are ejected as a result. Photoelectron spectroscopy is based on a single photon/electron ejection process. Adsorption of an X-ray, of known energy, by an atom on the sample surface leads to the ejection of a single electron from the inner shell of the atom, and the resulting kinetic energy of the ejected electron is analyzed.

$$KE = h\nu - BE - \Phi \tag{2.36}$$

where BE is the binding energy of the electron in the atom that is ionized, h is the Planck constant, ν is the frequency of the X-ray, KE is the kinetic energy of the emitted electron, and is Φ the work function [16]. The work function is a combination of the sample work function and the work function induced by the spectrometer. The sample work function is the minimum amount of energy required to move an electron from the Fermi level of the sample into vacuum. From the measured kinetic energy, the binding energy of the emitted electron is calculated using equation 2.36 (with knowledge of $h\nu$ and Φ) [16].

A typical XPS spectrum is a plot of the measured photoelectron intensity as a function of the binding energy of the electrons detected. Each element produces a set of XPS peaks or lines at characteristic binding energy values. The varying binding energies of a particular element, for example iron, can be useful in determining the varying oxidation states of the elements present. The sizes of the peaks are directly related to the amount of a particular element within the sample volume that is irradiated.

2.3.4 Raman Spectroscopy

Raman spectroscopy is a surface analytical method used to probe the composition of materials that are Raman active. The instrumentation of the Raman spectrometer consists of a laser source, a sample-illumination system and a suitable detector. Raman spectroscopy detects induced changes in the polarizability of the electron cloud around a molecule following an interaction of the molecule with light [17]. Most of the interactions results in elastic, or Rayleigh scattering. However, a small fraction of the interactions results in inelastic scattering. If the molecule absorbs the incident photon, is excited to a virtual energy state and relaxes to a higher than initial vibrational state, the scattered photon will have a lower energy than the energy of the incident photon, for what is called Stokes scattering. Also, if the molecule was initially in a high vibrational energy state and then excited to a virtual energy state by absorption of a photon, followed by return to a lower vibrational state, the energy of the scattered photon is larger than that of the incident light, resulting in what is called Anti-Stokes scattering. The relative ratio of Stokes and Anti-Stokes scattering is proportional to temperature, as regulated by the Boltzmann distribution.

The energy between the incident and scattered light appears as a frequency shift between the scattered light frequency, ν', and the excitation frequency, ν''. The relationship between these frequencies and the vibrational energy is given by

$$h\nu'' = h\nu' + \Delta E_{vibration} \tag{2.37}$$

where $\Delta E_{vibration}$ is the energy gap between the two vibrational levels that is involved in the transition. It is the $\Delta E_{vibration}$ that is examined in Raman spectroscopy.

For a transition to be Raman active, the molecule must possess constant polarizability, the ability to deform the electron cloud with respect to the vibrational coordinate. The polarizability will determine the Raman scattering intensity, whereas the Raman shift is equal to the energy gap between the two vibrational levels that are involved in the transition [17]. A benefit of Raman spectroscopy for corrosion based studies is that water has weak Raman scattering and therefore analysis can be performed in-situ or without interference from an incompletely dried sample. Raman spectroscopy also has the advantages of using visible light and being easily combined with an optical microscope. It does have disadvantages of long acquisition times and since it is difficult to normalize, it does not have the quantitative advantage of techniques such as XPS.

2.4 EXPERIMENTAL PROCEDURES

The following describes general experimental procedures that were used in multiple chapters. Unique experimental techniques, procedures, and equipment are described in individual chapters.

2.4.1 Electrochemical Cell

A three-electrode cell, consisting of a reference electrode, a Pt mesh counter electrode and a carbon steel working electrode, was used. In the case of all experiments conducted outside of the radiation environment, the reference electrode used was a saturated calomel electrode (SCE) (Fisher Scientific), whereas for radiation experiments a Hg/HgO reference electrode (Radiometer Analytical) in 1.0 M KOH solution was employed. The Hg/HgO electrode has been found to be more resistant to radiation than

the SCE or Ag/AgCl electrode, and has a potential of 0.112 V versus SHE. All potentials are quoted on the SCE scale (0.242V vs. SHE). The working electrode in all experiments was A516 Gr70 carbon steel, purchased from Goodfellow (in wt%: C, 0.23; Mn, 1.05; Si, 0.32; Al, 0.04; P, 0.015; S, 0.008; balance Fe). The carbon steel electrode was set in an epoxy resin within polytetrafluoroetheylene (PTFE) cylinders so that only the flat front face was exposed to the solution in the cell. Prior to each experiment, the working electrode was polished manually with 400 and 600 grit silicon carbide papers, followed by polishing on a Texmet microcloth (Buehler) with a 1 μm MetaDi Supreme diamond paste suspension (Buehler), and lastly sonicated in an acetone/methanol mixture for 5 min to remove polishing residues.

A Solartron potentiostat (either model 1480 or 1287) and model 1252 frequency response analyzer were used in all electrochemical measurements. Corrware™ and Zplot™ software (Scribner and Associates) were used for experiment control and data analysis. EIS was performed by applying a 10 mV sinusoidal potential stimulus, either at E_{CORR}, or E_{APP}. The frequency was varied over the range 10^4 Hz to 10^{-2} Hz or 10^{-3} Hz. A second frequency scan consisting of measurements at several frequencies spanning the same range was then acquired to verify that the electrode surface remained at steady state over the course of the EIS measurement. Linear polarization measurements were performed by scanning the potential from E_{CORR} to –0.015 V vs. E_{CORR}, then to +0.015 V vs. E_{CORR}, and finally back to E_{CORR}, at a rate of 0.17 $mV \cdot s^{-1}$.

2.4.2 Surface analytical instrumentation

Carbon steel surfaces were regularly analyzed by SEM, XPS, and Raman spectroscopy. The SEM was performed using an Hitachi S-4500 field emission SEM in a high resolution mode. The XPS was performed using a KRATOS Axis Ultra spectrometer using monochromatic Al Kα radiation operating at 150 W, with a base pressure of 10^{-8} Pa. A low resolution survey was obtained with a pass energy of 160 eV and a step size of 0.7 eV over a range from 0 eV to 1100 eV. The spectra were calibrated by setting the main line for the C-1s spectrum of adventitious carbon to 284.8 eV. High resolution spectra were obtained using a pass energy of 20 eV and a step size of 0.05 eV over the Fe-2p (720.0 eV ±20.0 eV), O-1s (532.0 eV ± 8.0 eV) and C-1s (286.7 eV ± 8.5 eV) regions. The high resolution spectra were deconvoluted using standard peaks generated from reference materials. All XPS spectral analyses were performed using CasaXPS software (version 2.3.14). Raman spectra were taken using a Renishaw model 1000 Raman spectrometer with a Melles Griot 35 mW HeNe laser at 632 nm.

2.4.3 Solution Analysis

The aqueous phase was analyzed by UV spectrophotometry for hydrogen peroxide. All spectrophotometric measurements were performed using a diode array UV spectrophotometer (BioLogic Science Instruments). The hydrogen peroxide analysis was performed immediately after the termination of irradiation to minimize any thermal decomposition of H_2O_2 in the solution. The concentration of hydrogen peroxide was determined by the Ghormley tri-iodide method [18, 19]. In the presence of ammonium

molybdate catalyst, I^- is oxidized to I_3^- by H_2O_2, which has a maximum absorption at 350 nm with a molar extinction coefficient of 25500 $M^{-1} \cdot cm^{-1}$.

2.5 REFERENCES

[1] D.W. Shoesmith, Kinetics of Aqueous Corrosion in ASM Handbook on Corrosion, ASM Internationals, Materials Park, OH, (2003) pp. 42-51.

[2] A.J. Bard, L.R. Faulkner, Electrochemical Methods: Fundamentals and Applications, 2nd Ed., John Wiley & Sons, New York, NY, (2000).

[3] R.G. Kelly, J.R. Scully, D.W. Shoesmith, R.G. Buchheit, Electrochemical Techniques in Corrosion Science and Engineering, Marcel Dekker, New York, NY, (2003).

[4] W. Nernst, Z. Phys. Chem., 47 (1904) 52-55.

[5] W. Plieth, Electrochemistry for Material Scientists, Elsevier, Amsterdam, The Netherlands, (2008).

[6] R. Baboian, Electrochemical Techniques for Corrosion Engineering, National Association of Corrosion Engineers, Houston, TX, (1986).

[7] L.S. Van Delinder, Corrosion Basics: An Introduction, National Association of Corrosion Engineers, Houston, TX, (1984).

[8] J.A.V. Butler, Trans. Faraday Soc., 19 (1924) 729-733.

[9] C.V. Wagner, W.Z. Traud, Z. Elktrochem. P. Angew., 44 (1938) 391-454.

[10] F. Mansfeld, The Polarization Resistance Technique for Measuring Corrosion Currents in Advances in Corrosion Science and Technology, M.G. Fontana, R.H. Staehle (Eds.), Plenum Press, New York, NY, (1976).

[11] G.S. Frankel, J. ASTM Int., 5 (2008) 1-27.

[12] K.J. Vetter, Electrochemical Kinetics, Academic Press, New York, NY, (1967).

[13] E.E. Stansbury, R.A. Buchanan, Fundamentals of Electrochemical Corrosion, ASM Internationals, Materials Park, OH, (2000).

[14] M. Orazem, B. Tribollet, Electrochemical Impedance Spectroscopy, John Wiley & Sons, New York, NY, (2008).

[15] R.F. Egerton, Physical Properties of Electron Microscopy: An Introduction to TEM, SEM and AEM, Springer, New York, NY, (2005).

[16] D.J. O'Connor, B.A. Sexton, Surface Analysis Methods in Materials Science, Springer-Verlag, Berlin, Germany, (1992).

[17] E. Smith, G. Dent, Modern Raman Spectroscopy - A Practical Approach, John Wiley & Sons, West Sussex, England, (2005).

[18] A.O. Allen, C.J. Hochandel, J.A. Ghormley, T.W. Davis, J. Phys. Chem. A, 56 (1952) 575-586.

[19] J.A. Ghormley, A.C. Stewart, J. Am. Chem. Soc., 78 (1956) 2934-2939.

Chapter 3

Oxide Growth and Conversion on Carbon Steel as a Function of Temperature Over 25 and 80 °C under Ambient Pressure

3.1 INTRODUCTION

It is well established that the chemical nature and morphology of surface oxide films and deposits is an important parameter in controlling the steel corrosion rate. While iron and carbon steel corrosion has been studied extensively many uncertainties over film composition, phase structure and surface morphology that affect corrosion kinetics still persist [1-16].

Detailed room temperature studies on the oxide film growth and conversion as a function of electrode potential under both potentiodynamic and potentiostatic conditions [12, 13, 15] have established that there are three distinct potential regions for anodic oxidation and film growth on carbon steel at pH 10.6.

This Chapter examines the effect of temperature on oxide film growth and conversion as a function of potential in a temperature range between 25 °C and 80 °C at $pH_{25°C}$ = 10.6 using primarily electrochemical techniques. This temperature range was chosen since the electrochemical measurements can be carried out under ambient pressure, thus allowing more accurate in-situ measurements to probe surface oxidation and corrosion kinetics in detail. Also, this study aims to establish an overlap with other analyses. Chapter 8 discusses some electrochemical studies that were performed in a temperature range of 100 °C to 280 °C and Chapters 5 and 6 discuss parallel surface and chemical analysis studies on carbon steel coupons in leak-tight vials in a temperature range of 80 °C to 150 °C. By combining the ex-situ surface analyses and electrochemical

analyses over partially overlapping temperature ranges there is a hope to develop a consistent interpretation of the mechanism and provide a technical basis for extrapolation of the results to wider conditions that may not be easily achieved in laboratory.

For this study, one of the processes that can significantly influence high temperature corrosion is the Schikorr reaction, a thermal oxidation reaction of Fe^{II} hydroxide/oxide to magnetite [17]. Since this reaction is known to occur at temperatures as low as 70 °C, the effect of this reaction on the corrosion mechanism on carbon steel can be observed in the studied temperature range. The oxide film growth and conversion kinetics in the temperature range were followed by various electrochemical and ex-situ surface analyses. The results of the electrochemical study are discussed in detail and only limited surface analyses are presented here.

3.2 EXPERIMENTAL

3.2.1 Solutions

All experiments were conducted in Ar-sparged 0.01 M sodium borate solutions. The Ar (PRAXAIR) was 99.999% purity. The solutions were prepared using reagent grade $Na_2B_4O_7 \bullet 10H_2O$ (Caledon Laboratories Ltd.) and water purified using a NANOpure Diamond UV ultra-pure water system (Barnstead International) with a resistivity of 18.2 MΩ·cm. Reagent grade NaOH (Caledon Laboratories Ltd.) was added drop-wise to the solutions to adjust the pH. All experiments were conducted at a $pH_{25°C}$ of 10.6. Solution temperatures were controlled with a cycled water bath and a thermal jacket on the exterior of the electrochemical cell. Solutions were pre-heated to the

desired temperature before the working electrode was added to the cell and experiments began.

3.2.2 Procedure

After polishing, the working electrodes were rinsed with deionized water and placed in the electrochemical cell which had been sparged with Ar gas for at least 1 h to purge any oxygen from the solution. Electrochemical experiments then began with cathodic cleaning at –1.1 V_{SCE} for 5 min to remove any residual air-formed oxides on the working electrode, thereby creating a reproducible starting condition for all experiments. Following cathodic cleaning, two types of experiments were performed, cyclic voltammetry and 7 d potentiostatic film growth. All CVs were performed between the potential limits of –1.1 V_{SCE} and 0.4 V_{SCE} at a scan rate of 5, 1, or 0.17 $mV \cdot s^{-1}$. The dependence of CVs on temperature and pH was investigated. For the potentiostatic experiments, immediately following cathodic cleaning, the electrode was anodized at an E_{APP} of –0.7 V_{SCE}, –0.2 V_{SCE}, or 0.2 V_{SCE} with the intention of generating oxide films with different compositions and properties. EIS was recorded at regular intervals during the 7 d potentiostatic experiments.

3.3 RESULTS AND DISCUSSION

3.3.1 Cyclic Voltammetry

Cyclic voltammetry was performed on carbon steel in Ar-purged 0.01 M borate solution at $pH_{25°C}$ = 10.6 at four different temperatures, 25 °C, 50 °C, 70 °C, and 80 °C. The effects of scan cycling and potential-scan rate were examined at each temperature.

At a given temperature and scan rate, the current peaks appeared at the same potentials, albeit different intensities. Exceptions are the first cycles, whose voltammograms show very different behaviour from those of the subsequent cycles. This difference was larger at a faster scan rate (Figure 3.1 versus Figure 3.2). The singular first cycle behaviour is attributed to the fact that the oxidative dissolution of iron can be significant prior to the formation of a uniform layer of a magnetite (Fe_3O_4)-like oxide. Magnetite can be formed on carbon steel at relatively low potentials (> –0.95 V_{SCE} at pH 10.6, Figure 3.3) [18]. Nevertheless, the Fe_3O_4 formation on a freshly prepared electrode surface requires some time and competes with Fe^{II} dissolution from a bare metal surface. It is believed that these competing processes lead to the observations of the first cycle. Subsequent cycles are the same because the surface has an established Fe_3O_4 layer.

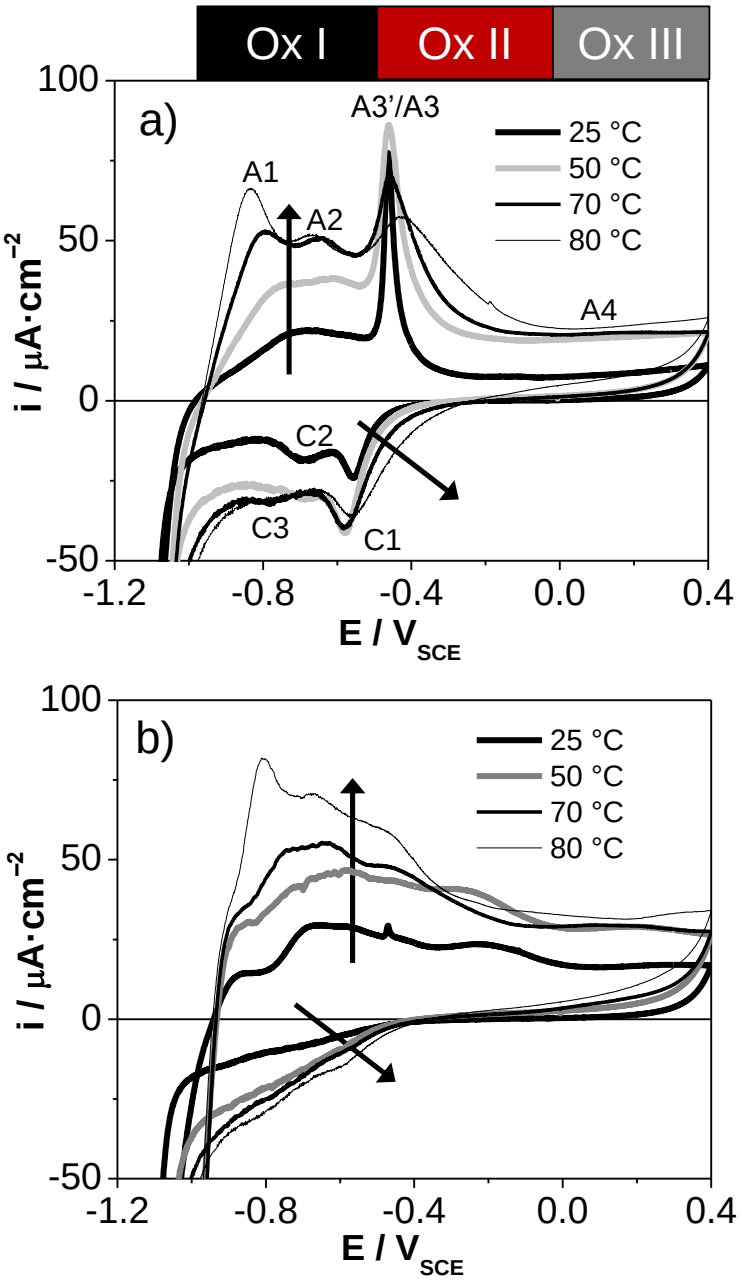

Figure 3.1: (a) Third and (b) first cycles of cyclic voltammograms recorded on carbon steel in Ar-sparged 0.01 M borate solution at pH 10.6. Cycles were recorded from –1.1 V_{SCE} to 0.4 V_{SCE} to –1.1 V_{SCE} at a scan rate of 5 $mV \cdot s^{-1}$. The arrow represents the direction of change when temperature increased from 25 °C to 50 °C, 70 °C, and 80 °C. See the text for the description of the labeled anodic and cathodic peaks.

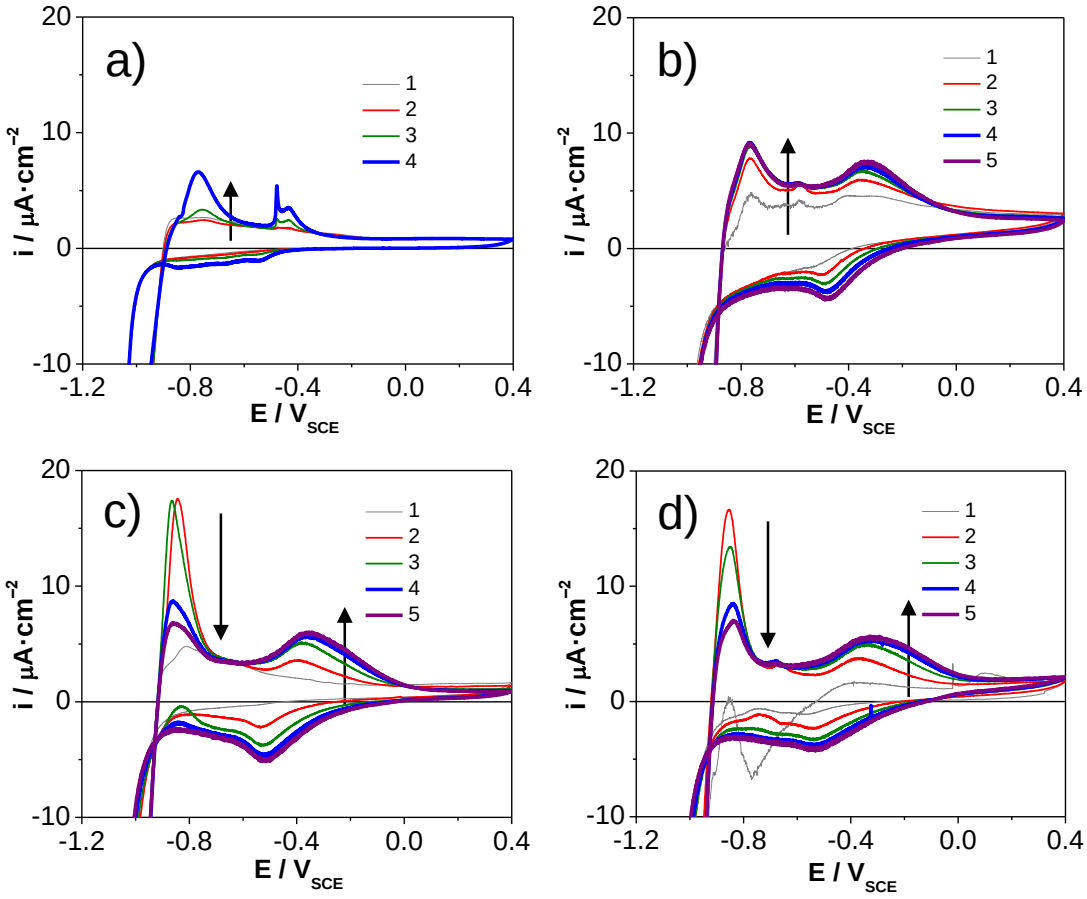

Figure 3.2: Cyclic voltammograms recorded on carbon steel in Ar-sparged 0.01 M borate solution at pH 10.6 at (a) 25 °C, (b) 50 °C, (c) 70 °C, and (d) 80 °C. Shown are the scans as a function of five consecutive cycles (–1.1 V_{SCE} to 0.4 V_{SCE} to –1.1 V_{SCE}) recorded at a scan rate of 0.17 $mV \cdot s^{-1}$. The arrows show the direction of change as the number of cycles increased from 2 to 3, 4, and 5.

Studies at 25 °C have shown that, once formed on pure iron or carbon steel, Fe_3O_4 is difficult to reduce [12]. This has been attributed to the fact that Fe_3O_4, being nearly insoluble but electronically conducting, can support water reduction more easily than Fe_3O_4 reduction to Fe^{II} or Fe^0 at potentials low enough for Fe_3O_4 reduction to occur [12]. Thus, although the voltammogram of the first cycle when compared with those of the

subsequent cycles can aid the interpretation of the electrochemical oxidation mechanism as a function of potential, the current observed during the first scan does not reflect the corrosion behaviour of carbon steel that has been in contact with water for any length of time, and the remaining discussion focuses mainly on the CVs of the subsequent cycles.

The CVs obtained during the 2^{nd} to 5^{th} cycles show at least four distinct anodic current peaks, labeled as A1, A2, A3'/A3 and A4 in Figure 3.1. This labeling scheme was based off previous studies [12-15]. Peak A2 was not prominent at room temperature and was not characterized previously [12]. The CVs presented in Figures 3.1 and 3.2 show that the positions of anodic current peaks did not vary with cycling, scan rate or temperature, except for a small shift of peak A1 to a lower potential at a higher temperature and at a slower scan rate. On the other hand, the current density of all of the peaks varied with the scan parameters and temperature. Equilibrium potentials of redox reactions on carbon steel (shown in Figure 3.3) [18] are not as temperature sensitive as dissolution and other transport processes that have strong temperature dependences. Since the anodic current is the sum of the rates of oxidative dissolution and oxide growth and these rates have different temperature dependences, the CVs obtained as a function of temperature and scan conditions can provide information on the nature of the oxide formed as a function of electrode potential.

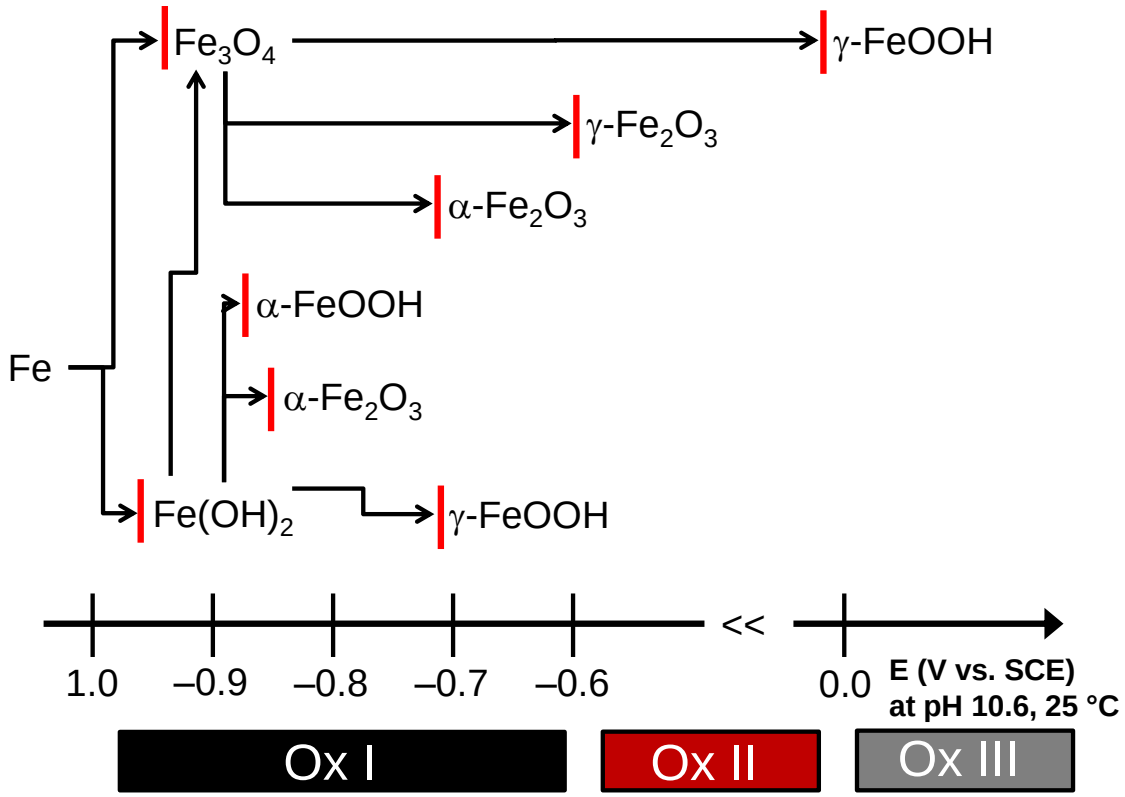

Figure 3.3: Calculated equilibrium potentials for various iron redox reactions on the electrochemical potential scale; where the equilibrium potentials are indicated by vertical lines and the potential values are those at pH 10.6 and 25 ºC. The three oxidation potential regions are also indicated.

3.3.1.1 Anodic Peak A1

This peak is observed at potentials where the base metal, Fe^0, can oxidize to Fe^{II} oxide/hydroxide and then to Fe_3O_4, as shown with the equilibrium potentials of the iron redox reactions in Figure 3.3. At a given temperature, the electrochemical oxidation of Fe^{II} oxide/hydroxide to a Fe_3O_4-like oxide occurs at a faster rate at pH 10.6 than at neutral pH due to the much lower solubility of Fe^{II} species at pH 10.6 [12]. At pH 10.6 the rate of deposition of the nearly insoluble Fe_3O_4-like oxide is fast relative to the Fe^{II}

dissolution, leading to formation of a uniform layer of the inverse spinel oxide [14]. The oxide formed on carbon steel is termed as a Fe_3O_4-like oxide since it is likely to have gradients of Fe^{II} and Fe^{III} concentrations within the oxide lattice, compared to the uniform distribution of Fe^{II} and Fe^{III} in a pure Fe_3O_4 lattice [19].

Oxide growth on a uniform and compact layer requires charge transport through the solid phase. The exact mechanism of the charge transport in a spinel or any general oxide is still debated [20, 21]. For the oxide grown under the test conditions, it is proposed that once a uniform layer of Fe_3O_4-like oxide is formed, the oxide layer grows by electrochemical oxidation processes consisting of injection of Fe^{II} into the oxide lattice at the metal/oxide interface and oxidation of Fe^{II} to Fe^{III} at or near the oxide/water interface. The accompanying reduction processes consist of water reduction to H_2 and O^{2-} injection into the oxide lattice at the oxide/solution interface. The Fe^{II} injected at the metal/oxide interface is either oxidized to Fe^{III}, incorporated into the oxide lattice or dissolved into the aqueous phase. Any Fe^{III} formed is also either incorporated into the oxide lattice or dissolved in the aqueous phase. A net migration of Fe^{II} occurs from the metal/oxide to oxide/water interface. This is assisted by electron hopping between the Fe^{II} and Fe^{III} sites in the oxide lattice. This mechanism for oxide growth will be referred to as “solid-state growth” as opposed to the growth by dissolution and precipitation, and is schematically illustrated in Figure 3.4.

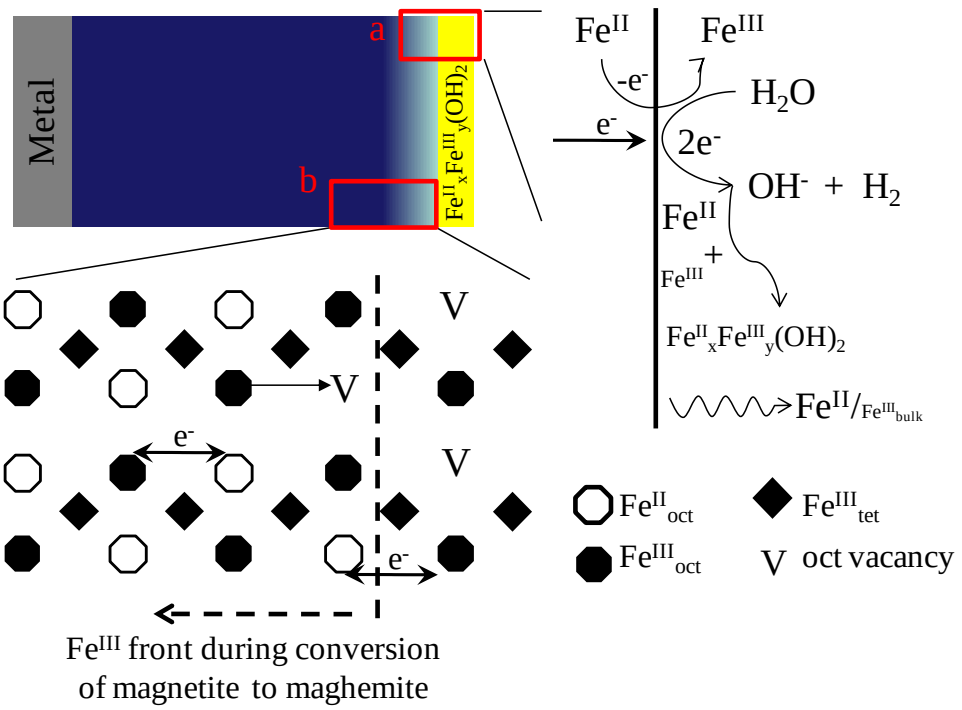

Figure 3.4: Simplified schematic of the oxide/solution interface and electron hopping between Fe^{II} and Fe^{III} sites in the spinel structure. For simplification, O^{2-} is not shown in the schematics of the oxide.

The conversion of Fe^{II} to Fe^{III} accompanied by oxide injection at the oxide/water interface is limited to oxidation to Fe_3O_4 in the potential region of peak A1. Once the surface is covered with a uniform Fe_3O_4-like layer, dissolution of iron occurs at the oxide/water interface and involves surface hydration of Fe^{II} and Fe^{III} followed by diffusion of the hydrated species away from the interface into the bulk aqueous phase. Due to the hydration, the surface of the Fe_3O_4 is most likely a mixed hydroxide $Fe^{II}_xFe^{III}_y(OH)_z$. This layer could not positively be identified in this study. However, in surface analysis studies at 80 °C and 150 °C (Chapters 5 and 6), the results did suggest the presence of surface hydrated species.

The electrochemical oxidation mechanism proposed above for peak A1 is consistent with all of the observations. The current density of peak A1 generally increased with an increase in temperature and this can be attributed to an increase in hydration and dissolution of Fe^{II} (and Fe^{III} to a smaller extent) from the Fe_3O_4 surface. The dependence of the current density on scan cycling was, however, different at temperatures ≥ 70 °C from that at lower temperatures and particularly so at slow scan rates. At scan rates ≤ 1 $mV \cdot s^{-1}$, peak A1 increased with cycling, with the largest increase occurring from cycle 2 to cycle 3 at lower temperatures, but it decreased with each cycle at temperatures ≥ 70 °C. By comparison, peak A3, whose behaviour is discussed later, increased with cycling at all temperatures. The effect of temperature on the dependence of peak A1 on cycling (from the 2^{nd} cycle and onwards) can be explained as follows. Although the Fe_3O_4-like layer thickened with cycling, the Fe_3O_4 film would still be relatively thin at temperatures below 50 °C. Due to the conductive nature of Fe_3O_4, the charge transport through the oxide layer from the metal/oxide to the oxide/water interface would not be the rate determining step for the electrochemical oxidation of base metal to Fe_3O_4. The inverse spinel structure of Fe_3O_4 can accommodate ion transport due to its spacious lattice structure, although the exact mechanism may still be debated. In addition, Fe^{II} and Fe^{III} occupy the same octahedral sites in Fe_3O_4, further facilitating charge transport. In addition, the thickness of the Fe_3O_4 layer should have little effect on iron dissolution since the dissolution is limited by the hydration and diffusion of Fe^{II} species at the oxide/water interface. This would result in very little change in the current density upon cycling at the potential range of peak A1.

Above 50 °C (tests at 70 °C and 80 °C) the Fe_3O_4-like layer thickens upon cycling due to thermally promoted oxidation of $Fe(OH)_2$ to Fe_3O_4 by a process known as the Schikorr reaction [17, 22]:

$$3\ Fe(OH)_2 \leftrightarrows Fe_3O_4 + H_2 + 2\ H_2O \quad (3.1)$$

The Schikorr reaction would accelerate not only the deposition of a uniform layer of Fe_3O_4 on a bare metal surface at low potentials, but also minimize the dissolution of hydrated Fe^{II} species from the Fe_3O_4 surface. The net result is thickening of the Fe_3O_4 layer. With a thicker oxide layer, the charge transport from the metal/oxide interface to the oxide/water interface is slower and it becomes a contributing factor in determining the rate of electrochemical oxidation. This results in a decrease in the current density of peak A1.

3.3.1.2 Anodic Peak A2/Cathodic Peak C3

The current densities of anodic peak A2 and the corresponding cathodic peak C3 were very small and, as a result, often not visible when peaks A1 and A3 (or C2) were prominent, particularly at higher numbers of scan cycles and at higher temperatures, Figure 3.2. At lower numbers of cycles (2^{nd} and 3^{rd}), the current density of peak A2 decreased with an increase in peak A1. These observations suggest that the process responsible for this peak is the anodic oxidation of an adsorbed layer of hydrated Fe^{II} species at the oxide/water interface, such as:

$$Fe(OH)_2 \text{ on } Fe_3O_4 \text{ surface} + OH^- \leftrightarrows FeOOH + H_2O + e^- \quad (3.2)$$

The oxidized species is likely an undetermined oxyhydroxide phase. While the oxidation of $Fe(OH)_2$ to α-FeOOH is thermodynamically feasible at this potential, it has been

shown to be a relatively slow process [23] and cannot compete with the oxidation to δ-FeOOH. The formation of δ-FeOOH, which has an equilibrium potential of approximately –0.7 V_{SCE} at pH 10.6 determined from free energies [24], is kinetically more favourable due to its isostructure to $Fe(OH)_2$ and the formation of δ-FeOOH in high pH solutions has been confirmed by Raman spectroscopy [25]. γ-FeOOH may also be forming at this potential, however the relative kinetics are not clear. The importance of this oxidation to the corrosion kinetics of carbon steel is likely to diminish with increases in time and temperature. The corresponding reduction peak, C3, was only visible in instances when peak A2 was clearly visible, for example, at $T \geq 50$ °C at a scan rate of 5 $mV \cdot s^{-1}$ (as seen in Figure 3.1a).

3.3.1.3 Anodic Peaks A3' and A3/Cathodic Peaks C1 and C2

Room temperature studies [12] have shown that the anodic peaks A3' and A3 on the forward scan are associated with two cathodic peaks C2 and C1, respectively, observed on the reverse scan (see Figures 3.1 and 3.2). Peak A3' labels the sharp current peak at the more negative potential while A3 is the broader peak at a more positive potential. For the cathodic peaks, C2 labels the peak at the lower potential and C1 the peak at the higher potential.

The separation of peaks A3'/A3 was less pronounced at a higher scan rate and at a higher temperature. This study also shows that the temperature dependence of A3'/C2 was very different from that of A3/C1. While the anodic peak A3' and its corresponding cathodic peak C2 became negligible at temperatures > 70 °C, peak A3 broadened significantly with increasing temperature. This is consistent with the mechanisms

previously proposed based on room temperature studies [12] where the broader peak A3, coupled with the larger reduction peak C1 at approximately –0.55 V_{SCE}, is due to the oxide-phase conversion from a more Fe_3O_4-like phase to a more maghemite (γ-Fe_2O_3)-like phase. The sharper peak A3', coupled with the smaller reduction peak C2 at –0.7 V_{SCE}, is attributed to the anodic conversion of the surface layer of the Fe_3O_4 phase. Considering the potential for peak A3', the oxidation is most likely that of a mixed hydroxide that had been formed at the lower potentials, leading to the formation of a few monolayers of an Fe^{III} oxide/hydroxide.

Magnetite and maghemite share the same inverse spinel structure which consists of cubic close packing arrays of oxide ions with cations in the octahedral and tetrahedral interstices [19]. Both oxides have nearly the same distance between two adjacent O^{2-} ions (0.295 nm) and the same unit cell dimensions. Maghemite can be considered to be Fe^{II} deficient Fe_3O_4 or conversely Fe_3O_4 can be considered to be γ-Fe_2O_3 doped with Fe^{II}. The conversion between Fe_3O_4 and γ-Fe_2O_3 is thus be nearly reversible, and this reversibility can be better seen at higher temperatures when peak A3 is much larger than peak A3'.

Peak A3, and the corresponding cathodic peak C1, broadened with increasing temperature, Figure 3.1a. The oxidative conversion of the Fe_3O_4 to the γ-Fe_2O_3 phase also requires charge transport through the solid phase for the growth of the Fe_3O_4-like oxide. A similar mechanism is proposed for the Fe_3O_4 growth in the potential range of peak A1, but with some key differences. These differences arise from the fact that in the higher potential region of peak A3 the Fe_3O_4-like oxide at the oxide/water interface can be further oxidized to the more γ-Fe_2O_3-like oxide. Charge transport through a pure

γ-Fe_2O_3 phase is much slower than through a Fe_3O_4 since it requires the migration of a Fe^{III} cation vacancy and this limits the rate of further growth of the oxide layer. Injection of Fe^{II} into the oxide layer at the metal/oxide interface, oxidation of Fe^{II} to Fe^{III} at the oxide/water interface, and the charge transport assisted by electron hoping between the two cation sites can still occur. However, as the outer layer becomes more oxidized, the ratio of Fe^{II}/Fe^{III} decreases and the rate of charge transport via electron hopping decreases. The Fe^{II} to Fe^{III} conversion front moves from the oxide/water interface further into the inner Fe_3O_4-like layer, broadening the Fe_3O_4 and γ-Fe_2O_3 interface. In this proposed mechanism (illustrated in Figure 3.4) a net migration of cations still occurs from the metal/oxide to the oxide/water interface while the Fe^{III} front within the oxide layer shifts toward the metal/oxide interface as more Fe_3O_4 is converted to γ-Fe_2O_3. With the formation of Fe^{III} from Fe^{II}, the concentration of interstitial Fe^{II} would decrease in the two oxide phases and the overall ionic transport rate would decrease. Once a layer of mostly Fe^{III} oxide forms on the surface, the carbon steel exhibits passivity.

The broadening of peak A3 with increasing temperature and the near reversibility of the process responsible for peaks A3 and C1 are consistent with the proposed mechanism. With this mechanism, the amount of the Fe^{II} to Fe^{III} conversion will depend on the thickness of the inner Fe_3O_4-like layer that has been formed prior to the oxidation to γ-Fe_2O_3. Thus, the net rate of charge transport will also be a function of temperature since it will depend on the concentrations of Fe^{II} and Fe^{III} and their distribution within the oxide lattice.

3.3.1.4 Anodic Peak A4

Peak A4 is associated with the broad peak that appears at potentials above –0.1 V_{SCE}. The current in this region was nearly constant with potential. The effect of temperature on the current is difficult to discern due to the large contribution of peak A3. In this potential region, anodic conversion of the γ-Fe_2O_3-like layer (Fe_3O_4/γ-Fe_2O_3) to γ-FeOOH is possible (see Figure 3.3) and this can lead to structural changes that can induce micro-fracture. In the presence of aggressive anions the micro-fractures can lead to pitting, but in the absence of aggressive anions the surface quickly repassivates and forms a thicker but defective (or porous) oxide film [12, 13].

3.3.1.5 Potential Regions of Film Growth and Conversion

The above CV analyses show that from the perspective of oxide film growth and conversion, division of the potential into three regions as defined in previous studies at room temperature continues to be appropriate at the higher temperatures. The oxide growth and conversion in each region at $pH_{25°C}$ 10.6 can be summarized as follows. In Ox I (–0.9 V_{SCE} < E < –0.6 V_{SCE}) a uniform layer of Fe_3O_4-like spinel oxide is formed and grows by a solid state charge transport mechanism as schematically presented in Figure 3.4. Dissolution increases with temperature. However, at temperatures > 70 °C, the Schikorr reaction accelerates the conversion of the hydrated species to Fe_3O_4. In Ox II (–0.6 V_{SCE} < E < 0.0 V_{SCE}) the Fe_3O_4 layer continues to grow, but the potential is high enough to convert a Fe_3O_4-like layer to a more γ-Fe_2O_3-like layer [12, 15]. Oxide growth and conversion in this region also occur by a solid-state charge transport mechanism, Figure 3.4. In this region, the oxide growth is rather limited and the anodic current is

used for oxide phase conversion. In Ox III (0 V_{SCE} < E < 0.4 V_{SCE}) anodic conversion of the Fe_3O_4/γ-Fe_2O_3 oxide to γ-FeOOH can induce micro-fracture but, in the absence of aggressive anions, the surface quickly repassivates. The oxide layer can grow by continuous film fracture and repassivation, producing a thicker but defective (or porous) oxide film on a Fe_3O_4-like base layer [12, 13].

3.3.2 Current Behaviour During Potentiostatic Film Growth and EIS Analysis

The film growth and conversion as a function of temperature were further investigated under potentiostatic conditions. Three potentials, one from each potential region; –0.7 V_{SCE} (Ox I), –0.2 V_{SCE} (Ox II) and 0.2 V_{SCE} (Ox III), were investigated. While applying a potential the current was monitored as a function of time, Figure 3.5. Periodically EIS was performed to characterize the oxide film present on the electrode. The current behaviour is discussed first.

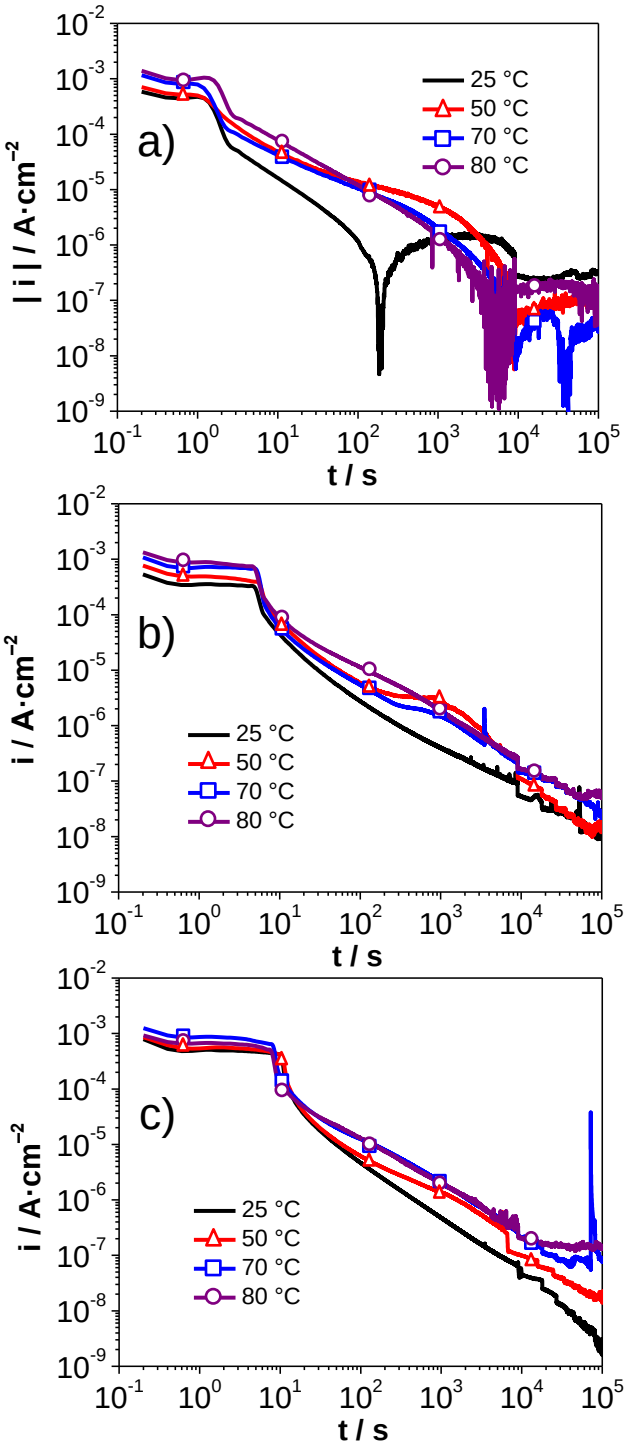

Figure 3.5: Log current vs. log time during potentiostatic film growth at (a) –0.7 V_{SCE}, (b) –0.2 V_{SCE}, and (c) 0.2 V_{SCE}.

At all temperatures and all applied potentials, the current observed was initially high at ~ 1 $mA \cdot cm^{-2}$ and remained at that level for a few seconds. When there is a sudden potential jump, electrical measurements can be distorted by an iR effect. Nevertheless, the high current values and their increase with temperature, although small, strongly indicate that a significant oxidative dissolution from a freshly polished surface is occurring. A sudden drop in current occurred after approximately 2 s at –0.7 V_{SCE} and at longer times for the higher applied potentials. These changes may all be attributed to the iR effect, but another possibility is that iron species have concentrated at the metal/water interface and were then deposited as an oxide or hydroxide layer leading to a more resistive surface.

The sudden drop in current was then followed by a steady decrease in current with time. The temperature dependences of the current behaviour in this period at the three different potentials are consistent with the proposed film growth and conversion mechanisms based on the CV analysis discussed.

3.3.2.1 Current Behaviour at –0.7 V_{SCE} in Ox 1

At room temperature, the logarithmic plot of current versus time was nearly linear, indicating linear film growth of mainly one type of oxide, Figure 3.5a. This is consistent with the formation of a Fe_3O_4-like oxide in Ox I. At approximately 200 s, the current switched signs, becoming cathodic. The catholic currents quickly reached a steady state value and remained constant at approximately 10^{-6} $A \cdot cm^{-2}$ over the 7 d potentiostatic experiments. Magnetite is electronically conducting and, hence, its formation on carbon steel can continually support water reduction to H_2. The cathodic

current due to water reduction was present from the early stages of potentiostaic film growth on carbon steel. However, as the oxide thickened and the anodic current decreased, the cathodic current from water reduction on the conducting surface dominated the current behaviour at longer times (> 200 s). At a higher temperature the current value was higher and the current decreased more slowly with time, Figure 3.5a. These observations are attributed to an increase in the rate of dissolution of Fe_3O_4 and slowing of the growth of the Fe_3O_4 layer thickness. The rate of decrease in current, however, accelerated again when temperature was raised to 80 °C. As noted above, this is attributed to an increase in the rate of thermal conversion of Fe^{II} species to Fe_3O_4 by the Schikorr reaction. This counters the iron dissolution process and increases the rate of oxide film growth. At times > 1000 s, the net current decreased sharply at all temperatures. At –0.7 V_{SCE}, this rapid decrease is due to an increase in the contribution of cathodic current arising from water reduction to the net current. The current eventually switched to cathodic and remained steady in the range of 50 - 500 $nA \cdot cm^{-2}$.

The switch from anodic to cathodic current was not observed at the higher potentials where the current remained anodic over the 7 d long potentiostatic growth. These observations are consistent with the formation of a conducting Fe_3O_4 layer which can support water reduction.

3.3.2.2 Current Behaviour at –0.2 V_{SCE} in Ox II

Within the first 1000 s, at –0.2 V_{SCE} the current decreased with time in a similar manner to that observed at –0.7 V_{SCE}, but at a faster rate, Figure 3.5b. This decrease, and a longer initial duration during which there was a high constant current, are attributed to

faster anodic oxidation at this potential compared to the behaviour at -0.7 V_{SCE}. However, at times longer than 1000s, the current behaviour at –0.2 V_{SCE} differed from that of –0.7 V_{SCE}. At 50 °C and 70 °C, the current became nearly constant over the period of 200 – 1000 s before it decreased linearly with time again. This behaviour is attributed to an increase in the rate of dissolution of Fe^{II} from the conducting Fe_3O_4 layer. The dissolution current was approximately 2 $\mu A \cdot cm^{-2}$ at 50 °C and would normally be expected to increase with temperature. However, the rate of the Schikorr reaction also increases with temperature, at 70 °C and leads to thickening of the Fe_3O_4 layer. This creates a more insulating and less soluble γ-Fe_2O_3 oxide layer that suppresses the dissolution current.

At –0.2 V_{SCE}, the current remained anodic and continuously decreased until it reached a constant value, Figure 3.5b. This steady-state current increased with temperature, ranging from 8 to 80 $nA \cdot cm^{-2}$ for 25 °C to 80 °C. As discussed above, the conversion of the Fe_3O_4 oxide layer to a more insulating γ-Fe_2O_3 layer reduces the rate of dissolution of Fe^{II} species from the oxide layer and suppresses electrochemical oxidation. As the conversion takes place, the anodic current decreases nearly linearly with time until the anodic current is limited by the dissolution current and becomes constant. Since dissolution of metal ions from a uniform oxide layer involves hydration and diffusion of the metal ions, the observed temperature dependence can be attributed to the temperature dependence of the rates of hydration and diffusion of Fe from the oxide.

3.3.2.3 Current Behaviour at 0.2 V_{SCE} in Ox III

The time dependent behaviour of the current observed at 0.2 V_{SCE} was similar to that at –0.2 V_{SCE} but with some differences. These differences included a longer initial constant current period and a diminished influence of temperature on the rate of decrease in current. These observations can be attributed to faster rates of anodic oxidation processes. These include oxidation of Fe^0 to soluble Fe^{II}, then to Fe_3O_4 and then to a γ-Fe_2O_3-like oxide within a relatively short time scale of approximately 10^4 s. However, system temperature at 0.2 V_{SCE} had a more pronounced effect on the current level reached at times >10^4 s, with the current increasing from 1 nA·cm^{-2} at 25 °C to 200 nA·cm^{-2} at 80 °C. The increase in the long-term anodic current with increasing temperature can be explained by a film growth mechanism in this potential range that results in micro-fracture of the protective oxide layer due to the anodic conversion of the Fe_3O_4/γ-Fe_2O_3 oxide to γ-FeOOH, followed by repassivation of the film [12, 13]. This can lead to the formation of a defective film which can then grow at a faster rate at a higher temperature.

3.3.3 Oxide Film Characterization by EIS

After the current reached steady state, EIS was performed periodically starting at 2.5 h to characterize the oxide film present on the electrode, Figures 3.6-3.11.

3.3.3.1 Film Grown at –0.7 V_{SCE} in Ox I

The EIS spectra recorded for the film grown at –0.7 V_{SCE} did not change significantly over the course of the 140 h experiment and only those spectra taken at 35 h

at the four different temperatures are shown in Figure 3.6a. The EIS at 25 °C shows one-time constant behaviour and an equivalent circuit composed of a resistor (R1) and a constant phase element (CPE1) representing the metal-oxide-water system in series with the solution resistance (see inset of Figure 3.7) was used to fit to the data. The impedance of a CPE is often attributed to a distribution of time-constants [26], and it is defined as

$$Z_{CPE} = [Y_0(j\omega)^{\alpha}]^{-1} \tag{3.3}$$

where Y_0 is the CPE parameter, and the exponent α is independent of the frequency, ω. The CPE has no simple physical meaning except for α = one; in this case, CPE represents capacitance and $Y_0 = C$. When α is close to unity, the CPE parameter can be converted to an effective capacitance value by the formulas derived by Brug [27] or Hsu and Mansfeld [28]. The α values obtained for the EIS taken at various times during film growth and between experiments were all greater than 0.8. Recently Hirschorn et. al. [29] showed that the analysis of Brug applies to a case when the time-constant distribution arises from spatial inhomogeneity, while the analysis of Hsu and Mansfeld is appropriate for the time-constant distribution arising from depth inhomogeneity.

At –0.7 V_{SCE} the spatial inhomogeneity method developed by Brug et al. [27] was first applied, with an assumption that the capacitance arises from a double layer capacitance (see below). Conversion of CPE to capacitance values using the Brug method involves the formula,

$$C = \left[Y_0 \left(\frac{1}{R_x} + \frac{1}{R_s} \right)^{(\alpha-1)} \right]^{1/\alpha} \tag{3.4}$$

where C is the capacitance in units $s \cdot \Omega^{-1}$ or F, Y_0, the measured CPE parameter, is in units of $s^{\alpha} \cdot \Omega^{-1}$ or $Fs^{(\alpha-1)}$, R_x the resistance in parallel with the capacitance in units of Ω, and R_s the solution resistance in units of Ω.

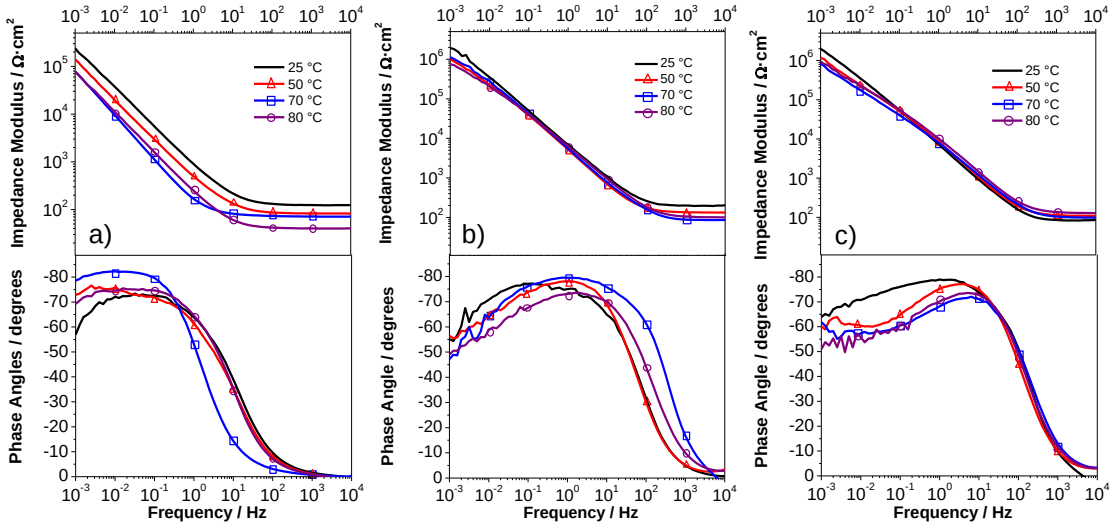

Figure 3.6: Electrochemical impedance spectra for the films grown at (a) –0.7 V_{SCE}, (b) –0.2 V_{SCE}, and (c) 0.2 V_{SCE} as a function of temperature after 35 h of film growth.

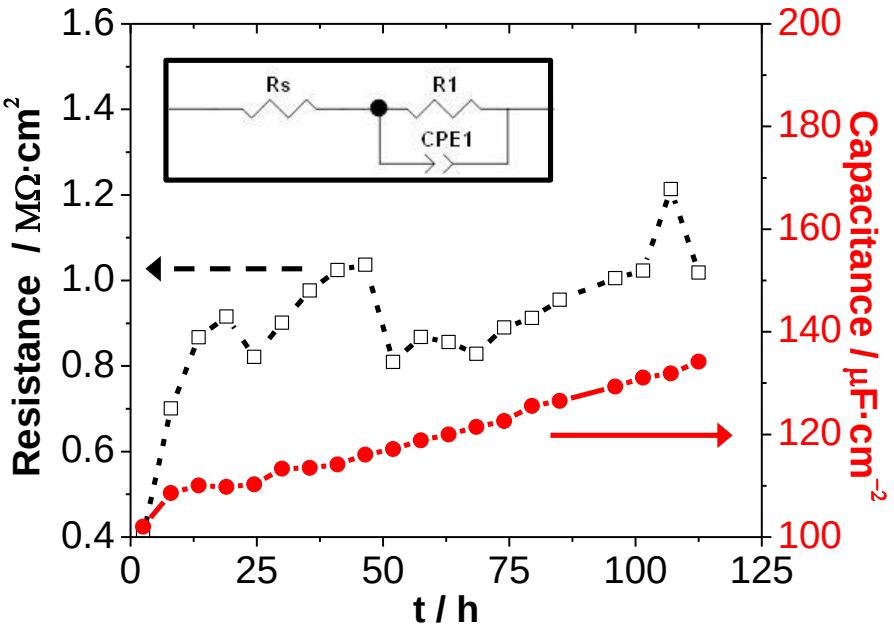

Figure 3.7: Equivalent circuit fitting results for the resistance and capacitance for potentiostatic film growth at $-0.7V_{SCE}$ and 25 °C as a function of time. Inset is a single time-constant equivalent circuit fit to all EIS experimental data

The charge transfer resistance, R1, and the capacitance, C1, derived from the EIS taken as a function of time at 25 °C are presented in Figure 3.7, and CPE1 and the capacitance derived as a function of time at different temperatures is shown in Figure 3.8. At room temperature, the resistance increased with time from 0.8 to 1.2 MΩ·cm^2 and the capacitance increased from 100 to 140 μF·cm^{-2} over the 140 h test period. At temperatures > 25 °C large extrapolations were made to determine R1, resulting in errors of ~ 15% and highly scattered data (results not shown). However, within error, all R1 values were near 1 MΩ·cm^2. By the time the first EIS was taken, the net current was cathodic and was already at steady state (see Figure 3.5a). Earlier, this current was attributed to the formation of an electronically conducting Fe_3O_4 layer that supported

water reduction. The high resistance can then be attributed to arising from charge transfer at the oxide/solution interface and not from charge transport in the electronically conducting, but ionically less conducting Fe_3O_4-like layer at this potential.

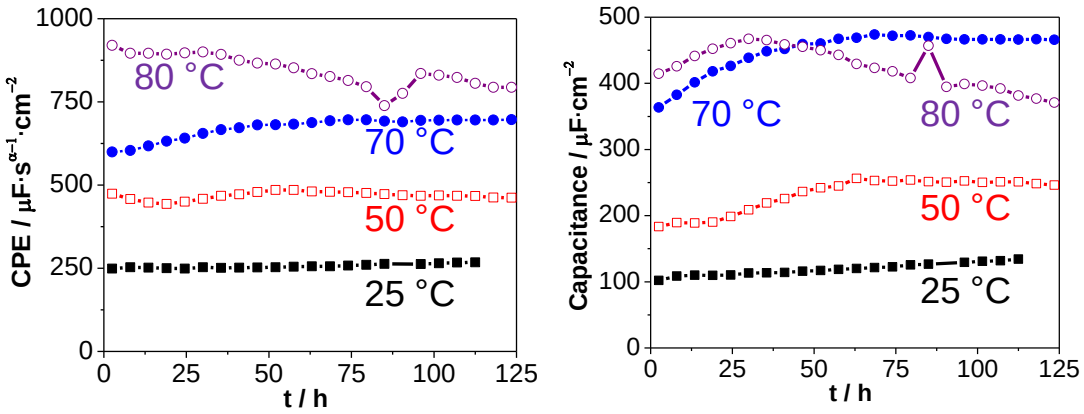

Figure 3.8: Equivalent circuit fitting results of (a) constant phase element CPE1 and (b) capacitance of films grown at –0.7 V_{SCE}, for all temperatures studied, as a function of time.

When a bias potential is applied to a semi-conductor in an electrolyte solution, the applied potential is distributed over the surface charge layer in the semi-conductor and the double layer, in the solution. When the potential falls mainly in the double layer, a capacitance value in the range of 20 to 50 $\mu F \cdot cm^{-2}$ would be expected [26]. On rough surfaces the double layer capacitance can exceed 100 $\mu F \cdot cm^{-2}$ [30], and the surface roughness of the oxide film and its change with time is one potential explanation for the capacitance behaviour observed at 25 °C. However, the capacitance increased significantly with an increase in temperature, reaching a value as high as 500 $\mu F \cdot cm^{-2}$ at

70 °C and 80 °C. The surface morphology of the film grown at −0.7 V_{SCE} at 80 °C observed by SEM, shown in section 3.3.4 later, suggests that the surface roughness did not increase appreciably when temperature increased from 25 °C to 80 °C. At 25 °C, the oxide layer was very thin and the polish marks were visible (SEM image not shown). Therefore, such high capacitance values were attributed to processes other than surface roughening at the oxide/solution interface. Mathematical models have shown that the introduction of a Faradaic process at the solution interface can greatly increase the double layer capacitance [31]. It has also been observed that inverse spinel oxides, and specifically Fe_3O_4, can increase a measured capacitance up to an order of magnitude [32-34]. The observed capacitance increase is attributed to a pseudo capacitance, which can result from electron transfer between surface cations (Fe^{II}/Fe^{III}) coupled to processes such as transfer or adsorption/desorption ($O^{2-} \leftrightarrow OH^-$) at the interface. The origin of a pseudo capacitance depends on the system, but is generally accepted to arise from electron transfer between cation sites coupled with charge transfer to adsorbed or aqueous species [32-34]. Thus, it is reasonable to assume an existence of a pseudo capacitance on the Fe_3O_4 grown in Ox I. The observed dependence of capacitance on temperature can then be explained if the Faradaic processes at the oxide/solution interface increase with temperature. The existence of a pseudo capacitance also suggests the bulk oxide phase is relatively conductive [33], which further confirms the description of a uniform, electronically-conductive Fe_3O_4 formed in Ox I. The discussion here must be treated as qualitative since the pseudo capacitance may require modeling beyond a 2D spatial description. However, the relatively minor differences between the CPE values and capacitance values obtained using the method of Brug (Figure 3.8) indicate that the

capacitance values obtained by this method can still provide valuable and semi-quantitative information.

3.3.3.2 Film Grown at –0.2 V_{SCE} in Ox II

The EIS spectra obtained in Ox II (Figure 3.6) were analyzed with the same single-time constant circuit as shown in Figure 3.7. Since the capacitance (initially CPE) in this redox region was considered to be primarily due to the oxide film, the 2D spatial dispersion method developed by Brug could not be applied. Instead a conversion method based on dispersion within on oxide film developed by Hsu and Mansfeld [28, 29] was applied to convert the derived CPEs to capacitances. The mathematical conversion is performed with the following formula,

$$C=Y_0^{1/\alpha}R_x^{(1-\alpha)/\alpha} \tag{3.5}$$

The exponential parameter, α, of the constant phase element ranged from 0.85 to 0.9 for all cases and therefore CPE values could be interpreted as capacitance values with the proper mathematical correction. The best-fit results for both capacitance and resistance in Ox II are shown in Figure 3.9.

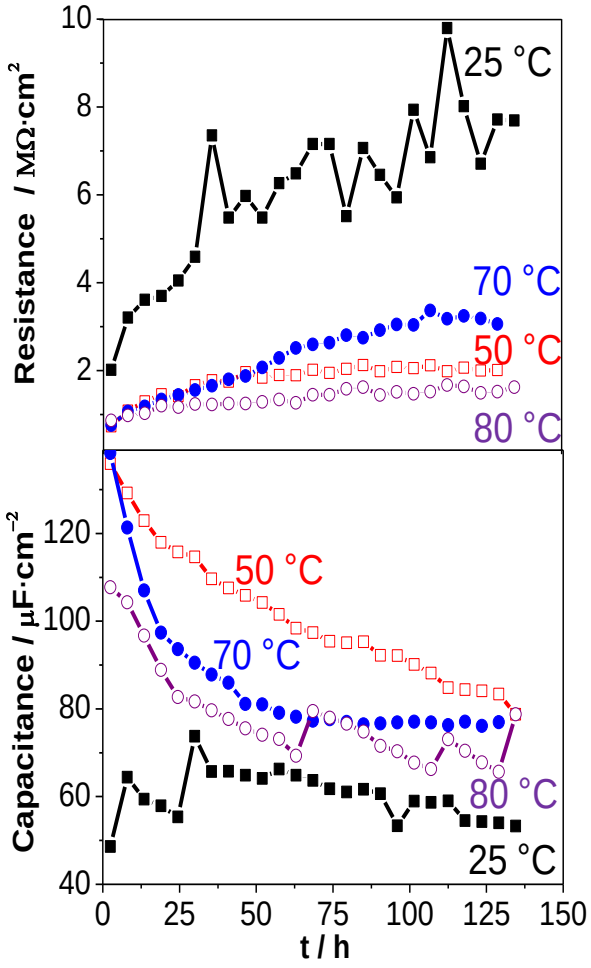

Figure 3.9: Equivalent circuit fitting results for the resistance and capacitance of films grown at –0.2 V_{SCE}, for all temperatures, studied as a function of time.

At a given temperature the resistance increased while the capacitance decreased with time. The resistance decreased with increasing temperature from 25 °C to 50 °C but then increased when the temperature increased from 50 °C to 70 °C. On the other hand, the capacitance increased when the temperature was raised from 25 °C to 50 °C and then decreased when the temperature increased > 50 °C. The capacitance values at the end of

the tests at all temperatures were in the range of 50 – 80 $\mu F \cdot cm^{-2}$. These values are considerably smaller than those observed at –0.7 V_{SCE}, but they are similar to those previously reported for a passive film formed on iron in borate buffer solutions at potentials in the Ox II region [35] and they are in the range expected for the passive oxide film.

These observations are consistent with the conversion of a Fe_3O_4-like layer to a more passivating γ-Fe_2O_3-like layer over time, Figure 3.4. The large decrease in resistance seen with temperatures above 25 °C is attributed not to film breakdown, but rather to an increase in the rate of dissolution at the oxide/water interface with increasing temperature. The change in the temperature dependences of the resistance and the capacitance at temperatures ≥ 70 °C are attributed to the increasing contribution of the Schikorr reaction at the interface and the suppression of the oxide dissolution rate.

3.3.3.3 Film Grown at 0.2 V_{SCE} in Ox III

To analyze the EIS spectra of the films grown at this potential, Figure 3.6c, at least one additional resistance-capacitance component was required in the equivalent circuit. This is consistent with the need to model the existence of a diffusion process and is also consistent with the formation of a defective or porous film. As noted above, this film can be created by the conversion of the γ-Fe_2O_3-like oxide to γ-FeOOH (leading to a volume increase in the oxide, causing micro-fractures). The diffusion component of the electric circuit may arise from the diffusion of redox species (Fe^{3+}, Fe^{2+}, H^+ and OH^-) in the pores or the diffusion of point defects within the film at the high potential of Ox III. A number of options for equivalent circuits to analyze the EIS spectra were considered

and two circuits shown in Figure 3.10 were chosen. These both have an appropriate physical description of the oxide surfaces and interfaces and provided the best fits to the experimental data. In the first model equivalent circuit, two RC components are connected in series to represent a film consisting of two different types of oxides. The second model is a commonly used equivalent circuit for porous oxide films [36]. Although both circuit models yielded reasonable fits, the second circuit model (Circuit 2b) was used for more detailed analysis because it was judged to better represent the assumed mechanism in Ox III of the incorporation of a diffusion process due to the formation of a defective or porous film.

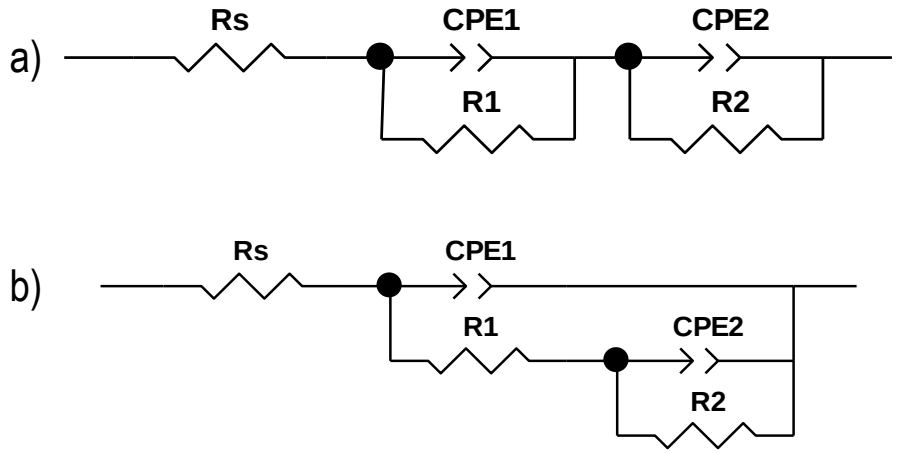

Figure 3.10: Two equivalent circuits tested to fit to all EIS experimental data for the films grown at 0.2 V_{SCE}: (a) Circuit 2a and (b) Circuit 2b.

Analysis of the EIS using the second circuit yielded values for the exponent, α, of the CPE2 parameter ranging between 0.5 and 0.6 and, hence, the above mathematical methods could not be used to convert the CPE values to a capacitance. However, when the exponent for a CPE element is equal to 0.5, the CPE can be envisioned to represent an

infinite Warburg (diffusion) element [37] and therefore, it was chosen to fix the value for α at 0.5 for further analyses. For α = 0.5, the overall CPE value is proportional to the square root of the diffusion constant for the diffusion process responsible for the current response. Although somewhat scattered, the fitting results, Figure 3.11, show that the diffusion rate increased with temperature (with a dramatic increase occurring between 25 °C and 50 °C). It is not surprising that the diffusion rate should increase with temperature, but it remains unclear as to what this diffusion process may represent. One possibility involves the diffusion of H^+ or OH^- from the oxide/water interface into the oxide lattice since these species need to reach the Fe^{II} in the Fe_3O_4 to form FeOOH.

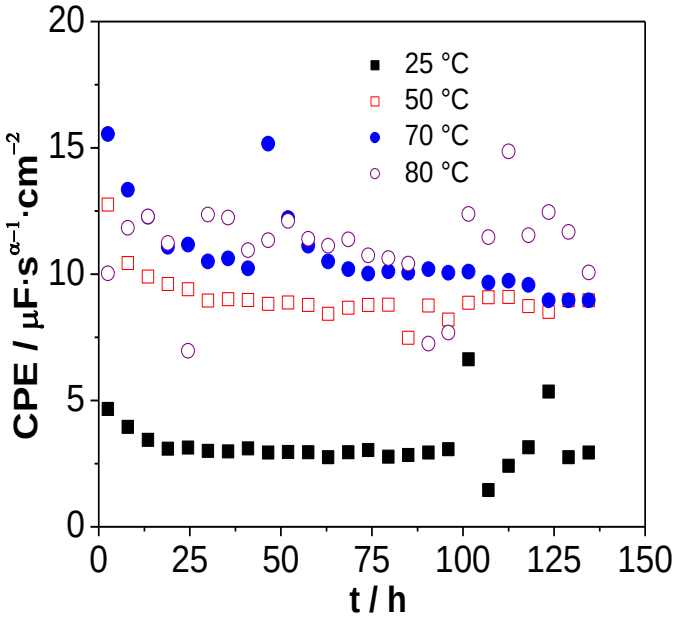

Figure 3.11: Constant phase element CPE 2 equivalent circuit fitting results using Circuit 2b for films grown at 0.2 V_{SCE}, for all temperatures studied, as a function of time.

3.3.4 Surface Analysis

Surface analysis of oxide films grown potentiostatically further supports the proposed oxide film growth and conversion mechanism. SEM images are shown in Figure 3.12. The oxide film grown at –0.7 V_{SCE} was uniform and compact after 1 week of growth. This is consistent with the proposed mechanism for the film growth in Ox I of fast formation of a uniform layer of Fe_3O_4-like oxide which then grows by a solid-state charge-transport mechanism. The oxide film grown at –0.2 V_{SCE} was very thin and the SEM image of the surface shows the residual polishing marks from the metal electrode preparation, indicating that the oxide film was only a few nanometers thick. Such a thin layer is expected in Ox II since the conversion of a Fe_3O_4-like layer to a poorly conducting γ-Fe_2O_3-like layer at early times during potentiostatic film growth would limit overall film growth. The oxide film grown at 0.2 V_{SCE} also contained a very thin base layer similar to that seen for the film grown at –0.2 V_{SCE}, but this film had a number of filaments (or crystallites) on top. The thin base oxide layer is expected for a similar reason to that discussed for the oxide film grown in Ox II. The formation of the small crystallites has been observed even at 25 °C, but to a lesser degree, and in this previous study these crystallites were identified as γ-FeOOH [13].

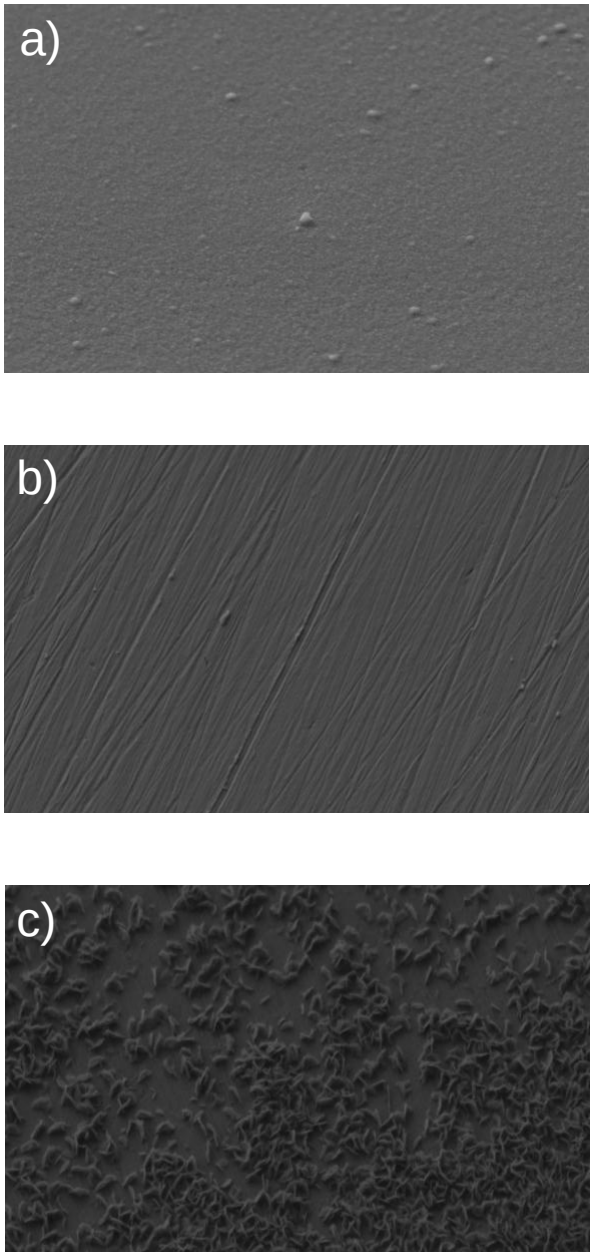

Figure 3.12: SEM images of carbon steel surfaces following 7 d potentiostatic film growth at (a) –0.7 V_{SCE}, (b) –0.2 V_{SCE}, and (c) 0.2 V_{SCE}. The potentiostatic experiments were performed at 80 °C, pH 10.6 in Ar-sparged 0.01 M borate solutions.

3.4 CONCLUSIONS

Surface oxide film growth and conversion on carbon steel in Ar-purged solution at pH 10.6 was studied as a function of potential and temperature under both potentiostatic and potentiodynamic conditions. The current behaviour observed as a function of various CV scan conditions, and the current and EIS spectra as a function of time during 7 d potentiostatic experiments support an oxide growth and conversion mechanism that depends mainly on electrode potential.

From the perspective of oxide film growth and conversion, the potential can be divided into three regions. In Ox I (–0.9 V_{SCE} to –0.6 V_{SCE}), a uniform layer of a Fe_3O_4-like inverse spinel oxide is formed that grows by a solid state charge transport mechanism. Iron dissolution occurs via hydration of Fe^{II} (and Fe^{III} to a smaller extent) at the oxide/water interface followed by diffusion of the hydrated species from the interface to the aqueous phase. The dissolution rate increases with temperature, but at temperatures > 70 °C, the Schikorr reaction accelerates the conversion of the hydrated species to Fe_3O_4. In Ox II (–0.6 V_{SCE} to 0.0 V_{SCE}), the Fe_3O_4 layer continues to grow, but the potential is high enough to convert the Fe_3O_4-like layer to more γ-Fe_2O_3-like layer. The oxide growth and conversion in this region also occurs by a solid-state charge transport mechanism. As the concentration of Fe^{II} decreases due to further oxidation to Fe^{III} near the oxide/water interface, the rate of iron dissolution is greatly suppressed and the oxide becomes more insulating. In this region, thickening of the oxide layer is rather limited due to the anodic conversion of the more conducting Fe_3O_4 to the more insulating γ-Fe_2O_3. In Ox III (0 V_{SCE} to 0.4 V_{SCE}) anodic conversion of the Fe_3O_4/γ-Fe_2O_3 oxide to γ-FeOOH can induce micro-fractures but in the absence of aggressive anions the surface

quickly repassivates. The oxide layer can grow by continuous film fracture and repassivation, producing a thick but defective (or porous) oxide film.

This study further concludes that temperature affects the oxide growth and conversion on carbon steel and, hence, the corrosion rate, mainly by influencing the rates of thermal processes such as dissolution/precipitation and phase transformation, whereas the potential at the oxide/water interface determines the extent of electrochemical oxidation of the oxide layer.

3.5 REFERENCES

[1] A.J. Davenport, J.A. Bardwell, C.M. Vitus, J. Electrochem. Soc., 142 (1995) 721-724.
[2] V. Markovac, M. Cohen, J. Electrochem. Soc., 114 (1967) 674-678.
[3] M. Buchler, P. Schmuki, H. Bohni, Electrochim. Acta, 43 (1998) 635-637.
[4] J. Gui, T.M. Devine, Corros. Sci., 138 (1991) 1105-1124.
[5] J. Gui, T.M. Devine, J. Electrochem. Soc., 138 (1991) 1376-1384.
[6] G.G. Long, J. Kruger, D.R. Black, M. Kuriyama, J. Electroanal. Chem., 150 (1983) 603-610.
[7] G.G. Long, J. Kruger, D.R. Black, M. Kuriyama, J. Electrochem. Soc., 130 (1983) 240-242.
[8] V. Schroeder, T.M. Devine, J. Electrochem. Soc., 146 (1999) 4061-4070.
[9] C.T. Lee, M.S. Odziemkowski, D.W. Shoesmith, J. Electrochem. Soc., 153 (2006) B33-B41.
[10] M. Bojinov, K. Gaonkar, S. Ghosh, V. Kain, K. Kumar, T. Saario, Corros. Sci., 51 (2009) 1146-1156.
[11] J. Robertson, J.E. Forrest, Corros. Sci., 32 (1991) 521-540.
[12] W. Xu, K. Daub, X. Zhang, J.J. Nöel, D.W. Shoesmith, J.C. Wren, Electrochim. Acta, 54 (2009) 5727-5738.
[13] K. Yazdanfar, X. Zhang, P.G. Keech, D.W. Shoesmith, J.C. Wren, Corros. Sci., 52 (2010) 1297-1304.
[14] K. Daub, X. Zhang, J.J. Nöel, J.C. Wren, Corros. Sci., 53 (2011) 11-16.
[15] K. Daub, X. Zhang, J.J. Noël, J.C. Wren, Electrochim. Acta, 55 (2010) 2767-2776.
[16] A.J. Davenport, L.J. Oblonsky, M.P. Ryan, M.F. Toney, J. Electrochem. Soc., 147 (2000) 2162-2173.
[17] G. Schikorr, Z. Anorg. Allg. Chem., 212 (1933) 33–38.
[18] T. Misawa, Corros. Sci., 13 (1973) 659-676.
[19] R.M. Cornell, U. Schwertmann, The Iron Oxides: Structures, Properties, Reactions, Occurrences and Uses, 2nd Ed., Weinheim, New York, NY, (2003).

[20] C.Y. Chao, L.F. Lin, D.D. Macdonald, J. Electrochem. Soc., 128 (1981) 1187-1194.
[21] I. Betova, M. Bojinov, P. Kinnunen, K. Mäkelä, T. Saario, J. Electroanal. Chem., 572 (2004) 211-223.
[22] B. Beverskog, I. Puigdomenech, Corros. Sci., 38 (1996) 2121-2135.
[23] M. Yamashita, H. Miyuki, Y. Matsuda, H. Nagano, T. Misawa, Corros. Sci., 36 (1994) 283-299.
[24] J. Majzlan, C.B. Koch, A. Navrotsky, Clays Clay Miner., 56 (2008) 526-530.
[25] A. Hugot-Le Goff, J. Flis, N. Boucherit, S. Joiret, J. Wilinski, J. Electrochem. Soc., 137 (1990) 2684-2690.
[26] M. Orazem, B. Tribollet, Electrochemical Impedance Spectroscopy, John Wiley & Sons, New York, NY, (2008).
[27] G.J. Brug, A.L.G. Van Den Eeden, M. Sluyters-Rehbach, J.H. Sluyters, J. Electroanal. Chem., 176 (1984) 275-295.
[28] C.H. Hsu, F. Mansfeld, Corros., 57 (2001) 747-748.
[29] B. Hirschorn, M.E. Orazem, B. Tribollet, V. Vivier, I. Frateur, M. Musiani, Electrochimica Acta, 55 (2010) 6218-6227.
[30] E. Laouini, M. Hamdani, M.I.S. Pereira, Y. Berghoute, J. Douch, M.H. Mendonça, R.N. Singh, Int. J. Electrochem. Sci., 4 (2009) 1074-1084.
[31] C. Lin, J.A. Ritter, B.N. Popov, R.E. White, 146 (1999) 3168-3175.
[32] S.-Y. Wang, K.-C. Ho, S.-L. Kuo, N.-L. Wu, J. Electrochem. Soc., 153 (2006) A75-A80.
[33] N.-L. Wu, S.-Y. Wang, C.-Y. Han, D.-S. Wu, L.-R. Shiue, J. Power Sources, 113 (2003) 173-178.
[34] A.A.F. Grupioni, T.A.F. Lassali, J. Electrochem. Soc., 148 (2001) A1015-A1022.
[35] W.S. Li, S.Q. Cai, J.L. Luo, J. Electrochem. Soc., 151 (2004) B220-B226.
[36] C.T. Lee, Z. Qin, M. Odziemkowski, D.W. Shoesmith, Electrochim. Acta, 51 (2006) 1558-1568.
[37] M. Sluyters-Rehbath, J.H. Sluters, Electroanalytical Chemistry, Marcel Dekker, New York, NY, (1970).

Chapter 4

Effects of γ-Radiation Versus H_2O_2 on Carbon Steel Corrosion

4.1 INTRODUCTION

The influence of ionizing radiation on corrosion of metals in general, and, of carbon steel in particular, has been studied only to a limited extent, and the mechanism by which radiation affects corrosion kinetics has not been established [1-5]. The observed effects of ionizing radiation on the corrosion of metals are conflicting [1-12], and many key questions remain unanswered, including whether the radiation energy initially absorbed in the bulk metal phase, or that in the aqueous phase, is what drives materials degradation, and whether the key aqueous redox species for steel corrosion are the radical products or the molecular products from water radiolysis.

This study investigates the effects of γ-radiation on carbon steel corrosion and compares them with those of chemically-added H_2O_2 that is considered to be the key radiolytically-produced oxidant at room temperature. The corrosion kinetics are monitored by measuring the corrosion potential, E_{CORR}, and the polarization resistance, R_P, using linear polarization (LP) and electrochemical impedance spectroscopy (EIS). Since surface morphology and composition, in addition to the change in the aqueous redox environment induced by γ-irradiation, are important factors controlling the corrosion rate, this study has been performed with various oxide films that were pre-grown potentiostatically on carbon steel electrodes prior to exposure to either γ-radiation at a dose rate of ~6.8 $kGy \cdot h^{-1}$ or to H_2O_2 at concentrations in the range of 10^{-6} M to 10^{-2} M.

4.2 EXPERIMENTAL

4.2.1 Solutions

All experiments were conducted at room temperature in Ar-sparged 0.01 M sodium borate solutions. The solutions were prepared using reagent grade $Na_2B_4O_7 \bullet 10H_2O$ (Caledon Laboratories Ltd.) and water purified using a NANOpure Diamond UV ultra-pure water system (Barnstead International), with a resistivity of 18.2 MΩ·cm. Reagent grade NaOH (Caledon Laboratories Ltd.) was added dropwise to the solutions to adjust the pH. All experiments were conducted at a pH of 10.6. H_2O_2 was added from a 3 wt. % stock solution from Fisher Chemicals.

4.2.2 Irradiation Source

All irradiation experiments were conducted in a MDS Nordion Gammacell 220 Excel Cobalt-60 irradiator. The electrochemical cell was positioned inside the gammacell sample chamber, and the chamber was lowered into the gammacell irradiation zone, consisting of 11 tubular pencils containing ^{60}Co. The dose rate during the period of experimentation was ~6.8 $kGy \cdot h^{-1}$.

4.2.3 Procedure

Following application of the polishing procedure, the working electrodes were rinsed with deionized water and placed in the electrochemical cell, which had been sparged with argon gas for at least 1 h to purge any oxygen from the solution. Electrochemical experiments then began with cathodic cleaning at –1.1 V_{SCE} for 5 min to remove any residual air-formed oxides on the working electrode, thereby creating a

reproducibly clean metal surface. The electrode was then anodized for 2.5 h at –0.7 V_{SCE}, –0.2 V_{SCE}, or 0.2 V_{SCE} with the intention of generating a variety of oxide films with differing compositions and properties. When the potentiostatic film growth was completed, either the electrochemical cell was irradiated in the gammacell for 6 h, or a specific concentration of H_2O_2 was added to the solution; E_{CORR} was measured during the entire procedure. E_{CORR} monitoring continued for a number of hours (generally 24 to 48 h) to follow any changes occurring in solution and on the metal oxide surface.

Over the course of the experiments, periodic measurements of either EIS or LP were performed to aid in determining the change in the resistive nature of the oxide film. Also, to evaluate the radiolytic production of redox species, aqueous samples were taken periodically for H_2O_2 analysis by UV-Vis spectrophotometry.

In some cases, 24 h after the addition of H_2O_2, carbon steel samples were removed and analyzed using X-ray photoelectron spectroscopy (XPS).

4.3 RESULTS AND DISCUSSION

4.3.1 Electrochemical Growth and Conversion of Oxide on Carbon Steel

The objective of this study was to determine how the change in the solution redox environment arising from water radiolysis affects the rate of carbon steel corrosion. However, the chemical composition and morphology of the surface oxide are also important parameters in controlling the corrosion rate of a metal. To differentiate the influence of the initially present oxide film on the corrosion behaviour from the effect induced by irradiation or H_2O_2, the carbon steel samples were polarized for 2.5 h at potentials of –0.7 V_{SCE}, –0.2 V_{SCE} or 0.2 V_{SCE} prior to the start of each exposure

experiment. These potentials represent values from the three oxidation regions identified in previous studies, and in Chapter 3 [13, 14]. The extent of oxidation, or the average valence of Fe in the oxide layer, is determined by the film growth potential (or corrosion potential, under naturally corroding conditions), while the film thickness at steady state is related to the solubilities of the oxides formed, as well as the potential.

These studies suggest that, on carbon steel at room temperature, the oxide grown at –0.7 V_{SCE} (in Ox I) is mainly Fe_3O_4, that at –0.2 V_{SCE} (in Ox II) is a mixed layer of Fe_3O_4/γ-Fe_2O_3, and that at 0.2 V_{SCE} (in Ox III) is a mixture of γ-FeOOH, Fe_3O_4, and γ-Fe_2O_3. These films, referred to as pre-grown films hereafter, were then exposed to either γ-radiation or H_2O_2.

4.3.2 Corrosion Potential of Carbon Steel in a γ-Irradiation Field

The corrosion kinetics of carbon steel with a pre-grown film in a γ-radiation field were followed by monitoring E_{CORR} and periodically performing LP measurements. The LP results are discussed in Section 4.3.6.2 after first establishing that the polarization resistance, R_P, for the carbon steel system reproduce those found by EIS in solutions containing various concentrations of H_2O_2.

Figure 4.1 compares the E_{CORR} transients observed in the presence and absence of γ-radiation on the films pre-grown at three different potentials. In the absence of radiation, E_{CORR} quickly relaxed to approximately –0.65 V_{SCE} (Ox I) within ~ 5 h for all three pre-grown films. Prior to reaching the final steady-state E_{CORR} value, the corrosion potential of films pre-grown in potential Ox II and III reached a metastable value at approximately –0.5 V_{SCE}. This meta-stable E_{CORR} value corresponds to the potential at

which the reduction from γ-Fe_2O_3 to Fe_3O_4 can couple with the oxidation of Fe/Fe^{II} to Fe_3O_4:

$$Fe(substrate) \xrightarrow{-e^-} Fe_3O_4 \quad (4.1)$$

$$\gamma\text{–}Fe_2O_3 \xrightarrow{e^-} Fe_3O_4 \quad (4.2)$$

These reactions may be the dominant processes controlling the E_{CORR} behaviour until all the γ-Fe_2O_3 has been reduced. For the film grown at –0.2 V_{SCE} the metastable potential of –0.5 V_{SCE} was maintained for a longer period of time than it was for the film grown at a higher potential 0.2 V_{SCE}. This may be attributed to the fact that at –0.2 V_{SCE}, the anodic oxidation is limited to the formation of γ-Fe_2O_3/Fe_3O_4, thus a thicker and more compact film of the oxides grows, whereas at 0.2 V_{SCE}, the further oxidation of Fe_3O_4 to γ-FeOOH occurs, forming a thicker but less compact film consisting of less γ-Fe_2O_3. In all cases, once all the γ-Fe_2O_3 is consumed, E_{CORR} is likely determined by the oxidation of Fe/Fe^{II} to Fe_3O_4, Reaction 4.1, and water reduction to H_2, Reaction 4.3 [13]:

$$H_2O \xrightarrow{e^-} H_2 \quad (4.3)$$

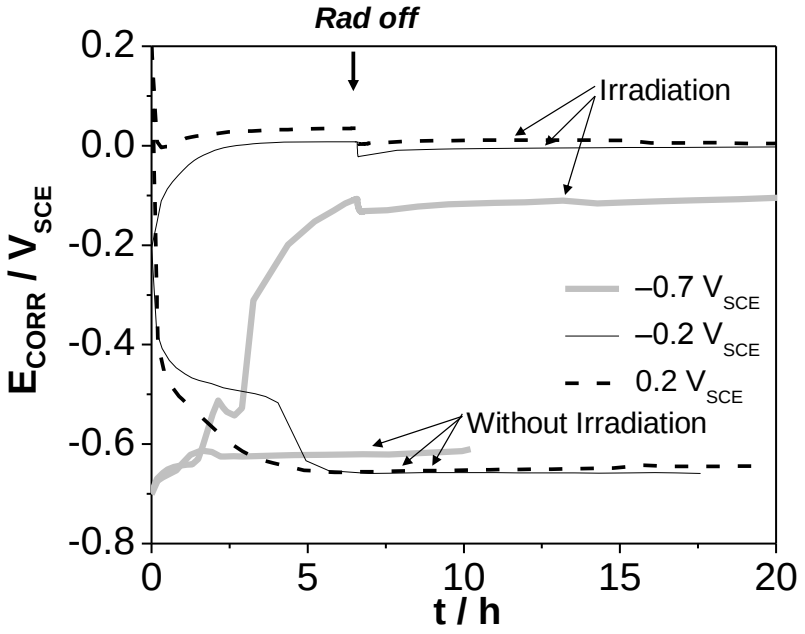

Figure 4.1: Corrosion potential as a function of time during and post 6 h irradiation and without irradiation. Prior to the E_{CORR} measurement, oxide films were grown potentiostatically at 0.2 V_{SCE}, –0.2 V_{SCE}, or –0.7 V_{SCE}.

In the presence of γ-radiation, E_{CORR} showed the same initial sharp decrease, but quickly recovered, eventually reaching a steady state within the 6 h irradiation period, except for the films pre-grown at –0.7 V_{SCE}, which required a longer irradiation time to reach steady state. The steady-state E_{CORR} value was nearly independent of the pre-grown film, and equal to approximately 0.0 V_{SCE}, being slightly lower in the case with the film pre-grown at –0.7 V_{SCE}. These values are significantly higher than the E_{CORR} reached without irradiation. The E_{CORR} remained the same over a long period following the termination of irradiation. The slight drop in potential when the electrochemical cell was removed from the gammacell was attributed to an electrical baseline disturbance.

4.3.3 Water Radiolysis Products in a γ-Irradiation Field

During the irradiation period, the electrolyte solution was also periodically sampled to determine the concentration of radiolytically-produced H_2O_2, Figure 4.2. At pH 10.6 the radiolytic production of H_2O_2 does not reach steady state immediately, but the concentration gradually increases over the 6 h irradiation period, from $[H_2O_2]$ = ~ 10^{-6} M at 0.5 h to $[H_2O_2]$ = ~ 10^{-4} M at 6 h. In Figure 4.2, the measured H_2O_2 concentration is compared to that calculated using a water radiolysis model that has been tested under a wide range of conditions [15, 16]. The model reproduces the measured $[H_2O_2]$ very well, and is used to aid interpretation of the behaviour of unstable (and hence not easily measurable) radical redox species ($\bullet O_2^-$, •OH), whose calculated concentrations are also presented in Figure 4.2. The solution pH values measured before and after irradiation were the same (pH 10.6), confirming that the buffer solution was able to maintain the pH.

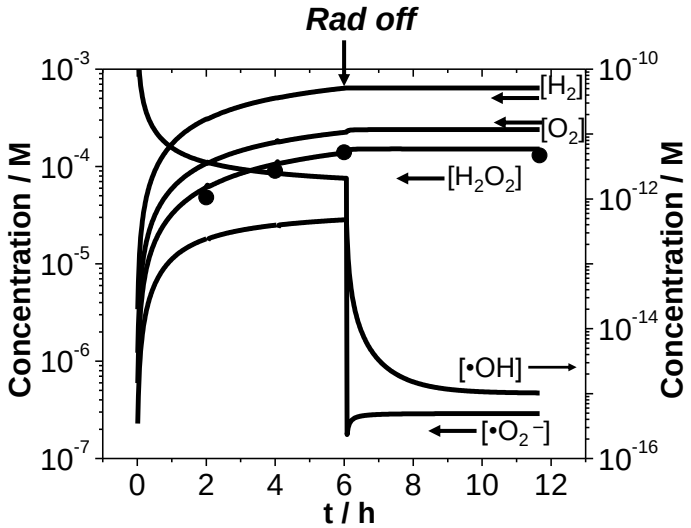

Figure 4.2: Concentration of water radiolysis products during and post 6 h irradiation. The lines indicate the calculated concentrations and the symbols represent the measured concentrations of H_2O_2.

Although E_{CORR} is a complicated function of the nature of the oxide film as well as of the aqueous redox condition, the comparison of the time-dependent behaviour of E_{CORR} (Figure 4.1) and the radiolysis product speciation (Figure 4.2) suggest that under the experimental conditions (pH 10.6 and room temperature) the molecular products, not the radical products, are the main radiolysis products controlling E_{CORR}. During irradiation the concentration of •OH is several orders of magnitude lower than that of any of the molecular species, and even the more stable (and hence less reactive) superoxide radical $\bullet O_2^-$ is also an order of magnitude lower. Furthermore, upon the termination of irradiation, these radicals quickly decay to background levels, whereas no change in E_{CORR} is observed. These comparisons strongly suggest that it is the radiolytically-produced molecular species, in particular H_2O_2, and not the radical species that determines the E_{CORR} of carbon steel. This claim is consistent with the expectation for solid-liquid reactions, which, in general, have higher activation energies and lower reaction rates than bulk homogeneous solution reactions. Thus, the radical species would be more likely to recombine with other radical species or react with dissolved impurities, if present, than to be involved in surface oxidation and reduction reactions. From the radiolysis perspective, OH^- is an impurity that can considerably reduce the radical concentrations [15, 16], and under the experimental conditions (pH 10.6) the ratio of molecular species to radical species is much higher than that expected for pH less than 8 [16].

4.3.4 Corrosion Potential of Carbon Steel in H_2O_2 Solution

The E_{CORR} transients observed at different [H_2O_2] concentrations in the absence of γ-radiation, Figure 4.3, further support the idea that the change in E_{CORR} during γ-irradiation is a result of the concentration change of radiolytically produced H_2O_2. Except over a short initial exposure time period, the time-dependent behaviour of E_{CORR} observed for the three different pre-grown films was essentially identical. Upon removal of the applied potential and exposure of the carbon steel electrode to H_2O_2, E_{CORR} decreased immediately, but recovered, quickly reaching (pseudo-) steady state at a significantly higher value than the E_{CORR} observed in H_2O_2-free solution (see Figure 4.1). Even at 1×10^{-6} M, the lowest [H_2O_2] studied, E_{CORR} reached approximately –0.3 V_{SCE}, almost immediately upon exposure to H_2O_2 for the films pre-grown at –0.2 V_{SCE} and 0.2 V_{SCE}, and in less than 3 h for the film pre-grown at –0.7 V_{SCE}. When E_{CORR} reaches a potential in Ox II, the rate of change in E_{CORR} slows down considerably, consistent with the formation of a passive γ-Fe_2O_3 layer expected in Ox II. Nevertheless, E_{CORR} in all cases reaches a steady state that is strongly dependent on [H_2O_2] but nearly independent of the nature of the pre-grown film.

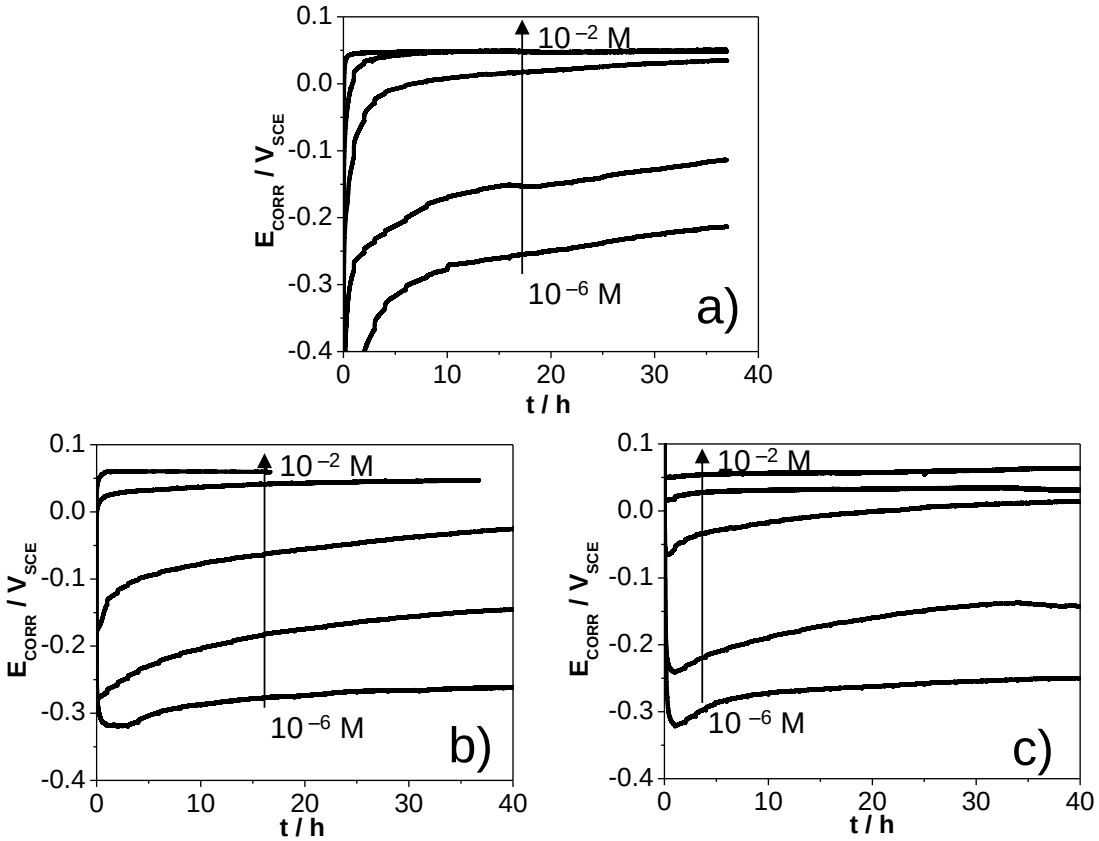

Figure 4.3: E_{CORR} as a function of time following exposure to various concentrations of H_2O_2 for the films pre-grown potentiostatically at (a) –0.7 V_{SCE}, (b) –0.2 V_{SCE}, and (c) 0.2 V_{SCE}. $[H_2O_2]$ ranged from 10^{-6} to 10^{-2} M. The concentrations added were, 10^{-6}, 10^{-5}, 10^{-4}, 10^{-3}, and 10^{-2} M.

The steady-state E_{CORR}, $(E_{CORR})_{SS}$, Figure 4.4, shows a linear dependence on log $[H_2O_2]$ in the low concentration range, $[H_2O_2] < 1 \times 10^{-3}$ M. Thus, at $[H_2O_2] < 1 \times 10^{-3}$ M, E_{CORR} is likely to be determined mainly by the cathodic half reactions of H_2O_2:

$$H_2O_2 \xrightarrow{e^-} OH^- + \bullet OH \xrightarrow{e^-} 2OH^- \qquad (4.4)$$

coupled with the anodic half-reactions of an oxide-covered steel surface:

$$Fe(\text{substrate}) \xrightarrow{-e^-} Fe_3O_4 \xrightarrow{-e^-} \gamma\text{–}Fe_2O_3 \qquad (4.5)$$

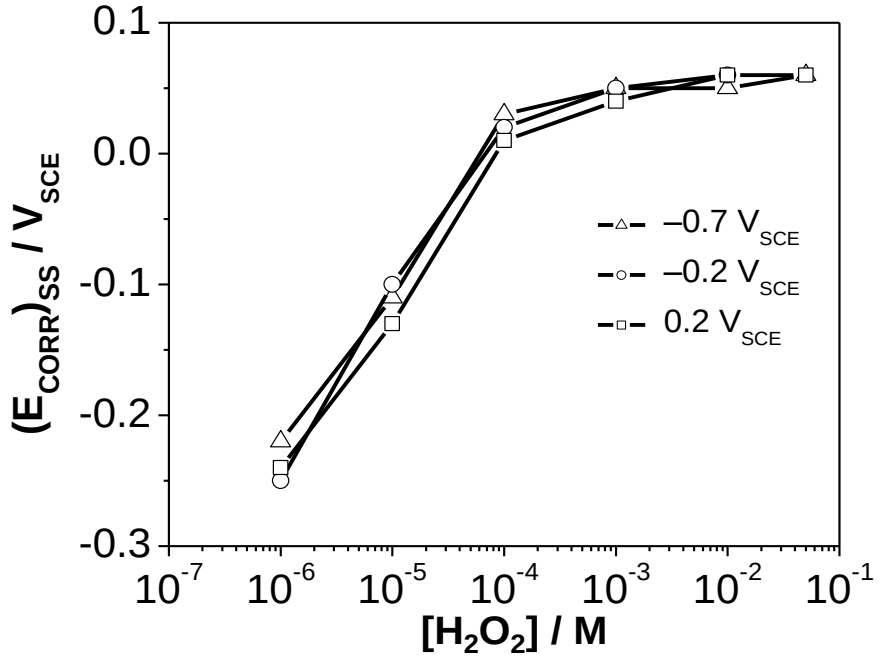

Figure 4.4: Steady-state E_{CORR} as a function of $[H_2O_2]$ for the films pre-grown potentiostatically for 2.5 h at –0.7 V_{SCE}, –0.2 V_{SCE}, and 0.2 V_{SCE} for 2.5 h.

This oxide layer of Fe_3O_4/γ-Fe_2O_3 will grow, and the average valence of Fe (Fe^{III}/Fe^{II}) will increase, with time, resulting in an increase in E_{CORR} with time. However, as the average valence increases, the surface will become more passive, and film growth will slow down. At the steady state, the anodic (or cathodic) reaction rate will be determined by the dissolution rate of the oxide formed.

At high $[H_2O_2]$ ($\geq 1 \times 10^{-3}$ M), E_{CORR} rapidly reached a steady-state value of 0.05 V_{SCE}, independent of $[H_2O_2]$ and of the pre-grown film, Figure 4.4. This potential value is between the equilibrium potentials for H_2O_2 reduction to OH^- (0.80 V_{SCE} at pH 10.6 and $[H_2O_2] = 1 \times 10^{-3}$ M) and H_2O_2 oxidation to O_2 (–0.14 V_{SCE} at pH 10.6,

P_{O_2} = 0.01 bar and $[H_2O_2] = 1 \times 10^{-3}$ M). Thus, at high $[H_2O_2]$, E_{CORR} is likely to be determined mainly by the cathodic half-reactions of H_2O_2, Reaction 4.4, coupled with the anodic half reactions of H_2O_2:

$$H_2O_2 \xrightarrow{-e^-} \bullet O_2^- + 2H^+ \xrightarrow{-e^-} O_2 + 2H^+ \quad (4.6)$$

These H_2O_2 reactions involve the use of Fe^{III}/Fe^{II} sites in the oxide film on carbon steel as an electron donor-acceptor relay:

$$Fe^{III} \xrightarrow{e^-} Fe^{II} \xrightarrow{-e^-} Fe^{III} \quad (4.7)$$

It is reasonable to assume that this electron donor-acceptor relay occurs easily in the $Fe_3O_4/\gamma\text{-}Fe_2O_3$ oxide since the conversion between Fe^{II} and Fe^{III} in the oxide is kinetically reversible [17]. Under these conditions, the net change in the nature of the surface or in the Fe valence (Fe^{II}/Fe^{III}) will be negligible, while the electrochemical reduction and oxidation of H_2O_2, and hence the decomposition of H_2O_2, can progress catalytically. E_{CORR} reached at high $[H_2O_2]$ is, however, approximately 0.05 V_{SCE} at which the formation of γ-FeOOH is also possible [13, 14]. Previous studies on the electrochemical reduction and oxidation kinetics of H_2O_2 on single-phase γ-FeOOH films have shown that the Fe^{III}/Fe^{II} electron donor-acceptor relay even occurs in the insulating γ-FeOOH, albeit at a slower rate than in the $Fe_3O_4/\gamma\text{-}Fe_2O_3$ oxide [18]. This study has shown that both reduction and oxidation have a first-order dependence on $[H_2O_2]$, that the rate-determining step is the reduction or oxidation of the adsorbed H_2O_2 to the corresponding radical intermediates, and that this step is likely to involve the use of Fe^{III}/Fe^{II} sites in the γ-FeOOH surface as an electron donor-acceptor relay. Since both oxidation and reduction rates have the same first order dependence on $[H_2O_2]$, E_{CORR} on

single-phase γ-FeOOH was observed to be independent of $[H_2O_2]$, and its value at pH 10.6 is ~ + 0.1 V, close to the value observed in this study at $[H_2O_2] \geq 1 \times 10^{-3}$ M.

In summary, E_{CORR} at high $[H_2O_2]$ is controlled by the surface decomposition of H_2O_2 on carbon steel and its surface oxide films, whereas at lower concentrations, H_2O_2 acts as either a reductant or oxidant for the corrosion reaction depending on the nature of the oxide.

4.3.5 Comparison of E_{CORR} During Exposure to γ-Radiation and to H_2O_2.

In Figure 4.5, E_{CORR} during the exposure to γ-radiation is compared with E_{CORR} observed in solutions containing 1×10^{-6} M and 1×10^{-4} M H_2O_2. Considering the change in $[H_2O_2]$ with irradiation time (see Figure 4.2 showing $[H_2O_2]$ ranging from approximately 10^{-6} M at 0.5 h to 10^{-4} M at 6 h), the E_{CORR} radiation results compare very well with the H_2O_2 results.

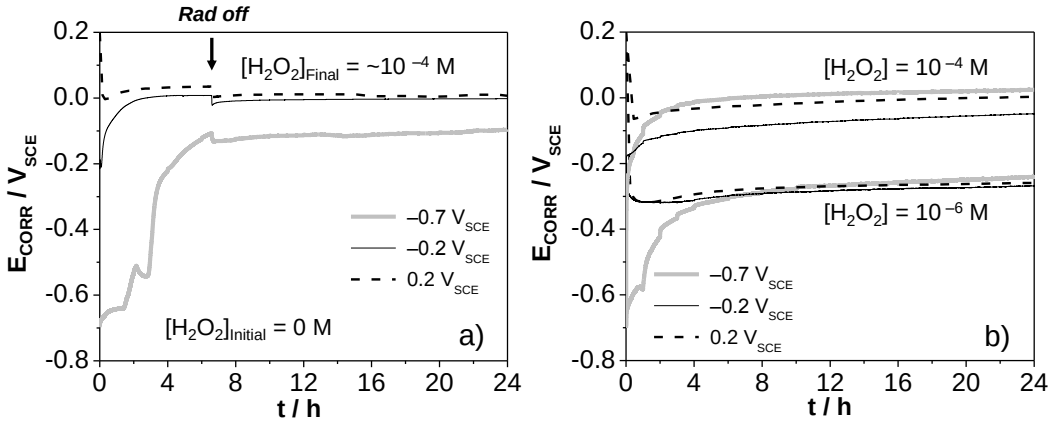

Figure 4.5: E_{CORR} observed (a) during and after exposure to 6 h γ-irradiation; and (b) during exposure to H_2O_2 for the films pre-grown at 0.2 V_{SCE}, –0.2 V_{SCE}, and –0.7 V_{SCE}. Two sets of data obtained in 10^{-4} M H_2O_2 and 10^{-6} M H_2O_2 are shown in b).

The slower approach to steady state of E_{CORR} of the irradiated systems, compared to E_{CORR} of the 1×10^{-4} M H_2O_2 solution, is attributed to the gradual increase in $[H_2O_2]$ during irradiation. However, when the concentration of radiolytically produced H_2O_2 reached steady-state at ~ 1×10^{-4} M, the $(E_{CORR})_{SS}$ values of the irradiated systems are those observed in 1×10^{-4} M H_2O_2 solutions. The reason for the slightly lower E_{CORR} observed at the end of irradiation with the film pre-grown at –0.7 V_{SCE} is not clear. One explanation may be that due to the gradual increase in $[H_2O_2]$ during the 6 h irradiation E_{CORR} reaches a value in Ox II at a later time, and once it reaches Ox II E_{CORR} increases very slowly due to the passivity of the film formed in this potential region.

These results strongly support the claims that the key radiolytically-produced redox species is H_2O_2 and that E_{CORR} during and post γ-irradiation is reasonably well simulated by adding H_2O_2 of chemical origin at the time-dependent concentration levels achieved radiolytically. As will be shown later, the system resistance behaviour observed under γ-irradiation conditions could also be simulated in a solution containing a representative concentration of H_2O_2, further supporting the above claim.

Monitoring the potential differences between platinum electrodes in solutions purged with Ar, CO_2, N_2O and O_2, where only one of the electrodes was subject to γ-irradiation, Fujita et al. [6, 7] reported that the potential was lower in the radiation environment by approximately 400 to 100 mV, depending on the aqueous environment. Upon termination of radiation exposure, the potential difference between the two electrodes was restored back to 0 V. The authors attributed the decrease in potential in a radiation environment to the preferential responsive nature of Pt to the water radiolysis product H_2. On the other hand, electrochemical studies on various grades of stainless

steel in acidic and chloride-containing solutions [9-11] reported an increase in corrosion potential by approximately 150 to 400 mV under γ-irradiation conditions. The authors of these studies attributed the increase in corrosion potential to the production of oxidizing radiolytic species, and specifically to the dominant effect of H_2O_2. Titanium alloys have also been shown to achieve a more noble potential upon irradiation, and the potential and polarization behaviour were reproduced with the addition of equivalent amounts of H_2O_2 [12].

A study on stainless steel by Marsh et al. [10], however, reported a decrease in corrosion potential upon termination of γ-irradiation, and attributed it to the effect of radical species, although no detailed explanation was given. There are many factors that may have contributed to the different post irradiation behaviour between this and their studies. One possibility arises from the fact that carbon steel is more redox-active than stainless steel. However, preliminary studies on the effect of radiation on stainless steel at pH 10.6 show a similar trend in the E_{CORR} behaviour, albeit the rate of change is slower, and no decrease in E_{CORR} upon termination of irradiation was observed [19]. A more likely explanation may be the different pH used in their study; they employed a neutral NaCl solution. Comprehensive studies on γ-radiolysis [15, 16] have shown that, under continuous irradiation conditions, the concentrations of molecular radiolysis products are inversely related to those of the radical products, but their concentrations are highly dependent on pH in the pH range 8.5 to 10 [16]. At low pH (< 9), the radical concentrations are reasonably high and radicals may have been involved in the corrosion process in their study.

Radiation dose rate also affects the steady-state concentrations; at a given pH the steady-state concentrations have a square root dependence on dose rate [15]. Since H_2O_2 is the key radiolysis product controlling carbon steel corrosion, but its concentration depends on the radiation dose rate, a more detailed investigation of the effect of [H_2O_2] on carbon steel corrosion, in particular on the oxide film growth and conversion kinetics, has been performed.

4.3.6 Oxide Film Growth and Conversion in H_2O_2 Solutions

The oxide film growth and conversion kinetics during exposure to H_2O_2 were further examined by LP and EIS measurements, and later compared with the LP measurements performed under irradiation conditions in Section 4.3.7. The in-situ film conversion kinetic study was augmented by ex-situ surface analysis by XPS.

4.3.6.1 EIS and XPS Analyses

The EIS spectra taken periodically during exposure of the film pre-grown at –0.7 V_{SCE} to H_2O_2 are shown in Figure 4.6. In all three different [H_2O_2], the time-dependence of the EIS spectra shows a fast initial response to H_2O_2 addition, followed by a slow change, with the final impedance depending on [H_2O_2]. The films pre-grown at –0.2 V_{SCE} and 0.2 V_{SCE} showed similar EIS behaviour (their EIS spectra are not shown, but the equivalent circuit analysis results are presented in Figure 4.7).

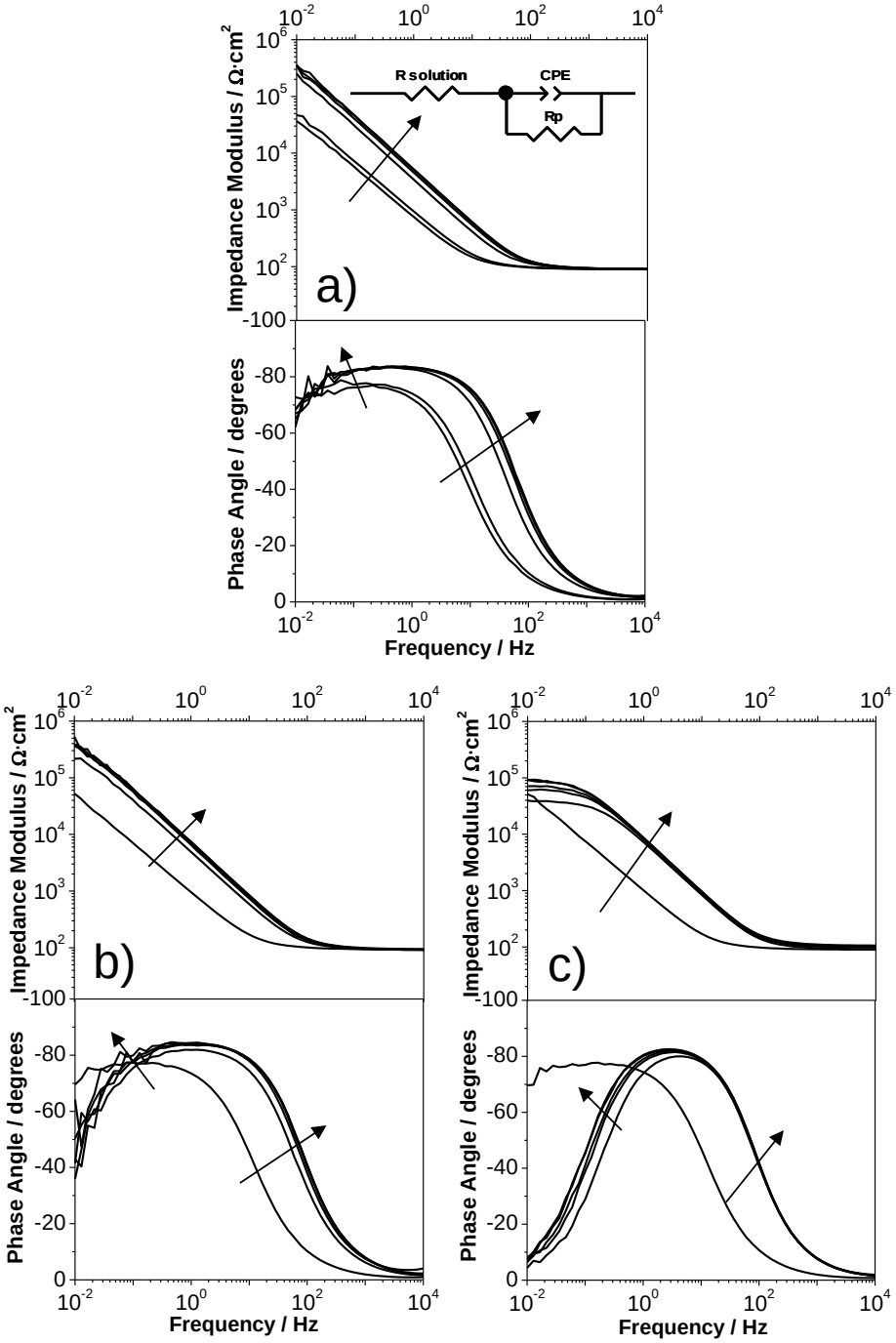

Figure 4.6: Electrochemical impedance spectra for the film pre-grown at –0.7 V_{SCE} during exposure to [H_2O_2] of; (a) 1×10^{-6} M, (b) 1×10^{-4} M, and (c) 1×10^{-2} M. The EIS were taken at 0, 1, 8, 24, and 37 h after the addition of H_2O_2. The arrows show the progression of EIS spectra as a function of time. The initial experiment on each plot represents EIS run at the film growth potential (–0.7 V_{SCE}), before the addition of H_2O_2. The experimental data was fit with an equivalent circuit (inset) as described in the text.

For all EIS measured, a simple electric equivalent circuit model as shown in Figure 4.6 could be fit to the resulting spectra. In this circuit model, R_s and R_P are the resistances of the solution and oxide polarization, and CPE is the constant phase element that relates to the capacitance of the film. For the system studied, the polarization resistance, R_P, is composed of a film resistance, R_{film}, and charge transfer resistance, R_{ct}, in series with one another. The analysis methods used are not capable of distinguishing between contributions from R_{film} and R_{ct}, so the additive polarization resistance was used. The inclusion of a film resistance suggests that there would be a graded structure with changing resistivity and dielectric constant with depth. Therefore, CPE is converted to a capacitance according to a derivation from Hsu and Mansfeld, [20, 21] as discussed in Chapter 3.

The system resistance and capacitance obtained from the circuit analysis, referred to as R_P and C_P, respectively, are shown in Figure 4.7.

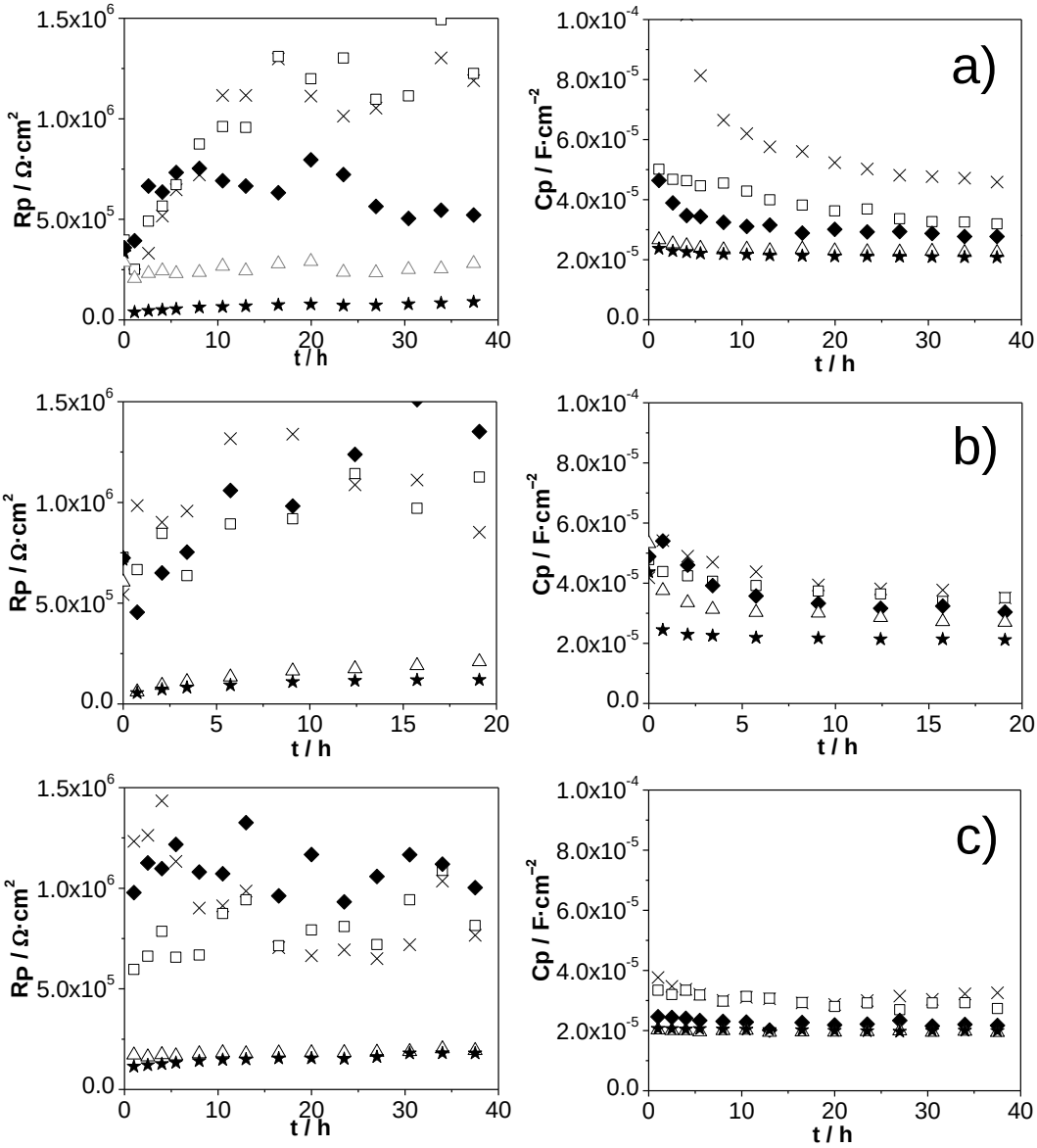

Figure 4.7: Polarization resistance and capacitance determined from the equivalent circuit (Figure 4.6a inset) for films pre-grown at (a) –0.7 V_{SCE}, (b) –0.2 V_{SCE}, (c) 0.2 V_{SCE} after the addition of H_2O_2. $[H_2O_2] = 1 \times 10^{-6}$ M (×), 1×10^{-5} M (□), 1×10^{-4} M (◆), 1×10^{-3} M (△), and 1×10^{-2} M (★).

The capacitance decreased immediately upon exposure of the electrode to H_2O_2, and subsequently remained almost constant, edging down only slightly over many hours.

The slow decrease in capacitance was accompanied by an increase in resistance, indicating thickening of a passive film. Both the capacitance and resistance eventually reached a steady state determined by [H_2O_2]. It is noted that the measured capacitance values are larger than those expected for an oxide film. This is presumed to result from surface roughness (ie. the actual surface area of the electrode was larger than the assumed geometric area). While higher in magnitude than expected, the general trends in capacitance with changing pre-grown film potential and [H_2O_2] can still be used to characterize the system.

The films pre-grown at –0.2 V_{SCE} and 0.2 V_{SCE} show similar behaviour, Figures 4.7b and 4.7c. One minor but important difference observed is that both R_p and C_P decreased with time for the film pre-grown at 0.2 V_{SCE} in 1×10^{-6} M H_2O_2 solution, the lowest concentration used in this study, see Figure 4.7c. This is attributed to the nature of the pre-grown film since the film grown at a potential in Ox III initially consists of more defective oxides or hydroxides, with higher Fe^{III} content (γ-Fe_2O_3 and γ-FeOOH) as described in Section 4.3.1. Upon removal of the applied potential, these Fe^{III} oxides could be reduced to Fe_3O_4, until the average valence of Fe in the film reaches the value expected at E_{CORR}. At low H_2O_2 concentrations, this reduction is slow, but the main contributor to the net corrosion current, due to the low level of aqueous oxidizing species. This results in an increase in the conductivity of the surface film, as observed by EIS. The decreases in both R_P and C_P further indicate a change in film property rather than in film thickness.

The steady-state R_P observed for the pre-grown films are plotted as a function of [H_2O_2] in Figure 4.8. R_P showed two distinct types of behaviour over the range of H_2O_2

concentrations: (1) at low $[H_2O_2]$ (< 10^{-3} M), the steady-state R_P was high, ~ 1 MΩ·cm^2, and increased slightly with an increase in $[H_2O_2]$; and (2) at high $[H_2O_2]$ (≥ 10^{-3} M) the steady-state R_P was approximately an order of magnitude smaller, and decreased slightly with increasing $[H_2O_2]$.

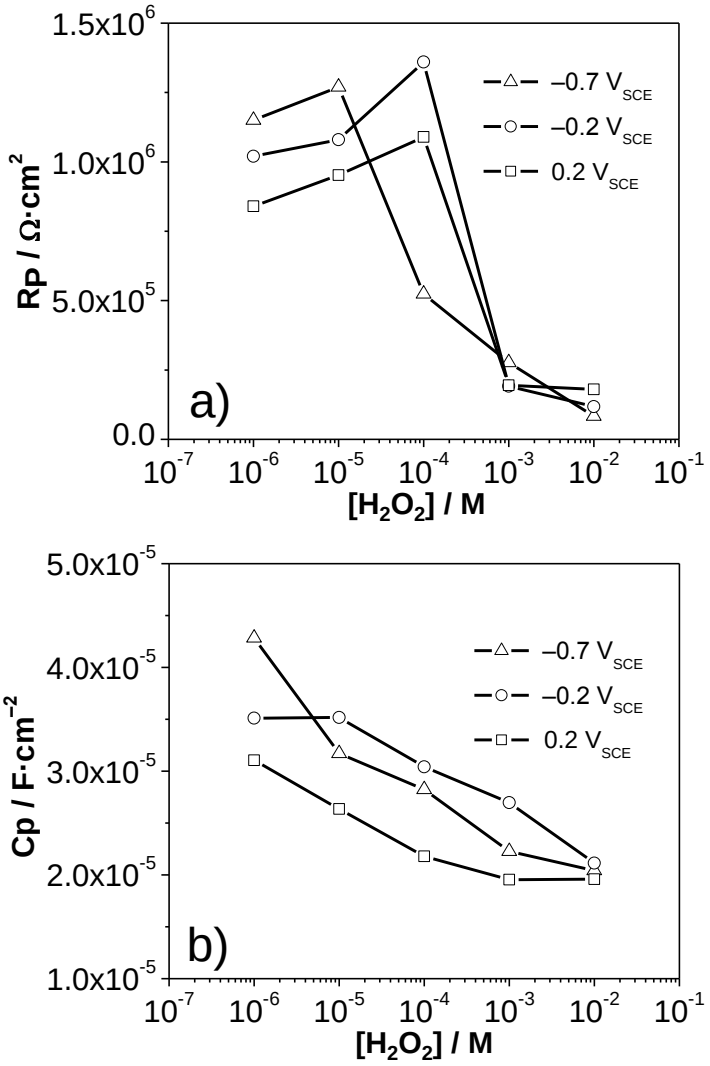

Figure 4.8: Steady-state (a) polarization resistance and (b) capacitance as a function of added H_2O_2 for the films pre-grown at (□) 0.2 V_{SCE}, (O) –0.2 V_{SCE}, and (Δ) –0.7 V_{SCE}.

The film conversion due to exposure to various [H_2O_2] was further examined using XPS. For the XPS study the pre-grown films were exposed to H_2O_2 for 24 h. Figure 4.9 shows an example of the high-resolution XPS spectra for the Fe–2p band. The shoulder, attributed to metallic Fe (binding energy 706.74 eV [22-24]), was observed in the XPS of all samples, suggesting that the thickness of the oxide films studied were thin enough to allow for the escape of photoelectrons. The Fe–2p band around 710 eV from iron oxides/hydroxides was deconvoluted using the reference XPS spectra obtained with single phase Fe_3O_4, γ-Fe_2O_3 and γ-FeOOH, with each oxide spectrum consisting of multiple Fe–2p peaks (inset of Figure 4.9) [25, 26]. This multiple-peak per oxide approach of fitting XPS results has been successfully applied on pure iron oxide samples [24]. From the reference oxide peaks, a weighted composite peak for Fe-2p in oxides was constructed, and used to fit spectra, via the commercial software CASAXPS®, for the analyses presented here [22-26]. The weighted composite spectra reproduced the observed spectra very well in all cases, Figure 4.9.

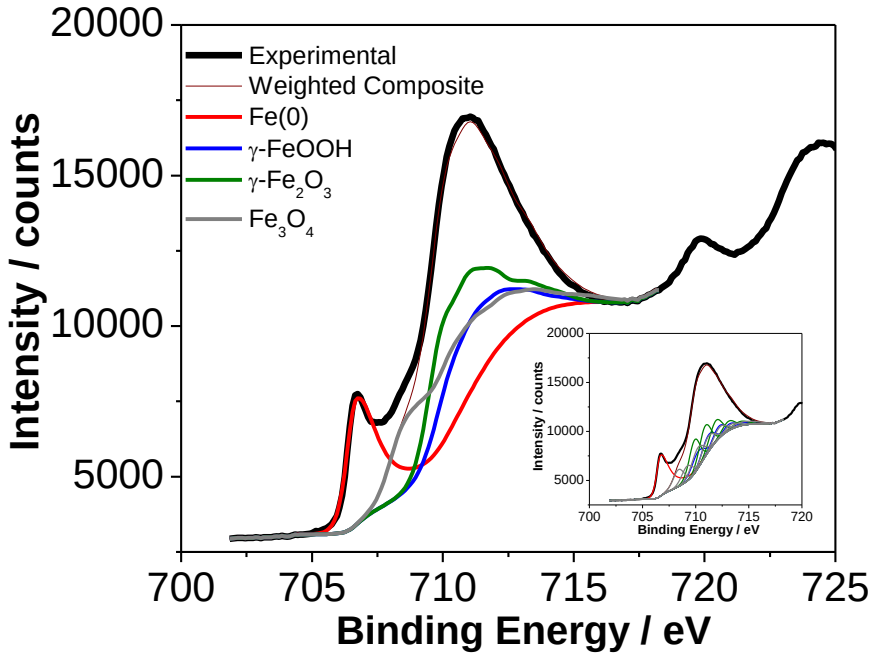

Figure 4.9: High resolution XPS spectra for the Fe–2p region. The Fe–2p band around 710 eV from iron oxides/hydroxides was deconvoluted using reference XPS spectra. The inset figure represents the multiple-peak per oxide approach before their combination for experimental analysis.

The results of the fitting analysis are summarized in Figure 4.10. Due to the uneven spatial distribution of the oxide films on surfaces, the absolute peak areas are not used for the analysis, but the ratio of the sum of the contributions of γ-Fe_2O_3 and γ FeOOH to the Fe-2p band to the contribution of Fe_3O_4. Note that the γ-Fe_2O_3 and γ-FeOOH contributions were not separated due to the similarity of their XPS spectra, which results in large uncertainties in determining the individual contributions. Although the XPS analysis data scattered considerably, two [H_2O_2] ranges can be discerned; a noticeable increase in the ratio of Fe^{III} to $Fe^{II/III}$ oxide at [H_2O_2] $\geq 10^{-3}$ M.

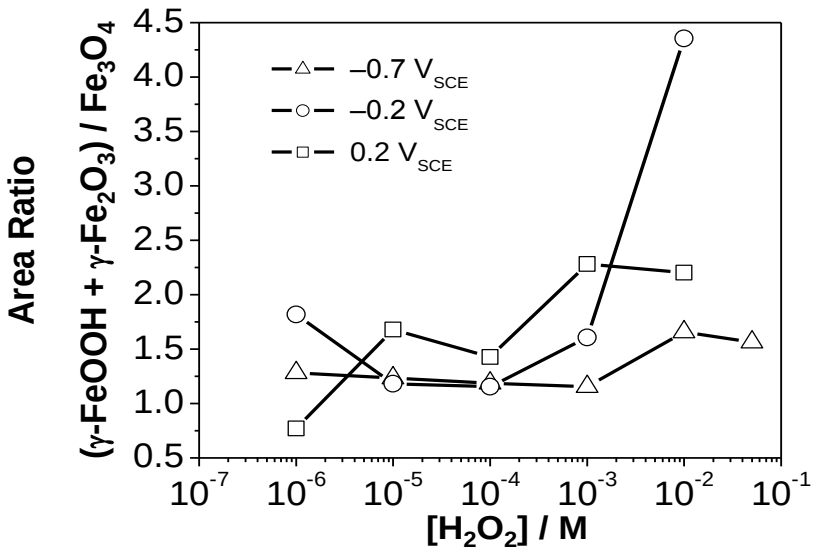

Figure 4.10: Fitting analysis of high-resolution Fe-2p XPS spectra. The individual peak area contributions of γ-Fe_2O_3, γ-FeOOH, and Fe_3O_4 are summed and presented as a ratio.

The E_{CORR}, R_P and the Fe^{III} to $Fe^{II/III}$ oxide ratio (Figures 4.4, 4.8 and 4.10, respectively) all provide a consistent picture of the film conversion as a function of $[H_2O_2]$. At $[H_2O_2]$ ($< 10^{-3}$ M), E_{CORR} increased with an increase in $[H_2O_2]$, but its values remained within Ox II (Figure 4.3). The film growth in this potential region consists of continuous growth of the conducting Fe_3O_4 layer accompanied by its anodic conversion to a more maghemite (γ-Fe_2O_3)-like phase near, or at, the oxide/solution interface [14, 17]. The oxide formed is mainly a compact Fe_3O_4/γ-Fe_2O_3 layer whose growth is limited mainly by the dissolution rate of the oxide, and, to a smaller extent, E_{CORR}. This oxide formation mechanism can thus explain the small increase in film resistance with $[H_2O_2]$, Figure 4.8. The XPS results showing a negligible change in the ratio of Fe^{III} oxides to

Fe_3O_4 with increasing $[H_2O_2]$, Figure 4.10, further supporting the thickening of a Fe_3O_4/γ-Fe_2O_3 layer in the lower $[H_2O_2]$ range.

At $[H_2O_2] \geq 10^{-3}$ M, E_{CORR} (Figure 4.4) was at the cusp of Ox III, where the anodic conversion of this Fe_3O_4/γ-Fe_2O_3 oxide to γ-FeOOH can lead to micro-fractures and the layer of Fe_3O_4/γ-Fe_2O_3 can grow by continuous film fracture and repassivation, producing a thicker and more defective (or porous) oxide film [14, 17]. This mechanism is consistent with the XPS results showing a higher ratio of Fe^{III} oxides to Fe_3O_4 at $[H_2O_2] \geq 10^{-3}$ M, Figure 4.10. It has been shown while in the presence of aggressive anions the film fracture can lead to pitting corrosion, in their absence the film quickly passivates and does not result in pitting [14, 17]. The results of the carbon steel electrodes exposed to high $[H_2O_2]$ did not show any sign of pitting corrosion. Irrespective of the exact nature of the Fe^{III} oxides, high R_P values are expected if the polarization resistance obtained by EIS is determined by the charge transfer resistance on the film surface. This is what was observed in the absence of H_2O_2 [13, 14], where high R_P values were observed for the films grown electrochemically in this potential range. Thus, the significantly lower resistance observed at $[H_2O_2] \geq 1 \times 10^{-3}$ M is attributed not to a breach of film passivity, but to surface-catalyzed H_2O_2 decomposition coupled with the Fe^{III}/Fe^{II} electron donor-acceptor relay, Reaction 4.7, as discussed in Section 4.3.4 (i.e., electronic, not ionic, conductivity increases and enhances H_2O_2 decomposition). The claim is further supported by the independence of E_{CORR} on $[H_2O_2]$ (Figure 4.4) and the increase in the Fe^{III} oxides composition in the film (Figure 4.10) at $[H_2O_2] \geq 10^{-3}$ M.

The steady-state E_{CORR} and R_P show negligible dependence on the type of pre-grown film. The nature and thickness of the pre-grown film appear to affect the initial

kinetics of the film conversion and the time to reach steady state. For both E_{CORR} and R_P, the time to reach steady state is longest for the film pre-grown at –0.2 V_{SCE}, as expected, since the pre-grown film would be composed of a more passive and compact Fe_3O_4/γ-Fe_2O_3 layer. The effect of the nature of pre-grown film can be also seen in the ratio of Fe^{III} to $Fe^{II/III}$ oxide at 10^{-2} M H_2O_2. The ratio is observed to be much higher for the film pre-grown at –0.2 V_{SCE} than for those grown at the other two potentials. Due to its compact structure, the film pre-grown at –0.2 V_{SCE} has not gone through the same extensive restructuring by continuous film fracture and repassivation as those grown at other potentials over the 24 h exposure to H_2O_2.

4.3.6.2 Linear Polarization and EIS

Although EIS provides more detailed information on film properties, it cannot be used when the film changes rapidly. Under these conditions, the linear polarization technique provides better information on the system resistance. Thus, the change in system resistance during the exposure to H_2O_2 was also studied by LP measurements. The first task was to establish that both EIS and LP measurements on carbon steel yield the same results, Figure 4.11. Only the results obtained with the films pre-grown at –0.7 V_{SCE} are shown, but EIS and LP for the films pre-grown at –0.2 V_{SCE} and 0.2 V_{SCE} also yield the same results. Once this was confirmed, the change in the system resistance during exposure to γ-irradiation was studied only by LP measurements, due to the faster change in E_{CORR}, and less stable electrochemical environment inside the gammacell.

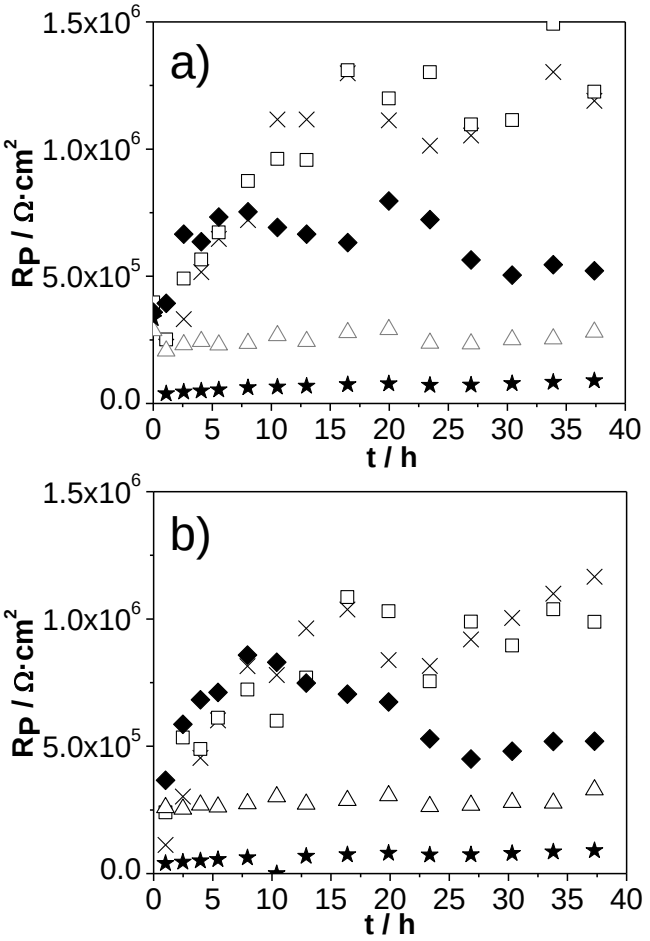

Figure 4.11: Comparison of R_P calculated from (a) EIS and (b) LP fitting after the addition of H_2O_2 to films pre-grown at –0.7 V_{SCE}. $[H_2O_2] = 1 \times 10^{-6}$ M (×), 1×10^{-5} M (□), 1×10^{-4} M (◆), 1×10^{-3} M (△), and 1×10^{-2} M (★).

4.3.7 Comparison of the Influences of Exposure to γ-Irradiation and to H_2O_2 on R_P

R_P values determined by LP measurements made under gamma irradiation and during exposure to chemically-added H_2O_2, where $[H_2O_2] = 10^{-4}$ M, are compared in Figure 4.12. This concentration was chosen for the comparison since it is close to the

steady-state concentration of radiolytically-produced H_2O_2 at the end of 6 h irradiation at the dose rate used in this study.

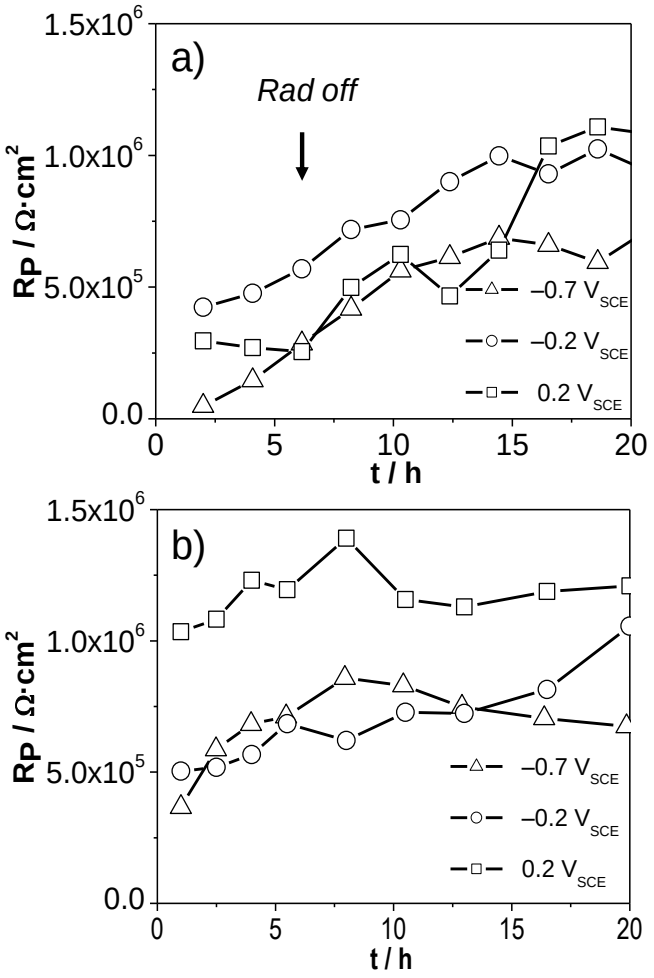

Figure 4.12: Comparison of R_P values calculated from LP fitting (a) during and after γ-irradiation and (b) after the addition of H_2O_2 to pre-grown films.

Consistent with the EIS results, in a given H_2O_2 solution R_P immediately reached a pseudo-steady-state value, and this was followed by a progressively smaller increase for the first 3-4 measurements (5 h) for all three pre-grown films, with the final steady-state values ranging from approximately 0.75 to 1.25 MΩ·cm^2. Although R_p was initially lower under irradiation conditions, in the range of 0.25 to 0.5 MΩ·cm^2, R_p increased at a

fast rate, and the increase continued for another few hours after the termination of irradiation, until R_p reached the values observed in the 10^{-4} M H_2O_2 solutions. The observation that the same final R_P (Figure 4.12) and E_{CORR} (Figure 4.3) values were achieved in both cases further supports the suggestion that similar oxide films formed under irradiation and H_2O_2 exposure conditions. The rate of increase in R_P following the termination of irradiation was similar to that observed in the H_2O_2 solution, as the film thickened spontaneously under a constant solution condition. The lower initial R_p values, but faster rate of increase during irradiation, was the result of the initially low but constantly increasing concentration of radiolytically-produced H_2O_2 (Figure 4.2), which was also responsible for the observed E_{CORR} behaviour discussed in Section 4.3.5.

The comparison of the R_P values determined from the LP measurements made under both exposure conditions provides more evidence that the corrosion behaviour of carbon steel under gamma irradiation at room temperature could be simulated well by exposing the steel to solutions containing an equivalent concentration of H_2O_2.

4.4. CONCLUSIONS

The effects of γ-irradiation and of H_2O_2 on carbon steel corrosion at pH 10.6 and room temperature were investigated by E_{CORR}, EIS, and LP measurements. Both E_{CORR} and R_P behaviour under radiation conditions could be simulated in a solution containing a representative concentration of H_2O_2, indicating that H_2O_2 is the key radiolysis product controlling carbon steel corrosion.

Both the steady-state E_{CORR} and R_P are strong functions of [H_2O_2], but nearly independent of the initial oxide film composition. The E_{CORR} and R_P behaviour showed

two distinct ranges dependent on $[H_2O_2]$. For $[H_2O_2] < 10^{-3}$ M, E_{CORR} is determined mainly by the cathodic half-reactions of H_2O_2 to yield OH^-, coupled with the anodic half-reactions of the oxide-covered steel surface. On the other hand, for $[H_2O_2] \geq 10^{-3}$ M, E_{CORR} is likely to be determined primarily by the cathodic half-reactions of H_2O_2, coupled with the anodic half-reactions of H_2O_2.

This study clearly illustrates that the corrosion rate of carbon steel in a γ-radiation environment at pH 10.6 and room temperature can be predicted from the dependence of E_{CORR} and R_P on $[H_2O_2]$ if the concentration of radiolytically-produced H_2O_2 can be determined or measured.

4.5 REFERENCES

[1] S. Neufuss, V. Cuba, R. Silber, V. Mucka, M. Posisil, A. Vokál, Czech J. Phys., 56 (2006) D365-D372.
[2] K. Ishigure, N. Fujita, T. Tamura, K. Oshima, Nucl. Technol., 50 (1980) 169-177.
[3] T.E. Gangwer, K.K.S. Pillay, Nucl. Technol., 58 (1982) 548-550.
[4] N. Fujita, C. Matsuura, K. Saigo, Radiat. Phys. Chem., 58 (2000) 139-147.
[5] N. Fujita, C. Matsuura, K. Saigo, Radiat. Phys. Chem., 60 (2001) 53-60.
[6] N. Fujita, C. Matsuura, K. Saigo, Radiat. Phys. Chem., 49 (1997) 357-362.
[7] N. Fujita, C. Matsuura, K. Saigo, Radiat. Phys. Chem., 50 (1997) 457-463.
[8] T. Yamamoto, S. Tsukui, S. Okamoto, T. Nagai, M. Takeuchi, S. Takeda, Y. Tanaka, J. Nucl. Mater., 228 (1996) 162-167.
[9] W.E. Clark, J. Electrochem. Soc., 105 (1958) 483-485.
[10] G.P. Marsh, K.J. Taylor, G. Bryan, S.E. Worthington, Corros. Sci., 26 (1986) 971-982.
[11] S. Glass, G.E. Overturf, R.A. Van Konynenburg, R.D. McCright, Corros. Sci., 26 (1986) 577-590.
[12] Y.J. Kim, K.J. Oriani, Corros., 43 (1987) 92-97.
[13] X. Zhang, W. Xu, D.W. Shoesmith, J.C. Wren, Corros. Sci., 49 (2007) 4553-4567.
[14] K. Yazdanfar, X. Zhang, P.G. Keech, D.W. Shoesmith, J.C. Wren, Corros. Sci., 52 (2010) 1297-1304.
[15] J.M. Joseph, B.S. Choi, P. Yakabuskie, J.C. Wren, Radiat. Phys. Chem., 77 (2008) 1009-1020.
[16] P. Yakabuskie, J.M. Joseph, J.C. Wren, Radiat. Phys. Chem., 79 (2010) 777-785.

[17] W. Xu, K. Daub, X. Zhang, J.J. Nöel, D.W. Shoesmith, J.C. Wren, Electrochim. Acta, 54 (2009) 5727-5738.
[18] D. Fu, X. Zhang, P. Keech, D.W. Shoesmith, J.C. Wren, Electrochim. Acta, 55 (2010) 3787-3796.
[19] Q.W. Knapp, J.C. Wren, Electrochim. Acta, 80 (2012) 90-99.
[20] C.H. Hsu, F. Mansfeld, Corros., 57 (2001) 747-748.
[21] B. Hirschorn, M.E. Orazem, B. Tribollet, V. Vivier, I. Frateur, M. Musiani, Electrochimica Acta, 55 (2010) 6218-6227.
[22] C.R. Brundle, T.J. Chuang, K. Wandelt, Surf. Sci., 68 (1977) 459-468.
[23] M.W. Roberts, P.R. Wood, J. Electron Spectrosc. Relat. Phenom., 11 (1977) 431-437.
[24] A.P. Grosvenor, B.A. Kobe, N.S. McIntyre, Surf. Sci., 572 (2004) 217-227.
[25] A.P. Grosvenor, B.A. Kobe, M.C. Biesinger, N.S. McIntyre, Surf. Interface Anal., 36 (2004) 1564-1574.
[26] A.P. Grosvenor, B.A. Kobe, N.S. McIntyre, Surf. Sci., 565 (2004) 151-162.

Chapter 5

Deconvoluting the Effects of pH, Temperature and Electrolyte Concentration on Carbon Steel Corrosion

5.1 INTRODUCTION

It is well understood that solution parameters such as pH, temperature and electrolyte concentration can significantly influence corrosion kinetics. Although the oxidation of pure iron and carbon steel has been studied extensively (including, but not limited to the work cited in references [1-21]), most of these studies were performed under a narrow range of solution conditions, and the primary interest was determining the corrosion rates or oxide growth mechanism under a particular set of experiments. Aqueous corrosion is an electrochemical process involving metal oxidation coupled with reduction of an aqueous species, where the oxidized metal atoms are either incorporated into a solid oxide film or they dissolve into the water. Since individual solution parameters can affect the film growth and metal dissolution rates differently, it is difficult to separate the effects of individual parameters or to extrapolate the corrosion rate obtained under one set of conditions to another set of conditions. The objective of this study is to provide some insights into the separate effects of temperature, pH, and electrolyte concentration (ionic strength) on the corrosion of carbon steel.

The effects of the solution parameters on carbon steel corrosion was investigated at two temperatures, 80 °C and 150 °C, at $pH_{25°C,}$ 6.0, 8.4 and 10.6, and at three different borate concentrations, 0, 1 and 10 mM. The corrosion kinetics under a given set of conditions were followed by characterizing the chemical composition, morphology and structure of the oxide films formed on carbon steel coupons as a function of corrosion

time. The experiments were performed with the coupon samples submerged in various solutions in contact with cover gases in leak-tight vials. The surface and the cross section of the oxide films were examined by scanning electron microscopy (SEM) or transmission electron microscopy (TEM), Raman spectroscopy, and X-ray photoelectron spectroscopy (XPS). The test solutions were also analyzed for dissolved metal ion concentrations using inductively coupled plasma mass spectrometry (ICP-MS). In Chapter 6 the results are further compared to equivalent experiments performed in the presence of gamma irradiation.

5.2 EXPERIMENTAL

5.2.1 Experimental Setup

For the samples, the carbon steel rod was cut into solid cylindrical wafers (coupons) with a diameter of 10 mm and a thickness of 3 mm. Prior to each test a freshly-cut coupon was abraded manually with 400 and 600 grit silicon carbide papers. This was followed by polishing on a Texmet microcloth (Buehler) with a 1 μm MetaDi Supreme diamond paste suspension (Buehler) and lastly sonication in a 50:50 acetone:methanol mixture for 5 min to remove polishing residues.

The corrosion tests were performed with the test coupon located in a sealed vial, Figure 5.1. For the work reported here, we used specially fabricated vials. Borosilicate vials (20-ml crimp-cap-sealable) were purchased from Agilent Technologies. To minimize silicate dissolution the commercial vials were then modified by hand. The bottom half of a vial was replaced with an equivalent segment made of quartz. The

interior of the vial also included a quartz projection on the bottom that was used to suspend the coupon ~ 15 mm above the bottom of the vial.

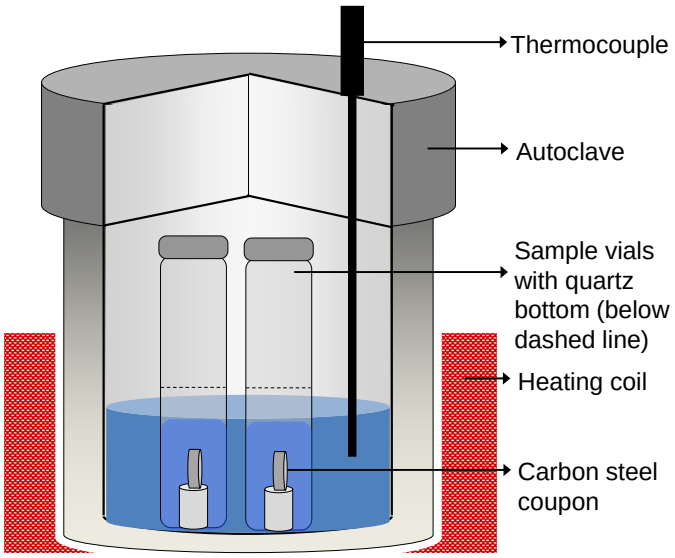

Figure 5.1: Schematic diagram of the experimental set-up, showing the test vial arrangement in the pressure vessel.

Preparation of a test vial was performed inside an Ar-purged glove box where the oxygen concentration was maintained at a low level. Sampling determined that the oxygen concentration in a test solution was approximately 0.4 ppm at room temperature. First, the coupon was placed inside a vial on the quartz stand. Sufficient electrolyte solution was then added to the vial to fully immerse the coupon, but, to minimize the dissolution of silicate, the amount of water added was limited such that the water level at 150 °C (taking into account thermal expansion of the liquid) would remain below the quartz/borosilicate transition. The vial was capped using an aluminum crimp cap with a PTFE silicone septum to provide a vacuum tight seal and ensure no loss of gas during a

test. The sealed vials were placed inside an autoclave and the autoclave was filled with water to approximately the same level as the water in the vials. This provided a pressure balance on the vial walls when heated. With this experimental design the seals on all sample vials remained intact throughout the tests.

A 250 mL type 316 stainless steel autoclave was used (Parr Instrument Company, model 4760). The autoclave was sealed and placed inside a coil heater whose temperature was controlled by a Parr 4836 controller. The entire autoclave and coil heater was insulated. Each test began at room temperature. The autoclave was heated to 80 °C or 150 °C over a period of approximately 15 or 60 min, respectively, and then held at the desired temperature for the desired test duration (20 h, 66 h, or 170 h).

At the end of each test the heater was turned off and the autoclave was allowed to cool to a comfortable handling temperature (roughly 80 °C) for the 150 °C experiments (this took approximately 15 min). When the autoclave was sufficiently cool, it was opened and the sample vials were removed. The vials were opened and the coupons were removed and dried in flowing argon gas. The oxide films on the coupons were then analyzed using various surface analytical techniques. The residual solution in the sample vials was analyzed for pH and dissolved metal content.

Experiments were performed in solutions prepared using water, purified by a NANOpure Diamond UV ultra-pure water system (Barnstead International) giving a final resistivity of 18.2 MΩ·cm. Solutions of 1 mM and 10 mM sodium borate were prepared using reagent grade $Na_2B_4O_7 \bullet 10H_2O$ (Caledon Laboratories Ltd.). Reagent grade NaOH (Caledon Laboratories Ltd.) was added dropwise to the solutions to adjust the pH to 10.6. These solutions are referred to as pH 10.6, 1 mM borate and pH 10.6, 10 mM borate

solutions. Unbuffered solutions with pH 10.6, prepared by adding reagent grade LiOH (Sigma-Alridch) to purified water, are referred to as 0 mM borate solutions. Reagent grade H_3BO_3 (Caledon Laboratories Ltd.) was added to sodium borate to adjust the pH to 8.4 to prepare pH 8.4, 10 mM borate solutions. Solutions of pH 6.0, 0 mM borate were prepared from the dropwise addition of H_3BO_3 to deionized water, with no sodium borate present. All pHs are given with respect to measurement at 25 °C. Due to the small solution volumes and potential changes in the solution during the heating corrosion experiments, the pH of all solutions was measured after experiments, Table 5.1.

Table 5.1: Changes in pH for all solutions studied.

80 °C												
Initial pH	8.4			10.6			10.6			10.6		
Borate (mM)	10			0			1			10		
Time (h)	20	66	170	20	66	170	20	66	170	20	66	170
Final pH	8.8	8.8	8.5	9.9	9.6	9.3	9.8	9.9	9.5	10.3	10.3	10.0
150 °C												
Initial pH	6.0			8.4			10.6			10.6		
Borate (mM)	0			10			0			10		
Time (h)	20	66	170	20	66	170	20	66	170	20	66	170
Final pH	7.4	nd[1]	6.4	8.9	8.5	8.4	8.8	8.2	8.4	9.8	10.0	9.7

1. not determined

5.2.2 Surface Analysis

After surface examination, selected locations on the coupon surfaces were subjected to a focused ion beam (LEO 1540XB) which was used to erode a tightly controlled area on the sample, leaving a cross-sectional cut through the surface film and into the underlying metal. A thin layer of Pt was deposited on the coupon surface before focused ion beam cutting to demarcate and provide contrast at the oxide surface. Cross-

sections prepared in this way were then imaged by SEM and the oxide thickness determined. Cross-sectional TEM was performed on wedge samples, using a FEI-Titan 80-300 cubed electron microscope. To determine the chemical composition and phase of the oxides present in the surface film, Raman spectra were compared to Raman spectra of standard iron oxide samples (Alfa Aesar).

The oxide films grown at 80 °C were so thin that the cross sections of the films were not obtained. For these films the thickness was determined by analyzing the Fe-2p bands of high resolution XPS. To determine the thickness of the oxide films, the Fe-2p bands of high resolution XPS of the coupons were deconvoluted into Fe oxide (all oxides) and metallic Fe^0 components, Figure 5.2 [22-24]. The metallic Fe oxide contribution to the measured band was used to determine an oxide thickness using normalized molar masses, mean free path of electrons, and densities of the oxide and metal, and assuming that oxide was entirely composed of magnetite [25-27].

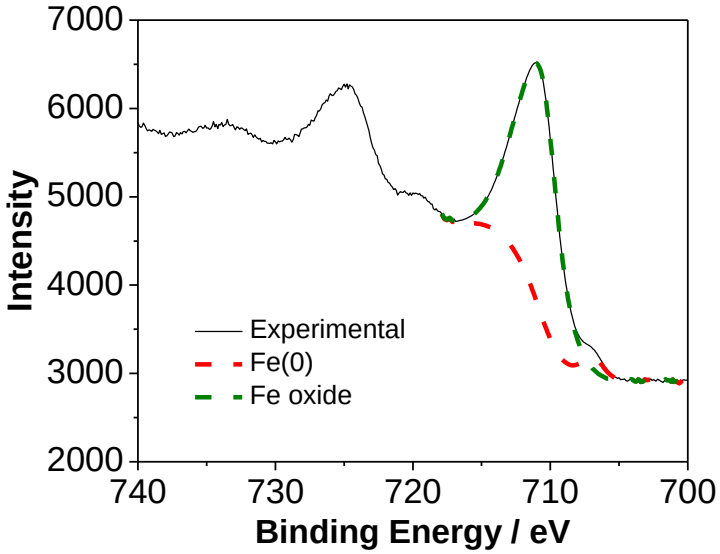

Figure 5.2: Sample spectra for the Fe–2p region and deconvoluted contributions of Fe oxide and Fe^0.

5.3 RESULTS

Since the solution parameters studied (pH, temperature, and electrolyte concentration) can affect the film growth and metal dissolution rates during corrosion differently, the corrosion kinetics were investigated by examining the surfaces as a function of corrosion time under a specific set of conditions. The time dependent behaviour of corrosion illustrates the different effects of the individual solution parameters more clearly. Thus, the matrix of the solution parameters was not chosen for completeness but judicious combinations of the solution parameters that can differentiate the different effects more clearly during corrosion under the set of conditions. The results are presented according to the studied temperature, 80 °C or 150 °C.

5.3.1 Corrosion at 80 °C

5.3.1.1 Effect of Electrolyte Concentration at pH 10.6

The first parameter explored is the dependence of corrosion on electrolyte concentration. The oxide formed on carbon steel was studied at pH 10.6 with three different borate concentrations, 0, 1 and 10 mM. The morphology of the corroded surfaces is shown in Figure 5.3. The surfaces are featureless and smooth, independent of the electrolyte concentration and the corrosion time. Polishing marks are visible on all of the surfaces, indicating that any oxide film present is very thin. On some surfaces, very small evenly distributed 'pin-holes', approximately 0.1 μm in diameter, were observed. The presence of these holes has no visible effect on the neighbouring areas. The origin of the 'pin-holes' is not clear, but they do not appear to interfere with or participate in the corrosion process significantly.

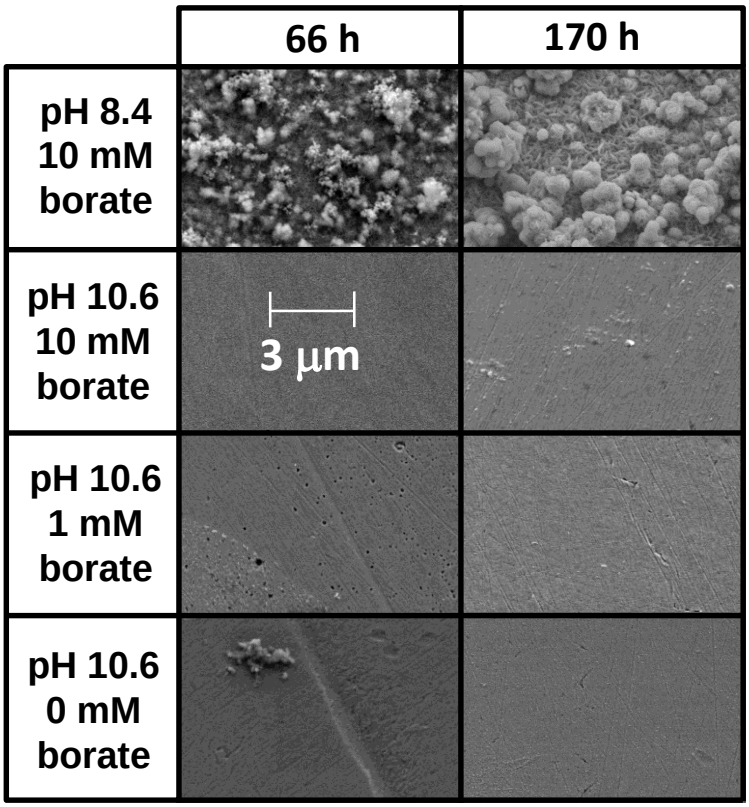

Figure 5.3: SEM micrographs of the carbon steel coupon surfaces after 66 and 170 h at 80 °C.

The oxide thicknesses obtained from XPS analysis are shown in Figure 5.4. The results show that the oxide thickness increased with an increase in corrosion time and decreased with an increase in electrolyte concentration. The thickness of the oxide grown for the longest time was still less than 10 nm at pH 10.6.

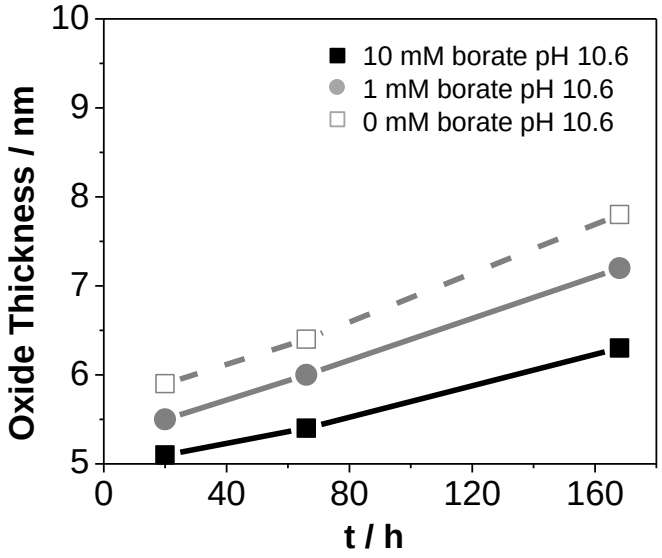

Figure 5.4: Oxide thickness as a function of corrosion time and borate concentration determined by XPS analysis.

The Raman spectra of the coupon surfaces corroded at pH 10.6 (Figure 5.5a) are compared to reference spectra for different single-phase iron oxides (Figure 5.5b). Due to the thinness of the films, interference from surface reflections, and poor scattering, the Raman signals from the surfaces are very weak. However there is a distinct peak at ~670cm^{-1} that is characteristic of magnetite (Fe_3O_4) [28] that is most noticeable for the 0 mM borate test. The Raman intensity of this peak increased with corrosion time (the results not shown). No other identifiable oxide peaks were present. A weak peak observed at ~825 cm^{-1} does not correspond to any iron oxide standards or any reported values of hydroxides or green rusts. Nearly identical Raman spectra, with a weak secondary peak above 800 cm^{-1}, have been previously observed on carbon steel surfaces corroded in borate solutions at pH 10.6 and at room temperature [29]. Similar spectra

have been observed using in-situ surface enhanced Raman on iron films grown at pH 8.4 [30] and minor structures have been attributed to surface carbon contamination, most likely from CO_2 [30]. The large increase in the background starting at 1250 cm^{-1} is attributed to fluorescence.

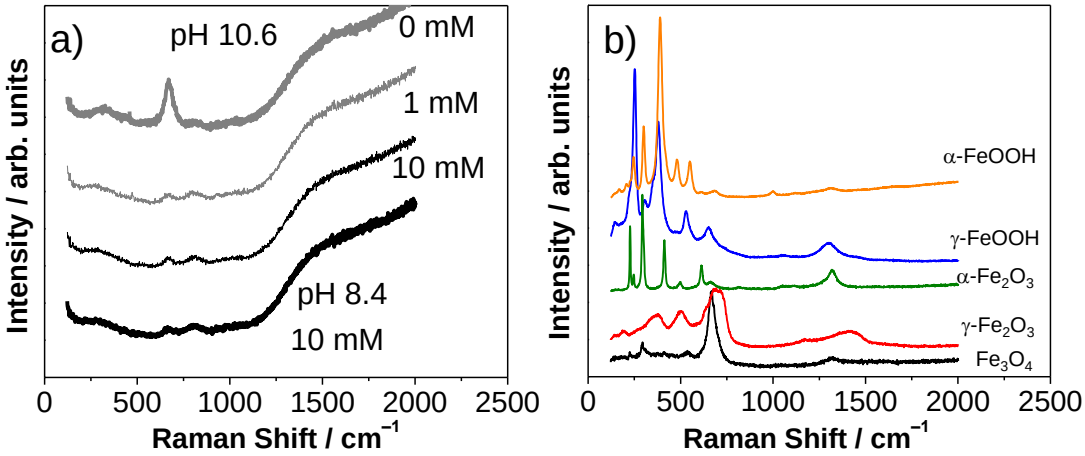

Figure 5.5: (a) Sample Raman spectra of carbon steel coupon surfaces after exposure at 80 °C (concentrations of borate are labelled) and (b) Raman spectra of reference iron oxide minerals.

For tests performed at pH 10.6 the measured dissolved iron concentration in solutions at the end of the 170 h test was very small, but a slight increase in concentration was observed at the highest borate concentration, Table 5.2.

Table 5.2: Iron concentration in solution after 170 h.

80 °C		
pH	**Borate (mM)**	**Iron concentration (ppb)**
10.6	**0**	37
10.6	**1**	36
10.6	**10**	57
150 °C		
6.0	**0**	3000
8.4	**10**	420
10.6	**0**	110
10.6	**10**	640

5.3.1.2 Effect of pH in 10 mM Borate Solutions

A limited study on the effect of pH on film growth was performed at 80 °C by corroding coupons at pH 8.4 and pH 10.6 in 10 mM solutions. The coupons corroded at the lower pH have a very different surface morphology, Figure 5.3. Large, unevenly distributed deposits are seen on the surface of a coupon, even after the shortest corrosion time of 20 h. As corrosion progressed for longer times, more deposits were formed and became more evenly distributed. However, the Raman spectrum of a coupon corroded at pH 8.4 was identical to the spectra of coupons corroded at pH 10.6 (Figure 5.4a), indicating that the oxide formed at pH 8.4 were also mainly composed of Fe_3O_4. In contrast, the Fe-2p band in the XPS of a coupon corroded at pH 8.4 had no Fe^0 component, indicating the presence of an oxide layer thicker than 15 nm, the analysis

depth of the XPS. The results suggest that different mechanisms are responsible for the oxide formation and growth at pH 8.4 and pH 10.6 at 80 °C.

Measurements of the pHs of the test solutions at the end of a test show that there are only small changes in pH (for tests with 10 mM borate) (Table 5.1), and the changes were too small to impact on the oxide formation mechanism.

5.3.2 Corrosion at 150 °C

5.3.2.1 Varying Electrolyte Concentration at pH 10.6

The SEM images of coupons corroded at pH 10.6 for two electrolyte concentrations are presented in Figures 5.6 and 5.7. The surfaces are much more altered than the surfaces of coupons corroded at 80 °C and there are no visible residual polishing marks. There are no differences in the appearance of coupons corroded for different times (66 h and 170 h), but oxides with different morphologies are formed with different electrolyte concentrations. The oxide formed in the higher concentration borate solution has a finer grain, more filament-like structure, Figure 5.6. The oxide appeared to be relatively uniform with no visible areas of different or localized corrosion, there were no distinct crystalline structures, and there were very few particulates, Figure 5.7. The SEM of the coupon corroded for 66 h in 10 mM borate solution does show areas of two different shades, Figure 5.7. This may be due to the underlying structure of the mixed ferrite and pearlite phases in the carbon steel. The pearlite phase is typically distributed in carbon steel as a random oblong shape, 20-30 μm in length and 5-10 μm in width [31]. The darker patches in the SEM image in Figure 5.7 may correspond to this phase. Similar images with two different phases were also observed for coupons corroded for

only 20 h in both 0 mM and 10 mM borate solutions (results not shown). The underlying structure became less visible as corrosion progressed, consistent with the growth of a thicker oxide which obscured the view of the steel phase structure. The underlying structure was visible in samples at 80 °C in lower magnification SEM (not shown).

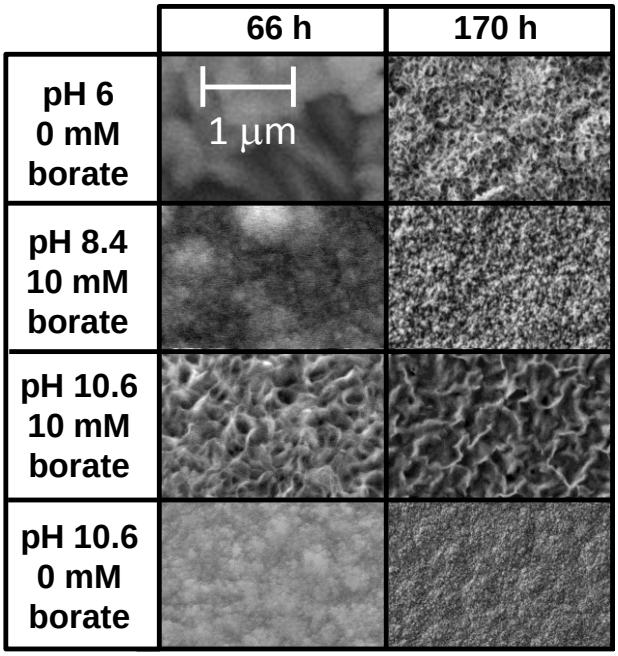

Figure 5.6: High magnification SEM micrographs of steel coupon surfaces after 66 and 170 h corrosion at 150 °C.

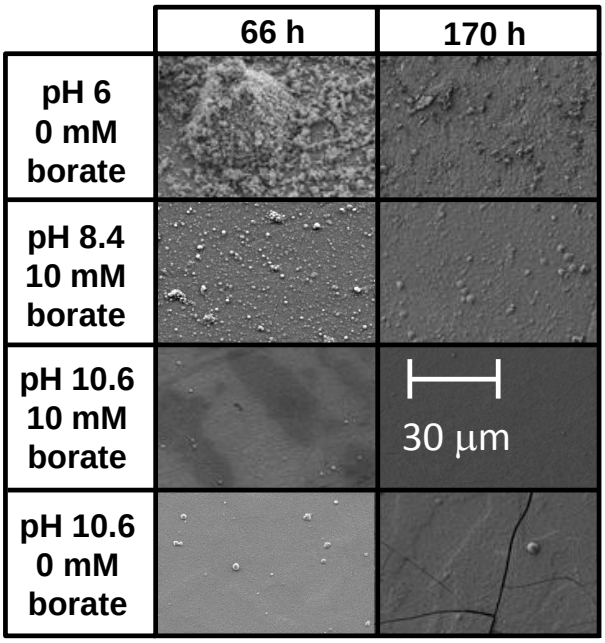

Figure 5.7: Low magnification SEM micrographs of steel coupon surfaces after 66 and 170 h corrosion at 150 °C.

Some cracks were seen in the oxide grown in the 0 mM borate solutions for 170 h. These elongated cracks show clean breaks and may have been created during cooling of the rapid cooling of the test coupons. The cracks are not associated with the phase boundary of the underlying carbon steel microstructure (ferrite or pearlite).

Raman spectra of the coupons corroded for 170 h, Figure 5.8, show a dependence on electrolyte concentration. The coupon corroded in a solution with no borate has a very distinct main peak at 670 cm^{-1} and a secondary peak at ~540 cm^{-1} that correspond to Fe_3O_4 [28]. In contrast, the spectrum for a coupon corroded with 10 mM borate present contains a very much smaller peak at the same location. Minor peaks at wavenumbers below 500 cm^{-1} are attributed to the presence of low concentrations of a range of hydrated iron oxides or hydroxides on the surface [32, 33].

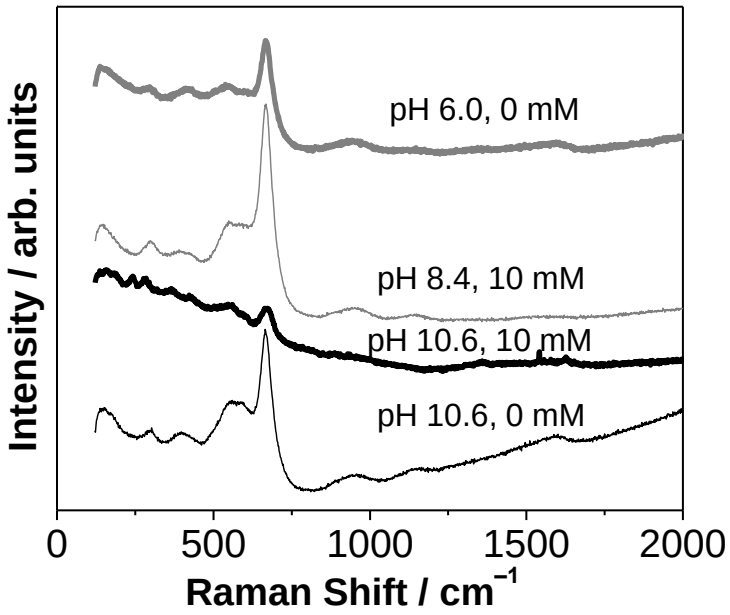

Figure 5.8: Raman spectra of carbon steel coupon surfaces after exposure for 170 h at 150 °C. Labelled are the pH and borate concentrations.

Cross-section analysis of corroded coupons show visibly thick oxides had formed as shown in Figure 5.9. The oxides grown were all uniform and compact, and the oxide grown in 0 mM borate was much thicker that that grown in 10 mM borate solutions (see Table 5.3 for thicknesses). This is consistent with the much less pronounced Fe_3O_4 peak in the Raman spectrum of a coupon corroded in a 10 mM borate solution.

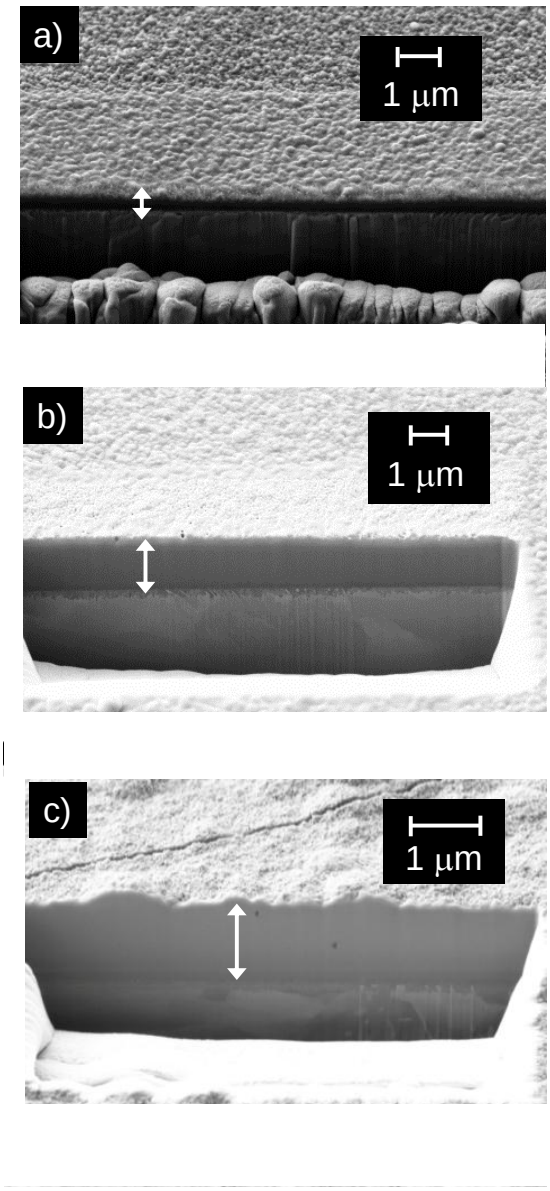

Figure 5.9: SEM images of the cross section of the carbon steel coupons subject to 66 h corrosion at 150 °C for (a) pH 10.6, 10 mM borate, (b) pH 10.6, 0 mM borate, and (c) pH 8.4, 10 mM borate. Arrows indicate the oxide film.

The cross sections of the samples corroded for 170 h were analyzed further with TEM and the features of the metal/oxide interfacial region could be more clearly observed, Figure 5.10. The TEM images of the sample corroded for 170 h in pH 10.6 and 0 mM borate solution show the metal grains in the bulk metal substrate. They show a

lighter contrast area below the distinct oxide phase that does not show a distinct structure but shows the extension of the metal grain structure, Figure 5.10b. Thus, this layer is not a distinct oxide phase and hence, is referred to as the metal/oxide interfacial region.

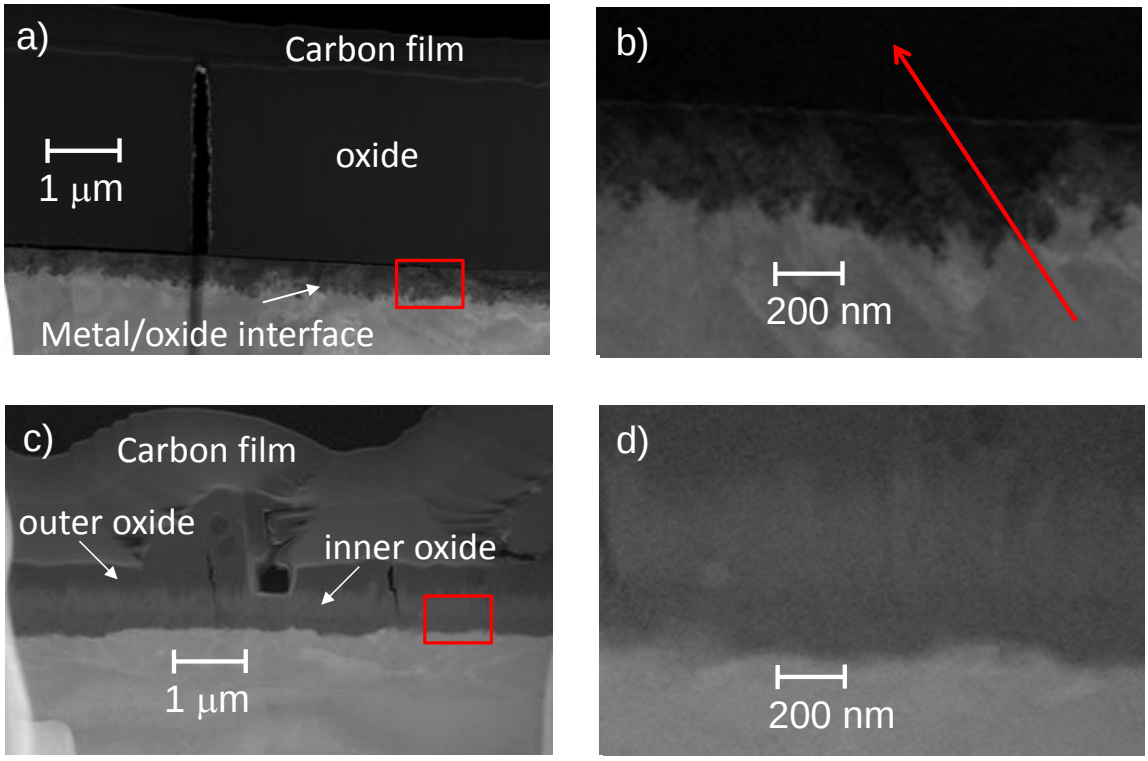

Figure 5.10: TEM images of the cross section of carbon steel coupons subject to 170 h corrosion at 150 °C for (a) pH 10.6 and 0 mM borate and (c) pH 6.0 and 0 mM borate. Also shown is (b) the interfacial region for pH 10.6 and 0 mM borate that was labelled in a red box in (a) and (d) the interfacial region for pH 6.0 and 0 mM borate that was labelled in a red box in (c).

The cracks that had been observed on the surface propagated across the oxide film to the base metal surface and lifted the oxide slightly. Over all samples studied, the crack formation probability appeared to increase with increasing thickness of the oxide. As described earlier, the crack was introduced during the cooling process. Due to different

thermal expansion properties of the base metal substrate and the oxide, the rapid cooling induces stress in the compact oxide structure, lifting it from the base metal [34].

The iron concentrations measured in the test solutions at the end of a tests were much higher than those measured in tests at 80 °C. Also, a much higher concentration of iron was seen for a coupon corroded in 10 mM borate compared to a coupon corroded in 0 mM borate. This is the inverse of the oxide thicknesses seen for coupons corroded in the different electrolyte concentrations.

Table 5.3: Oxide thickness for samples corroded at 150 °C.

pH	Borate (mM)	Oxide Film Thickness	
		66 h	**170 h**
6.0	**0**	nd[1]	0.5-2.0 μm
8.4	**10**	1.5 μm	1.8 μm (170 nm)[2]
10.6	**0**	1.5 μm	3.0 μm (400 nm)[2]
10.6	**10**	0.35 μm	0.48 μm (< 50 nm)[2]

1. not determined
2. thicknesses of the metal/oxide interfacial region determined by TEM.

5.3.2.2 Effect of pH

The effect of pH on carbon steel corrosion at 150 °C was investigated by comparing the surfaces corroded at pH 10.6 and pH 8.4 cases both in 10 mM borate solutions, and at pH 10.6 and pH 6.0 both in 0 mM borate solutions. The SEM images of the surfaces of the coupons corroded at pH 10.6 and pH 8.4 show only slight differences, Figures 5.6 and 5.7. The coupons corroded at pH 8.4 show the presence of small deposits on a smooth underlying oxide layer.

The SEM (Figure 5.9c) and TEM (results not shown) images of the cross sections show that the metal/oxide interfacial and the oxide structures are very similar at pH 8.4 and pH 10.6, but the thicknesses of both the interfacial and the oxide layers were greater at pH 8.4, Table 5.3. The Raman spectra of coupons corroded at pH 8.4 were similar to the spectra of coupons corroded at pH 10.6 showing the presence of Fe_3O_4, Figure 5.8.

To further examine the effect of pH, tests were conducted at pH 6.0 and in 0 mM borate solutions. The surface corroded for 66 h at pH 6.0 show larger particulates with co-deposited smaller crystallites, Figures 5.6 and 5.7. After 170 h the surfaces are evenly distributed with smaller crystallites, becoming more uniform and smoother. The SEM and TEM images of the cross-sections of the films formed at pH 6.0 show a two oxide layer structure (Figures 5.10 and 5.11b). The inner oxide layer has a filament-like structure whereas the outer oxide grows more compactly showing no discernible features. At pH 6.0, no distinct metal/oxide interfacial layer was observed. Instead, the metal/oxide boundary is not uniform but shows significant variation in the corrosion front, Figure 5.10. Consequently the oxide thickness varies along the surface, ranging from 0.5 to 2.0 μm, Table 5.3. The Raman spectra of coupons corroded at pH 6.0 and pH 10.6 were similar (Figure 8), indicating that the oxide is still mainly Fe_3O_4. The dissolved iron concentration is more than an order of magnitude higher at pH 6.0 compared to that at pH 10.6, Table 5.2.

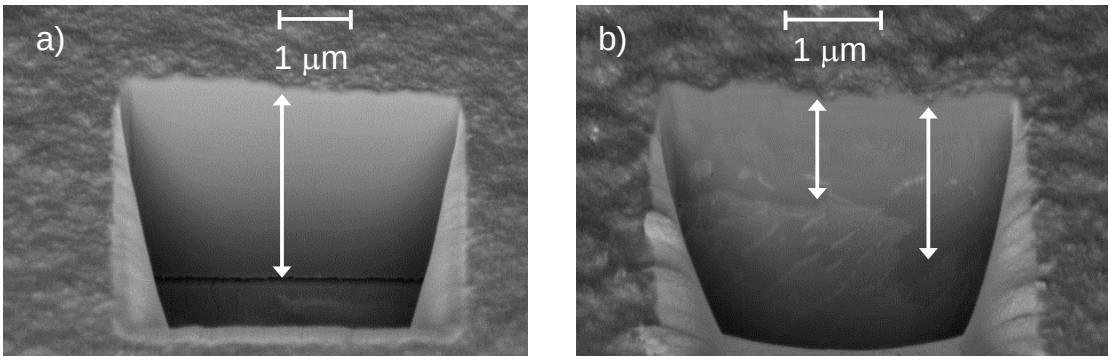

Figure 5.11: SEM images of the cross section of the carbon steel coupons subject to 170 h corrosion at 150 °C for (a) pH 10.6, 0 mM borate and (b) pH 6.0, 0 mM borate. Arrows indicate the oxide film.

5.4 DISCUSSION

5.4.1 Corrosion Potential and the Oxide Chemical and Phase Composition

Analysis results indicate that the oxides formed in the deaerated corrosion tests most likely consist of Fe_3O_4 with minor quantities of hydrated Fe^{II} and Fe^{III} species, likely adsorbed on the Fe_3O_4 surface. The presence of any Fe^{III} oxyhydroxides or oxides such as α-Fe_2O_3 was not observed.

The formation of Fe_3O_4 is expected from the thermodynamic properties of the systems. Assuming the dissolved oxygen (determined to be 0.4 ppm at room temperature, which would be even lower at elevated temperatures) is negligible, the electrochemical potential of pure water can oxidized Fe^0 only to Fe^{II} and $Fe^{II/III}$ (i.e., Fe_3O_4) oxides/hydroxides. In the previous electrochemical studies of carbon steel corrosion, Chapter 3, three separate regions (or potential ranges) for iron oxidation were identified. The electrochemical potential on an isolated iron coupon in pure water is located in region Ox I. Figure 5.12 shows this region and the equilibrium Nernst

potentials of the redox reactions of iron species at pH 10.6 and room temperature, derived from Gibbs free energies [25, 35].

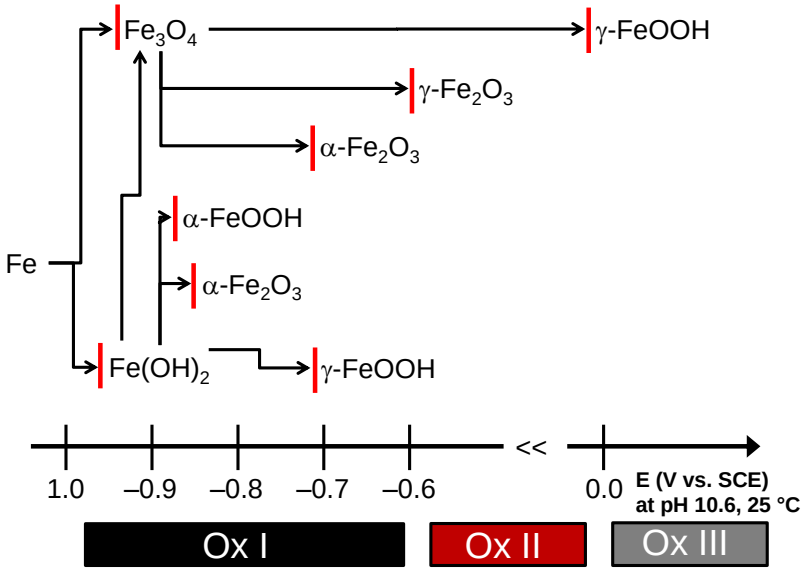

Figure 5.12: Calculated equilibrium potentials for various iron redox reactions (at pH 10.6 and 25ºC) are indicated by vertical lines and oxidation potential regions are indicated at the bottom of the figure.

Variations in temperature do not significantly affect the equilibrium potentials of the redox reactions of solid pairs. The relative positions of the equilibrium potentials also do not change with pH since a change in pH shifts all of the equilibrium potentials by an equal amount for a redox process involving an H^+/e^- ratio of one. All redox reactions presented in Figure 5.12 have this ratio.

Figure 5.13 shows the corrosion potentials that are reached after several hours of corrosion in 10 mM borate solutions with variable pH and temperature.

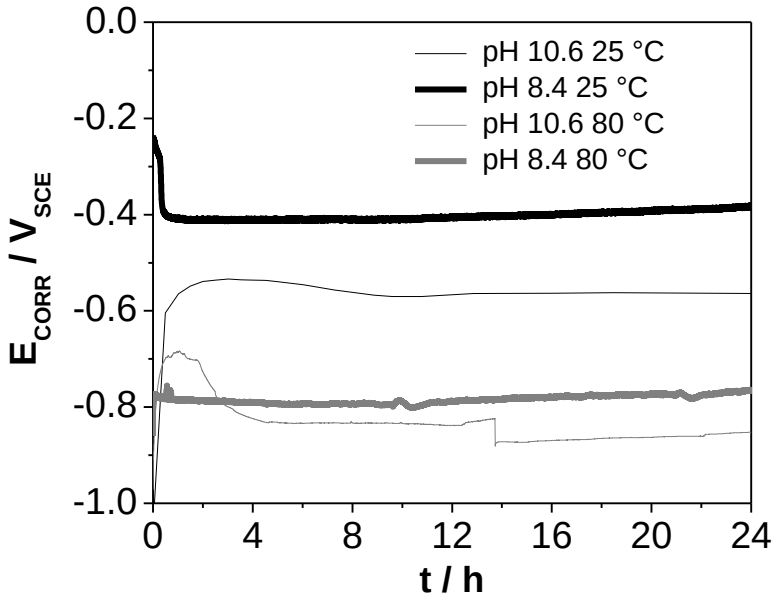

Figure 5.13: Corrosion potential as a function of time for carbon steel in $pH_{25°C}$ 10.6 and 8.4 borate solutions at 25 °C and 80 °C.

The corrosion potential is the potential measured at the outer surface, in this case the oxide/water interface. The overpotential,η, at the metal/metal oxide interface, the difference between the potential at this interface and the equilibrium potential for a metal redox pair, determines the metal oxidation rate. Due to the potential drop across the oxide, the corrosion potential is not the same as the potential at the metal/oxide interface (illustrated schematically in Figure 5.14). Thus, the oxidation potential will be less than the measured corrosion potential. Figure 5.13 shows that the corrosion potential on a coupon in 10 mM borate at 80 °C in pH 10.6 and pH 8.4 solutions is approximately –0.85 V_{SCE} and –0.78 V_{SCE} respectively. Since the potential at the metal/oxide interface can only reach a value in Ox I in deaerated solutions, independent of temperature and pH,

the oxide that can grow is limited mainly to $FeO/Fe(OH)_2$ or Fe_3O_4, Figure 5.12. The thermodynamics of the electrochemical reaction system puts constraints on the type of oxide that can grow on carbon steel.

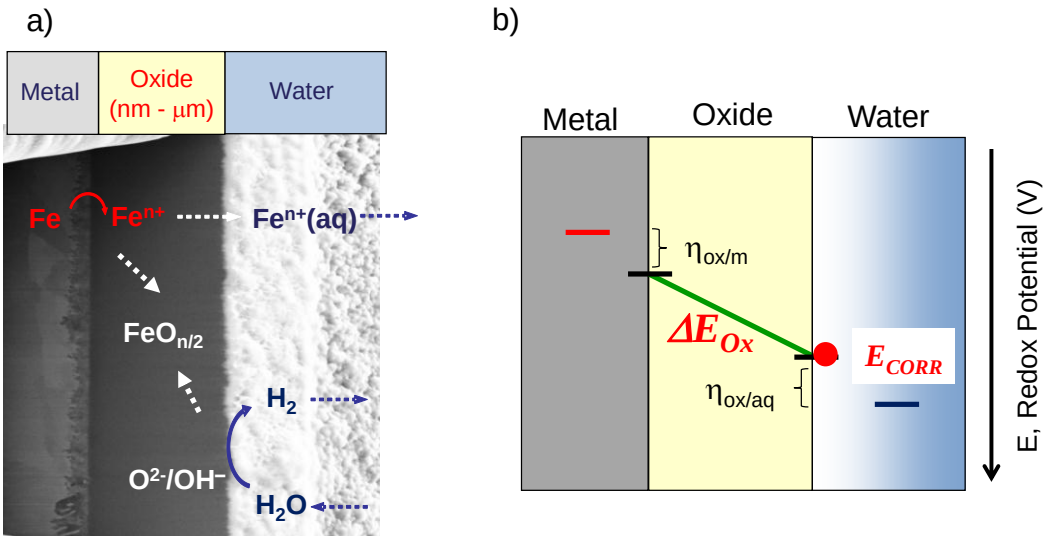

Figure 5.14: (a) Schematic of oxide film growth involving the injection of Fe^{n+} at the metal/oxide interface and O^{2-} at the oxide/aqueous interface and (b) potential drop, ΔE_{ox}, across the oxide and overpotentials, η, at both interfaces.

5.4.2 Competing Kinetics and Oxide Formation

5.4.2.1 Effects of Temperature and pH on Metal Solubility

The initial reaction when a clean, unreacted carbon steel surface is immersed in a deaerated solution is the oxidation of surface Fe to $Fe^{II}_{(aq)}$. Here, the label $Fe^{II}_{(aq)}$ refers to all soluble hydrated Fe^{II} species, presented below. This oxidation is coupled with a reduction of H_2O adjacent to the surface (or its acid or base ions) to form H_2:

$$Fe_{(s)} \leftrightarrows Fe^{II}_{(aq)} + 2\,e^- \qquad (5.1)$$

$$2\,H_2O_{(l)} + 2\,e^- \leftrightarrows 2\,OH^-_{(aq)} + H_{2(g)} \qquad (5.2)$$

The $Fe^{II}_{(aq)}$ is in acid-base equilibrium as:

$$Fe^{II}_{(aq)} \equiv (Fe^{2+}_{(aq)} + Fe(OH)^{+}_{(aq)} + Fe(OH)_2^{-}{}_{(aq)}) \quad (5.3)$$

$$Fe^{2+}_{(aq)} \leftrightarrows Fe(OH)^{+}_{(aq)} \leftrightarrows Fe(OH)_2^{-}{}_{(aq)} \quad (5.4)$$

The dissolved iron species are in equilibrium with solid $Fe(OH)_{2(s)}$, and, as a consequence, the solubility of $Fe(OH)_{2(s)}$ is a strong function of pH. The solubility of $Fe(OH)_{2(s)}$ at pH 10.6 is more than four orders of magnitude smaller than it is at pH 6.0 at room temperature, Figure 5.15 [36]. Therefore, solution pH has a large influence on the metal dissolution rate.

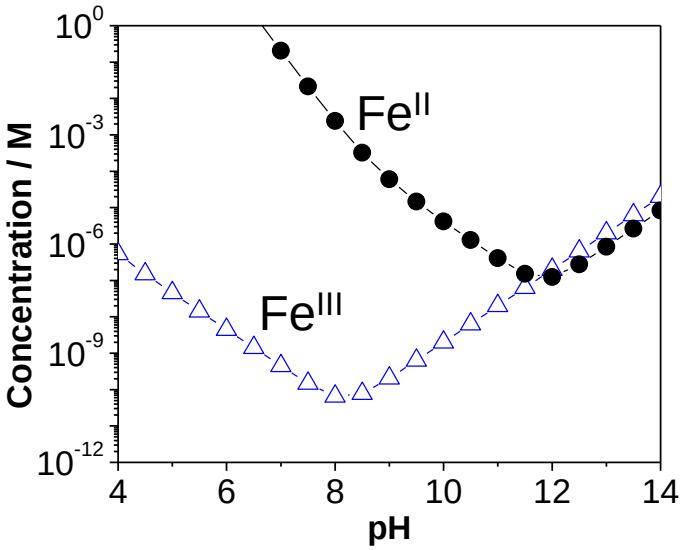

Figure 5.15: Solubility of hydrolyzed Fe^{II} and Fe^{III} as a function of pH at 25 °C.

Temperature also affects the solubility of $Fe(OH)_{2(s)}$. In general, increasing temperature leads to increased solubility. However, due to the complexity of iron metal oxy/hydroxide systems and the insufficiently well known temperature dependences of the

thermodynamics of the various hydrated equilibrium partners, the temperature dependences of the solubilities of Fe^{II} and Fe^{III} hydroxides are not well known above room temperature [37, 38].

The solubilities of the more stable iron oxides, such as Fe_3O_4, are better defined at elevated temperatures. The pH dependence of Fe_3O_4 solubility is very similar to the solubility of the summation of all $Fe^{II}_{(aq)}$ and $Fe^{III}_{(aq)}$ species in acid-base equilibrium at 25 °C, Figure 5.15. The combined solubility (simple arithmetic average) has a minimum between pH 10 and 11 [39]. For Fe_3O_4, as temperature is increased, the solubility minimum of shifts to a lower pH (approximately 1.5 pH unit per 100 °C increase). At the same time the solubility increases by approximately five times per 100 °C increase [39]. The combined solubilities of $Fe^{II}_{(aq)}$ and $Fe^{III}_{(aq)}$, are expected to follow similar trends with the solubility minimum shifting to a lower pH and increasing in magnitude.

5.4.2.2 Effect of pH on Oxide Growth

Corrosion starts with the conversion of Fe^0 to Fe^{II} at the metal/water interface. Some of this Fe^{II} will dissolve to form $Fe^{II}_{(aq)}$. As the concentration of $Fe^{II}_{(aq)}$ grows in the metal/water interface region, some will diffuse into solution and some will come out of solution as solid $Fe(OH)_{2(s)}$ which will condense on the adjacent solid surface. Initially this will be on a bare metal surface, but that will quickly be covered by a layer of metal oxide if the oxide solubility is low, as is the case for iron at high pH (at or above pH 8.4). Due to the thermodynamic stability of Fe_3O_4, the initially formed $Fe(OH)_{2(s)}$ can be converted by further oxidation to a mixed Fe^{II} and Fe^{III} oxide (i.e. Fe_3O_4) at a fast rate. The metal oxidation prior to the film deposition is limited to the reactive sites, i.e., the

grain boundaries, which can result in a dependence on the underlying microstructure on growth of the interfacial layer. There did appear to be some evidence that in pH 10.6 0 mM borate, the interfacial layer, which was thickest in this case (Table 5.3), had a directional growth, Figure 5.10b. The fast initial oxidation results in the carbon steel surface being quickly covered by a uniform layer (largely composed of Fe_3O_4). Once a uniform layer is established, the rate of further oxidation may be controlled by mass and charge transport through the layer and this slows down the metal oxidation rate. This results in horizontal growth of the layer that slowly evens out, creating a surface on which the electrochemical reactions occur uniformly. Further oxidation moves the front of the interfacial region, while the oxide grows.

At lower pHs (e.g., pH 6.0) the $Fe^{II}_{(aq)}$ solubility is higher. At this pH the condensation of $Fe(OH)_{2(s)}$ is not as favoured and more $Fe^{II}_{(aq)}$ will diffuse away from the metal/water interface into the bulk solution. This will result in the slower growth of a uniform layer on the metal, resulting in less impedance to mass and charge transport. Therefore; further metal oxidation will occur faster than at a higher pH. A fraction of the $Fe^{II}_{(aq)}$ can also be oxidized to $Fe^{III}_{(aq)}$. The solubility of hydrated $Fe^{III}_{(aq)}$ at pH 6.0 is much lower than the solubility of $Fe^{II}_{(aq)}$ and would favour the formation of a species like α-$FeOOH_{(s)}$. However, when the concentrations of hydrated Fe^{II} and Fe^{III} species near the metal/water interface eventually reach the solubility limit of Fe_3O_4, formation of this thermodynamically more stable species will be favoured, and condensation of Fe_3O_4 particulates on the surface will occur. The surface coverage of the Fe_3O_4 particulates is thus not uniform initially. As corrosion proceeds the particulates accumulate, coalesce, and eventually form a Fe_3O_4 layer, however, the rate to obtain surface coverage is slower

than pH 10.6. The cross section of the oxide film formed this way is very porous and uneven, Figures 5.10c and 5.11b.

The pathway for oxidation can vary with pH. At high pHs (pH 8.4 and 10.6) low iron oxide solubility leads to the early formation of an interfacial layer which controls further oxidation. At lower pHs (pH 6.0) high iron oxide solubility delays uniform film growth and the oxide largely forms from the coalescing of large Fe_3O_4 crystals. This results in a much more porous oxide film that is much less protective, allowing relatively higher rates of mass and charge transport through the film. The oxide would be less protective of the underlying metal and this will further drive Fe oxidation. The effect of the lack of protection due to porosity can be seen through the large range in oxide thickness at 170 h (500 - 2000 nm) and the uneven base metal structure, Figure 5.11.

At all pHs, for long term oxide growth, the metal dissolution is limited to the dissolution of the outer surface, and thus depends on the combined rates of surface hydration and the diffusion of the hydrated metal ion species.

5.4.2.3 Effect of Temperature on Oxide Growth

Increasing temperature leads to an increase in the rate of corrosion and the thicknesses of the oxide films that are grown for the temperatures studied. At pH 10.6 a uniform, compact, and thin oxide film is formed at 80 °C (< 10 nm after 170 h). At 150 °C the oxide film is much thicker, but still uniform and compact (hundreds of nm to a few μm). The composition of these films was independent of the electrolyte.

At pH 8.4, the films grown at different temperatures varied. At 80 °C uneven Fe_3O_4 deposits formed. At 150 °C, a more uniform interfacial layer was formed upon

which further growth occurred via a similar oxidation mechanism to that at pH 10.6. The differences in film formation at pH 8.4 may be due to the contribution of the Schikorr reaction [40]:

$$3\,Fe(OH)_2 \rightarrow Fe_3O_4 + 2\,H_2O + H_2 \quad (5.5)$$

This reaction will occur with $Fe(OH)_{2(s)}$ on the metal coupon surface and will be faster at 150 °C than at 80 °C, accelerating the formation of a uniform Fe_3O_4 layer. After the formation of a uniform Fe_3O_4 layer and over prolonged oxide film growth, temperature largely influences processes related to dissolution by both increasing the rate of surface hydration as well as the diffusion rate. This can be seen in surfaces at 150 °C, which showed a filament-like surface structure, most likely resulting from an increased rate and preferential dissolution of $Fe^{II}_{(aq)}$ from the oxide surface [41], (Figure 5.6) and Raman spectra (Figure 5.8), which showed the increased presence of a range of surface hydrated species.

5.4.2.4 Effect of Electrolyte Concentration on Oxide Growth

In tests, the electrolyte concentration was altered by changing the concentration of a dissolved sodium borate buffer. The borate ion concentration affects the ionic strength of an aqueous solution. This affects the Debye length, or the characteristic thickness of the electric double layer at an interface, with a higher concentration electrolyte resulting in a thinner double layer [42]. This change in the double layer thickness affects the potential distribution across the oxide/solution region and the charge transport behaviour in the double layer region. Additionally, a thinner double layer can lead to a steeper diffuse layer (concentration gradient) at the interface and increase the rate of mass

transport of a metal cation away from the charged surface. The net effect of changing the electrolyte concentration will depend on the relative contributions of the potential-dependent metal oxidation rate and the metal cation mass transport rate to the net corrosion rate.

During the initial stage of corrosion on carbon steel, the metal oxidation rate is partially limited by the mass transport rate of the metal cation away from the interface, particularly at higher pHs. Thus, an increase in the electrolyte concentration decreases the thickness of the interfacial layer and increases the rate of metal dissolution. However, once a uniform oxide film is formed, the rate of charge transport through the oxide film to the water interface is slowed and the rate of metal ion mass transport away from the interface is no longer rate determining. At 80 °C for all pH 10.6 samples the rate of the oxide film growth is observed to be nearly linear over 20 h to 170 h, Figure 5.4. The rate of the film growth is slightly slower in a higher electrolyte concentration solution. The decrease in film growth rate means either that the net metal oxidation rate decreases or that the net metal oxidation rate remains the same but the metal dissolution is promoted preferentially over the oxide growth in a higher electrolyte concentration solution. As a result we observed that at pH 10.6 and 80 °C the oxide thickness decreased with an increase in borate concentration in solution. As well, the amount of iron dissolved in solution was higher in a 10 mM borate solution than in lower concentration borate solutions. Similar trends were observed at 150 °C. The effect of electrolyte concentration on the surface hydration and dissolution of the hydrated species from the oxide surface resulted in subtle changes in the morphology of corrosion at pH 10.6, Figure 5.6. Also, comparison of the interfacial region and the oxide films formed in 0

and 10 mM borate solutions at pH 10.6 (Table 5.3) show that films were thinner in the higher concentration borate solutions.

5.5 CONCLUSIONS

The oxide formed on carbon steel in deaerated water is Fe_3O_4, independent of pH, temperature and electrolyte concentration, over the ranges tested. However, the growth rate kinetics, morphology, thickness of the oxide film, and the amount of metal ion dissolution depend on the solution parameters. The varying solution parameters affected both the initial reactions on the bare metal surface and the long term corrosion of a growing oxide film.

Increasing the temperature increases the rate of iron dissolution, but it also accelerates the formation of Fe_3O_4 via the Schikorr reaction and this results in thicker oxide films. At pH 10.6, the oxide film formed on carbon steel is compact and uniform and does not show any localized corrosion, whereas at pH 6.0 the surface film formed is more porous and uneven. Metal dissolution decreases with an increase in pH and this is due to the pH dependence of the solubilities of ferrous and ferric ions. The low iron hydroxide solubility at pH 10.6 results in the fast formation of a uniform, thin layer. Higher electrolyte concentrations lead to a thinner oxide film and an increased amount of dissolved metal. This is attributed to the influence of the electrolyte concentration on the double layer at the metal/water interface. The change in the double layer structure affects the potential distribution across the interfacial region and the charge transport behaviour in the diffuse double layer region. The net effect is an increase in metal dissolution and a decrease in the oxide growth rate. The implication of the results is that changing solution

parameters not only affects the rates of various processes involved in the corrosion process, but it may also affect the mechanism pathway under which corrosion occurs.

5.6 REFERENCES

[1] P. Schmuki, J. Solid State Electrochem., 6 (2002) 145-164.
[2] C.L. Foley, J. Kruger, C.J. Bechtoldt, J. Electrochem. Soc., 114 (1967) 994-1001.
[3] N. Sato, K. Kudo, T. Noda, Electrochim. Acta, 16 (1971) 1909-1921.
[4] A. Hugot-Le Goff, C. Pallotta, J. Electrochem. Soc., 132 (1985) 2805-2806.
[5] A. Hugot-Le Goff, J. Flis, N. Boucherit, S. Joiret, J. Wilinski, J. Electrochem. Soc., 137 (1990) 2684-2690.
[6] G.L. Song, C.N. Cao, S.H. Chen, Corros. Sci., 47 (2005) 323-339.
[7] K.-S. Jung, L.d. Pierrefeu, Corros. Sci., 52 (2010) 817-825.
[8] G.G. Long, J. Kruger, D.R. Black, M. Kuriyama, J. Electrochem. Soc., 130 (1983) 240-242.
[9] B.D. Cahan, C.-T. Chen, J. Electrochem. Soc., 129 (1982) 474-480.
[10] C.-T. Chen, B.D. Cahan, J. Electrochem. Soc., 129 (1982) 17-26.
[11] M. Nagayama, M. Cohen, J. Electrochem. Soc., 109 (1962) 781-790.
[12] J. Gui, T.M. Devine, Corros. Sci., 138 (1991) 1105-1124.
[13] A.J. Davenport, M. Sansone, J. Electrochem. Soc., 142 (1995) 725-730.
[14] S.P. Harrington, F. Wang, T.M. Devine, Electrochim. Acta, 55 (2010) 4092-4102.
[15] S.J. Ahn, H.S. Kwon, Electrochim. Acta, 49 (2004) 3347-3353.
[16] A.J. Davenport, L.J. Oblonsky, M.P. Ryan, M.F. Toney, J. Electrochem. Soc., 147 (2000) 2162-2173.
[17] J. Robertson, J.E. Forrest, Corros. Sci., 32 (1991) 521-540.
[18] T. Satoh, Y. Shao, W. Cook, D.H. Lister, S. Uchida, Corros., 63 (2007) 770-780.
[19] Z.F. Yin, Y.R. Feng, W.Z. Zhao, Z.Q. Bai, G.F. Lin, Surf. Interface Anal., 41 (2009) 517-523.
[20] N.R. Smart, Corros., 65 (2009) 195-212.
[21] F. King, C. Padovani, Corros. Eng. Sci. Technol., 46 (2011) 82-90.
[22] A.P. Grosvenor, B.A. Kobe, N.S. McIntyre, Surf. Sci., 572 (2004) 217-227.
[23] A.P. Grosvenor, B.A. Kobe, M.C. Biesinger, N.S. McIntyre, Surf. Interface Anal., 36 (2004) 1564-1574.
[24] A.P. Grosvenor, B.A. Kobe, N.S. McIntyre, Surf. Sci., 565 (2004) 151-162.
[25] R.M. Cornell, U. Schwertmann, The Iron Oxides: Structures, Properties, Reactions, Occurrences and Uses, 2nd Ed., Weinheim, New York, NY, (2003).
[26] T.A. Carlson, G.E. McGuire, J. Electron Spectrosc. Relat. Phenom., 1 (1972) 161-168.
[27] B.R. Strohmeier, Surf. Interface Anal., 15 (1990) 51-56.
[28] O.N. Shebanova, P. Lazor, J. Solid State Chem., 174 (2003) 424-430.
[29] X. Zhang, W. Xu, D.W. Shoesmith, J.C. Wren, Corros. Sci., 49 (2007) 4553-4567.
[30] L.J. Oblonsky, T.M. Devine, Corros. Sci., 37 (1995) 17-41.

[31] R. Heidersbach, Metallurgy and Corrosion Control in Oil and Gas Production, John Wiley & Sons, Hoboken, NJ, (2011).
[32] S.J. Oh, D.C. Cook, H.E. Townsend, Hyperfine Interact., 112 (1998) 59-66.
[33] J. Dunnwald, A. Orro, Corros. Sci., 29 (1989) 1167-1176.
[34] S. Osgerby, Mater. High Temp., 17 (2000) 307-310.
[35] T. Misawa, Corros. Sci., 13 (1973) 659-676.
[36] C.F. Baes Jr., R.E. Mesmer, The Hydrolysis of Cations, Krieger Publishing Co., Florida, USA, (1986).
[37] C.F. Baes Jr., R.E. Mesmer, Am. J. Sci., 281 (1981) 935-962.
[38] R.H. Byrne, Y.-R. Luo, R.W. Young, Mar. Chem., 70 (2000) 23-35.
[39] B. Beverskog, I. Puigdomenech, Corros. Sci., 38 (1996) 2121-2135.
[40] G. Schikorr, Z. Anorg. Allg. Chem., 212 (1933) 33–38.
[41] D.S. Mancey, D.W. Shoesmith, J. Lipkowski, A.C. McBride, J.J. Noël, J. Electrochem. Soc., 140 (1993) 637-642.
[42] P.H. Rieger, Electrochemistry, Chapman & Hall, New York, NY, (1994).

Chapter 6

Varying Effect of γ-Irradiation on Carbon Steel Corrosion Depending on Solution pH, Temperature and Electrolyte Concentration

6.1 INTRODUCTION

The electrochemical studies at room temperature and pH 10.6, Chapter 4, showed regardless of initial sample oxidation, the corrosion potential of carbon steel increased by roughly 0.6 V when exposed to gamma irradiation. The increase in corrosion potential was also accompanied by an increase in Fe^{III} content in the oxide and an increase in oxide film resistance. The changes in potential and oxide structure were attributed to the formation of H_2O_2 via water radiolysis.

In Chapter 5, carbon steel coupon corrosion experiments were performed without irradiation under a number of ranging solution conditions: temperature (80 °C and 150 °C), $pH_{25°C}$ (6.0, 8.4 and 10.6) and electrolyte concentration (0, 1 and 10 mM borate). In this Chapter, identical experiments have been performed with exposure to gamma irradiation in order to isolate the effects of gamma irradiation, and specifically, water radiolysis, on the oxidation mechanism of carbon steel. Additional experiments were performed with the chemical additions of an oxidant, O_2, to compare to the effects of bulk phase water radiolysis.

6.2 EXPERIMENTAL

The experimental setup and procedure is identical to that reported in the absence of irradiation, Chapter 5. The only difference for these experiments was the use of two different cover gases and a gamma irradiation source. The irradiation of the system

began as the system was heated. As in Chapter 5, all pHs are with respect to measurement at 25 °C. The final pH measured after experiments for all solutions were similar to the equivalent experiments without radiation, Table 6.1.

Table 6.1: Changes in pH for all solutions studied.

80 °C												
Initial pH	8.4			10.6			10.6					
Borate (mM)	10			1			10					
Time (h)	20	66	170	20	66	170	20	66	170			
Final pH	8.7	8.7	8.6	9.9	9.6	9.5	10.2	10.2	9.9			
150 °C												
Initial pH	6.0			8.4			10.6			10.6		
Borate (mM)	0			10			0			10		
Time (h)	20	66	170	20	66	170	20	66	170	20	66	170
Final pH	7.3	6.4	6.1	nd[1]	nd[1]	8.7	8.7	8.3	8.7	9.9	9.9	9.8

1. not determined

6.2.1 Cover Gas

6.2.1.1 Argon Cover Gas

For deaerated experiments, the placement of the coupons in the vials, addition of solution, loading of the pressure vessel, and sealing of the pressure vessel occurred inside an Ar-purged glove box. Unless specifically noted, all experiments were under deaerated conditions.

6.2.1.2 Oxygen

For aerated experiments, the solutions were pre-purged with hydrocarbon free air, 21 % O_2, (Praxair) and the placement of coupons in the vials, addition of solution, and sealing of system was done in an open atmosphere environment.

6.2.2 Gamma Radiation Source

All irradiation experiments were conducted in a MDS Nordion Gammacell 220 Excel Cobalt-60 irradiator. The vessel was positioned inside the gammacell sample chamber, and the chamber was lowered into the gammacell irradiation zone, consisting of 11 tubular pencils containing ^{60}Co. The dose rate during the period of experimentation was ~5.5 $kGy \cdot h^{-1}$.

6.3 RESULTS

6.3.1 Corrosion at 80 °C

6.3.1.1 Effect of Radiation and Electrolyte Concentration at pH 10.6

The SEM micrographs of the surfaces corroded in the absence and the presence of γ-radiation are compared in Figure 6.1. Although the surfaces corroded for 20 h and 170 h were also examined, only 66 h results are presented. Under a given set of solution conditions, the surface morphology did not change significantly with corrosion time. At pH 10.6 and 80 °C, the surfaces corroded in the absence and presence of radiation are very similar, Figure 6.1. The surfaces are largely featureless with polishing marks still visible on all of the surfaces, indicating the oxide films are very thin. The density of small pin-holes is much smaller on the irradiated samples than unirradiated samples. The origin of the 'pin-holes' is not completely clear. However, the diameters of the holes are nearly the same and the presence of these holes has no visible effect on the neighbouring areas.

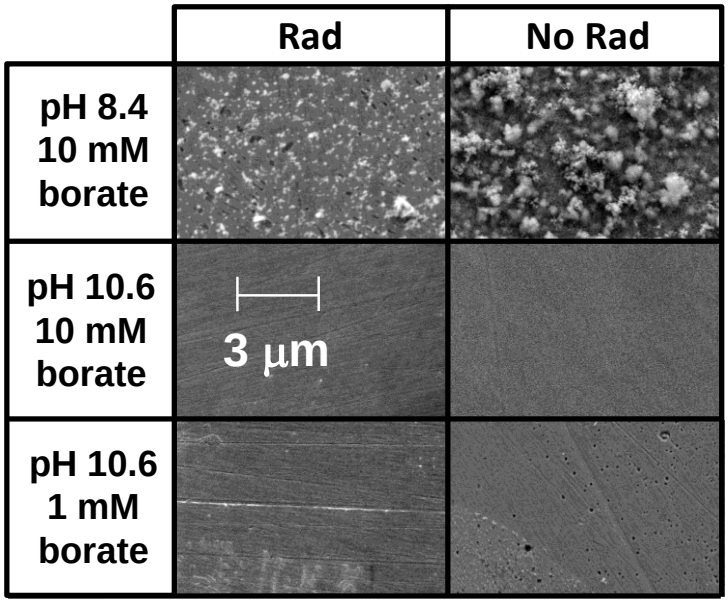

Figure 6.1: SEM micrographs of the carbon steel coupon surfaces after 66 h in all solutions at 80 °C for irradiated and unirradiated experiments.

The oxide film thickness analyzed using XPS as in Chapter 5 and as previously reported [1-3] is shown in Figure 6.2. The results obtained for irradiated samples are compared with those without radiation. At pH 10.6 under irradiation conditions the oxide thickness initially increased with time but the oxide growth slows down and there is very little change in the thickness between the samples corroded for 66 h and 170 h. Under unirradiated conditions, the oxide growth increased initially at a slower rate, but the growth continued at a linear rate up to 170 h, the longest time studied. Thus, at shorter times (20 h), a thicker oxide is formed on the irradiated carbon steel than on the unirradiated sample. However, at longer times the oxide formed on unirradiated carbon steel can grow thicker. Under both irradiated and unirradiated conditions, thicker oxides are formed in a lower electrolyte concentration solution. As proposed in the study in

Chapter 5, the increase in electrolyte concentration preferentially increases the dissolution over the solid oxide formation from the oxidized metal.

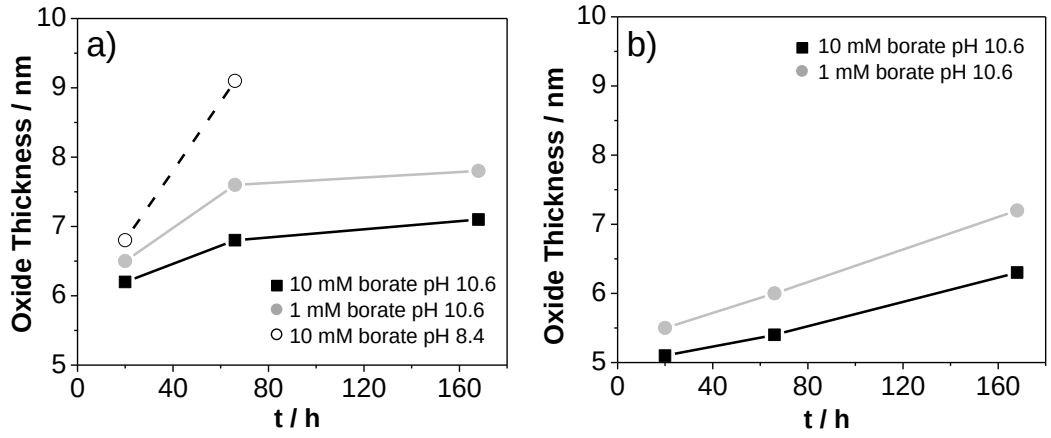

Figure 6.2: Fitting analysis of high-resolution Fe-2p XPS spectra to determine the thickness of a Fe_3O_4 oxide layer 80 °C for (a) irradiated and (b) unirradiated experiments.

The Raman spectra of the surfaces corroded for 170 h show a peak at ~ 670 cm^{-1}, Figure 6.3. Comparison of the spectra with the reference spectra taken with single-phases oxides indicate this oxide is mainly composed of Fe_3O_4 [4]. No other identifiable oxide peaks are present. The weak peak above 800 cm^{-1} has been previously observed in studies on iron and carbon steel oxidation at room temperature and has been attributed adsorbed carbon contamination originating from CO_2 [5, 6]. The increase in the background intensity at high wavenumbers was also seen in the no radiation case. Due to the thin oxide, reflective surface and poor scattering probability of Fe_3O_4, the Raman signals from the surfaces corroded under both irradiated and unirradiated conditions are very weak.

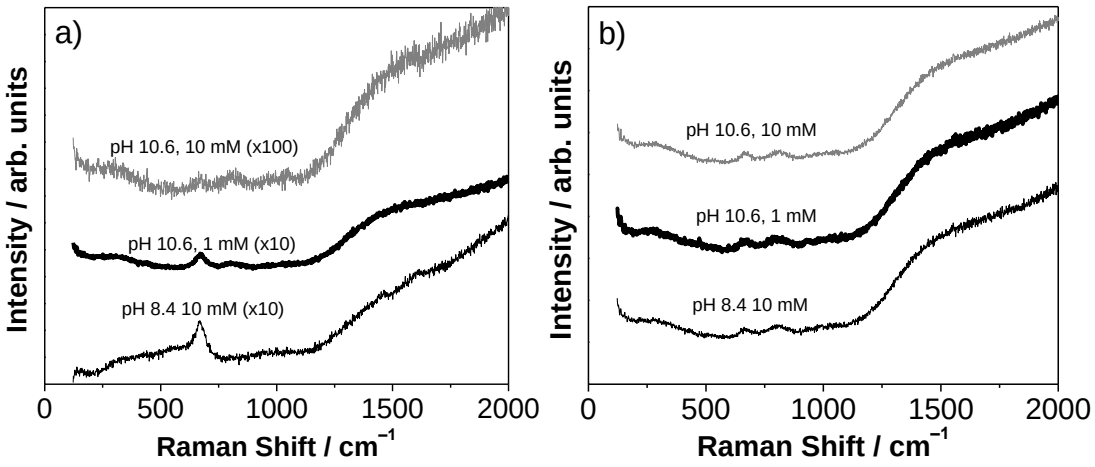

Figure 6.3: Sample Raman spectra of carbon steel coupon surfaces after exposure to all solutions at 80 °C for 170 h for (a) irradiated and (b) unirradiated experiments. The bracketed numbers are the magnification of the Raman intensity signal.

Measurements of the dissolved iron concentration after 170 h experiments, as determined by inductively-coupled plasma mass spectrometry (ICP-MS) analysis, are shown in Table 6.2. The dissolved metal ion concentration shows a small increase with an increase in electrolyte concentration under both irradiated and unirradiated cases. For a given electrolyte concentration, γ-irradiation also slightly increases the dissolved metal ion concentration.

Table 6.2: Iron concentration in solution after 170 h.

pH	Borate (mM)	Iron concentration (ppb)	
		Radiation	No Radiation
80 °C			
8.4	**10**	nd[1]	nd[1]
10.6	**1**	53	36
10.6	**10**	89	57
150 °C			
6.0	**0**	4500	3000
8.4	**10**	620	420
10.6	**0**	310	110
10.6	**10**	690	640

1. not determined

6.3.1.2 Effect of Radiation at pH 8.4

The effect of radiation at pH 8.4 and 80 °C was studied only in 10 mM borate solutions. Radiation had a more profound affect at this pH than at pH 10.6. The surface of the unirradiated sample shows large, unevenly distributed deposits on a more compact underlying layer, Figure 6.1. The surface of the irradiated sample shows the underlying compact layer more clearly, much smaller particulate deposits and higher density of small pin-holes. The Fe-2p band in the high resolution XPS of the unirradiated surface at pH 8.4 had no observable metallic Fe^0 component, suggesting that the oxide formed at as early as 20 h is thicker than ~15 nm, the analysis depth of the XPS. On the other hand, the oxide on irradiated carbon steel (Figure 6.2) was thinner than 10 nm for the 20 h and 66 h corroded samples and thicker than 15 nm only for the 170 h corroded sample. The

Raman spectra of the samples corroded for 170 h under both irradiated and unirradiated conditions (Figure 6.3) show a peak at 670 cm^{-1}, corresponding to Fe_3O_4.

6.3.2 Corrosion at 150 °C

6.3.2.1 Effect of Radiation and Electrolyte Concentration at pH 10.6

The SEM micrographs of coupon surfaces at a low magnification are presented in Figure 6.4. The surfaces for both pH 10.6 solutions and all irradiation times were generally featureless with no areas of differing or localized corrosion. For the 10 mM borate solutions, the underlying microstructure was visible at 20 and 66 h, suggesting the oxide was thin enough to observe the microstructure. The underlying microstructure was also observed in 0 mM borate at 20 h (not shown). Similar results were seen for unirradiated samples. Additional high magnification SEM images for the 10 mM cases are compared to the unirradiated samples, showing a similar filament-like topology, Figure 6.5. A slight difference can be observed between the two cases, in which little to no change in surface topology was observed under radiation, while the filament-like structure underwent some changes with time, largely between 20 and 66 h, for the unirradiated case.

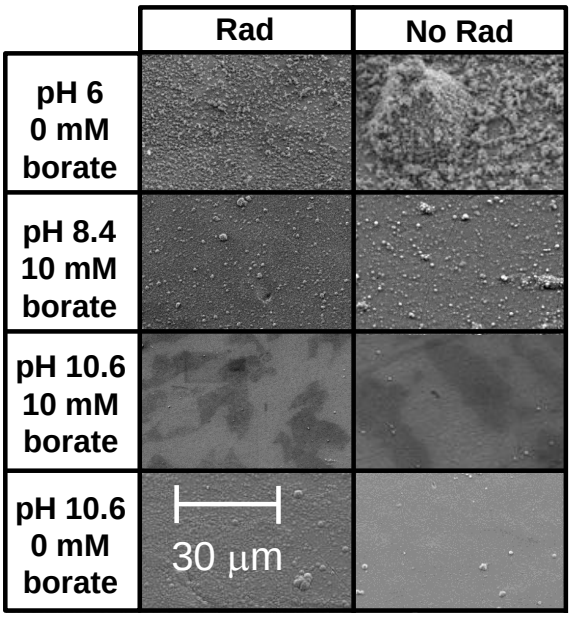

Figure 6.4: Low magnification SEM micrographs of the steel coupon surfaces after 66 h at 150 °C for irradiated and unirradiated experiments.

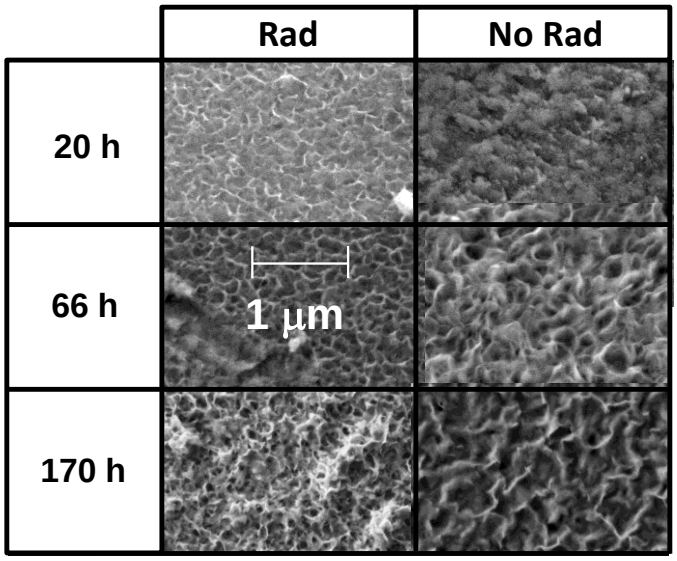

Figure 6.5: High magnification SEM micrographs of the steel coupon surfaces in pH 10.6 10 mM borate at 150 °C for irradiated and unirradiated experiments.

Cross-section analysis was performed for 66 and 170 h samples. The cross-section morphologies were very similar to those without radiation. An example of the pH 10.6, 10 and 0 mM borate samples are shown in Figure 6.6.

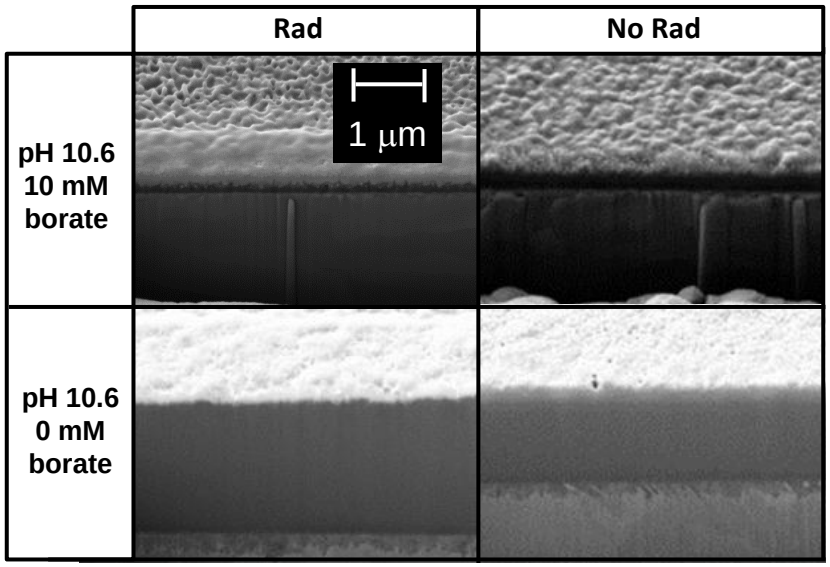

Figure 6.6: SEM images of the cross section of the carbon steel coupons subject to 170 h heating at 150 °C for pH 10.6 0 mM borate and pH 10.6 10 mM borate for irradiated and unirradiated experiments.

Analysis by TEM on the samples corroded for 170 h showed similar features to those observed with no radiation, Figure 6.7. An interfacial region, which was described in detail in the no radiation summary, was clearly observable in the 0 mM borate case. The thickness of the interfacial region and total oxide film determined from SEM and TEM are summarized in Table 6.3. The thicknesses from the no radiation samples are provided for direct comparisons. The trend of a thicker interfacial region corresponding to a thicker bulk oxide continued.

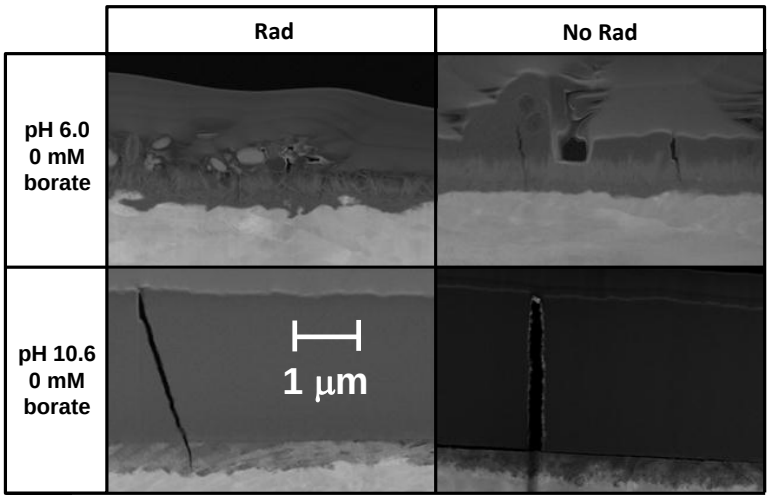

Figure 6.7: TEM images of the cross section of the carbon steel coupons subject to 170 h heating at 150 °C for pH 6.0 0 mM borate and pH 10.6 0 mM borate for irradiated and unirradiated experiments.

Raman analysis was performed for all samples and a comparison is shown for 66 h samples in Figure 6.8. They showed the oxide to be largely composed of Fe_3O_4 [4]. The only difference between the spectra were some differences in signal intensity, where lower intensities were seen for 10 mM borate cases compared to 0 mM borate cases. These differences mostly arise from varying surface roughness and thickness of the oxide.

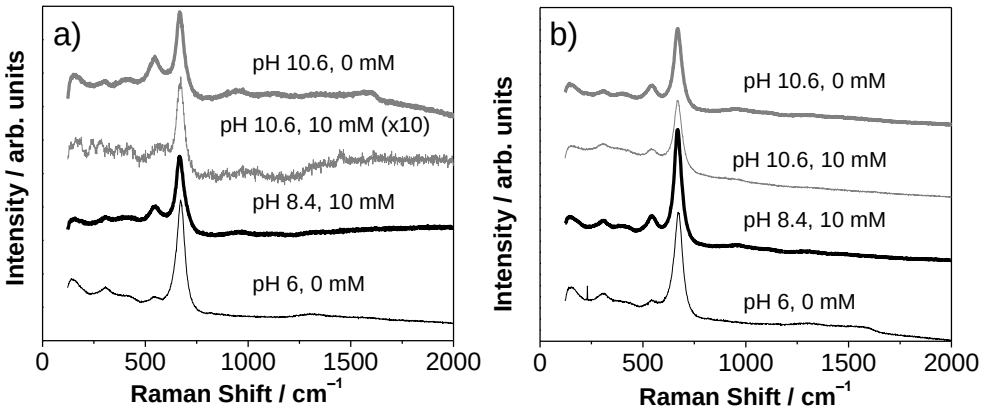

Figure 6.8: Raman spectra of carbon steel coupon surfaces after exposure for 66 h at 150 °C for (a) irradiated and (b) unirradiated experiments. Labelled are concentrations of borate and increase in magnification of intensity is indicated in brackets.

Measurements of the dissolved iron concentration after 170 h experiments, as determined by ICP-MS are shown in Table 6.2 and were found to be higher compared to the corresponding unirradiated cases.

Table 6.3: Oxide thickness for samples corroded at 150 °C.

pH	Borate (mM)	Oxide Film Thickness			
		Radiation		No Radiation	
		66 h	170 h	66 h	170 h
6.0	**0**	0.5-1.6 μm	2.0-3.2 μm	nd[1]	0.5-2.0 μm
8.4	**10**	nd[1]	1.0 μm (200 nm)[2]	1.5 μm	1.8 μm (170 nm)[2]
10.6	**0**	2.2 μm	2.9 μm (525 nm)[2]	1.5 μm	3.0 μm (400 nm)[2]
10.6	**10**	0.14 μm	0.20 μm (< 50 nm)[2]	0.35 μm	0.48 μm (< 50 nm)[2]

1. not determined
2. thicknesses of the metal/oxide interfacial region determined by TEM.

6.3.2.2 Effect of Radiation with Varying pH

The varying effect of radiation on carbon steel corrosion at 150 °C depending on pH was studied at pH 10.6 and pH 6.0 in 0 mM borate solutions, and at pH 10.6 and pH 8.4 in 10 mM borate solutions. The SEM images of the surfaces corroded for 66 h are compared in Figure 6.4 and cross-section morphologies are shown in Figure 6.9.

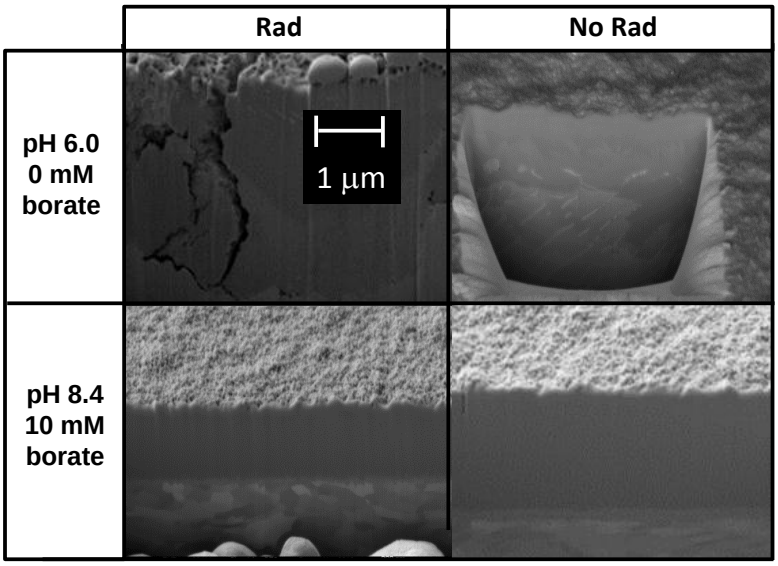

Figure 6.9: SEM images of the cross section of the carbon steel coupons subject to 170 h heating at 150 °C for pH 6.0 0 mM borate and pH 8.4 10 mM borate for irradiated and unirradiated experiments.

Compared to the uniform and even oxide at pH 10.6, at pH 6.0, octahedron-like deposits 500 nm to 1 μm in size were dispersed on the surfaces at all irradiation times. Mineral Fe_3O_4 commonly forms uniform octahedral crystals that can grow to many centimetres in size [7]. While some deposits were observed for pH 6.0 unirradiated samples, the deposits were less frequent and had a less defined shape. An additional

sample was analyzed for 20 h under irradiation in a solution of purely deionized water, pH 7.0. The oxide structure was identical to that observed at pH 6.0, Figure 6.10. Unlike at pH 10.6, the oxides at pH 6.0 were thicker than the corresponding unirradiated samples, Table 6.3.

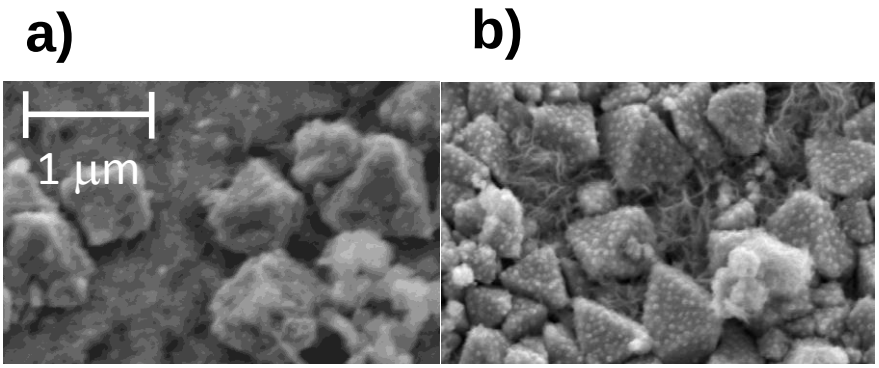

Figure 6.10: SEM micrographs of the steel coupon surfaces after 20 h at 150 °C in solutions of (a) pH 6.0 and (b) pH 7.0.

At pH 8.4, the surface had a similar flat and featureless surface to those at pH 10.6, except additional spots of oxide deposits were seen across the surface at all corrosion times, similar to the unirradiated samples, Figure 6.4. In 10 mM borate, the oxides at pH 8.4 were thicker than pH 10.6, but like at pH 10.6, the oxides were thinner than the corresponding unirradiated samples, Table 6.3.

6.3.3 Corrosion at 150 °C in Aerated Conditions

Aerated experiments were performed for pH 6.0 and 10.6, 0 mM borate samples both with and without radiation. Under aerated conditions, very little difference was observed between samples either with or without radiation, however differences were

observed from the deaerated samples. The SEM micrographs show a surface oxide of coalesced spheres with some platelets throughout, Figure 6.11. Raman spectra showed the presence of α-Fe_2O_3 Figure 6.12.

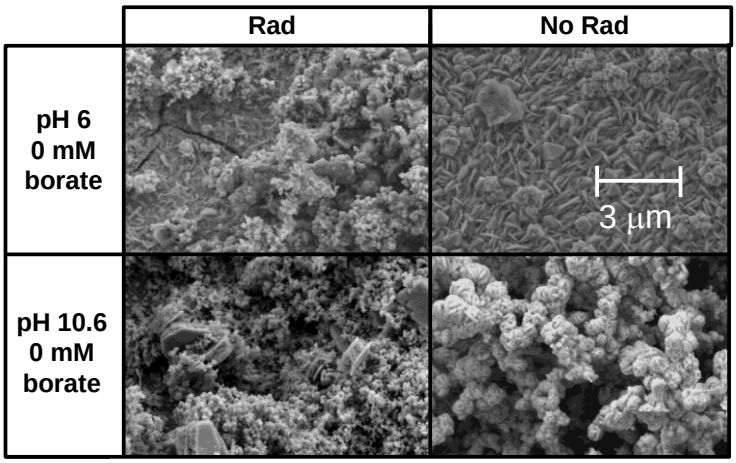

Figure 6.11: SEM micrographs of the carbon steel coupon surfaces in aerated systems subject to 66 h heating at 150 °C for pH 10.6 0 mM borate and pH 6.0 0 mM borate for irradiated and unirradiated experiments.

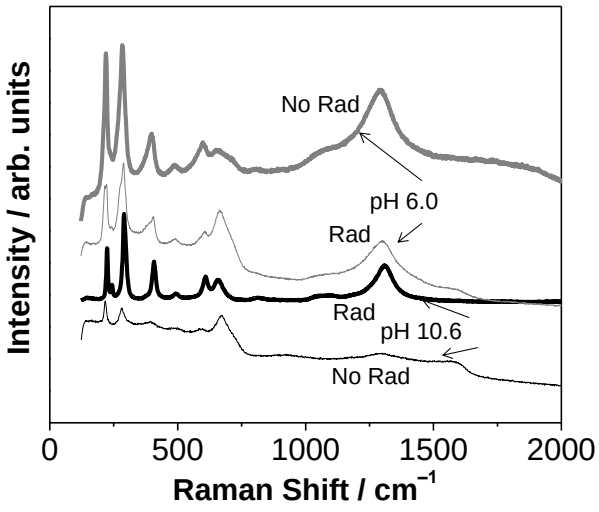

Figure 6.12: Raman spectra of the carbon steel coupon surfaces in aerated system after 66 h at 150 °C for irradiated and unirradiated experiments.

After a 66 h corrosion time, cross-section analysis was performed for pH 10.6 0 mM borate and found the oxide thickness to be 130 nm without radiation and 150 nm to 170 nm with radiation. Therefore, the oxide films in aerated conditions for pH 10.6, 0 mM borate had thicknesses that were approximately 10 % of the deaerated cases. Visually, the coupons showed non-uniform surfaces, Figure 6.13. At pH 6.0, the surface was covered with varying amounts of a brown and black oxide, and at 10.6 the corrosion products had a top orange-red oxide, which was likely α-Fe_2O_3, that flacked off when the coupon was removed from solution, exposing an underlying black oxide, likely Fe_3O_4.

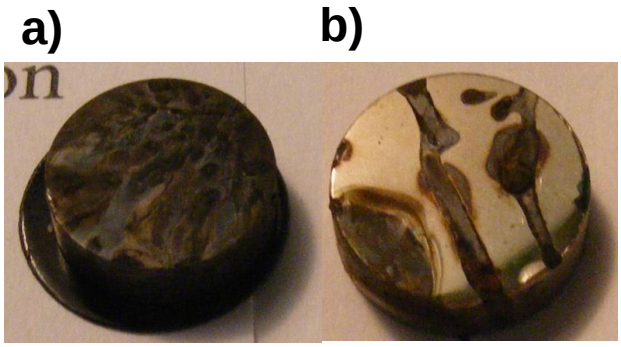

Figure 6.13: Photographs of the carbon steel coupon surfaces in aerated system after 66 h at 150 °C under radiation conditions.

6.4 DISCUSSION

In the previous study deconvoluting the effects of solution parameters, it was determined that the changing solution parameters can affect the relative rates of various corrosion related processes and as a result, affect which oxidation pathway is followed. The general oxidation process was seen to occur through the initial oxidation on a bare

metal surface, which at 150 °C resulted in the formation of a distinct metal/oxide interfacial layer, followed by further bulk oxide (Fe_3O_4) growth. Discussed below are the effects of irradiation on the initial oxidation process on the bare metal surface and on the prolonged oxide film growth, along with the coupled effects of changing solution parameters. Finally, the effects of two possible oxidants (H_2O_2 or O_2) are compared.

6.4.1 Initial Oxidation Process on a Bare Metal Surface

As discussed in Chapter 5, the initial oxide process involves horizontal growth of an interfacial region that slowly evens out, creating a surface on which the electrochemical reactions occur uniformly. The combined results suggested the interfacial region is a less dense Fe_3O_4 that is highly hydrated. The non-uniform nature, low density and dependence on solution conditions suggest that the initial oxide growth involves a dissolution and precipitation process. Under the highly oxidizing radiation conditions, the oxidation of a bare metal surface would be enhanced, with an increased level of iron dissolution and subsequently increased formation of the intial layer would be expected. Limited ICP-MS analysis, Table 6.2, showed a slight increase in iron concentration under irradiation conditions. The increase in iron concentration is likely resulting from the initial high overpotential on the bare metal surface, and initially high corrosion rates. In systems in which an initial uniform Fe_3O_4 layer forms (pH 8.4 and 10.6) the dissolution would be expected to drop significantly from the high rates on the bare metal surface. This also agrees with previous comparisons of steel corrosion under irradiation conditions, which found an initial spike in the corrosion rate of bare steel when exposed to gamma radiation. After the initial spike, the corrosion rates quickly

lowered to those similar to the unirradiated samples [8-10]. Also, as the interfacial region is established and irradiation continues to result in a higher net metal oxidation rate, the increase in metal oxidation rate not only results in increased dissolution, but also an increased injection of oxidized iron into the interfacial region. During bulk oxide growth, discussed below, the iron is further transported through the bulk oxide, either thickening the oxide, or eventually dissolving. An increase in net metal oxidation was observed in TEM micrographs, where the metal/oxide interfacial region was found to be thicker under irradiation cases compared to the corresponding unirradiated samples, Table 6.3.

At pH 6.0, the lack of a clear interfacial region was determined to result from the higher solubility of $Fe^{II}_{(aq)}$, Chapter 5. The relative solubility would not be affected by irradiation, and thus no difference was seen from the unirradiated sample. The oxide continued to be composed of a mixed filament-like structure, with no defined interfacial region, Figure 6.7.

6.4.2 Prolonged Growth of an Oxide Film

6.4.2.1 Effect of pH with Irradiation

At pH 10.6, the surface and cross-section morphologies were similar to those without radiation (a uniform and compact Fe_3O_4 oxide film grown on the initially formed interfacial region). However, the total oxide thicknesses were thinner under irradiation, Table 6.3. An exception to this is the 66 h, 0 mM borate case. As discussed previously in the study of electrolyte conditions, the rate of oxide growth and approach to steady state is influenced by electrolyte concentration. As time was extended to 170 h the radiation and no radiation coupons were of similar thickness in the 0 mM borate cases. It

appears as though after the initially accelerated corrosion rate on the bare metal surface, the rate of further oxidation dropped, compared to unirradiated samples, once a uniform Fe_3O_4 layer was formed. Similarly at 80 °C, the oxides initially grew thicker under irradiation conditions compared to unirradiated samples, Figure 6.2. However, as corrosion time progressed almost no change in thickness was observed between 66 h and 170 h for irradiated samples, while unirradiated samples showed linear oxide growth rates between 20 and 170 h. This suggests a faster approach to steady state under irradiation conditions. Additionally, at pH 10.6 and 150 °C under unirradiated conditions, the filament-like topology becomes more and more refined with time, suggesting preferential dissolution of certain sites from the oxide; for example, preferential dissolution of Fe^{II} over Fe^{III} from the mixed Fe^{II}/Fe^{III} oxide (Fe_3O_4) surface, Figure 6.5. Under irradiation conditions, the refined structure shows up early (at 20 h) but the size of the filaments did not significantly change with time, Figure 6.5. These observations suggest that the dissolution is initially high, but further dissolution is suppressed at later times under irradiation conditions and a faster approach to steady state occurs.

At pH 8.4 and 150 °C, the surface (Figure 6.4) and cross-section morphologies (Figure 6.9) were similar to those without radiation, however, the oxides were thinner, Table 6.3. At 80 °C the unirradiated and irradiated systems were markedly different. After 20 and 66 h, the oxide was observably thinner under irradiation (Figure 6.2) and the extent of deposits on the underlying surface was decreased significantly under irradiation, Figure 6.1. In unirradiated systems, the increase in deposits was attributed to an uneven Fe_3O_4 formation on the surface. Under irradiation, while the oxide continues to be

largely composed of Fe_3O_4 (Figure 6.3) the results suggest an increased rate in surface coverage, with slowed or suppressed further oxide growth.

At pH 6.0, where the solubility of $Fe^{II}_{(aq)}$ is higher, the oxide growth was identical to that without radiation, showing an uneven and porous oxide, with large octahedral Fe_3O_4 deposits. This was presumed to form from the high solubility of $Fe^{II}_{(aq)}$ (and to a lesser extent $Fe^{III}_{(aq)}$) , which eventually reaches the solubility limit of Fe_3O_4 near the metal/water interface and condensed out of solution. An additional experiment, performed with pH 7.0 deionized water, which would have similar solubilities of $Fe^{II}_{(aq)}$ and $Fe^{III}_{(aq)}$, showed an identical surface structure, Figure 6.10. At pH 6.0, a difference from the unirradiated experiments was an increase in the thickness of the oxide. As observed in the solution parameter study, the oxide formed at pH 6.0 is expected to provide limited passivity. For an oxide with limited passivity, or a small potential drop across the oxide, the increased overpotential due to water radiolysis products would be expected to increase the corrosion rate of the carbon steel. This resulted in an increased rate in Fe^0 to Fe^{II} oxidation. Additionally if the presence of oxidizing water radiolysis products increased the oxidation of $Fe^{II}_{(aq)}$ to $Fe^{III}_{(aq)}$ near the metal/water interface, the solubility limit of Fe_3O_4 would be achieved faster, resulting in increased Fe_3O_4 formation. This resulted in smaller, yet more defined Fe_3O_4 crystals (Figure 6.10) that further coalesced to create an oxide thicker than that observed without radiation, Table 6.3.

The pathway for oxidation can vary with pH. At high pHs (pH 8.4 and 10.6) low iron oxide solubility leads to the early formation of an interfacial layer, upon which bulk Fe_3O_4 oxidation occurs. At lower pHs (pH 6.0) high iron oxide solubility delays uniform film growth and the oxide largely forms from the coalescing of large Fe_3O_4 crystals. It is

clear that irradiation is affecting these two pathways differently. At high pHs irradiation is increasing the initial growth rate, yet supressing long term growth, while at low pHs irradiation is increasing the formation rate of an uneven Fe_3O_4 surface.

6.4.2.2 Effect of Temperature with Irradiation

The irradiation studies at room temperature in 10 mM borate solutions (Chapter 4) have shown that under gamma irradiation the corrosion potential of carbon steel increases, regardless of any initial oxide film on the steel surface. The increase in potential moves carbon steel from a region of oxidation forming Fe_3O_4 to a region where further oxidation of Fe_3O_4 to γ-Fe_2O_3 can occur. Electrochemical and surface analysis showed the relative amount of Fe^{III} content in the oxide film to increase and the resistance of the oxide film to increase. The increase in corrosion potential was determined to be due to H_2O_2, which is produced by water radiolysis. At room temperature, irradiation was able to provide enough energy to the system to increase the corrosion potential from a described Ox I to the higher potential end of a described Ox II, Figure 6.14.

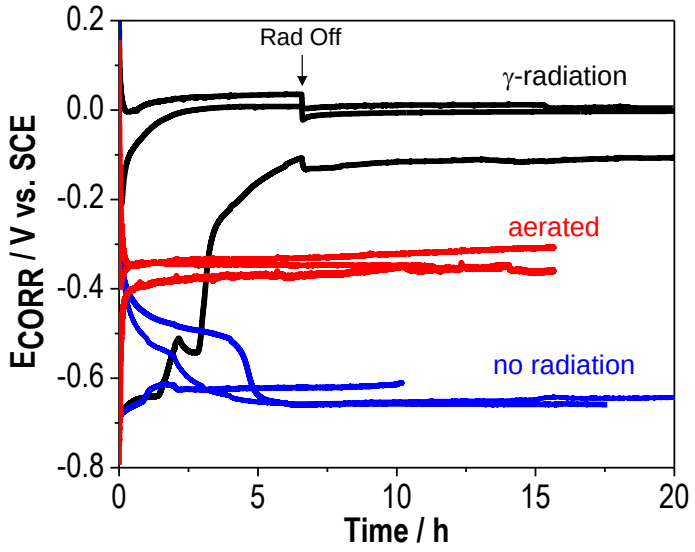

Figure 6.14: Corrosion potential as a function of time for carbon steel in $pH_{25°C}$ 10.6 borate solutions at 25 °C in deaerated solutions, aerated solutions, and under gamma irradiation.

It is clear that gamma irradiation at 80 °C and 150 °C is not resulting in the formation of distinct Fe^{III} oxide phases, as appeared to be the case at room temperature. However, there may be a less noticeable effect of limited Fe^{II} to Fe^{III} oxidation at the Fe_3O_4/solution interface. While not forming a distinct Fe^{III} phase, a limited oxidation may induce some passivity and somewhat limit further oxidation or dissolution. At elevated temperatures, the thermal favourable formation of Fe_3O_4, partially via the Schikorr reaction, appears to be hindering the significant change in passivation observed at room temperature. In a sense, there is a competition between the energy input of increasing temperature and the energy input from gamma irradiation.

One possible indication of increased Fe^{III} density from irradiation can be seen in the Raman spectra. A secondary Raman peak for Fe_3O_4 at approximately 540 cm^{-1} is

related to asymmetric vibration of Fe^{3+} and O^{2-}, with no bivalent cation involvement [4] and the exact position can vary somewhat in literature [4, 11]. The peak centred around 530 - 560 cm^{-1} has also been observed during in-situ Raman spectroscopic studies during electrochemical formation of passive films on iron in borate solutions by Harrington et al. [12]. They attributed this peak to an undetermined Fe^{III}oxide/hydroxide (i.e., partially-hydrated Fe^{III} species) on the surface of an anodically-grown Fe_3O_4/γ-Fe_2O_3 layer. Irrespective of the role of the partially-hydrated Fe^{III} species, their studies show that a passive oxide layer on Fe_3O_4 is essential for the peak at 540 - 560 cm^{-1}. For samples at 150 °C in which clear Raman spectra were observed in both the irradiated and unirradiated experiments, the ratio of the Raman peaks at 540 and 670 cm^{-1} as a function of pH and time was determined, Table 6.4.

Table 6.4: Ratio of the Raman intensities at 540 cm^{-1} and 670 cm^{-1}

pH	Borate (mM)	I_{540}/I_{670}			
		Radiation		No Radiation	
		20 h	66 h	20 h	66 h
6.0	**0**	0.08	0.08	0.01	0.08
10.6	**0**	0.29	0.45	0.25	0.25
10.6	**10**	0.30	0.27	0.31	0.10

For the pH 10.6, 0 mM borate samples, the ratio did not change much with time without radiation and increased greatly with radiation, leading to a much higher ratio with radiation than without radiation at 66 h. While again, a much higher ratio with radiation compared to that without radiation is observed for the 10 mM borate case, the change from 20 h is different. The ratio dropped in the unirradiated cases from 20 to 66 h, while

there was very little change with time for the irradiated cases. This difference in time effects for 10 mM and 0 mM borate at pH 10.6 is not clear. The difference in ratios observed may result from the crystallinity of the Fe_3O_4 layer, since the relative amorphous/crystalline nature of the oxide can affect the relative intensity of a minor peak of Fe_3O_4 at approximately 540 cm^{-1} [4]. At pH 6.0 a difference was observed at 20 h, however no difference is seen at 66 h. While perhaps qualitative, it does provide evidence of Fe_3O_4 oxidation under irradiation conditions. With increased oxidation of Fe^{II} to Fe^{III} and the formation of a more "γ-Fe_2O_3-like" surface oxide layer, a certain level of increased passivation would be expected. Raman analysis suggests that a clear γ-Fe_2O_3 signal is not present and it may be best to present the oxide as an oxidized Fe_3O_4, with an increased density of Fe^{III} ($Fe^{II}_1Fe^{III}_{2+x}O_{4+3x/2}$).

An additional observation to note is that for the irradiation studies at room temperature, when the carbon steel had a pre-grown oxide of Fe_3O_4 (polarized at –0.7 V_{SCE}), the corrosion potential response to irradiation was slower than those pre-grown with more Fe^{III} oxides present, Chapter 4. Perhaps the growth of Fe_3O_4, which under the elevated temperature conditions has been observed to increase, has a minor impact on the corrosion effects of water radiolysis products.

For the current study, an additional experiment was performed in which a different oxide was pre-grown on the coupon surface before the combined high temperature and irradiation studied. For the experiment, pH 10.6, 0 and 10 mM borate samples were irradiated at room temperature for 24 h, followed by a combined heat and irradiation at 150 °C for 170 h. The previous study (Chapter 4) observed that carbon steel samples in irradiated systems at room temperature were composed of a mixed

Fe_3O_4/γ-Fe_2O_3 oxide. In essence, this allowed for water radiolysis products to be introduced into the system and achieve a steady state before the system was heated. Although a weak signal was observed, Raman spectra for both samples only clearly showed the presence of Fe_3O_4, Figure 6.15.

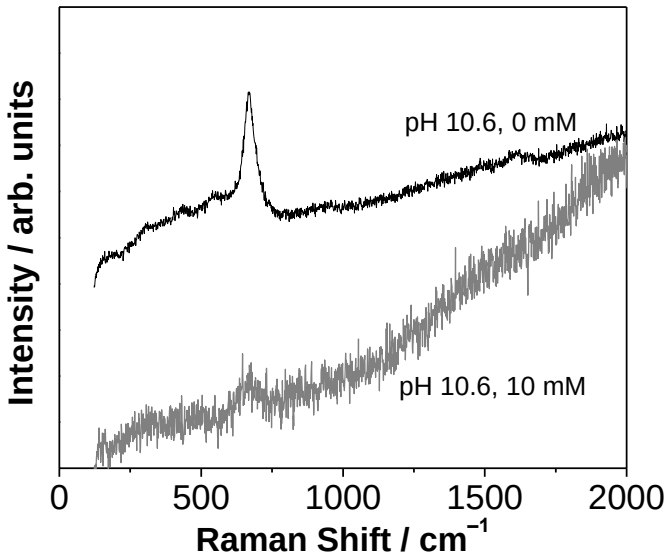

Figure 6.15: Raman spectra of carbon steel coupon surfaces after room temperature radiation, followed by radiation exposure and heating at 150 °C for 170 h.

Cross-section analysis found the oxide in 10 mM borate to be just below the detection limit of thickness, or a thickness < 30 nm, and the oxide in 0 mM to be 1.2 μm thick, Figure 6.16. These oxide thicknesses are significantly less that those performed in identical solutions starting from a freshly polished sample that was heated and irradiated at the same time, Table 6.3. Iron concentrations from ICP-MS were not determined for the 0 mM case, but were analyzed for the 10 mM case and found to be 450 ppb, which is

less than concentrations observed either with radiation and initial heating or without radiation. Therefore, with the introduction of heating, Fe_3O_4 continued to be formed preferentially, but the growth was limited, indicating possible increased Fe^{III} density ($Fe^{II}_1Fe^{III}_{2+x}O_{4+3x/2}$ formation).

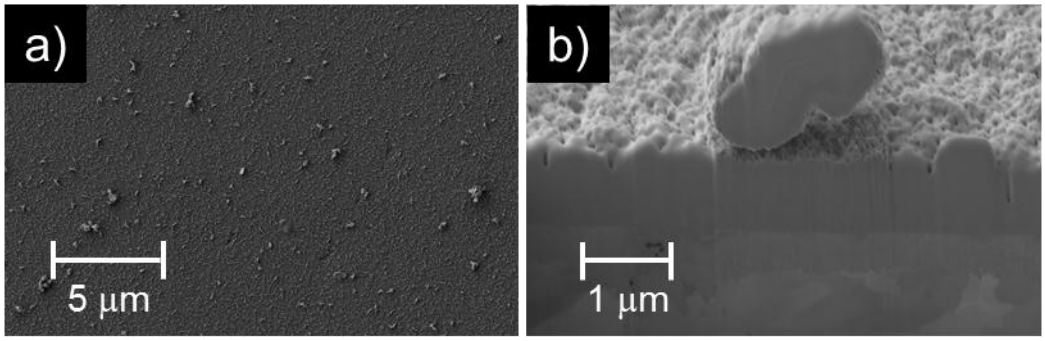

Figure 6.16: SEM micrographs of the carbon steel coupon surface and cross section after room temperature radiation, followed by radiation exposure and heating at 150 °C for 170 h. Shown are the (a) surface from pH 10.6 10 mM borate and (b) cross section from pH 10.6 0 mM borate.

6.4.3 Effect of the Oxidant

It appears as though, while limited, irradiation is affecting the growth rate of the oxide film, most likely by increasing the driving force, or overpotential, via oxidizing water radiolysis products. Another method used to increase the overpotential was through the chemical addition of an oxidant, specifically with aerated systems. As shown electrochemically at room temperature, Figure 6.14, aeration resulted in an immediate change in E_{CORR} into Ox II to values of approximately –0.35 V_{SCE}, regardless of an initial pre-grown oxide film. For pH 10.6 0 mM borate solutions, regardless of radiation or no radiation, the oxide was composed of a mixed oxide containing Fe_3O_4 and α-Fe_2O_3 with

thickness between 130 and 170 nm, Figures 6.11 and 6.12. Comparison of irradiated and unirradiated samples in aerated conditions showed very little difference, suggesting that the additive oxygen was the dominant oxidizing species and any additional effects from water radiolysis products was minimal. Under aerated systems the formation of α-Fe_2O_3 resulted in oxides that were 10 % the thickness of the corresponding deaerated experiments. The formation of α-Fe_2O_3 only with the addition of O_2 to the system provides further evidence that even at temperatures up to 150 °C, the production of O_2 as a water radiolysis is not the dominant oxidant in the system. Similarly at pH 6.0, little to no difference was observed between the radiation and no radiation samples in aerated conditions. Miyazawa et al. found that for stainless steel corrosion at 280 °C under oxidizing environments of either H_2O_2 or O_2 significantly differing corrosion mechanisms were observed [13]. Under H_2O_2 the oxides were much thicker than O_2 cases and the thickness of the oxide films were seen to decrease as [H_2O_2] increased and increase as [O_2] increased. This matches with what we suspect of H_2O_2 being the key oxidizing species under irradiation and deaerated conditions and O_2 being the key oxidizing species when it is chemically added to the system. Miyazawa et al. solely attributed the decrease in thickness as [H_2O_2] increased due to increased dissolution rates and not changes in the oxide composition. It is important to note that those studies were performed under neutral water conditions and higher temperatures than our studies, and therefore significantly higher dissolution rates would be expected. They found a range of small to large coalesced particles on the surface. Under less corrosive conditions, ferric ions were collected by Fe_3O_4 crystals and grew slowly, while under more oxidizing conditions (higher [H_2O_2]), higher concentrations of ferric ions led to a larger number of

Fe_3O_4 seeds, which grew quickly. The surfaces at pH 6.0 and 7.0, showed similar coalesced crystals under irradiation (or H_2O_2 produced) conditions, Figure 6.10.

While both oxidation routes may result in Fe_2O_3 in varying amounts, the formation mechanism of γ-Fe_2O_3 and α-Fe_2O_3 on the growing Fe_3O_4 oxide are very different. Under gamma irradiation conditions, the proposed oxidation of Fe_3O_4 via the water radiolysis product H_2O_2, produces an increase in Fe^{III} at the oxide/solution interface and a more γ-Fe_2O_3-like oxide at the oxide/aqueous interface ($Fe^{II}_{1-x}Fe^{III}_{2+x}O_4$). This is a facile process due to both oxides having a cubic close-packed inverse spinel structure. This oxidation process has been well defined and has been shown to produce a homogenous blend inverse spinel oxide [14-19].

With O_2 being the key oxidant, α-Fe_2O_3 was more easily formed. Since α-Fe_2O_3 has a hexagonal close-packed structure, far different from Fe_3O_4, [7] the formation of α-Fe_2O_3 cannot follow the same solid-state process. The surfaces of spherical and platelet structures appeared uneven, inhomogeneous, and highly porous, Figure 6.11. This resulted in uneven corrosion on the surface and a layered structure of Fe_3O_4 and α-Fe_2O_3 that were not well adhered. Although α-Fe_2O_3 has a lower solubility than γ-Fe_2O_3, [7] the physical removal of α-Fe_2O_3 from the steel surface was much easier and surface coverage was much less uniform, Figure 6.13.

6.5 CONCLUSIONS

The effect of the presence of ionizing radiation varies depending on the solution conditions. This study demonstrates that at elevated temperatures and higher pHs, irradiation leads to the formation of a slightly more protective oxide film on carbon steel,

while it does not appear to offer a similar advantage at a neutral or acidic pH. The oxide composition is mainly dependent on E_{CORR} and not significantly influenced by solution pH, temperature or ionic strength. However, these latter parameters do significantly affect the morphology and thickness of the oxide and the amount of metal dissolution. These effects arise from the solution parameter control of processes such as dissolution, condensation, and surface hydration. The solution dependent processes influence the competition between the different reaction paths to form oxides, giving rise to the formation of unique films under each solution conditions. Consequently, gamma irradiation increases the net metal oxidation rate, but it increases the metal dissolution preferentially over the oxide film formation with a decrease in pH and increases in ionic strength and temperature within the studied ranges. The effects of gamma irradiation are believed to arrive from oxidizing water radiolysis products, and specifically, H_2O_2. The chemical addition of an oxidant, O_2, resulted in the formation of α-Fe_2O_3 and an oxide structure very different from those formed under gamma irradiation.

6.6 REFERENCES

[1] A.P. Grosvenor, B.A. Kobe, N.S. McIntyre, Surf. Sci., 565 (2004) 151-162.
[2] A.P. Grosvenor, B.A. Kobe, M.C. Biesinger, N.S. McIntyre, Surf. Interface Anal., 36 (2004) 1564-1574.
[3] A.P. Grosvenor, B.A. Kobe, N.S. McIntyre, Surf. Sci., 572 (2004) 217-227.
[4] O.N. Shebanova, P. Lazor, J. Solid State Chem., 174 (2003) 424-430.
[5] X. Zhang, W. Xu, D.W. Shoesmith, J.C. Wren, Corros. Sci., 49 (2007) 4553-4567.
[6] L.J. Oblonsky, T.M. Devine, Corros. Sci., 37 (1995) 17-41.
[7] R.M. Cornell, U. Schwertmann, The Iron Oxides: Structures, Properties, Reactions, Occurrences and Uses, 2nd Ed., Weinheim, New York, NY, (2003).
[8] G.P. Marsh, K.J. Taylor, Corros. Sci., 28 (1988) 289-320.
[9] N.R. Smart, A.P. Rance, L.O. Werme, J. Nucl. Mater., 379 (2008) 97-104.
[10] R.J. Winsley, N.R. Smart, A.P. Rance, P.A.H. Fennell, B. Reddy, B. Kursten, Corros. Eng., Sci. Technol., 46 (2011) 111-116.

[11] L.J. Oblonsky, S. Virtanen, V. Schroeder, T.M. Devine, J. Electrochem. Soc., 144 (1997) 1604-1609.
[12] S.P. Harrington, F. Wang, T.M. Devine, Electrochim. Acta, 55 (2010) 4092-4102.
[13] T. Miyazawa, T. Terachi, S. Uchida, T. Satoh, T. Tsukada, Y. Satoh, J. Nucl. Sci. Technol., 43 (2006) 884-895.
[14] C.-T. Chen, B.D. Cahan, J. Electrochem. Soc., 129 (1982) 17-26.
[15] B.D. Cahan, C.-T. Chen, J. Electrochem. Soc., 129 (1982) 474-480.
[16] G.G. Long, J. Kruger, D.R. Black, M. Kuriyama, J. Electrochem. Soc., 130 (1983) 240-242.
[17] P. Schmuki, M. Buchler, S. Virtanen, H. Bohni, R. Muller, L.J. Gauckler, J. Electrochem. Soc., 142 (1995) 3336-3342.
[18] L.J. Oblonsky, A.J. Davenport, M.P. Ryan, H.S. Isaacs, R.C. Newman, J. Electrochem. Soc., 144 (1997) 2398-2404.
[19] A.J. Davenport, L.J. Oblonsky, M.P. Ryan, M.F. Toney, J. Electrochem. Soc., 147 (2000) 2162-2173.

Chapter 7

Effect of Dissolved Ferrous Iron on Oxide Film Formation

7.1 INTRODUCTION

Predicting the influence of radiation on corrosion is complicated by the role that dissolved corrosion products and other water additives can have on the concentrations of the radiolytically produced redox active species that are present [1-3]. In the circulating coolant of a nuclear reactor the presence of soluble corrosion products (metal ions) is expected. Thus, the net effect of radiation on steel corrosion, particularly, in the presence of dissolved transition metal ions is difficult to predict.

As discussed in Chapter 5, aqueous solution conditions play an important role in the corrosion process. The main objective of this study was to elucidate the impact that dissolved iron ions in solution have on the oxide growth and determine the type of oxide that is formed on carbon steel as a function of potential. These studies were done at pH 8.4 because the solubility of Fe^{II} species is sufficiently large that the effects of the presence of dissolved iron ions can clearly be observed. This is also a pH range in which oxide formation on carbon steel has been studied extensively [4-13]. The effects of dissolved iron ions on the oxide growth and conversion were studied using a range of electrochemical techniques. X-ray photoelectron spectroscopy (XPS) and scanning electron microscopy (SEM) analyses were also performed to determine the chemical compositions of the films formed at different potentials.

7.2 EXPERIMENTAL

7.2.1 Solutions

All experiments were conducted at room temperature in pH 8.4 borate buffer solutions to which solutions containing Fe^{2+} were added. The sodium borate solution was prepared using reagent grade $Na_2B_4O_7 \cdot 10H_2O$ (Caledon Laboratories Ltd.) and the boric acid solution was prepared using H_3BO_3 (Caledon Laboratories Ltd.). Reagent grade $FeSO_4 \cdot 7H_2O$ (Caledon Laboratories Ltd.) was used to produce Fe^{2+} solutions with a concentration of 1×10^{-4} M $FeSO_4$. The water purified using a NANOpure Diamond UV ultra-pure water system (Barnstead International) with a resistivity of 18.2 MΩ·cm.

7.2.2 Procedure

Prior to each experiment the electrolyte solution was degassed by sparging with argon for at least 1 h. During experiments, the solution was continuously purged with Ar to prevent air ingress. Immediately prior to the start of all electrochemical experiments, the working electrode was cathodically cleaned at -1.1 V_{SCE} for 5 min.

Three types of electrochemical experiments were performed: (1) CV, (2) potentiostatic polarization, and (3) EIS. The CV was performed as a function of the number of scan cycles, the electrode rotation rate, and the upper-limit of the potential scan. For potentiostatic polarization experiments, which lasted typically 22 h, current measurements were made as a function of time at a single applied potential. The current measurements were interrupted periodically to take electrochemical impedance spectra. After the potentiostatic measurements were complete, the carbon steel electrodes were further analysed by Raman spectroscopy, SEM, and XPS.

7.3 RESULTS AND DISCUSSION

7.3.1 Cyclic Voltammetry

The CVs of multiple scan cycles recorded on the carbon steel electrode in solutions initially free of $Fe^{2+}_{(aq)}$ are compared with those obtained in solutions initially containing 0.1 mM $Fe^{2+}_{(aq)}$ in Figure 7.1. The initial ferrous ion concentration, $[Fe^{2+}_{(aq)}]_0$, is slightly below the solubility limit of ferrous iron (~ 0.25 mM) at the studied pH of 8.4 [1, 14, 15]. The designation for the initial ferrous ion contribution is used because there will be some dissolution of ferrous ion from the steel during corrosion, particularly at high potentials, and the solution concentration will increase. However, the volume of the electrolyte in the cell is large relative to the amount of Fe^{2+} that was released from the carbon steel during corrosion. The other scan conditions were an electrode rotation rate of 200 rpm and potential scan rate of 5 $mV \cdot s^{-1}$. The CVs obtained in both solutions show two distinct potential regions of anodic current activity, region I ($-0.8\ V_{SCE} < E < -0.5\ V_{SCE}$) where a distinct peak a1 appeared and region II ($-0.3\ V_{SCE} < E < 0.4\ V_{SCE}$) where a broad, near potential independent, peak a2 appeared. In order to differentiate from the anodic and cathodic peaks labelled at pH 10.6 in Chapter 3, lower case lettering is used for the assignment of peaks. On the reverse scan, the current remained anodic until the potential reached a value below $-0.3\ V_{SCE}$. A distinct cathodic peak c1 centred at $-0.6\ V_{SCE}$ was observed only for tests in the $Fe^{2+}_{(aq)}$ solutions. The intensity of peak a1 increased with the number of scan cycles but the rate of increase progressively slowed with the number of cycles in both solutions. On the other hand, peaks a2 and c1 did not show any dependence on scan cycles (Figure 7.1).

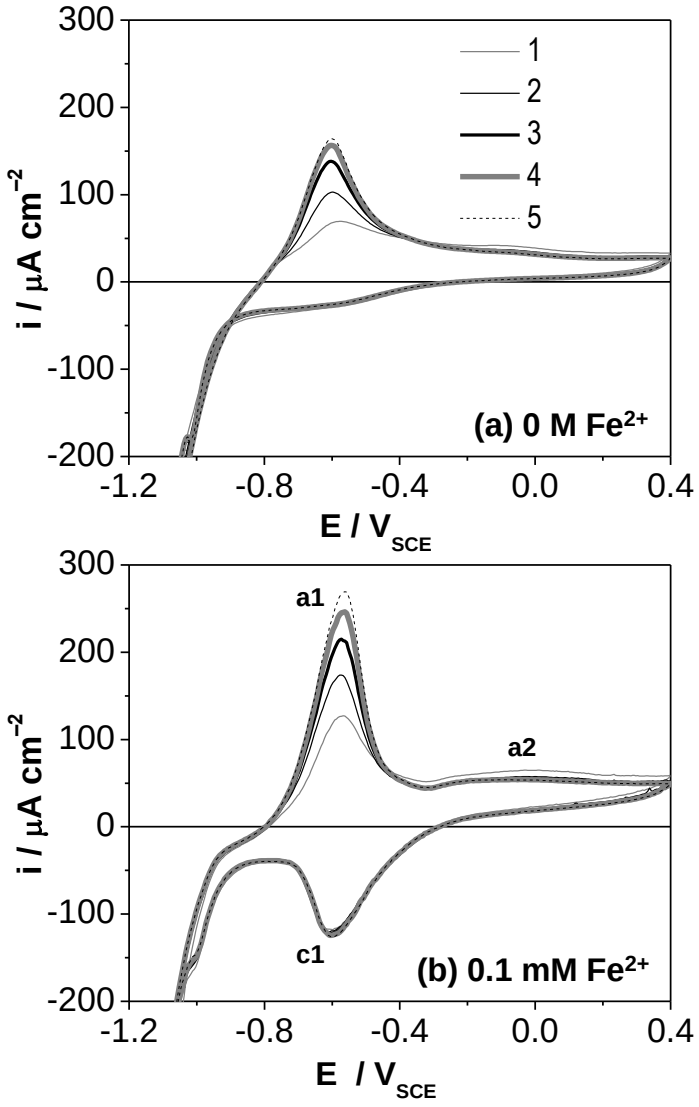

Figure 7.1: CVs recorded on carbon steel in pH 8.4 borate solutions with (a) no initial $Fe^{2+}_{(aq)}$ or (b) 0.1 mM $Fe^{2+}_{(aq)}$. The CV scan rate was 5 mV·s^{-1} and the electrode was rotated at 200 rpm.

The CVs obtained as a function of upper scan limit in the $Fe^{2+}_{(aq)}$ solutions (Figure 7.2) show that the cathodic peak c1 corresponds to the anodic peak a2. The effect of electrode rotation rate on the CVs of the first and fifth cycles in both solutions can be seen in Figure 7.3. In the solution initially free of $Fe^{2+}_{(aq)}$ (Figure 7.3a,b), the intensity of peak

a1 increased, and the peak maximum shifted to a more positive potential with an increase in rotation rate. Changing the electrode rotation rate had a negligible effect on the intensities of peaks a2 and c1 in the solution initially free of $Fe^{2+}_{(aq)}$. In the solution containing 0.1 mM $Fe^{2+}_{(aq)}$ (Figure 7.3c,d), the effect of electrode rotation on the intensity of peak a1 was diminished. The dependence of the peak intensity of a1 on rotation rate was not linear, with the largest increase observed at 1000 rpm. Alternatively, the intensities of peaks a2 and c1 increased with increasing rotation rate.

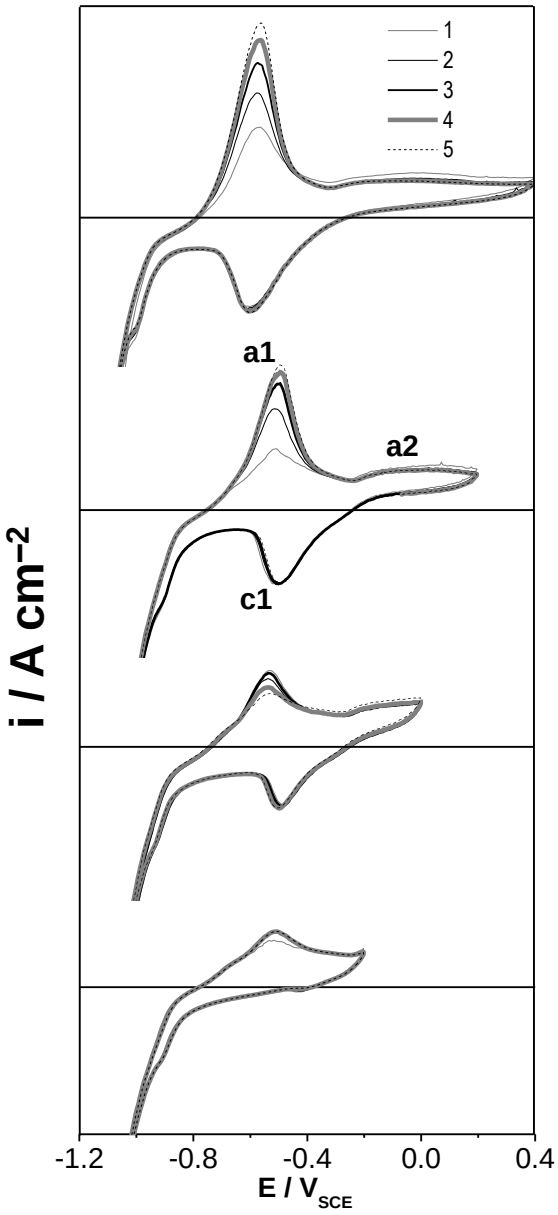

Figure 7.2: CVs recorded on carbon steel in pH 8.4 borate solutions containing 0.1 mM $Fe^{2+}_{(aq)}$ with different sweep vertices of 0.4 V_{SCE}, 0.2 V_{SCE}, 0 V_{SCE}, and –0.2 V_{SCE}. The CV scan rate was 5 $mV \cdot s^{-1}$ and the electrode was rotated at 200 rpm.

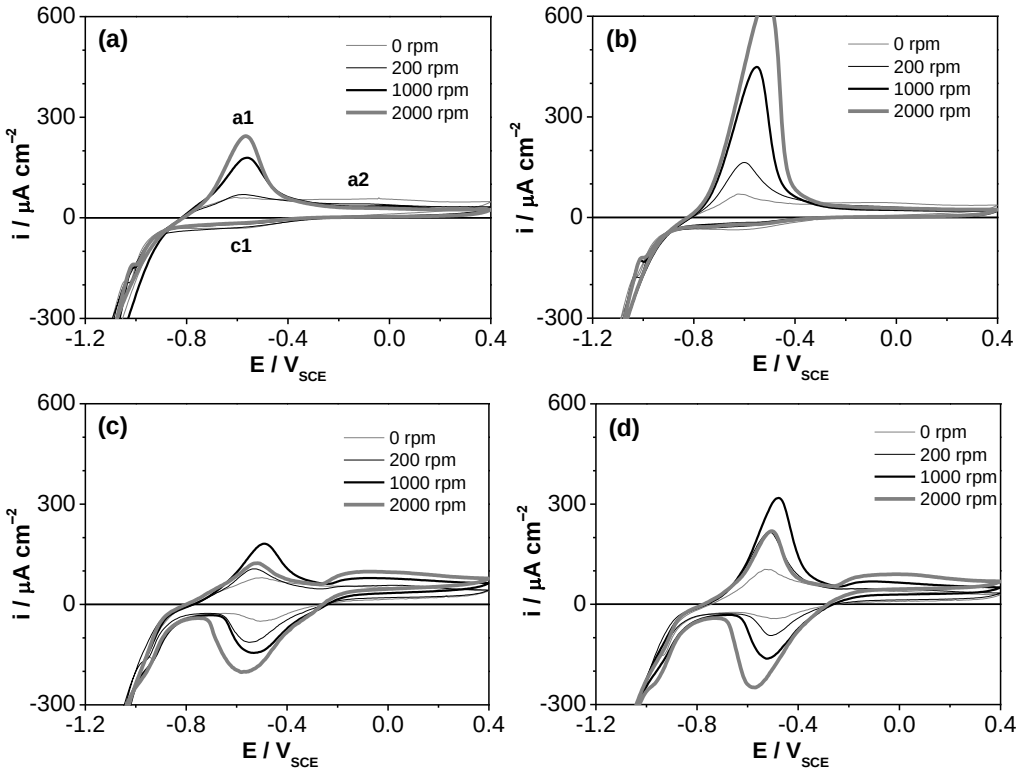

Figure 7.3: The (a,c) first and (b,d) fifth cycles for CVs recorded on carbon steel in pH 8.4 borate with (a,b) no initial $Fe^{2+}_{(aq)}$ or (c,d) 0.1 mM $Fe^{2+}_{(aq)}$. The CV scan rate was 5 $mV \cdot s^{-1}$ and a range of electrode rotation rates were employed.

To aid in the assignments of the peaks observed in the CVs, the thermodynamic equilibrium potentials for the reactions of iron and iron oxide redox pairs at pH 8.4 were calculated from the known Gibbs energies of reaction [16, 17]. The results are presented in Figure 7.4. Oxide species beyond those thermodynamically predicted by the Pourbaix diagram are included in Figure 7.4 since competing reactions that involve species that are not thermodynamically stable at a given potential can be important in dictating the main anodic reaction. For example, the FeOOH oxides are typically not the most thermodynamically stable oxides under certain conditions, but are often kinetically

favoured. The CV results suggest that peak a1 involves an electrochemical oxidation of Fe in the metal substrate to Fe^{II}. This ion can either be incorporated in an oxide film or dissolve into the aqueous phase as $Fe^{2+}_{(aq)}$. In an oxide film Fe^{II} is available for further oxidation to less soluble mixed $Fe^{II/III}$ oxides or Fe^{III} hydroxide/oxides (section 7.3.2.2.). For tests with a solution initially free of $Fe^{2+}_{(aq)}$, an increase in rotation rate will speed diffusion of $Fe^{2+}_{(aq)}$ from the metal oxide surface and enable an increase in the dissolution rate of $Fe^{2+}_{(aq)}$, resulting in an increase in the anodic current. However, when the concentration of $Fe^{2+}_{(aq)}$ is close to its solubility limit, diffusion of ferrous ion from the surface into the aqueous phase will be suppressed. The anodic oxidation of iron under this condition then mostly results in growth of an oxide film and not in metal dissolution. This explains the lesser impact of changing the electrode rotation rate on the current density of peak a1 for tests in 0.1 mM $Fe^{2+}_{(aq)}$, compared to that in the absence of $Fe^{2+}_{(aq)}$.

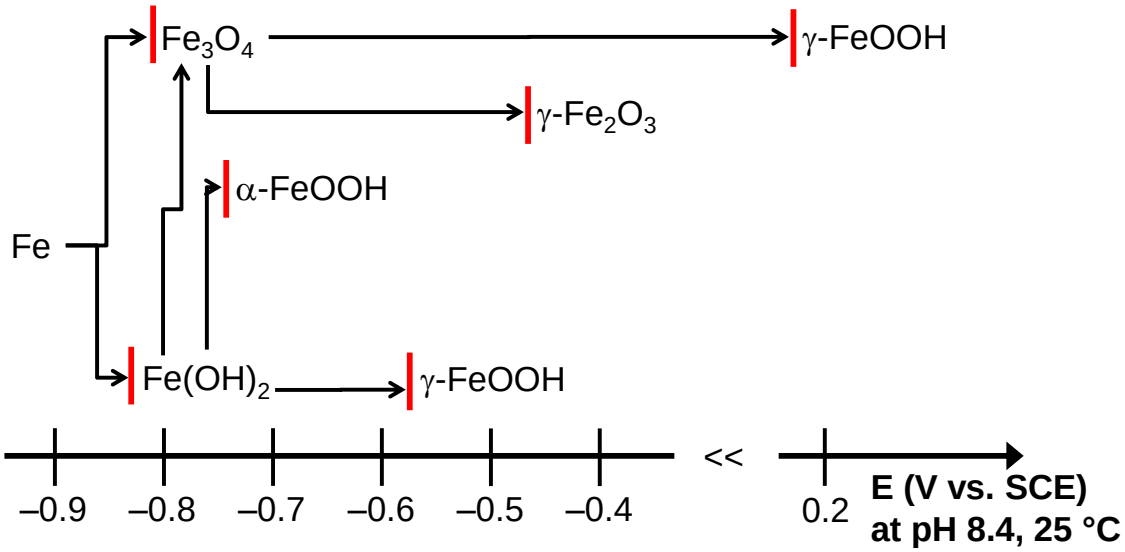

Figure 7.4: Calculated equilibrium potentials (vertical lines) for various iron redox reactions at pH 8.4 and 25°C.

Peak a2 is attributed to the anodic oxidation of $Fe^{2+}_{(aq)}$ (in acid-base and phase equilibrium with $Fe(OH)_2$) to γ-FeOOH and the corresponding cathodic peak c1 is attributed to the reduction of γ-FeOOH to Fe_3O_4. At potentials higher than –0.58 V_{SCE} (the equilibrium potential for the $Fe(OH)_2$/γ-FeOOH redox reaction at pH 8.4, see Figure 7.4), $Fe^{2+}_{(aq)}$ can diffuse to the carbon steel surface and further oxidize to form γ-FeOOH(s). Increasing the rotation rate promotes the diffusion of $Fe^{2+}_{(aq)}$ from the bulk aqueous phase to the oxide/water interface. The increase in peak c1 just reflects the increase in the amount of oxide formed.

7.3.2 Potentiostatic Film Growth

7.3.2.1 Experimental Results

The effect of $Fe^{2+}_{(aq)}$ on oxide formation on carbon steel was further studied under potentiostatic conditions. Three different applied potentials, E_{App}, were studied: (1) –0.7 V_{SCE}, a potential in region I, (2) –0.5 V_{SCE}, a potential between regions I and II, and (3) 0.3 V_{SCE}, a potential in region II. In these experiments the desired potential was applied immediately after cathodic cleaning at –1.1 V_{SCE} for 5 min and maintained for 22 h while continuously monitoring the current. The data are presented in plots of log i vs log t in Figure 7.5.

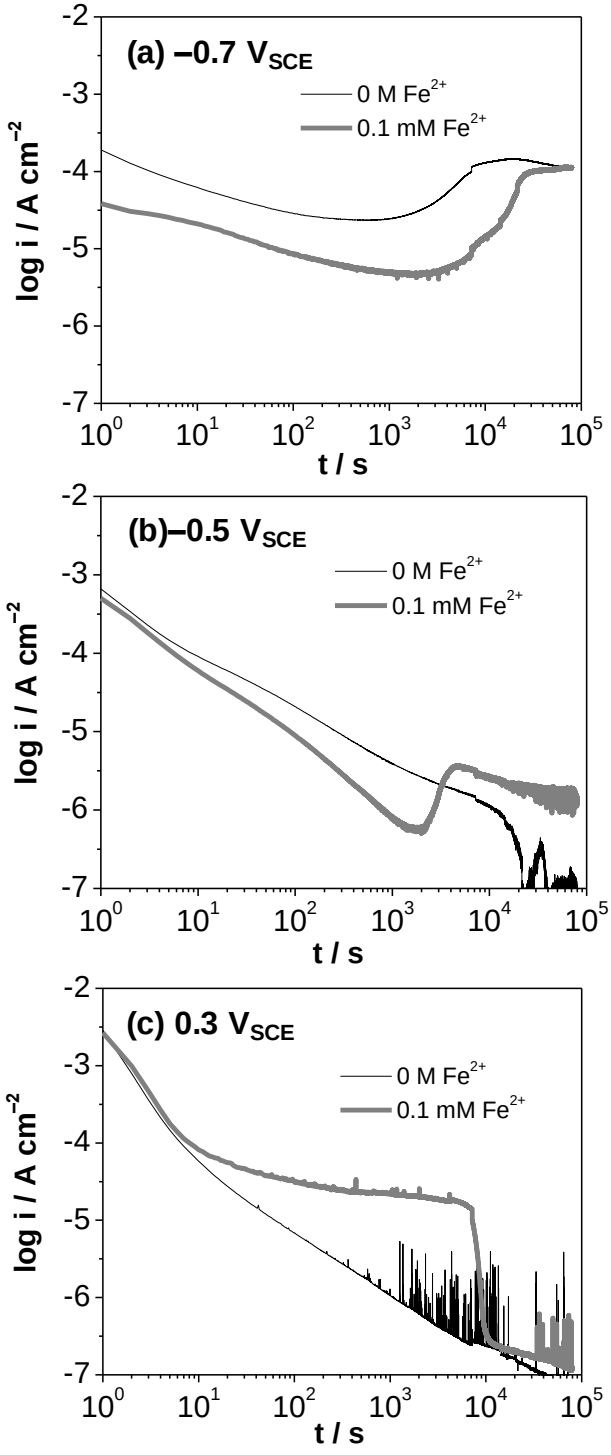

Figure 7.5: Log current vs. log time for films grown at: (a) –0.7 V_{SCE}, (b) –0.5 V_{SCE}, and (c) 0.3 V_{SCE} in pH 8.4 borate solutions with no initial $Fe^{2+}_{(aq)}$ or 0.1 mM $Fe^{2+}_{(aq)}$.

Electrochemical impedance spectra were also taken periodically during potentiostatic polarization experiments and the results are presented in both Bode and Nyquist plots in Figures 7.6 and 7.7. The EIS plots labelled 1, 2 and 3 in Figure 7.6 are the spectra taken at 4, 8, and 14 h of the polarization at each potential, respectively. The EIS did not show any further changes after 14 h. Electric equivalent circuit model analyses were not performed since analysis suggested that the EIS data (in particular the data obtained at –0.5 V_{SCE} and 0.3 V_{SCE}) were not adequate for quantitative circuit model fitting. However, the relative changes in the EIS can provide some qualitative information.

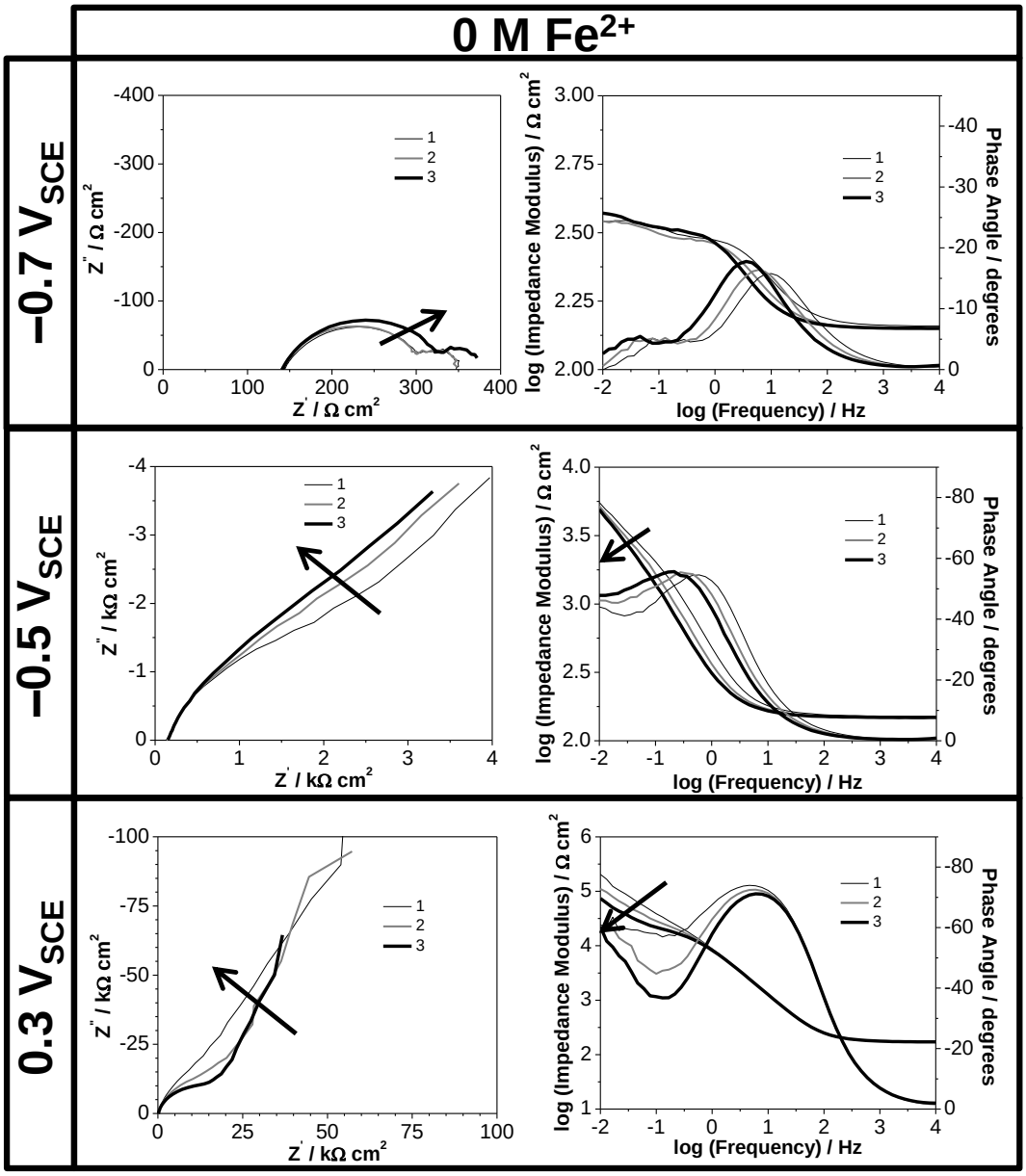

Figure 7.6: Bode and Nyquist plots obtained from EIS analysis for films grown at various potentials in pH 8.4 borate solutions with no initial $Fe^{2+}_{(aq)}$. The labels 1, 2, 3 correspond to 4, 8, and 14 h of immersion time respectively. Arrows for the Nyquist plots and impedance modulus in the Bode plots show the progression with time.

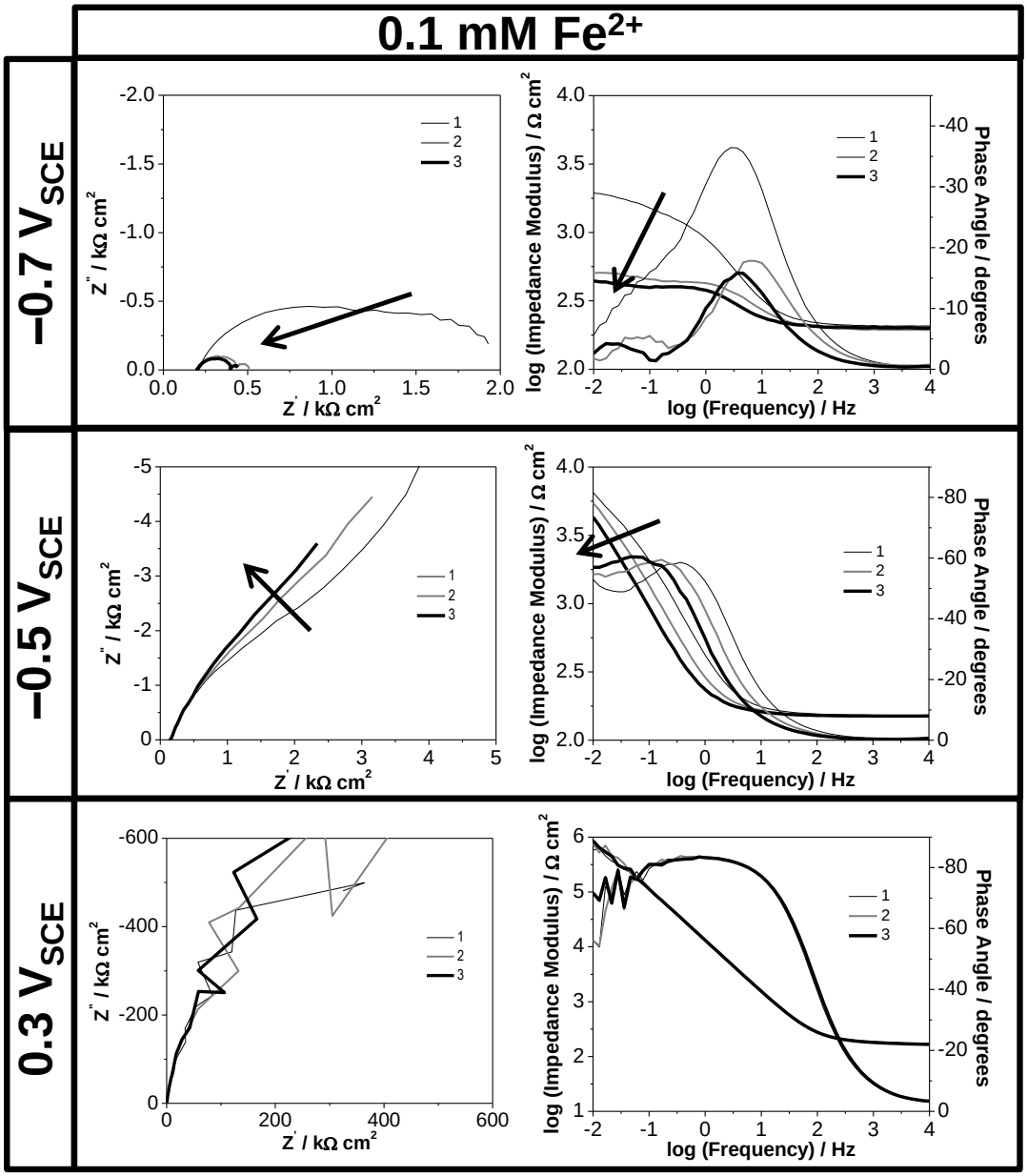

Figure 7.7: Bode and Nyquist plots obtained from EIS analysis for films grown at various potentials in pH 8.4 borate solutions with 0.1 mM $Fe^{2+}_{(aq)}$. The labels 1, 2, 3 correspond to 4, 8, and 14 h of immersion time respectively. Arrows for the Nyquist plots and impedance modulus in the Bode plots show the progression with time.

Upon the conclusion of each potentiostatic experiment, the carbon steel electrode surface was further characterized by SEM, Raman and XPS. The SEM images obtained for these surfaces are shown in Figure 7.8.

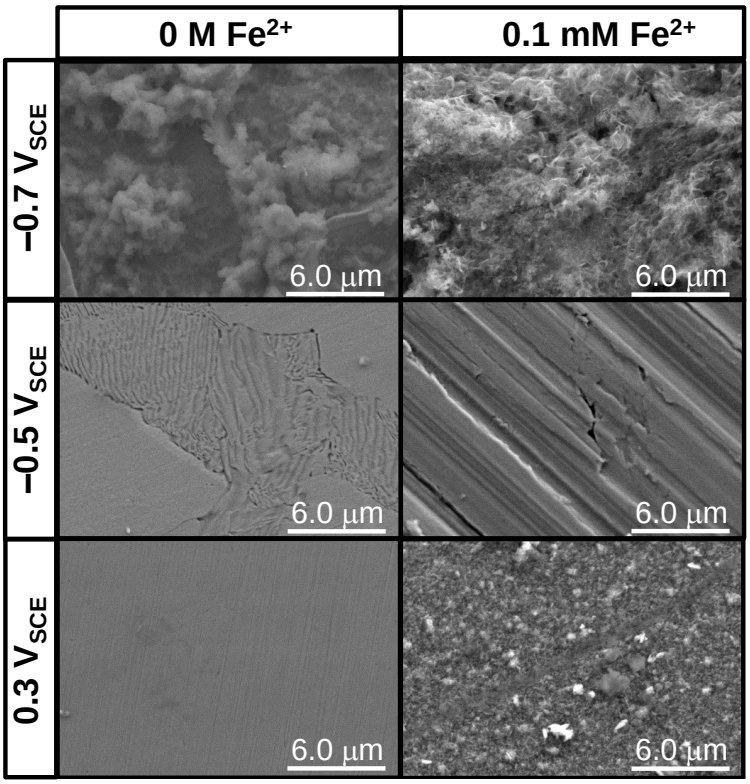

Figure 7.8: SEM micrographs of films grown for 22 h at various potentials in pH 8.4 borate solutions with 0 or 0.1 mM $Fe^{2+}_{(aq)}$.

The Raman spectra of these surfaces are compared to those of reference single-phase iron oxide/hydroxide samples in Figure 7.9. Reference spectra for less stable oxides such as $Fe(OH)_2$, $Fe(OH)_3$, β-FeOOH and δ-FeOOH were not taken but their Raman shifts have been reported [18, 19] (see Table 7.1).

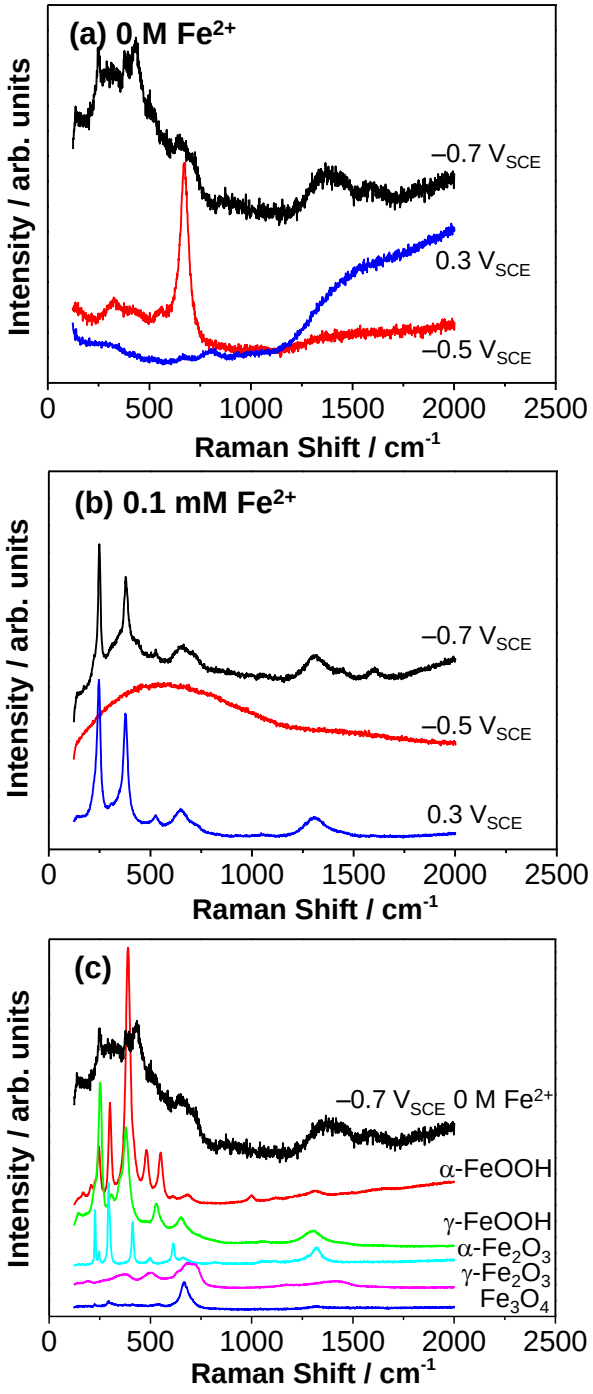

Figure 7.9: Raman spectra of carbon steel films grown for 22 h at various potentials in pH 8.4 borate solutions with (a) no initial $Fe^{2+}_{(aq)}$ or (b) 0.1 mM $Fe^{2+}_{(aq)}$. These spectra are compared to the spectra of reference iron-oxide minerals at 25°C, (c). All spectra are shifted in magnitude to prevent overlap.

Table 7.1: Raman peaks (in wavenumbers) for iron oxides and hydroxides not studied as standards

Iron oxide/hydroxide	Peaks (cm^{-1})
$Fe(OH)_2$	460, **550**, 692
$Fe(OH)_3$	395, **696**, 1335
β-FeOOH	**314**, **380**, 549, 722
δ-FeOOH	297, **392**, **666**

Bold indicates the strongest peaks in species spectrum

The high resolution spectra of the XPS Fe-2p and O-1s bands were deconvoluted using reference XPS spectra of standard iron oxide and hydroxide samples to obtain information on the composition of oxidation states. The reference spectra for iron oxide and hydroxide contain multiple peaks. A representative high resolution spectrum over the Fe-2p band region and its deconvolution into chemical components (Fe, $FeO/Fe(OH)_2$, Fe_3O_4 and γ-FeOOH) is shown in Figure 7.10. A similar deconvolution was employed in Chapter 4 and a detailed description of the total method used for the XPS analyses can be found in references [14, 20].

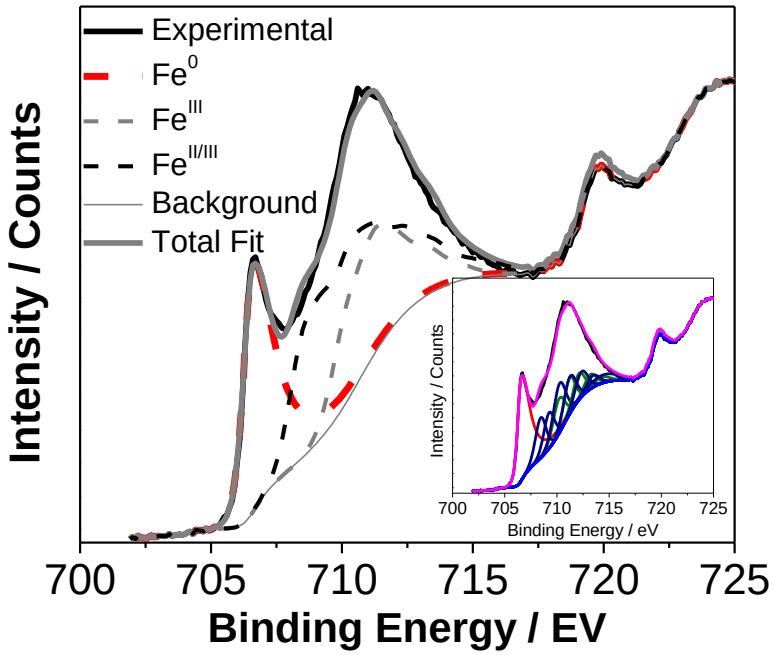

Figure 7.10: High-resolution XPS spectra of Fe-2p containing experimental data, composite of Fe^{0}, $Fe^{II/III}$, and Fe^{III} fits, and weighted composite of all fitted peaks. Inset is the deconvoluted XPS spectra with fitting for individual iron oxides and hydroxides used to obtain the composition of oxidation states.

The analysis results from XPS are shown in Figure 7.11, where the chemical components, Fe, $FeO/Fe(OH)_2$, Fe_3O_4 and γ-FeOOH are represented as Fe^{0}, Fe^{II}, $Fe^{II/III}$ and Fe^{III}, respectively.

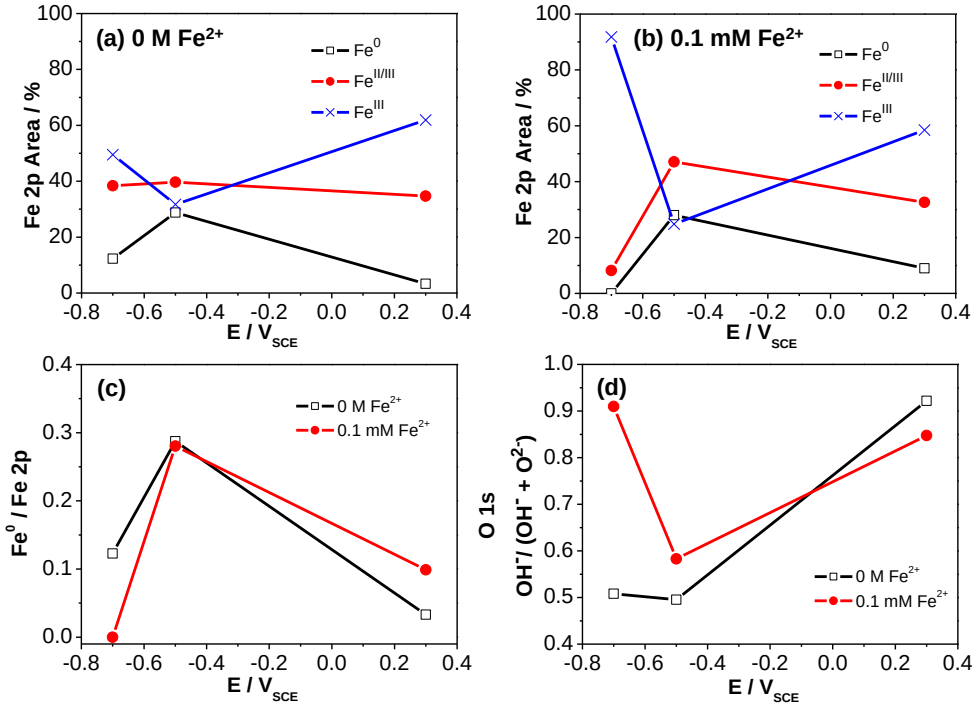

Figure 7.11: XPS analysis results: (a,b) Fe^{0}, $Fe^{II/III}$, and Fe^{III} components of the Fe 2p band, (c) Fe^{0}/Fe ratio in the Fe 2p band, and (d) area ratio of $OH^{-}/(OH^{-}+O^{2-})$ in the O 1s band.

7.3.2.2 Oxide Formation at –0.7 V_{SCE}

The SEM micrographs of the surfaces treated at –0.7 V_{SCE} for 22 h in solutions with and without the presence of $Fe^{2+}_{(aq)}$ showed small corrosion product deposits randomly distributed on the surfaces (Figure 7.8). The surface coverage by these deposits was more extensive for the tests in the $Fe^{2+}_{(aq)}$ containing solution.

Comparison of the Raman spectra of these surfaces with the reference spectra suggests the presence of Fe_3O_4 and Fe^{II} and Fe^{III} hydroxides or hydrated species (Figure 7.9). A small peak at approximately 670 cm^{-1} can be attributed to Fe_3O_4. The other peaks are attributed to a mixed amorphous phase of Fe^{II} and Fe^{III} hydroxides and/or FeOOH. The

spectrum of the surface oxidized in the $Fe^{2+}_{(aq)}$ solution also showed well-defined peaks at approximately 260 cm^{-1} and 380 cm^{-1} that closely match those of γ-FeOOH. The oxidation of $Fe(OH)_2$ to γ-FeOOH is not thermodynamically favoured at this potential (Figure 7.4). Thus, the formation of γ-FeOOH is attributed to the dehydration of Fe^{III} oxides/hydroxides.

The Raman spectrum also contains a broad background band in the range from 250 to 1200 cm^{-1} (Figure 7.9). These features can be attributed to the formation of hydrated ferrous and ferric species.

The XPS results for the tests at –0.7 V_{SCE} in the solution initially free of $Fe^{2+}_{(aq)}$ (Figure 7.11) show that Fe^0 contributes approximately 10 atomic % to the Fe-2p band. On the other hand, the Fe-2p band of a film grown in 0.1 mM $Fe^{2+}_{(aq)}$ shows no metallic (Fe^0) content, despite the surface underneath the platelet shaped deposits still showing in the SEM images (Figure 7.8). The combined SEM, Raman and XPS analyses suggest that a uniform inner layer of Fe_3O_4 with mixed ferrous and ferric hydroxide deposits on top has been formed. The EIS analysis of this film also shows two RC components, consistent with the presence of two distinct oxide layers (Figure 7.6). The absence of the Fe^0 component in the XPS Fe-2p band for a film grown in 0.1 mM $Fe^{2+}_{(aq)}$ (Figure 7.11b) indicates that the underlying Fe_3O_4 layer is thicker (> 15 nm) on the surface oxidized in the presence of $Fe^{2+}_{(aq)}$ than in its absence (15 nm is the analysis depth of the XPS instrument).

The ratio of $Fe^{II/III}$ (i.e., magnetite) to Fe^{III} of the XPS Fe-2p band is significantly lower in the film grown in the $Fe^{2+}_{(aq)}$ solution compared to that grown in the initially $Fe^{2+}_{(aq)}$ free solution (Figure 7.11). The SEM images show more extensive coverage of the hydroxide deposits for the surface oxidized in the $Fe^{2+}_{(aq)}$ solution. Thus, the lower ratio of

$Fe^{II/III}$ to Fe^{III} in the XPS Fe-2p band observed in the presence of $Fe^{2+}_{(aq)}$ is attributed to the thicker and more extensive hydroxide deposits in the outer layer and not to the absence of the underlying Fe_3O_4 layer. Analysis of OH^- and O^{2-} content in the oxide lattice (from the high resolution XPS O-1s spectra (Figure 7.11d)) further suggests that the Fe^{III} species in the film is mainly in an hydroxide form.

The surface analyses presented above provide the chemical and phase compositions of the surface layers formed after 22 h of potentiostatic polarization, but do not provide kinetic information. To obtain this, current and EIS measurements were performed as a function of time. At $-0.7\ V_{SCE}$ the current in solutions with and without initial $Fe^{2+}_{(aq)}$ initially decreased at a rate slower than linear (Figure 7.5). After ~ 10^3 s (20 min) the current started to increase with time and then either stabilized or started to decrease again. The current was lower in the tests with 0.1 mM $Fe^{2+}_{(aq)}$ in solution over the majority of polarization.

The decrease in current at t ~ 10^3 s is attributed to the growth of a layer of Fe_3O_4-like oxide (Fe_3O_4 or a graded structure of FeO to Fe_3O_4). The slower than linear decrease in the current suggests that the oxidation rate is also partially controlled by a dissolution process. This is consistent with the CV results that indicate that the anodic processes at this potential involve soluble Fe^{II} species. In the presence of an oxide layer, the electrochemical corrosion involves: (1) charge transfer reactions (metal oxidation coupled with reduction of aqueous species at the metal/oxide and oxide/water interfaces), (2) the net migration of metal cations from the metal/oxide interface to the oxide/water interface coupled with migration of oxygen anions in the opposite direction (growing the metal oxide layer), and (3) the hydration oxides at the oxide/water interface followed by

diffusion of oxyhydroxide species into the aqueous phase. These steps are schematically presented in Figure 7.12. Oxide growth involved the net migration of Fe^{II} from the metal/oxide to the oxide/water interface [21-24]. If the metal oxidation primarily grows the oxide layer and little dissolution occurs, the current will decrease with an increase in the oxide thickness and the rate will decrease linearly due to a linear increase in the potential drop across the thickening oxide layer. The slower than linear decrease in current thus suggests that the oxide is affected by the dissolution of Fe^{II} species.

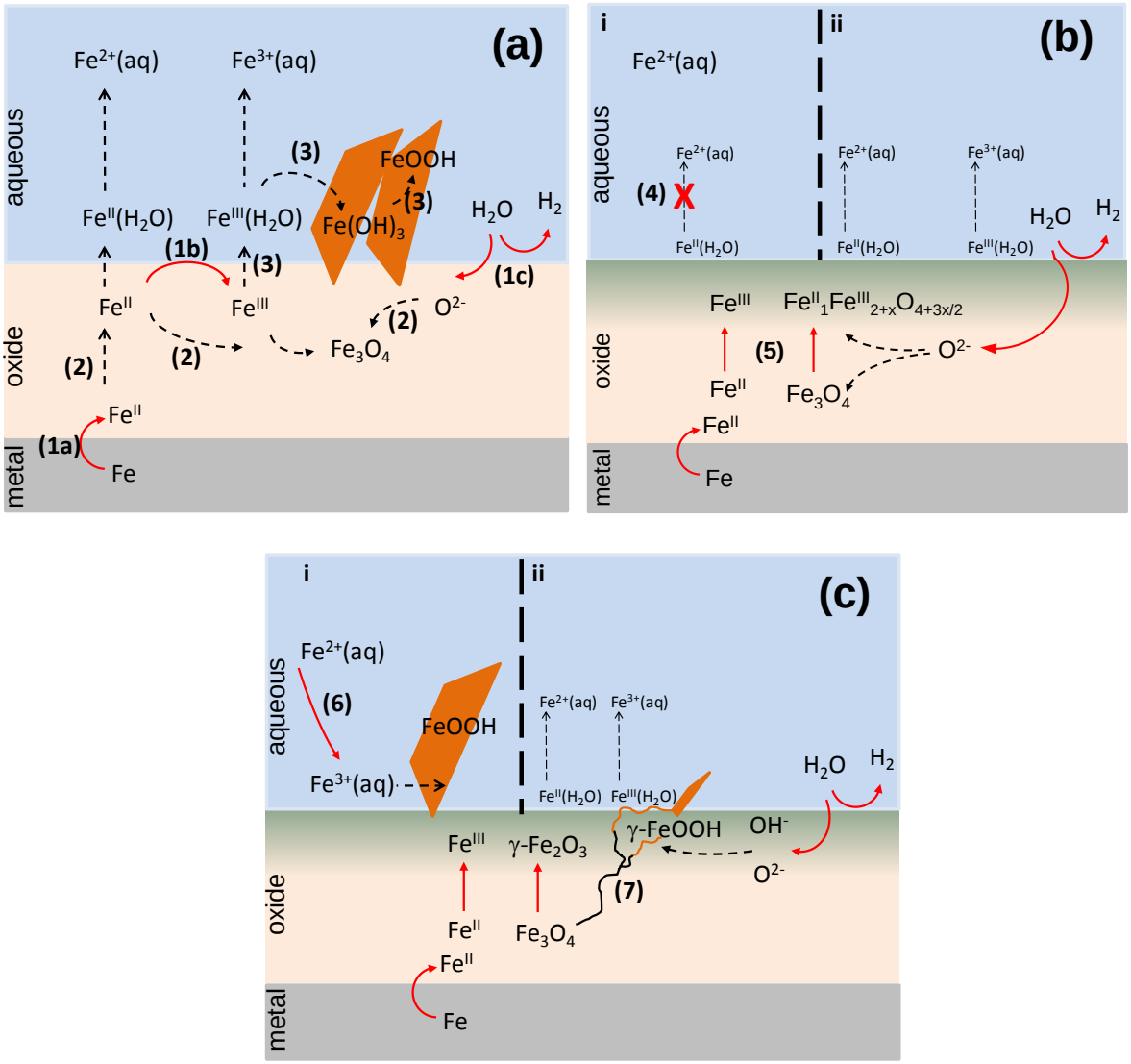

Figure 7.12: Schematic of proposed oxidation mechanism at (a) –0.7 V_{SCE}, (b) –0.5 V_{SCE}, and (c) 0.3 V_{SCE} and solutions (i) with pre dissolved $Fe^{2+}_{(aq)}$ and (ii) without pre dissolved $Fe^{2+}_{(aq)}$. Oxidation and reduction processes are labelled as solid red arrows and transport processes are labelled as dashed black arrows. For figures (b) and (c), some transport processes have been removed for figure clarity.

The presence of a high concentration of $Fe^{2+}_{(aq)}$ in the solution will slow the diffusion of hydrated Fe^{II} species from the oxide/water interface into the aqueous phase. This will consequently increase the Fe^{II} concentration at the oxide/water interface and,

hence, will lower the gradient of Fe^{II} in the oxide and lower the transport rate of Fe^{II} ion through solid oxide/hydroxide phases. Consequently, a smaller anodic current is observed during polarization in the solution containing 0.1 mM $Fe^{2+}_{(aq)}$ than in the solution initially free of $Fe^{2+}_{(aq)}$ (Figure 7.5a). On the other hand, at 200 rpm (Figure 7.1), the current in this potential region during the CV (peak a1) was higher in the presence of 0.1 mM $Fe^{2+}_{(aq)}$ while at rotation rates ≥ 1000 rpm, there was a higher current in the absence of dissolved $Fe^{2+}_{(aq)}$ (Figure 7.3). This is attributed to two opposing effects of the suppression of Fe^{II} diffusion from the metal/oxide interfacial region to the aqueous phase on the net electrochemical activity. The suppression of Fe^{II} diffusion initially promotes the conversion of Fe^{II} hydroxide to a more conducting Fe_3O_4 layer and, hence, increases electrochemical activity. This increases the current associated with peak a1. The opposite effect would be seen if the surface remained the same since the suppression of Fe^{II} diffusion decreases the dissolution current. The CVs shown in Figure 7.1 were obtained with a rotating electrode at 200 rpm. When the rotation rate was low (< 200 rpm), the effect of rotation on Fe_3O_4 formation is greater than its effect on Fe^{II} dissolution, and the net effect is to increase the current. When the rotation rate was high (> 500 rpm), the effect of rotation on current arises primarily via Fe^{II} dissolution. This is consistent with a process that is controlled by diffusion of the oxidized metal ion from the electrode surface to the solution phase.

In both solutions, the current started to increase at about 10^3 s. An increase in current with a fixed applied potential is often interpreted as the formation of a progressively more defective or porous film. This can result in an increase in local acidity and hence, an increase in oxidative dissolution. However, the increase in local acidity will

increase the rate of dissolution of Fe^{II} and also Fe^{III} species, and consequently less oxide/ hydroxide will precipitate. Although the SEM images of the film grown for 22 h at –0.7 V_{SCE} in both solutions show highly porous corrosion product deposits (Figure 7.8), these deposits are more extensive in the presence of $Fe^{2+}_{(aq)}$ (despite the lower total anodic charge passed in these tests). These observations are opposite to those expected from an increase in local acidity. However, these results are consistent with the dehydration of Fe^{III} oxides/hydroxides to FeOOH.

Based on these observations the electrochemical oxidation mechanism under potentiostatic polarization at –0.7 V_{SCE} is proposed as follows, see Figure 7.12a. At early times the electrochemical oxidation of Fe to Fe^{II} at the metal/oxide interface (step 1a in Figure 7.12a), followed by transport of Fe^{II} through the oxide layer (step 2) and oxidation of Fe^{II} to Fe^{III} at the oxide/water interface (step 1b), results in growing the Fe_3O_4 layer. At the Fe_3O_4/water interface, the ferrous and ferric species will be hydrated:

$$Fe^{II}(ad\text{-}H_2O) = [Fe^{2+} + Fe(OH)^{+} + Fe(OH)_2 + Fe(OH)_3^{-}] \quad (7.1)$$

$$Fe^{III}(ad\text{-}H_2O) = [Fe^{3+} + Fe(OH)^{2+} + Fe(OH)_2^{-} + Fe(OH)_3 + Fe(OH)_4^{-}] \quad (7.2)$$

where the hydrated species are in acid base equilibrium:

$$Fe^{II}(OH)_n^{2-n} + H^{+} \leftrightarrows Fe^{II}(OH)_{n-1}^{3-n} + H_2O \qquad n = 1,2, \text{ or } 3 \quad (7.3)$$

$$Fe^{III}(OH)_n^{3-n} + H^{+} \leftrightarrows Fe^{III}(OH)_{n-1}^{4-n} + H_2O \qquad n = 1,2,3, \text{ or } 4 \quad (7.4)$$

(Note that any water molecules that are coordinated to the metal cations are not included in the chemical structures.) The charged species will quickly dissolve into the aqueous phase. However, the neutral species, $Fe(OH)_2$ and $Fe(OH)_3$, are in dissolved and solid phase equilibrium, with their pKa values determining the solubility of the ferric and ferrous irons. At pH 8.4, the solubility of Fe^{II} is relatively high while that of Fe^{III} is at its minimum. Thus,

$Fe(OH)_3$ will condense, dehydrate and deposit as γ-FeOOH.

The solvated-to-solid phase transformation may be a slow process and hence, there is an incubation period of about 10^3 s observed before the growth of a more porous oxide can support an increase in current. As the conversion to γ-FeOOH removes the $Fe^{III}(ad\text{-}H_2O)$ from the Fe_3O_4 surface, it will also oxidize $Fe^{II}(ad\text{-}H_2O)$ at the water/oxide interface. The rate of anodic oxidation is then determined by the rate of this transformation of the ferric species. The rate of the transformation increases with increasing surface area of γ-FeOOH. This increase in surface area can explain the continuous increase in current.

At –0.7 V_{SCE} (Figures 7.6 and 7.7) the EIS plots show two RC loops indicating the presence of a two-layered film. This is consistent with the proposed mechanism. The first EIS spectrum of a film grown in a 0.1 mM $Fe^{2+}_{(aq)}$ solution was taken at a time (4 h) when the current is still increasing with time. The Nyquist plot taken at this time is asymmetric and this is attributed to the overlap of two RC components. After 4 h, the overall impedance reaches a near steady-state value. This steady-state value is similar to that observed for a film grown in the absence of $Fe^{2+}_{(aq)}$, on the order of a few hundred ohms. In the solution initially free of $Fe^{2+}_{(aq)}$ the current reached a near steady-state value by the time the first EIS spectrum was taken. The EIS spectra taken at longer times (8 h and 14 h) are very similar for systems with and without initial $Fe^{2+}_{(aq)}$ and clearly show two RC circuit components. The resistances of the two circuit components are very low, ~ 150 Ω cm^2 and ~ 50 Ω cm^2; values that are on the order of the electrolyte resistance. The reasons for these low resistances are not clear. It is speculated that they are a combination of the Fe_3O_4 film resistance and the interfacial charge transfer resistance for oxidation of $Fe^{II}(ad\text{-}H_2O)$ to $Fe^{III}(ad\text{-}H_2O)$ at the oxide/water interface.

7.3.2.3 Oxide Formation at –0.5 V_{SCE}

SEM images of the surfaces held at –0.5 V_{SCE} in solutions with and without initially added $Fe^{2+}_{(aq)}$ show that they remained shiny after 22 h at this potential (Figure 7.8) and there is no evidence of particulates. The film grown in the solution initially free of $Fe^{2+}_{(aq)}$ shows patches of pearlite structure indicating that dissolution of some iron species has occurred. The remaining surface was covered by an even, compact layer. The surface corroded in the 0.1 mM $Fe^{2+}_{(aq)}$ solution does not show a pearlite structure. The original abrasion marks are clearly visible indicating that there was less metal dissolution and the oxide layer is thinner that in the $Fe^{2+}_{(aq)}$ free case.

Analyses of the high resolution XPS spectra give similar Fe and O compositions in the surface films formed in both solutions (Figure 7.11). The fractions of the metallic Fe^0 component of the Fe-2p band were larger for the films grown at –0.5 V_{SCE} compared to those grown at –0.7 V_{SCE} (Figure 7.11c). The XPS results are consistent with the thin films seen in the SEM images. The fraction of oxygen as OH^- (compare to that as O^{2-}) in the oxide lattice was lower at this potential than at any of the other potentials studied (Figure 7.11d). This indicates the presence of limited hydroxide formation in the oxide layer at this potential.

The Raman spectrum of the film grown at –0.5 V_{SCE} in the solution initially free of $Fe^{2+}_{(aq)}$ shows that the surface oxide is composed mainly of Fe_3O_4, Figure 7.9a. The Raman spectrum of a film grown in the solution initially containing 0.1 mM $Fe^{2+}_{(aq)}$ did not reveal well-defined peaks and only contained a broad band spanning the range from 250 to 1200 cm^{-1}. The source of this could not be identified, but it is suspect that it is due to hydrated oxides on the outer oxide surface. The oxide layer is apparently too thin to

provide any other characteristic Raman peaks at levels above background noise.

At −0.5 V_{SCE} the slopes of log i vs. log t are close to −1, with the slope observed for the tests with 0.1 mM $Fe^{2+}_{(aq)}$ being slightly steeper for the first 10^3 s (Figure 7.5b). This near linear decrease in current with time indicates that a stable oxide film is growing and that the competing rates of Fe^{II}/Fe^{III} dissolution are relatively slow. This behaviour can be attributed to the growth of a nearly insoluble Fe_3O_4 and perhaps γ-Fe_2O_3 film [3]. At this potential, the rate of electrochemical oxidation of Fe to Fe^{II} and then to Fe_3O_4 is very fast. The electrochemical conversion between Fe_3O_4 and γ-Fe_2O_3 is also known to occur very easily since they share the same spinel structure [20]. The applied potential of −0.5 V_{SCE} is near, but below the calculated equilibrium potential of Fe_3O_4/γ-Fe_2O_3, and therefore oxidation to a single phase γ-Fe_2O_3 may not occur. Rather the surface oxide could be described as a Fe^{II} depleted, or Fe^{III} enriched magnetite structure ($Fe^{II}_1Fe^{III}_{2+x}O_{4+3x/2}$). Early formation of an insoluble Fe_3O_4/ $Fe^{II}_1Fe^{III}_{2+x}O_{4+3x/2}$ layer (step 5 in Figure 7.12b) reduces the concentration of hydrated Fe^{II} species at or near the oxide/water interface and thereby suppresses metal dissolution (step 4 in Figure 7.12b). The formation of a $Fe^{II}_1Fe^{III}_{2+x}O_{4+3x/2}$ oxide will passivate the surface, compared to Fe_3O_4, and suppress further growth of an inner Fe_3O_4-like layer, thus explaining why the oxide layer is very thin. Surface hydration energy should be higher on a Fe^{II} depleted oxide than on Fe_3O_4 and this will suppress the formation of γ-FeOOH by the precipitation of Fe^{III} species on the outer oxide surface.

The presence of 0.1 mM $Fe^{2+}_{(aq)}$ in the solution will suppress the oxidative dissolution, as described above (step 4 in Figure 7.12b) and, hence, accelerate the formation of Fe_3O_4 and its oxidative conversion to $Fe^{II}_1Fe^{III}_{2+x}O_{4+3x/2}$ (step 5 in Figure

7.12b). Faster conversion passivates the surface sooner, resulting in the production of a thin inner Fe_3O_4 layer. This behaviour explains the absence of the Fe_3O_4 peak in the Raman spectrum for this case.

In the 0.1 mM $Fe^{2+}_{(aq)}$ solution, after 10^3 s, the anodic current increased and then decreased again (Figure 7.5b). The reason for this behaviour is not clear. The SEM images show signs of microfractures and some metal oxide crystals on the edges of these fractures. It is speculated that the fast growth of the Fe_3O_4 and $Fe^{II}_1Fe^{III}_{2+x}O_{4+3x/2}$ layers in the initial presence of $Fe^{2+}_{(aq)}$ may induce stresses at the metal/oxide interface and cause the fractures to occur. There is also the possibility that dehydration of the outer layer during sample drying may have induced stress and fractured the oxide film.

At –0.5 V_{SCE}, the EIS spectra (see Figures 7.6 and 7.7) indicate that the surfaces may be modelled using more than one RC component, with one RC component being orders of magnitude larger than the other. Extrapolation at low frequency prevents the determination of relative components; however, again, the initial presence of $Fe^{2+}_{(aq)}$ in solution has only a small influence on the EIS behaviour at this potential suggesting that $Fe^{2+}_{(aq)}$ diffusion in the oxide or iron dissolution does not play as a significant direct role in the electrochemical process.

7.3.2.4 Oxide Formation at 0.3 V_{SCE}

SEM images of the electrode surfaces held at 0.3 V_{SCE} are shown in Figure 7.8. In the solution initially free of $Fe^{2+}_{(aq)}$ a compact and smooth film was formed. However, the surface corroded in the 0.1 mM $Fe^{2+}_{(aq)}$ solution shows extensive formation of uniformly distributed, filiform crystallites that are characteristic of γ-FeOOH [25, 26]. The Raman

spectrum of the surface grown in the 0.1 mM $Fe^{2+}_{(aq)}$ solution also contains the characteristic peaks of γ-FeOOH and Fe_3O_4 (Figure 7.9b). No distinct Raman peaks were observed for the surface corroded at 0.3 V_{SCE} in the solution initially free of $Fe^{2+}_{(aq)}$. Despite the different surface morphologies, the XPS analyses reveal significant contributions of Fe^{III} to the Fe-2p band and of OH^- to the O-1s band in the oxides grown in both solutions (Figure 7.11a and 7.11b).

At 0.3 V_{SCE}, the currents have a two stage time-dependent behaviour (Figure 7.5c). In the first stage (occurring at $t < 10$ s) the currents both with and without initial $Fe^{2+}_{(aq)}$ had the same time-dependent behaviour. However, at longer times the current observed for the solution initially free of $Fe^{2+}_{(aq)}$ continued to decrease, albeit at a slightly lower rate than in the first 10 s, while the current in the solution initially containing 0.1 mM $Fe^{2+}_{(aq)}$ became nearly constant with time and remained so until 10^4 s when it suddenly dropped at near-linear rate. The plateau period of near constant current is attributed to the anodic oxidation of aqueous $Fe^{2+}_{(aq)}$ species to γ-FeOOH (step 6 in Figure 7.12c). The sudden decrease in current at about 10^4 s can then be attributed to the completion of the formation of a protective layer of γ-FeOOH. Once a coherent γ-FeOOH layer is formed, the current decreases linearly with time as this layer continues to grow.

The EIS spectrum of the film grown at 0.3 V_{SCE} in the absence of initial $Fe^{2+}_{(aq)}$ (Figure 7.6) has more than one RC component, similar to that observed for the films grown at –0.5 V_{SCE}. However, the impedance spectra of the films grown at 0.3 V_{SCE} are an order of magnitude higher than those for the films grown at –0.5 V_{SCE}. This is consistent with the early formation of a mainly Fe_3O_4 and more γ-Fe_2O_3-like film compared to –0.5 V_{SCE}, Figure 11. The EIS spectra of the films grown in the presence of 0.1 mM $Fe^{2+}_{(aq)}$ (Figure

7.7) are very noisy. This is indicative of a bulk solution diffusion-limited process in the electrolyte where the Ar-purging introduces noise. Despite the noise, it can be seen that the initial presence of $Fe^{2+}_{(aq)}$ in solution has the most influence on the EIS behaviour at this potential than that at the lower potentials. These observations are consistent with the oxidation of $Fe^{2+}_{(aq)}$ to form an extensive layer of γ-FeOOH which grows in filiform shapes. Since capacitance will increase with increasing surface area, the extensive formation of γ-FeOOH can explain the near pure capacitance behaviour in the EIS spectra.

The corrosion mechanism at 0.3 V_{SCE} can be summarized as follows. Electrochemical oxidation of Fe^0 to Fe^{II} and $Fe^{II/III}$ (magnetite) oxides occurs very fast at first. This is accompanied by fast conversion of the Fe_3O_4 to both γ-Fe_2O_3 and γ-FeOOH. If $Fe^{2+}_{(aq)}$ is present in solution, it will also oxidize to form γ-FeOOH that condenses on the electrode surface (step 6 in Figure 7.12c). The potential is sufficiently high that even the formation of γ-Fe_2O_3 cannot completely suppress current flow and an inner Fe_3O_4 oxide layer can grow at a reasonable rate. In the absence of initial $Fe^{2+}_{(aq)}$ in the solution, the formation of Fe^{III} oxide and oxyhydroxide on the outer oxide surface will occur due to the oxidation of Fe_3O_4. This process requires metal ion transport through the solid oxide phase and results in the formation of a uniform oxide layer (step 7 in Figure 7.12c).

7.4 CONCLUSIONS

The effect of dissolved ferrous iron ($Fe^{2+}_{(aq)}$) on surface oxide film growth and conversion on carbon steel in pH 8.4 borate solutions was studied as a function of potential. At potentials < –0.4 V_{SCE}, Fe^0 in the metal substrate can oxidize to Fe^{II} and then be further oxidized at the oxide/water interface to form a $Fe^{II/III}$ (magnetite) oxide layer. At the

Fe_3O_4/water interface, hydrated ferrous hydroxide can be oxidized to ferric hydroxide which is then slowly transformed to γ-FeOOH. The presence of $Fe^{2+}_{(aq)}$ in solution somewhat suppresses the rate of dissolution of Fe^{II} from the metal oxide and thus reduces the net rate of anodic oxidation. At potentials > –0.4 V_{SCE}, Fe_3O_4 can further oxidize to form γ-Fe_2O_3 and γ-FeOOH, while $Fe^{2+}_{(aq)}$ continues to form γ-FeOOH. The presence of $Fe^{2+}_{(aq)}$ in the aqueous phase at a concentration of 0.1 mM substantially increases the rate of formation of needle-like γ-FeOOH crystals on the oxide surface and this material constitutes most of the oxide that forms.

7.5 REFERENCES

[1] J.M. Joseph, B.S. Choi, P. Yakabuskie, J.C. Wren, Radiat. Phys. Chem., 77 (2008) 1009-1020.
[2] P. Yakabuskie, J.M. Joseph, J.C. Wren, Radiat. Phys. Chem., 79 (2010) 777-785.
[3] L. Wang, K. Daub, Q.W. Knapp, Z. Qin, J.J. Noël, J.C. Wren, J. Electrochem. Soc., (2012) Accepted (JES-12-1784R1781).
[4] K. Kuroda, B.D. Cahan, G. Nazri, E. Yeager, T.E. Mitchell, J. Electrochem. Soc., 129 (1982) 2163-2169.
[5] J. Gui, T.M. Devine, J. Electrochem. Soc., 138 (1991) 1376-1384.
[6] A.J. Davenport, J.A. Bardwell, C.M. Vitus, J. Electrochem. Soc., 142 (1995) 721-724.
[7] L.J. Oblonsky, S. Virtanen, V. Schroeder, T.M. Devine, J. Electrochem. Soc., 144 (1997) 1604-1609.
[8] M. Buchler, P. Schmuki, H. Bohni, J. Electrochem. Soc., 145 (1998) 609-614.
[9] V. Schroeder, T.M. Devine, J. Electrochem. Soc., 146 (1999) 4061-4070.
[10] S.J. Ahn, H.S. Kwon, Electrochim. Acta, 49 (2004) 3347-3353.
[11] M. Nagayama, M. Cohen, J. Electrochem. Soc., 109 (1962) 781-790.
[12] C.L. Foley, J. Kruger, C.J. Bechtoldt, J. Electrochem. Soc., 114 (1967) 994-1001.
[13] S. Modiano, C.S. Fugivara, A.V. Benedetti, Corros. Sci., 46 (2004) 529-545.
[14] W. Xu, K. Daub, X. Zhang, J.J. Nöel, D.W. Shoesmith, J.C. Wren, Electrochim. Acta, 54 (2009) 5727-5738.
[15] A.E. Kehew, Applied chemical hydrogeology, Prentice Hall, Upper Saddle River, N.J., (2001).
[16] T. Misawa, Corros. Sci., 13 (1973) 659-676.
[17] R.M. Cornell, U. Schwertmann, The Iron Oxides: Structures, Properties, Reactions, Occurrences and Uses, 2nd Ed., Weinheim, New York, NY, (2003).
[18] S.J. Oh, D.C. Cook, H.E. Townsend, Hyperfine Interact., 112 (1998) 59-66.

[19] J. Dunnwald, A. Orro, Corros. Sci., 29 (1989) 1167-1176.
[20] K. Daub, X. Zhang, J.J. Noël, J.C. Wren, Electrochim. Acta, 55 (2010) 2767-2776.
[21] C.Y. Chao, L.F. Lin, D.D. Macdonald, J. Electrochem. Soc., 128 (1981) 1187-1194.
[22] B. Beverskog, M. Bojinov, A. Englund, P. Kinnunen, T. Laitinen, K. Mäkelä, T. Saario, P. Sirkiä, Corros. Sci., 44 (2002) 1901-1921.
[23] B. Beverskog, M. Bojinov, P. Kinnunen, T. Laitinen, K. Mäkelä, T. Saario, Corros. Sci., 44 (2002) 1923-1940.
[24] I. Betova, M. Bojinov, P. Kinnunen, K. Mäkelä, T. Saario, J. Electroanal. Chem., 572 (2004) 211-223.
[25] D. Fu, J.C. Wren, J. Nucl. Mater., 374 (2008) 116-122.
[26] D. Fu, P. Keech, X. Sun, J.C. Wren, Phys. Chem. Chem. Phys., 13 (2011) 18523-18529.

Chapter 8

Oxide Growth and Conversion on Carbon Steel as a Function of Temperature Between 100 °C and 280 °C

8.1 INTRODUCTION

This study examined the effect of temperature in a range between 100 °C and 280 °C on oxide film growth and conversion on carbon steel as a function of potential at $pH_{25°C}$ = 10.6 using primarily electrochemical techniques. High pressure vessels were used for all experimentation. The combined understanding of the data presented in this chapter and in Chapter 3 provides an electrochemical basis of the corrosion process, upon which, ex-situ surface analyses presented in Chapters 5 and 6 allow for the development of a more complete interpretation of the oxidation mechanism.

8.2 EXPERIMENTAL

8.2.1 Pressure Vessel (Static Cell)

A 1000 mL alloy C-276 pressure vessel (Parr Instrument Company) was used for all experiments. The pressure vessel contained a gauge block assembly system with a 0 to 2000 psi gauge, a gas hose assembly allowing for argon purging prior to an experiment, and NPT-type inlets for the fastening of various electrodes of interest. The vessel contained a removable 1000 mL plytetrafluoroethylene (PTFE) polymer liner creating an inert electrochemical cell environment free of solution contact with the pressure vessel wall. The three-electrode system added to the pressure vessel consisted of a reference electrode, a Pt mesh counter electrode and a carbon steel working

electrode. The reference electrode was a standard external pressure balanced Ag/AgCl reference probe (Corrinstruments) which can function in a temperature range of room temperature to 300 °C. The reference electrode system consists of the reference system of saturated Ag/AgCl being external to the pressure vessel and maintained at room temperature. The reference system is electrochemically connected to the system via an external probe 50 cm in length outside of the vessel and 12 cm in length internal to the vessel. The entire probe, 62 cm in length, contained saturated KCl, which is connected to a saturated KCl liquid junction exposed to solution. To ensure stability of the external saturated Ag/AgCl reference electrode and the accuracy of measurements, the reference electrode was measured against a master saturated calomel electrode (SCE) before and after all experiments. For the results presented, all potentials are reported as the measured potential against the external electrode, converted to the SCE scale. The combined effects of a thermal potential difference and changing solution pH on the measured oxidation reactions were not taken into account for potential conversion, which can be seen in the CV results to present a net minimal change in the potential window studied. The current study aims to present a generalized picture of the oxidation over a wide temperature range. Comparison to possible future E_{CORR} measurements or in-situ high temperature electrochemical studies will require further correction.

The carbon steel was machined into a cylindrical rod with a diameter of 10 mm and a surface of known area was exposed to solution. Prior to each experiment, the working electrode was abraded manually with 400 and 600 grit silicon carbide papers, and lastly sonication in an acetone/methanol mixture for 5 min to remove polishing residues.

8.2.2 Solutions

All experiments were conducted in 0.01 M sodium borate solutions. The solutions were prepared using reagent grade $Na_2B_4O_7 \cdot 10H_2O$ (Caledon Laboratories Ltd.) and water purified using a NANOpure Diamond UV ultra-pure water system (Barnstead International) with a resistivity of 18.2 MΩ·cm. Reagent grade NaOH (Caledon Laboratories Ltd.) was added drop-wise to the solutions to adjust the pH. All experiments were conducted at a $pH_{25°C}$ of 10.6.

8.2.3 Procedure

During the electrode polishing procedure argon was bubbled through the borate solution in the PTFE liner for 1 h. After polishing and sonication, the working electrodes were rinsed with deionized water, connected to the working electrode lead in the pressure vessel head, and the working electrode connection was tightly insulated with PTFE tape. The pressure vessel head was then sealed to the main body of the vessel, followed by argon purging for 1.5 h. After purging the pressure vessel was placed inside a 115 V heater assembly with one heater probe at the side wall on the vessel and a second at the bottom of the vessel (Parr Instrument Company). The entire system was insulated to minimize heat loss. Heating to the desired temperature (100 °C, 150 °C, 200 °C, or 220 °C) with the use of a programmable temperature control (Parr Instrument Company) began immediately when the pressure vessel was placed in the heater assembly. Electrochemical experiments then began with cathodic cleaning at -1.1 V_{SCE} for 5 min. Following cathodic cleaning, two types of experiments were performed, CV and 7 d potentiostatic film growth. For the potentiostatic experiments, immediately following

cathodic cleaning, the electrode was anodized at an E_{APP} of –0.7 V_{SCE}, –0.2 V_{SCE}, or 0.2 V_{SCE} with the intention of generating oxide films with different compositions and properties. Therefore, polarization of the working electrode began during the heating process, which took roughly 30 min, 90 min, or 120 min for 100 °C, 150 °C, and 200 °C respectively. EIS was recorded at periodic intervals during the 7 d potentiostatic experiments. For all CVs the system was heated to the desired temperature (150 °C or 220 °C) before the CV was performed. Therefore, the system remained under open circuit potential conditions, resulting in an initial oxide (most likely Fe_3O_4) to form before the CV was performed. Once at the desired temperature the CV was cycled between potential limits of –1.1 V_{SCE} and +0.4 V_{SCE} at a scan rate of 5 $mV \cdot s^{-1}$. Additional CVs were recorded following the 7 d potentiostatic polarization at E_{APP} of –0.2 V_{SCE}. The dependence of cyclic voltammograms on temperature was investigated to compare to results in Chapter 3.

8.2.4 Korean Atomic Energy Research Institute (KAERI) Flow Cell

The system consisted of a carbon steel working electrode, platinum counter electrode, and Ag/AgCl external reference electrode. The electrochemical cell body containing the three electrodes was approximately 10 mL in size. The steel was processed into a cylindrical rod with a diameter of 1.5 mm, insulated with shrink tube, and a surface of known area was exposed to solution. Prior to each experiment, the working electrode was abraded manually with 400 and 600 grit silicon carbide papers, and lastly sonication in an acetone/methanol mixture for 5 min to remove polishing residues. The platinum counter electrode was a platinum coil for maximum surface area.

The Ag/AgCl reference electrode was maintained at a distance and angle to ensure it remained at room temperature, and the electrode was checked regularly between experiments against a master SCE reference electrode. All experiments were conducted in Ar-sparged 0.001 M lithium borate (Sigma-Aldrich) solutions, adjusted to $pH_{25°C}$ 10.6 with lithium hydroxide (Sigma-Aldrich). The Ar (Daesung Industrial Gases Co. LTD) was 99.999% purity.

To date, completed details of the experimental setup have not been published by the research group of Dr. Yeon at KAERI. Figure 8.1 is a photograph that labels some of the key features of the flow cell and provides scale of the entire system.

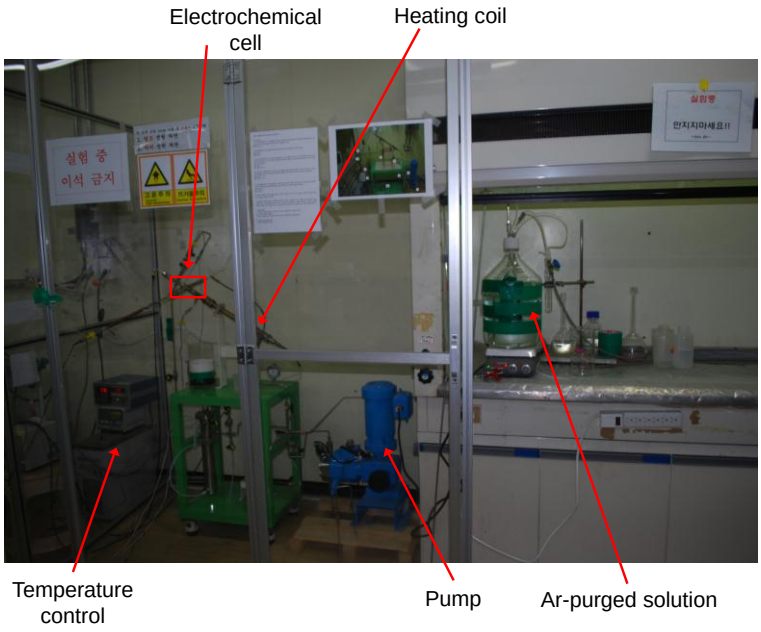

Figure 8.1: Photograph labeling some key components of the high-temperature flow cell developed at KAERI.

A Bio-Logic potentiostat/galvanostat/FRA, model SP-300 was used for all electrochemical studies. EC-Lab V10.1 was used for data analysis. The procedure began with purging the solution with Ar and saturating the entire system with the borate solution. The working electrode was abraded to 600 grit silicon carbide paper and rinsed with acetone followed by rinsing with water and drying. The working electrode was then inserted into the flow cell, and further saturation of the system continued for 1 h, while the pressure was raised and maintained at 110 bar for the remainder of the experiment. After 1 h, electrochemical experiments began with cathodic cleaning at –1.1 V_{SCE} for 5 min. After cathodic polarization, the electrode was anodized at an E_{APP} of –0.7 V_{SCE}, –0.2 V_{SCE}, or 0.2 V_{SCE} with the intention of generating oxide films with different compositions and properties. Upon the initiation of polarization, the system was heated to the desired temperature, of either 200 °C or 280 °C. Heating to the desired temperature took approximately 25 min. Upon completion of the experiment, polarization was stopped and the system was cooled to room temperature and pressure was lowered. After some polarization experiments, the temperature was not cooled and CVs were recorded between potential limits of –1.0 V_{SCE} and +0.5 V_{SCE} at a scan rate of 5 $mV \cdot s^{-1}$. For all experiments the flow rate was 15 $mL \cdot min^{-1}$.

8.3 RESULTS AND DISCUSSION

8.3.1 Cyclic Voltammetry

Cyclic voltammetry was performed at various temperatures to determine possible surface redox activity on carbon steel as a function of potential. The first and third cycle of CVs recorded at various temperatures in the static cell are presented in Figure 8.2. The

first cycle of the CV at room temperature shows different behaviour than the subsequent cycles which we attributed to time required for surface modification arising from the air-formed oxide that is present on a freshly prepared carbon steel electrode [1]. This difference decreases with an increase in temperature, except for the increase in current density of peak A1 and its accompanying cathodic peaks upon cycling.

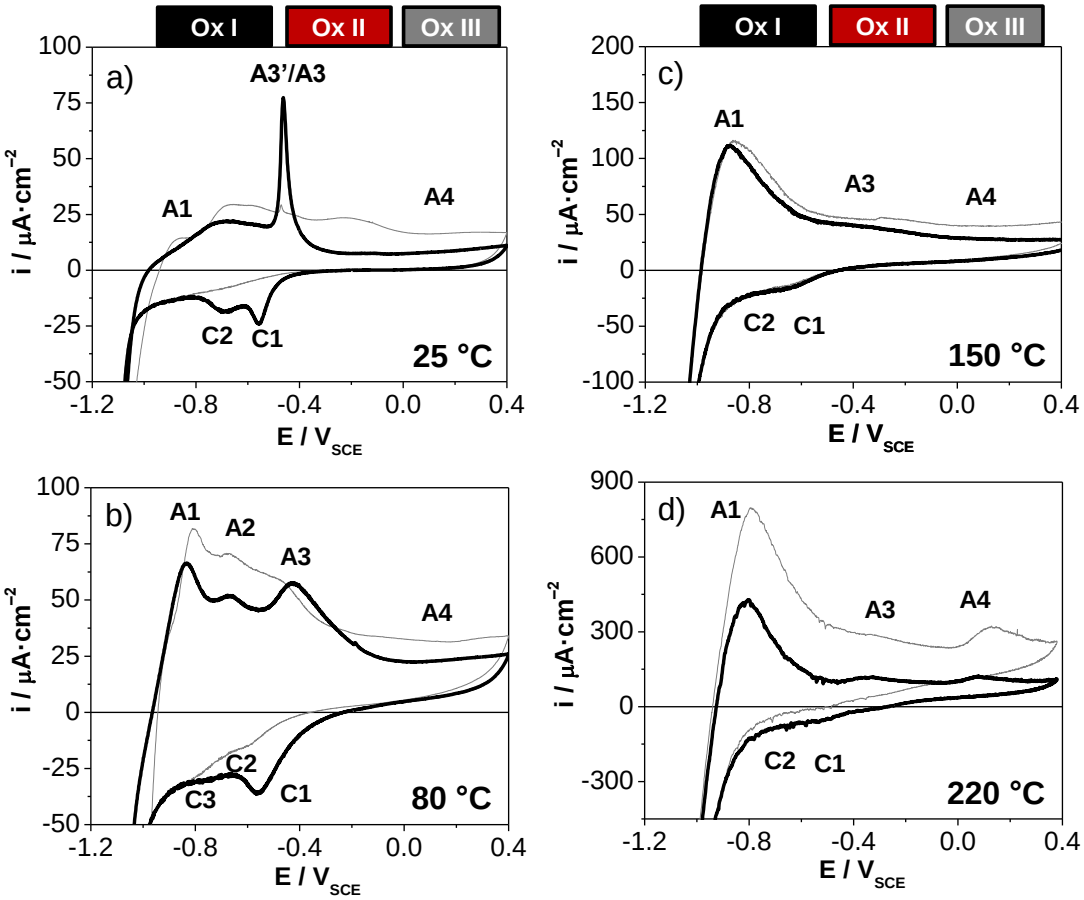

Figure 8.2: First (gray line) and third (black line) cycles of CVs at (a) 25 °C, (b) 80 °C, (c) 150 °C, and (d) 220 °C. All CVs were performed immediately after the system reached the desired temperature and were performed at a scan rate of 5 $mV \cdot s^{-1}$.

The CVs show that the three characteristic potential ranges assigned for the behaviour of anodic current at temperatures ≤ 80 °C are still maintained at higher temperatures. That is, the anodic current peak A3 starts at approximately −0.5 V_{SCE} and the broad peak A4 starts at approximately −0.1 V_{SCE} at all temperatures. These oxidation potential regions are indicated on the top of the CVs using bars labeled with Ox I, Ox II and Ox III. However, the current density and the potential dependence within each region vary with temperature.

In the previous studies at lower temperatures (Chapter 3), it was established that the three characteristic potential regions observed in CVs can be correlated to the thermodynamic stability regions of different oxides as shown in Figure 8.3. The equilibrium potentials of various iron redox pairs are shown and the oxidative conversion from one oxide to another as potential increases is shown by arrows. The potential scale shown in Figure 8.3 is for pH 10.6 and at room temperature. The oxidative conversions shown with dotted lines are thermodynamically possible but kinetically not favoured at least at low temperatures. The three potential regions shown on the top of the CVs are also indicated in this figure.

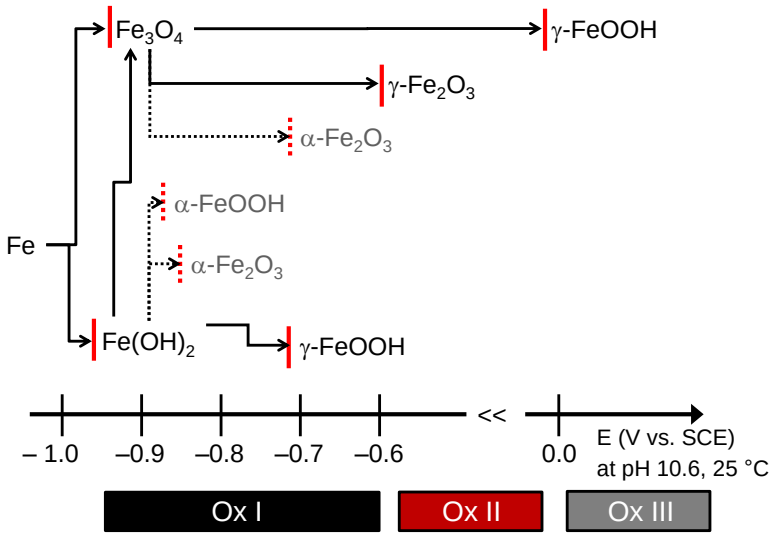

Figure 8.3: Calculated equilibrium potentials for various iron redox reactions on the electrochemical potential scale; where the equilibrium potentials are indicated by vertical lines and the potential values are those at pH 10.6 and 25 ºC. The three oxidation potential regions are also indicated.

Temperature affects the electrochemical potentials of the solid metal and metal oxides similarly. Since it is the difference in the electrochemical potentials of the reacting phases that drives the electrochemical reaction, temperature would not significantly influence the equilibrium potentials of the iron redox pairs [2, 3]. This is further confirmed in this study by the observation that the three characteristic potential regions are maintained. The observation suggests that the metal oxidation (electrochemical) reactions that can happen in each potential region are the same, independent of temperature over the studied range (up to 280^{o}C).

Temperature can, however, affect the rates of thermal processes such as diffusion, phase transformation and surface hydration. For this study the two processes largely effected by temperature are the Schikorr reaction ($Fe(OH)_2$ to Fe_3O_4 oxidation) and iron

dissolution. This results in a balance between the Schikorr reaction increasing oxide growth rate and thickening and dissolution limiting the growth and thickening of the oxide. The observed temperature-dependence of the current density and its potential dependence within each potential region can then be explained by examining how these thermal processes influence the rates of the electrochemical reactions responsible for the current peaks.

Additionally to the CVs presented in Figure 8.2, some CVs were performed after a period of prolonged potentiostatic film growth. Figure 8.4 compares CVs performed either immediately after reaching the desired temperature, or after the 7 d potentiostatic film growth of E_{APP} = –0.2 V_{SCE} in the static cell. A reducing potential of –1.1 V_{SCE} was applied for 5 min prior to both CVs. While applying –1.1 V_{SCE} can reduced a significant amount of the oxide formed on the surface, it has been shown that Fe_3O_4 is not fully reducible [1]. Therefore, a certain amount of Fe_3O_4 would be expected to remain on the electrode surface after cathodic cleaning for all CVs, with more Fe_3O_4 present on the CVs recorded after periods of polarization at –0.2 V_{SCE}.

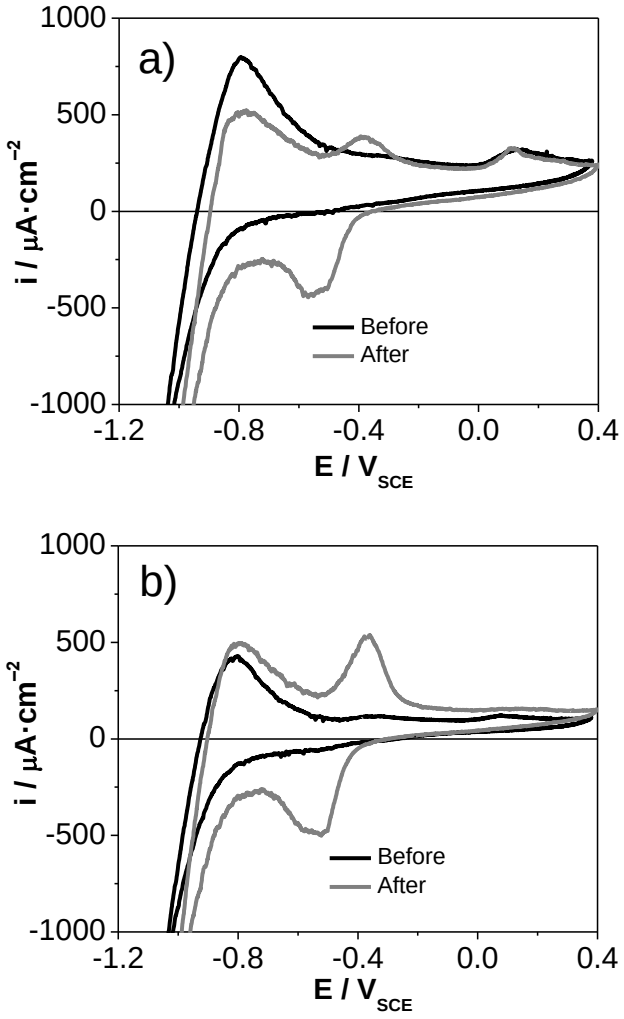

Figure 8.4: (a) First and (b) third cycles of CVs recorded at 220 °C at a scan rate of 5 $mV \cdot s^{-1}$. Compared are CVs recorded immediately after the system reached 220 °C (Before) and CVs recorded after a 7 d potentiostatic film growth of $E_{APP} = -0.2\ V_{SCE}$ (After).

Summarized below are the observed peaks in the CVs, the corresponding electrochemical reactions that can occur in each potential region, and the influence of temperature on the rates of the reactions. All observations are made as a comparison to the previously identified peaks at temperatures ≤ 80 °C, Chapter 3.

8.3.1.1 Anodic Peak A1

According to the electrochemical equilibrium potential diagram at a potential in Ox I the oxidation of Fe^0 to Fe^{II} species ($FeO/Fe(OH)_2$) and further to a mixed Fe^{II}/Fe^{III} oxide (Fe_3O_4) is possible, resulting in the anodic current peak A1 in region Ox I. Under mildly basic pH the rate of deposition of the nearly insoluble Fe_3O_4-like oxide is fast relative to the Fe^{II} dissolution, leading to formation of a uniform layer of the inverse spinel oxide.

Previously seen, at temperatures ≥ 70 °C the Fe_3O_4-like layer thickened significantly upon cycling due to the thermally promoted oxidation of $Fe(OH)_2$ to Fe_3O_4. With a thicker oxide layer, the charge transport from the metal/oxide interface to the oxide/water interface is slower and it becomes a contributing factor in determining the rate of electrochemical oxidation. This can be observed in the CVs recorded as a function of scan cycle, Figure 8.5, in which peak A1 decreased as scan cycle number increased due to a continued thickening of the Fe_3O_4 layer over the course of the CV.

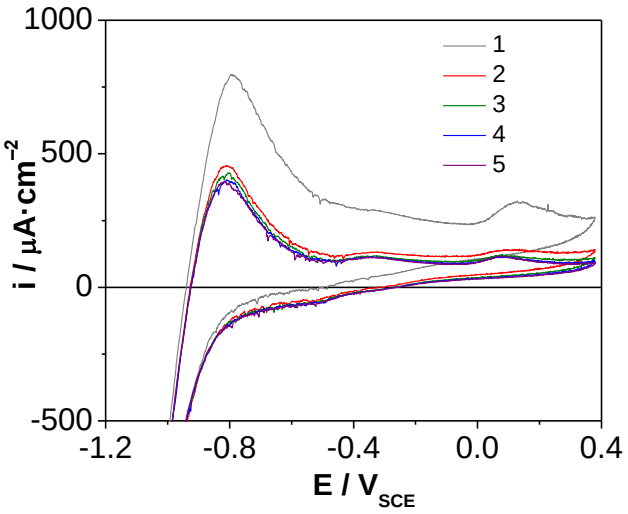

Figure 8.5: CV recorded at 220 °C at a scan rate of 5 $mV \cdot s^{-1}$. The CV was recorded immediately after the system reached 220 °C.

After the second cycle, peak A1 had a slight decrease in current density as function of scan cycle number, Figure 8.5. Once the surface is covered with a uniform Fe_3O_4-like layer, dissolution of iron occurs at the oxide/water interface and involves surface hydration of Fe^{II} and Fe^{III} followed by diffusion of the hydrated species away from the interface into the bulk aqueous phase. The current density of peak A1 generally increased with an increase in temperature (under identical experimental conditions) and this can be attributed to an increase in hydration and dissolution of Fe^{II} (and Fe^{III} to a smaller extent) from the Fe_3O_4 surface.

A previously observed peak A2 and its corresponding cathodic peak C3 was not detected in any recorded CVs. Peak A2 was attributed to the oxidation of surface $Fe(OH)_2$ to FeOOH. Peaks A2 and C3 had very small current densities and perhaps the

increased current density of peak A1 would limit the detection of peak A2. There is also the possibility that an increased consumption of $Fe(OH)_2$ via the Schikorr reaction would limit the oxidation of $Fe(OH)_2$ to other surface hydroxides.

The conversion of the Fe^{II} and the Fe^{II}/Fe^{III} species to α-FeOOH or α-Fe_2O_3 is also thermodynamically possible in region Ox I. However, the conversion requires a significant change in the oxide phase structure [4] and hence, is not kinetically favoured during the CV scans.

8.3.1.2 Anodic Peaks A3' and A3/Cathodic Peaks C1 and C2

Room temperature studies have shown that the anodic peaks A3' and A3 on the forward scan are associated with two cathodic peaks C2 and C1, respectively, observed on the reverse scan . Peak A3' labels the sharp current peak at the more negative potential while A3 is the broader peak at a more positive potential (Chapter 3). The sharper peak A3', coupled with the smaller reduction peak C2 at –0.7 V_{SCE}, is attributed to the anodic conversion of the surface layer of the Fe_3O_4 phase. The broader peak A3 is attributed to the oxidative conversion of Fe_3O_4 to a γ-Fe_2O_3 phase via charge transport through the solid phase. While the anodic peak A3' and its corresponding cathodic peak C2 became negligible at temperatures > 70 °C, peak A3 broadened significantly with increasing temperature. For the current studies, peak A3 continued to be a broad peak and A3' was not visible. As temperature increases, the underlying Fe_3O_4 layer thickens. The proposed solid-state oxidation method of Fe^{II} to Fe^{III} conversion will depend on the thickness of the inner Fe_3O_4-like layer that has been formed prior to the oxidation to γ-Fe_2O_3. Thus, the net rate of charge transport will also be a function of temperature

since it will depend on the concentrations of Fe^{II} and Fe^{III} and their distribution within the oxide lattice. The slower oxidation process leads to a broadening of peak A3.

Only in the case of the CV recorded at 280 °C in the flow cell after a 6 h potentiostatic experiment was a separation of peaks observed, Figure 8.6. Also, only in this case was the reduction peak C2 visible. As the number of scan cycles increased there was less of a distinction between two peaks and the cathodic peak C2 was no longer visible.

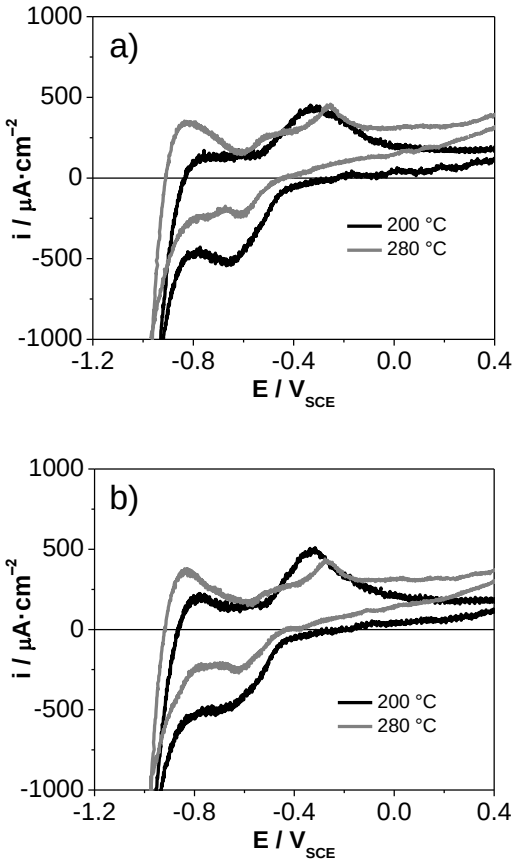

Figure 8.6: (a) First and (b) third cycles of CVs recorded at a scan rate of 5 $mV \cdot s^{-1}$ in the flow system. The CVs at both temperatures were recorded after a 6 h potentiostatic film growth of $E_{APP} = -0.2\ V_{SCE}$.

For each CV cycle it appears that a sharper appearance of peak A1 leads to a sharper appearance of A3, providing further evidence of the relation between peak A1 (oxidation to Fe_3O_4) and peak A3 (oxidation of Fe_3O_4 to γ-Fe_2O_3)

8.3.1.3 Anodic Peak A4

Peak A4 is associated with the broad anodic region above –0.1 V_{SCE} that has a relatively constant current with potential. The effect of temperature on the current is difficult to discern due to the large contribution of peak A3. Previously, this potential region has been attributed to the anodic conversion of the γ-Fe_2O_3-like layer (Fe_3O_4/γ-Fe_2O_3) to γ-FeOOH. This oxidation process has been observed to induce structural changes and micro-fractures in the oxide [5]. Peak A4 continued to be a region of mostly constant current with potential and the current density of peak A4 increased with an increase in temperature under identical experimental conditions. In the case of CVs recorded at 220 °C a distinguishable peak was present above 0.0 V_{SCE} in the first cycle, but was not evident on subsequent cycles, suggesting it is either the oxidation of a surface species that is no longer present on subsequent cycles, or is limited as the oxide changes (thickens) in subsequent cycles.

8.3.2 Current Behaviour During Potentiostatic Film Growth and EIS Analysis

The film growth and conversion as a function of temperature was further investigated under potentiostatic conditions. Three potentials, one from each potential region, were investigated. While applying a potential the current was monitored as a function of time, Figure 8.7. During polarization, EIS was performed periodically to

characterize the oxide film present on the electrode. The current behaviour is discussed first. Experiments were performed in both the static cell and flow cell and their behaviour is compared. All experiments were performed from a freshly polished electrode that was cathodically cleaned at –1.1 V_{SCE} followed by polarization. Polarization and heating began at the same time.

Similar to previous studies (Chapter 3), at all temperatures and all applied potentials, the current observed was initially high at ~ 1 $mA \cdot cm^{-2}$ and remained at that level for a few seconds. The most likely cause for the high initial current is significant oxidative dissolution from the freshly polished surface.

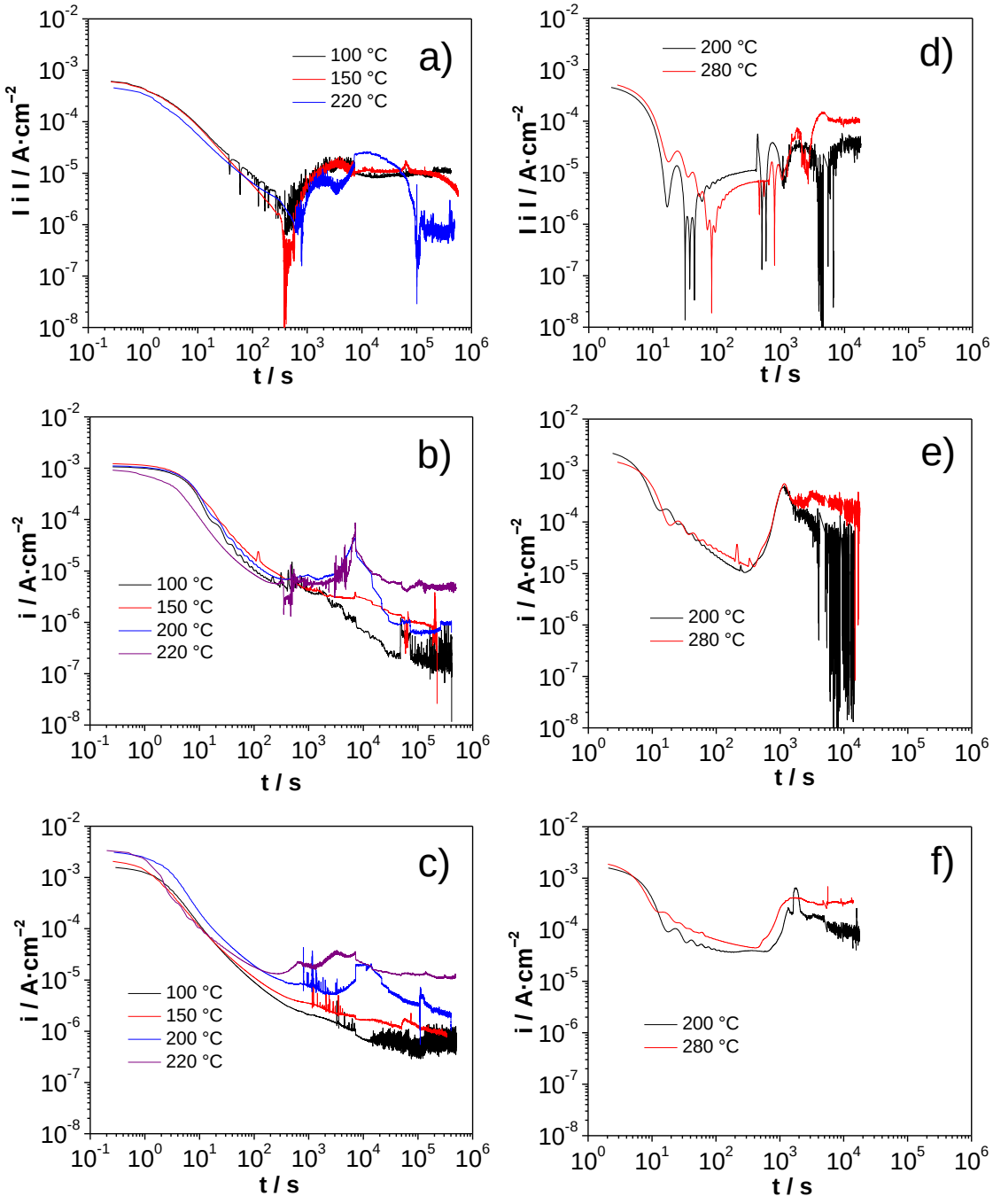

Figure 8.7: Log current vs. log time during potentiostatic film growth in the (a-c) static cell and (d-f) flow cell. Film growth was recorded at (a,d) –0.7 V_{SCE}, (b,e) –0.2 V_{SCE}, and (c,f) 0.2 V_{SCE}.

8.3.2.1 Current Behaviour in Ox I

In the static cell and for all temperatures studied, the initially anodic current switched signs, becoming cathodic at 500 to 700 s. Therefore, the switch to a cathodic current occurred during the heating process. The cathodic current quickly reached a steady-state value and remained constant at approximately 10^{-5} A·cm^{-2}. Similar observations were observed at temperatures ≤ 80 °C. The cathodic current is attributed to the fact that Fe_3O_4 is conducting and, hence, its formation on carbon steel can continually support water reduction to H_2. The cathodic current due to water reduction was present from the early stages of potentiostatic film growth on carbon steel. However, as the oxide thickened and the anodic current decreased, the cathodic current from water reduction on the conducting surface dominated the current behaviour at longer times. In the flow cell the switch to cathodic current occurred at 200 to 240 s and remained constant at approximately at 10^{-5} A·cm^{-2}. The introduction of a flowing solution would not affect the reduction of water since it is readily available and therefore a similar cathodic current would be expected in both systems.

At 100 °C, similar to the previous studies, the current remained cathodic for the duration of the experiment, however at 150 °C and 220 °C changes in the measured current occurred over periods of prolonged polarization. At 220 °C the current switched back to anodic at roughly 10^5 s and remained constant at approximately 10^{-6} A·cm^{-2} for the remainder of the experiment. At 150 °C the current began to decrease near the end of the experiment, suggesting that if the cathodic current is constant the anodic current is increasing. In the flow cell, the current switched back to anodic at 5000 s and 1000 s at 200 °C and 280 °C respectively. Since the measured current is a net current, it has

contributions from the reduction process (water reduction) and oxidation process (Fe and $Fe(OH)_2$ oxidation to Fe_3O_4, accelerated by dissolution). As temperature is increased, the dissolution is increased (Figure 8.2), explaining the switch to a net anodic current at earlier times with higher temperatures in both systems (Figure 8.7a) and the larger final net current at 280 °C compared to 200 °C. In a flowing solution, the loss of hydrolyzed iron species from the electrode surface to the bulk solution would be accelerated, thus accelerating the anodic process, explaining the switch to a net anodic current at times two orders of magnitude earlier than in the static cell. Since the final net anodic current was similar in magnitude (Figure 8.7f), or lower in magnitude (Figure 8.7a), than the net cathodic current, the cathodic and anodic processes must have been occurring at similar rates. This may explain some of the fluctuations in the net current observed in the flow cell, since periodic fluctuations of the dissolution of surface hydrated species could occur.

The switch from anodic to cathodic current was not observed at the higher potentials where the current remained anodic the potentiostatic growth.

8.3.2.2 Current Behaviour in Ox II

In the static cell, within the first 10^3 s the current decreased linearly with time, similar to what was observed at temperatures ≤ 80 °C. After 10^3 s, large variations in the anodic current as a function of temperature were seen. This was similarly observed previously, where at 50 °C and 70 °C, the current became nearly constant over the period of time around 10^3 s, before it decreased linearly with time again. This behaviour was attributed to an increase in the rate of dissolution of Fe^{II} from the conducting Fe_3O_4 layer. In the static cell, only a slight change in slope occurred at 100 °C, the current remained

constant between 10^3 and 10^4 s at 150 °C, and the current increased an order of magnitude between 10^3 and 10^4 s at 200 °C and 220 °C. The increase in current as a function of temperature due to dissolution would be expected. As the oxidation continued, the conversion of the Fe_3O_4 oxide layer to a more insulating γ-Fe_2O_3 layer reduces the rate of dissolution of Fe^{II} species from the oxide layer and thus suppresses electrochemical oxidation. This explains the further drop in current after 10^4 s at all temperatures. As the conversion takes place, the anodic current decreases with time until the anodic current is limited by the dissolution current and becomes constant. In the flow cell, at 200 °C and 280 °C, the behaviour of the anodic current was similar to that observed in the static cell at 200 °C and 280 °C. The current both increased as a function of temperature and was larger than that observed in the static cell. As in the case of Ox I, a flowing system would be expected to increase the rate of dissolution of surface hydrolyzed species, thus the resulting current would be accelerated by dissolution. Since the flow cell experiments were limited to times of roughly 6 h (~$2x10^{-4}$ s), it is unclear as to what extent the anodic current would decrease due to the conversion of some of the Fe_3O_4 oxide layer to a more insulating γ-Fe_2O_3 layer. For both temperatures the current was decreasing as a function of time when the experiment was stopped. In the flow cell, after the period of increased current due to dissolution, the current did decrease as well, however the decrease was less steep than in the static cell.

8.3.2.3 Current Behaviour in Ox III

As was previously observed, an initial linear decrease in the current was observed, which is attributed to the oxidation of the base Fe^0 to Fe_3O_4. At temperatures ≤ 80 °C,

the linear decrease continued until the end of the experiment for all temperatures. In the static cell, larger variations were seen as a function of temperature. Firstly, at temperatures ≤ 200 °C a number of sharp spikes in current were observed, which disappeared as time progressed, and the systems reached steady-state temperatures. Spikes in the anodic current during polarization in Ox III have previously been observed at room temperature [1]. The behaviour of the current was attributed to micro-fracture of the protective oxide layer due to the anodic conversion of the Fe_3O_4/γ-Fe_2O_3 oxide to γ-FeOOH, followed by repassivation of the film. The lack of spikes in current during prolonged oxidation agrees with the CVs at 220 °C which had a distinguishable peak in Ox III only in the first cycle, Figure 8.5. During subsequent cycles and likely growth of the underlying Fe_3O_4, the clear peak was no longer distinguishable.

At 100 °C and 150 °C the current continued to decrease as a function of time, however, at a shallower slope than that in the first 10^3 s. At 200 °C and 220 °C an increase in current, similar to what was observed in Ox II at the same temperatures, was observed. The increase in current is also likely due to the increased rate of dissolution as a function of temperature. At 200 °C, the increase in current at ~10^3 s was followed by a decrease in current, as was observed at 200 °C and 220 °C in Ox II. At 220 °C, the current only had a slight decrease after the increase due to dissolution, and remained relatively constant over the remainder of the measurement.

In the flow cell, the current also had an increase, followed by a period of relatively constant current over the remainder of the measurement. The current was larger under the flow cell, as compared to the static cell, due to the increased dissolution rate.

8.3.2.4 Temperature Dependence of Steady-State Current

Since at steady state the rate of metal oxidation is equal to the rate of dissolution of metal ions, the steady-state current represents the dissolution rate of metal ions from the surface oxide. The steady-state currents observed (including those obtained in Chapter 3) at 0.2 V_{SCE} and –0.2 V_{SCE} show Arrhenius temperature dependences, Figure 8.8. At these two potentials the steady-state current increased nearly exponentially as 1/T decreases. At –0.7 V_{SCE} an Arrhenius dependence was not observed because the steady-state current observed at –0.7 V_{SCE} is mainly due to the measured water reduction at most temperatures. Various regions of the temperature dependence of the steady-state current at –0.2 V_{SCE} and 0.2 V_{SCE} can be observed. At temperatures < 80 °C, a steeper slope (or higher activation energy) is present for the 0.2 V_{SCE} case compared to –0.2 V_{SCE}. In these cases, where the oxides are relatively thin (Chapter 3) the slight increase in surface Fe^{III} oxides (γ-FeOOH) at 0.2 V_{SCE} would have a higher activation energy for hydration and dissolution. At temperatures > 100 °C there is a loss of a linear Arrhenius temperature dependence, suggesting that the measured steady-state current is simply limited by diffusion (mass transport) of the hydrated species from the surface. The steady-state currents from the flow cell, which would lessen mass transport effects, show a linear behaviour with the measured steady-state currents in the static cell at lower temperatures. There is no difference in the Arrhenius slope (activation energy) between the two applied potential cases. This would be expected, since similar oxides, particularly composed of surface Fe^{III} oxides, would require similar surface hydration energies. The calculated activation energies are approximately 80 kJ/mol, which agrees well with previously reported dissolution activation energies of various Fe^{III} oxides [6].

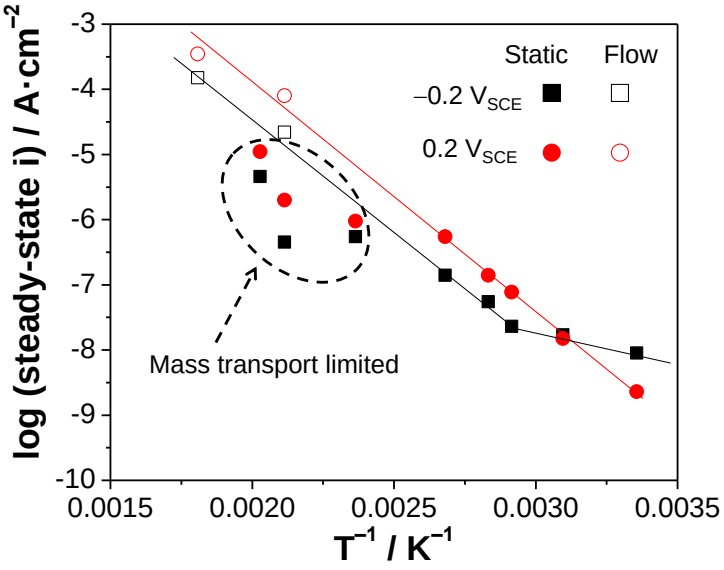

Figure 8.8: Arrhenius plot of measured steady state currents for 0.2 V_{SCE} and –0.2 V_{SCE}.

8.3.3 Oxide Film Characterization by EIS and Surface Analysis

Periodically, EIS was performed to characterize the oxide film present on the electrode. As the static cell is not an equivalent ideal electrochemical cell design as used at temperatures ≤ 80 °C, EIS analysis is limited. In the static cell, the 220 °C samples were removed for Raman analysis. Since the Raman analysis was performed ex-situ, the samples were removed after the system was cooled to a safe handling temperature and the system was depressurized. Once removed from the static cell, samples were rinsed with deionized water, dried under an argon gas flow, and stored under vacuum until Raman analysis was performed. The effects of the removal process and the potential introduction of oxygen at temperatures above room temperature are discussed.

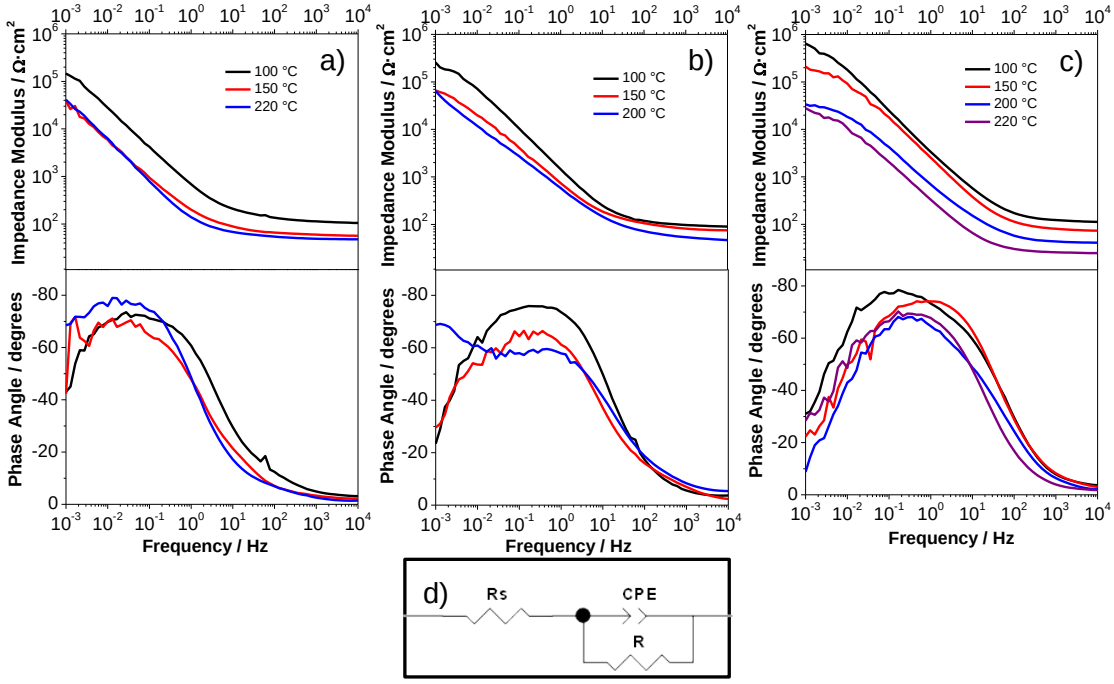

Figure 8.9: Electrochemical impedance spectra for the films grown at (a) –0.7 V_{SCE}, (b) –0.2 V_{SCE}, and (c) 0.2 V_{SCE} as a function of temperature after 70 h of film growth. The equivalent circuit (d) that was fit to all data is shown.

8.3.3.1 Film Grown in Ox I

A circuit composed of a solution resistance, and a parallel resistor and CPE was fit to all experimental data, Figure 8.9d. The fitting results of resistance and capacitance are show in Figure 8.10. Following the same assumptions made at temperatures ≤ 80 °C, the spatial inhomogeneity distribution developed by Brug et al. [7] was used to convert CPE to capacitance values. As observed at temperatures ≤ 80 °C, large capacitance values were measured, which increased with increasing temperature. The observed capacitance increase is attributed to a pseudo capacitance, resulting from electron transfer

between surface cations (Fe^{II}/Fe^{III}) coupled to processes such as transfer or adsorption/desorption of protons ($O^{2-} \leftrightarrow OH^-$) at the interface [8-10]. The origin of a pseudo capacitance depends on the system, but is generally accepted to arise from electron transfer between cation sites coupled with charge transfer to adsorbed or aqueous species. The additive effect of a faradaic process at the oxide/solution interface inducing a pseudo capacitance appears to still be present at temperatures ≥ 100 °C.

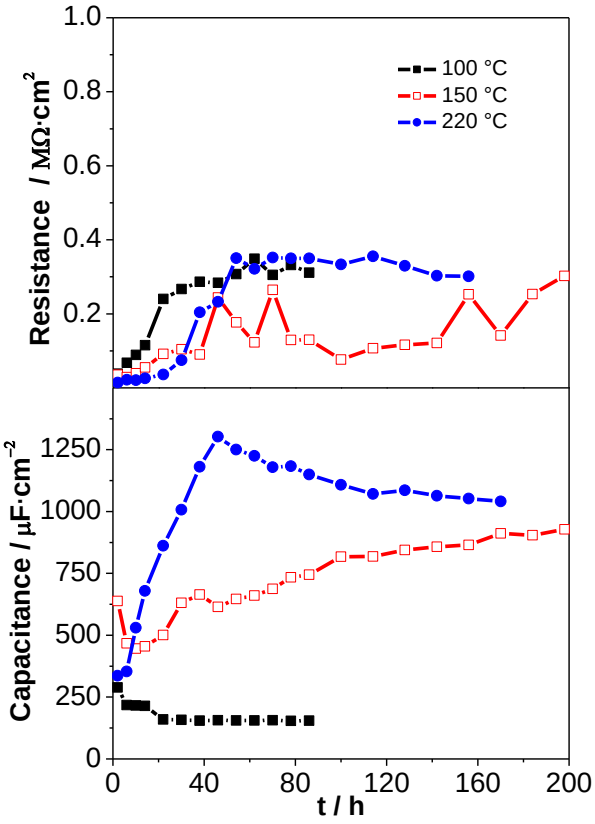

Figure 8.10: Equivalent circuit fitting results for the resistance and capacitance for potentiostatic film growth at –0.7 V_{SCE}.

On top of the temperature effects on the faradaic process, the increase in dissolution may contribute to an increase in surface roughness. Since capacitance is proportional to surface area and resistance is inversely proportional to surface area [11], an increase in surface area would add to the observed trends [12]. At all temperatures the resistance was initially low, before increasing, and becoming an approximately constant value after 40 h. This suggests an initially reactive surface, with minimal charge transfer resistance that steadies to a constant value as oxide growth progresses.

Raman spectroscopy was performed on the 220 °C samples. Comparison to standard iron oxide minerals, (Figure 8.11) shows that the oxide was Fe_3O_4, with a main characteristic peak at 670 cm^{-1}, Figure 8.12a [13, 14]. The surface shows some roughness, but is relatively uniform on the macroscopic scale, Figure 8.12. From the Raman, EIS, and above potentiostatic analysis, it can be summarized that over the temperatures studied, in Ox I, the oxidation process is dominated by the formation a relatively electronically conductive layer of Fe_3O_4, which has accelerated dissolution as temperature increases.

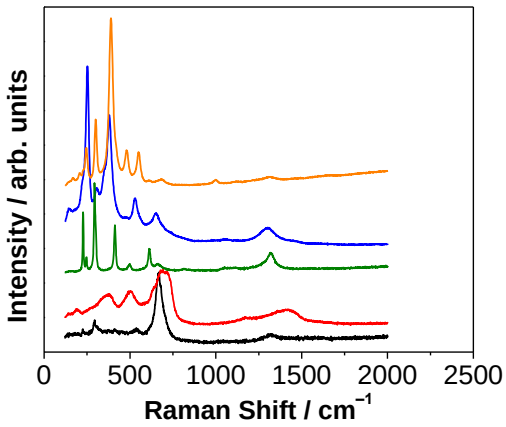

Figure 8.11: Raman spectra of reference iron oxide minerals.

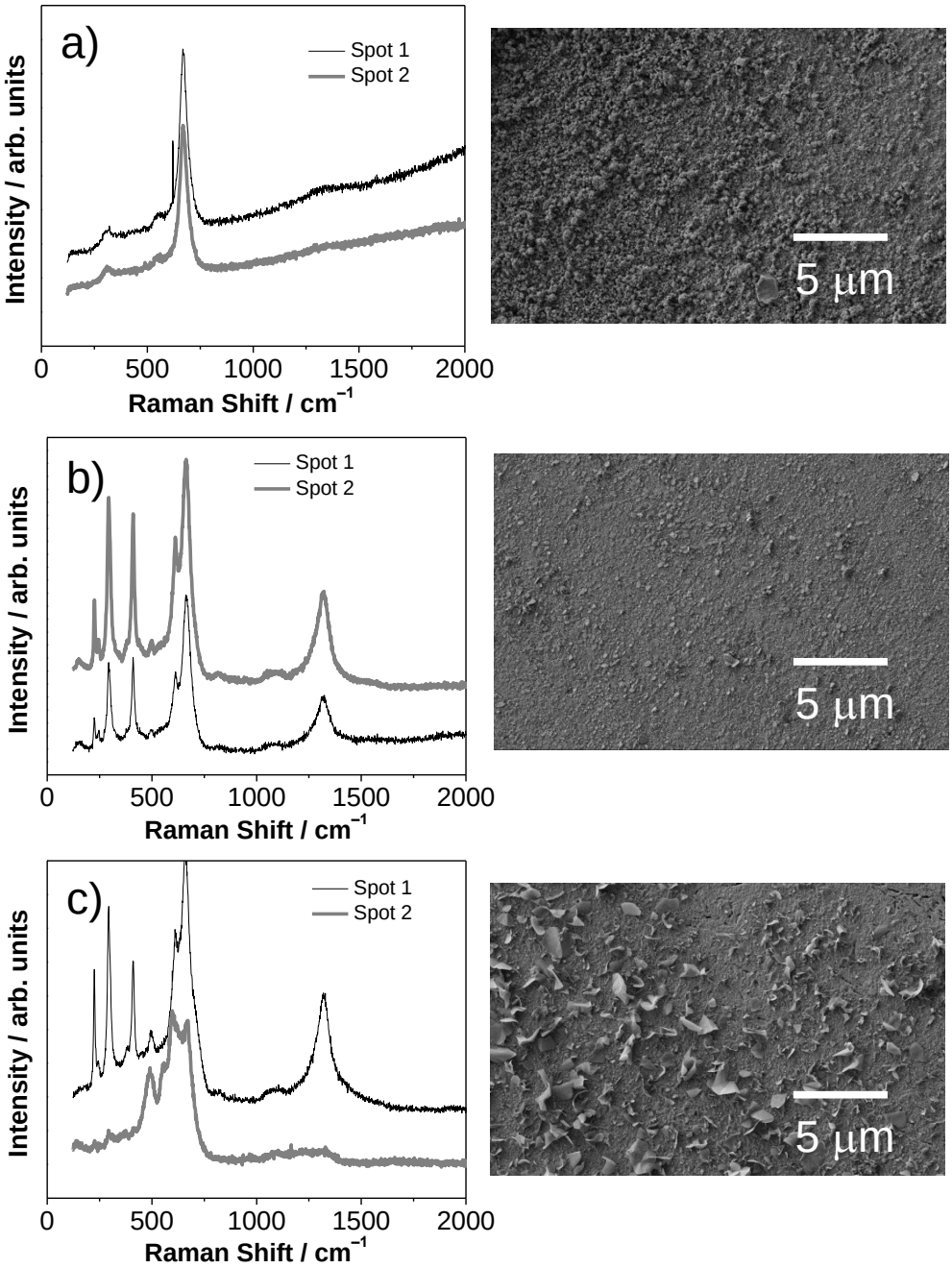

Figure 8.12: Raman spectra and SEM micrographs of samples removed after film growth at 220 °C and potentials of (a) –0.7 V_{SCE}, (b) –0.2 V_{SCE}, and (c) 0.2 V_{SCE}.

8.3.3.2 Film Grown in Ox II

For the 100 °C and 150 °C experiments, a single RC circuit, Figure 8.9d, could be fit to the data. The fitting results of resistance and capacitance are show in Figure 8.13. Following the same assumptions made at temperatures ≤ 80 °C, the depth time constant distribution developed by Hsu and Mansfeld [15, 16] was used to convert CPE to capacitance values, assuming the impedance was resulting from a distribution within the depth of the oxide layer. The results show a steady increase in resistance in the first 20 h. The resistance at 100 °C was approximately twice as large as the resistance at 150 °C. The capacitance was much larger at 150 °C, and had a slight decrease with time, after an initial increase in the first 20 h, while the resistance had a slight increase with time after the initial transition. Over time, the increase in resistance, coupled with a decrease in capacitance is attributed to oxide film thickening. At 100 °C the capacitance was constant. The overall decrease in resistance and increase in capacitance from 100 °C to 150 °C suggest the formation of an increasingly defective oxide as temperature is increased [17]. As discussed in section 8.3.3.1, an increased surface roughness due to dissolution may also contribute to the observed trends. Additionally as discussed with the current behaviour, an increase in dissolution is expected with increasing temperature. Therefore at a single potential, if the dissolution is high and larger than the effects of temperature promoting the formation of Fe_3O_4, the oxide film would become thinner. This would also give the observed trends of lower resistance and higher capacitance as temperature increased. Above 150 °C a change in the EIS spectra occurred; however, due to the onset at the lowest frequency measured, this change could not be completely characterized. One possibility of an additional RC may be due to the increased

broadening of peak A3 with temperature, Figure 8.2, and the system may have been at a transition between Fe_3O_4 and γ-Fe_2O_3.

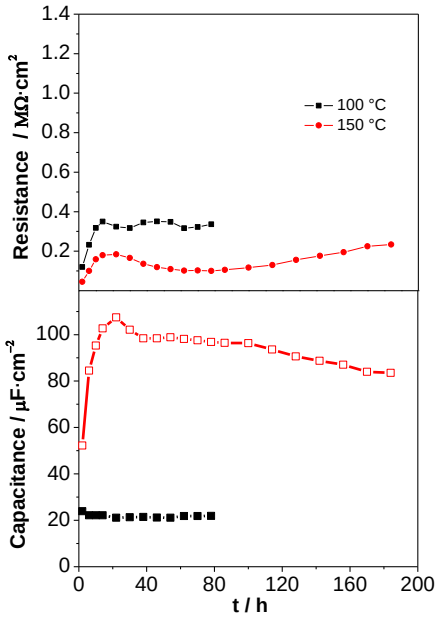

Figure 8.13: Equivalent circuit fitting results for the resistance and capacitance for potentiostatic film growth at –0.2 V_{SCE}.

The SEM micrograph of the surface shows a relatively uniform and compact structure. The Raman spectra of the sample removed after heating to 150 °C showed clear peaks at 1315 cm^{-1}, 670 cm^{-1}, 610 cm^{-1}, 410 cm^{-1}, 293 cm^{-1}, and 222 cm^{-1}, Figure 8.12b. The peak at 670 cm^{-1} is the main characteristic peak of Fe_3O_4 [13, 14], and the other peaks are all characteristic of hematite (α-Fe_2O_3), Figure 8.11 . Under the conditions studied, of a borate solution at pH 10.6, α-Fe_2O_3 has only been observed in the presence of an O_2 containing cover gas (Chapter 6). Therefore, it is likely that the introduction of O_2 during the sample removal led to the oxidation or conversion of

species to α-Fe_2O_3. Since α-Fe_2O_3 was not observed in Ox I, it is not likely that the formation of α-Fe_2O_3 came from the oxidation of Fe_3O_4. Rather, it is possible that the introduction of oxygen led to a thermodynamic conversion of a species present in Ox II. It is likely that γ-Fe_2O_3, which is believed to be present in Ox II, converted to α-Fe_2O_3. Studies of the Raman spectra of Fe-Ni-Cr alloys have shown that with the introduction of large enough concentrations of O_2, γ-M_2O_3 oxides disappear, while M_3O_4 and α-M_2O_3 remain (M represents any of the metallic species) [18]. The conversion of γ-Fe_2O_3 to α-Fe_2O_3 is thermodynamically favourable [4], although γ-Fe_2O_3 has been shown to be stable at temperatures > 300 °C [19], and the conversion has been shown to increase with increasing surface hydration [20]. Therefore, although the sample was removed as quickly as possible, the oxygen ingress during system depressurization likely resulted in the conversion of γ-Fe_2O_3 to α-Fe_2O_3. The high intensity of the Fe_3O_4 670 cm^{-1} peak relative to the α-Fe_2O_3 610 cm^{-1} peak suggests that there is at least 2-3 times more Fe_3O_4 than α-Fe_2O_3 on the surface due to the differing Raman scattering probabilities [21]. The relative ratio of the α-Fe_2O_3 610 cm^{-1} peak to the lower wavenumber peaks also suggests that it is not a pure α-Fe_2O_3 phase, rather a transitional hydrated α-Fe_2O_3-like phase [21].

8.3.3.3 Film Grown in Ox III

For all temperatures the circuit in Figure 8.9d could be fit to the data. The fitting results of resistance and capacitance are show in Figure 8.14. Following the same assumptions made at temperatures ≤ 80 °C, the depth time constant distribution developed by Hsu and Mansfeld was used to convert CPE to capacitance values [15, 16],

assuming the impedance was resulting from a distribution within the depth of the oxide layer. The CPE α values at 220 °C decreased from 0.8 to 0.75 during the experiment and therefore conversion of CPE to capacitance was not performed. The results show an increase in resistance with time for all temperatures, with the larger changes occurring at the lower temperatures, likely resulting from oxide film thickening. Similar to Ox II, there was a decrease in resistance and increase in capacitance as the temperature increased, which like in Ox II, could be the result of an increase of defects within the oxide structure, along with increased dissolution. As in the case of the other two oxidation regions, an increased surface roughness may also contribute to the observed trends. Most interestingly, there was no clear evidence of a diffusion related process, as was observed between 50 °C and 80 °C. The diffusion process was attributed to a micro-fracture mechanism resulting from the oxidation of Fe_3O_4 to γ-FeOOH. During the initial heating and film growth process, spikes in the measured current were observed, Figure 8.7c, which could be attributed to the micro-fracture process; however, they were not present during the prolonged polarization, when EIS analysis was performed. It appears as though the thickening of the underlying Fe_3O_4 layer is limiting the effects of any film micro-fracture, which is likely occurring near the oxide/solution interface.

As temperature is increased the relative surface coverage of γ-Fe_2O_3 may be limited, resulting in exposed magnetite to undergo further oxidation to FeOOH. At the higher temperatures, the alpha phase may begin to form preferentially. This would result in both an increase in surface area and some changes in the oxide structure, explaining the changes in resistance capacitance with temperature. There is evidence that an additional oxide phase formed at the oxide/solution interface at 220 °C, Figure 8.12,

however, the Raman spectra only clearly showed the presence of Fe_3O_4 and α-Fe_2O_3. For similar reasons described for γ-Fe_2O_3, some surface FeOOH may have been converted to α-Fe_2O_3 [20]. As discussed in section 8.3.3.2 the observed phase is likely a transitional hydrated Fe^{III} phase.

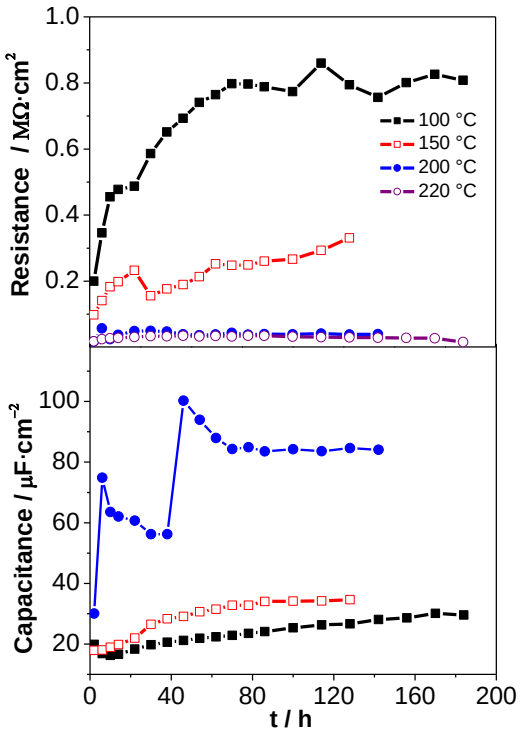

Figure 8.14: Equivalent circuit fitting results for the resistance and capacitance for potentiostatic film growth at 0.2 V_{SCE}.

8.4 CONCLUSIONS

The results between 100 °C and 280 °C appear to present an oxidation mechanism that is similar to that established below 100 °C. The oxidation process is largely dominated by the formation of a thick, but electronically conductive Fe_3O_4 layer. An

increase in potential can result in some oxidation of Fe_3O_4, most likely to a mixed Fe_3O_4/γ-Fe_2O_3-like structure at the oxide/solution interface. The mixed Fe_3O_4/γ-Fe_2O_3 oxide had a decrease in resistance as temperature increased; however, no oxide breakdown occurred. The formation of previously observed oxyhydroxides was largely not observed. Over the entire potential window studied, this study further concludes that temperature affects the oxide growth mainly by influencing the rates of thermal processes, and most specifically, dissolution rates.

8.5 REFERENCES

[1] W. Xu, K. Daub, X. Zhang, J.J. Nöel, D.W. Shoesmith, J.C. Wren, Electrochim. Acta, 54 (2009) 5727-5738.
[2] B. Beverskog, I. Puigdomenech, Corros. Sci., 38 (1996) 2121-2135.
[3] W.G. Cook, R.P. Olive, Corros. Sci., 55 (2012) 326-331.
[4] R.M. Cornell, U. Schwertmann, The Iron Oxides: Structures, Properties, Reactions, Occurrences and Uses, 2nd Ed., Weinheim, New York, NY, (2003).
[5] K. Yazdanfar, X. Zhang, P.G. Keech, D.W. Shoesmith, J.C. Wren, Corros. Sci., 52 (2010) 1297-1304.
[6] P.S. Sidhu, R.J. Gilkes, R.M. Cornell, A.M. Posner, J.P. Quirk, Clays Clay Miner., 29 (1981) 269-276.
[7] G.J. Brug, A.L.G. Van Den Eeden, M. Sluyters-Rehbach, J.H. Sluyters, J. Electroanal. Chem., 176 (1984) 275-295.
[8] C. Lin, J.A. Ritter, B.N. Popov, R.E. White, 146 (1999) 3168-3175.
[9] S.-Y. Wang, K.-C. Ho, S.-L. Kuo, N.-L. Wu, J. Electrochem. Soc., 153 (2006) A75-A80.
[10] A.A.F. Grupioni, T.A.F. Lassali, J. Electrochem. Soc., 148 (2001) A1015-A1022.
[11] M. Orazem, B. Tribollet, Electrochemical Impedance Spectroscopy, John Wiley & Sons, New York, NY, (2008).
[12] E. Laouini, M. Hamdani, M.I.S. Pereira, Y. Berghoute, J. Douch, M.H. Mendonça, R.N. Singh, Int. J. Electrochem. Sci., 4 (2009) 1074-1084.
[13] O.N. Shebanova, P. Lazor, J. Solid State Chem., 174 (2003) 424-430.
[14] D.L.A. de Faria, S. Venancio Silva, M.T. de Oliveira, J. Raman Spectrosc., 28 (1997) 873-878.
[15] C.H. Hsu, F. Mansfeld, Corros., 57 (2001) 747-748.
[16] B. Hirschorn, M.E. Orazem, B. Tribollet, V. Vivier, I. Frateur, M. Musiani, Electrochimica Acta, 55 (2010) 6218-6227.

[17] J. Pan, C. Leygraf, R.F.A. Jargelius-Pettersson, J. Linden, Oxid. Met., 50 (1998) 431-455.
[18] C.S. Kumai, T.M. Devine, Corros., 61 (2005) 201-218.
[19] A.U. Gehring, H. Fischer, M. Louvel, K. Kunze, P.G. Weidler, Geophys. J. Int., 179 (2009) 1361-1371.
[20] A. Navrotsky, L. Mazeina, J. Majzlan, Science, 319 (2008) 1635-1638.
[21] D.L.A. De Faria, F.N. Lopes, Vib. Spectrosc., 45 (2007) 117-121.

Chapter 9

Summary and Future Work

9.1 SUMMARY

This thesis examined the mechanism of carbon steel corrosion and the effects of gamma radiation on the corrosion process. To electrochemically characterize the oxidation process, surface oxide film growth and conversion on carbon steel in deaerated solutions at pH 10.6 was studied as a function of potential and temperature under both potentiostatic and potentiodynamic conditions. From the perspective of oxide film growth and conversion, the behaviour as a function of potential can be divided into three potential regions. In region Ox I, a uniform layer of a Fe_3O_4-like inverse spinel oxide is formed that grows by a solid state charge transport mechanism. Iron dissolution occurs via hydration of Fe^{II} (and Fe^{III} to a smaller extent) at the oxide/water interface followed by diffusion of the hydrated species from the interface to the aqueous phase. The dissolution rate increases with temperature, but at temperatures > 70 °C, the Schikorr reaction accelerates the conversion of the hydrated species to Fe_3O_4. A balance between increased dissolution rates and increased Fe_3O_4 formation rate was seen as the corrosion temperature was increased from 25 °C to 280 °C. In Ox II, the Fe_3O_4 layer continues to grow, but the potential is high enough to convert the Fe_3O_4-like layer to a more γ-Fe_2O_3-like layer. The oxide growth and conversion in this region also occurs by a solid-state charge transport mechanism. As the concentration of Fe^{II} decreases due to further oxidation to Fe^{III} near the oxide/water interface, the rate of iron dissolution is greatly suppressed and the oxide becomes more insulating. In this region, thickening of the oxide layer is limited by the anodic conversion of the more conducting Fe_3O_4 phase to the more insulating γ-Fe_2O_3 phase. As in Ox I, increasing

temperature promotes both the rate of formation of Fe_3O_4 and the rates of oxide dissolution. In Ox III anodic conversion of the Fe_3O_4/γ-Fe_2O_3 oxide to γ-FeOOH can induce micro-fractures, but, in the absence of aggressive anions, the surface quickly repassivates. The oxide layer can grow by continuous film fracture and repassivation, producing a thick but defective (or porous) oxide film. The oxidation to γ-FeOOH is suppressed at temperatures > 100 °C.

The effects of γ-irradiation and the presence of H_2O_2 on carbon steel corrosion at pH 10.6 and room temperature were investigated through electrochemical analysis. Both E_{CORR} and R_P behaviour under irradiation conditions could be simulated by use of a test solution containing H_2O_2, indicating that H_2O_2 is the key radiolysis product controlling carbon steel corrosion. Both the steady-state E_{CORR} and R_P are strong functions of $[H_2O_2]$, but they are nearly independent of the initial oxide film composition. The dependence of the E_{CORR} and R_P behaviour on $[H_2O_2]$ showed two distinct ranges. For $[H_2O_2] < 10^{-3}$ M, E_{CORR} is determined mainly by the cathodic half-reactions of H_2O_2 that yield OH^-, coupled with the anodic half-reactions of the oxide-covered steel surface. This results in oxidation to form a graded $Fe_3O_4/\ \gamma$-Fe_2O_3 oxide film. For $[H_2O_2] \geq 10^{-3}$ M, E_{CORR} is determined primarily by the cathodic half-reactions of H_2O_2, coupled with the anodic half-reactions of H_2O_2.

Surface analyses of carbon steel coupons corroded 80 °C and 150 °C found that the chemical and phase composition of the oxide formed under deaerated conditions is Fe_3O_4 and hydrated Fe^{II} and Fe^{III} species adsorbed on the Fe_3O_4 surface. Variation in the corrosion temperature and solution pH may affect the rates of oxide film growth and dissolution, but they do not play a significant role in determining the chemical composition of the oxide film. At near neutral pH significant dissolution of the growing oxide film results in a porous and less uniform and protective oxide than the films grown at more basic pHs. Electrolyte concentration also has

significant effects on film growth and dissolution. An increase in electrolyte concentration can increase the rates of iron dissolution from the oxide/solution interface, and this, in turn, affects the rates of solid-state oxide growth and the rate of approach of the system to steady state. To further understand the role of solution ionic strength on the corrosion process the test matrix will have to be expanded to include a larger variation of electrolyte concentration at a single pH. This research has also shown that the concentration of dissolved Fe^{2+} can affect the relative dissolution and oxidation rates of hydrated ferrous hydroxides. The role of dissolved Fe^{2+} was highly dependent on the potential on the carbon steel surface, since this potential determined the nature of the thermodynamically favourable oxidation process.

When the effects of system irradiation were isolated in coupon studies, it was found that irradiation affects the oxide growth mechanism in all conditions tested. In situations of limited passivation, such as corrosion of a bare metal surface, or in solutions with neutral or acidic pH, irradiation can enhance the rate of iron corrosion. When a passive film begins to form, the irradiation can lead to some increased passivation (by promoting Fe^{II} oxidation to Fe^{III}) and this can limit further corrosion. Due to the oxidation mechanism of Fe_3O_4, which was studied as a function of temperature electrochemically, oxidation of Fe^{II} to Fe^{III} does not lead to changes in the oxide structure. Rather, the oxidation results in a graded distribution of Fe^{II} and Fe^{III} in the corrosion film, with more Fe^{II} near the metal/oxide interface and more Fe^{III} at the oxide/water interface. However, the extent of oxidation at elevated temperatures was somewhat reduced compared to room temperature because the increase in the net metal oxidation rate with increased temperature also led to an increase in the net dissolution rate.

9.2 FUTURE WORK

This research has added to our understanding of the oxidation mechanism on carbon steel and the influence of gamma irradiation on the corrosion process. While the combination of results from separate electrochemical and surface analytical studies has been useful in elucidating the oxidation mechanism at elevated temperatures under gamma radiation, it would be desirable to look at integrated in-situ electrochemical studies in a radiation field at elevated temperatures. Due to the constraints of a gammacell, this type of experiment is a challenge and it requires the development of a small volume electrochemical pressure vessel with microelectrodes. As shown in this work, the initial metal corrosion and oxide growth period would be best characterized using in-situ electrochemical studies. Future work should also, extend our understanding of how dissolved Fe^{2+}affects oxide film formation under irradiation and at elevated temperatures.

Under the conditions studied, the key water radiolysis product that affects the corrosion process is hydrogen peroxide. The steady-state concentrations of water radiolysis products like H_2O_2 have a square root dependence on the radiation dose rate. The work presented in Chapter 4 on tests with varying concentrations of peroxide present, were in a way, a simulation of the effect of varying the dose rate. These experiments however, are an imperfect simulation of irradiation. They neglected the impact of other water radiolysis products and were limited to room temperature studies. At higher temperatures peroxide decomposition and the formation of O_2 by radiolysis may be more important. Studies on the effect of varying the radiation dose rate at elevated temperatures will unfortunately require access to radiation sources of different strengths as the limited volume in a gammacell precludes the use of lead shielding to vary the dose to the experimental vessel.

Radiation-assisted carbon steel corrosion is a topic of real interest in studies of options for used nuclear fuel disposal. Many disposal options include periods in which a carbon steel container would not be in contact with water, but would instead be exposed to air and undergoing gas-phase corrosion (either aerobic or anaerobic). Gas phase corrosion of carbon steel in an irradiation field is not well understood. We have performed some preliminary experiments in which carbon steel coupons were located in the gas phase, above a solution. Limited characterization of the corroded coupons has found the gas-phase corrosion process to be dominated by reactions associated with isolated water droplets on the carbon steel surface. The results were not sufficient to extract the effect that irradiation plays on that process. Further work is required, particularly to determine the function of humidity and to understand the localized corrosion process where the concentrations of radiolysis products in very small volumes of water may differ from those achieved in larger scale solutions.

Kevin Daub

EDUCATION

Ph.D. in Physical Chemistry, Western University 09/2007-Present

Honours Specialization in Chemistry, Western University 09/2003-05/2007

RELATED WORK EXPERIENCE

Graduate Student 09/2007-Present

- Electrochemical studies of the corrosion of carbon steel; experiments conducted with and without the presence of a gamma radiation field.
- Training and experience in the use of a gamma irradiation system
- Experience with the use of high-temperature autoclaves (up to 280 °C).
- Experience with a number of electrochemical techniques and analyses.
- Training and experience in the use of advanced surface analysis techniques.

Visiting Researcher at Korean Atomic Energy Research Institute 03/2012-07/2012

- International research experience using a high-temperature flow system equipped with electrochemical monitoring to study carbon steel corrosion.
- Conducted additional chemical research in areas relevant to the nuclear power industry.
- Gained experience with additional electrochemical hardware and software (Bio-Logic potentiostat and EC-Lab analysis software) and experience in an industrial research environment.

Teaching Assistant – Microscopic and Macroscopic Physical Chemistry 09/2007-04/2011

AWARDS & ACHIEVEMENTS

- 2011-2012: OGS Graduate Scholarship
- 2009-2010: OGS Graduate Scholarship
- 2007-2009: NSERC PGSM Graduate Scholarship
- 2011: Canadian Nuclear Society R.E. Jervis Award for excellence in research and development carried out by a full time graduate student in nuclear engineering or related fields
- 2010: 1st place poster prize for Ph.D. category 2010 Canadian Nuclear Society Conference
- 2009: 1st place poster prize for surface science chemistry at 92nd Canadian Chemistry Conference and Exhibition
- 2007: A.E. Scott Medal and Prize (Highest overall average for undergraduate studies in chemistry)

PUBLICATIONS

1. L. Wang, **K. Daub**, Q. Knapp, J.J. Noël , Z. Qin, J.C. Wren, *Effect of Ferrous Ions on Oxide Film Formation and Conversion on Stainless Steel*, J. Electrochem. Soc. 159 (2012) C503.

2. L. Wang, **K. Daub**, Z. Qin, J.C. Wren, *Effect of Dissolved Ferrous Iron on Oxide Film Formation on Carbon Steel*, Electrochim. Acta. 76 (2012) 208.

3. **K. Daub**, X. Zhang, L. Wang, Z. Qin, J.J. Noël, J.C. Wren, *Oxide Growth and Conversion on Carbon Steel as a Function of Temperature Over 25 and 80°C Under Ambient Pressure*, Electrochim. Acta. 56 (2011) 6661.

4. **K. Daub**, X. Zhang, J.J. Noël, J.C. Wren, *Gamma-Radiation-Induced Corrosion of Carbon Steel in Neutral and Mildly Basic Water at 150°C*, Corros. Sci. 53 (2011) 11.

5. **K. Daub**, X. Zhang, J.J. Noël, J.C. Wren, *Effects of Gamma-Radiation Versus H_2O_2 on Carbon Steel Corrosion*, Electrochim. Acta. 55 (2010) 2767.

6. W. Xu, **K. Daub**, X. Zhang, J.J. Noël, D.W. Shoesmith, J.C. Wren, *Oxide Formation and Conversion on Carbon Steel in Mildly Basic Solutions*, Electrochim. Acta. 54 (2009) 5727.